ASSESSMENT OF SINGLE CRYSTAL X-RAY DIFFRACTION DATA QUALITY

DISSERTATION

zur Erlangung des mathematisch-naturwissenschaftlichen Doktorgrades
„Doctor rerum naturalium“
der Georg-August Universität Göttingen
im Promotionsprogramm Chemie
der Georg-August University School of Science (GAUSS)

vorgelegt von
Lennard Krause
aus Langenhagen

Göttingen, 2017

Betreuungsausschuss
Prof. Dr. Dietmar Stalke
Prof. Dr. Bo B. Iversen

Mitglieder der Prüfungskommission
Referent: Prof. Dr. Dietmar Stalke
Korreferent: Prof. Dr. Bo B. Iversen

weitere Mitglieder der Prüfungskommission
Prof. George M. Sheldrick
Prof. Dr. Ricardo Mata
Dr. Heidrun Sowa
Dr. Francesca P. A. Fabbiani

Tag der mündlichen Prüfung: 02.03.2017

“This page is intentionally left blank.”

Table of contents

CHAPTER 1:

INTRODUCTION AND THEORETICAL BACKGROUND

1 General introduction

Before delving into the theoretical foundations, a few words on the motivation behind this document. This PhD thesis focuses on single crystal X-ray diffraction data quality, the handling of systematic errors during data collection and the appropriate modelling of experimental charge density distributions. The development of new methods as well as the adaption of already known concepts to these topics will also be addressed in detail. A large part of the investigations underlying this thesis was related to the proper handling of systematic errors in X-ray diffraction experiments. Moreover, the possibility of development of empirical corrections and the subsequent adaptation were of general interest.

Special attention was put on the understanding of the solid-state fluorescence of 9,10-bis(diphenylthiophosphoryl)anthracene, its co-crystals and polymorphs. Here, the investigation of intermolecular attractions following a combined approach using high resolution X-ray data as well as computational models and, in cooperation, solid-state NMR. In the regard of charge densities, comprehensive combined X-ray/neutron multipole model refinements were carried out and the concept of cross-validation was adopted to this investigative field of science.

A theoretical overview of the fundamentals is given following this short introduction; however, in order to help the understanding of the individual chapters, short additions are given at their beginnings (whether theoretical or informative in nature). There are several general texts on single crystal X-ray structure determinations, the interested reader is directed towards Massa (2009), Bennett (2010) and of course Johnson and Levy (1974) as these books will be cited frequently in this introduction and build the foundation of the following Chapters.

Parts of this PhD thesis have been published separately:

1. Lennard Krause, Regine Herbst-Irmer, Dietmar Stalke 'An empirical correction for the influence of low-energy contamination' *J. Appl. Cryst.* **2015**, *48*, 1907 – 1913.
2. Lennard Krause, Regine Herbst-Irmer, George M. Sheldrick, Dietmar Stalke 'Comparison of silver and molybdenum microfocus X-ray sources for single crystal structure determination' *J. Appl. Cryst.* **2015**, *48*, 3 – 10.

1.1 Foundations of X-ray diffraction

While a microscope uses light to image a given sample, X-rays, with their wavelength being about four orders of magnitudes shorter than the visible light, image the electronic charge. The X-ray diffraction experiment is effectively a microscope for the electron density in a periodically repeating material referred to as a single crystal. The periodicity can be described by a smallest unit, the unit cell that is tightly packed in three dimensions. The unit cell is adequately characterised by the primitive vectors $\boldsymbol{a},\boldsymbol{b},\boldsymbol{c}$ (or in Cartesian coordinates defined by its lengths a, b, c and angles α, β, γ) and every point r inside the unit cell is accessible by its spatial coordinates (x, y, z).

$$r = \boldsymbol{a} \cdot x + \boldsymbol{b} \cdot y + \boldsymbol{c} \cdot z \qquad \text{Eq. 1-1}$$

X-ray diffraction is the term describing the elastic scattering of photons by a three dimensional lattice. With the X-ray photons having dual properties and behaving like matter waves through the de Broglie relationship,

$$\lambda = \frac{h}{p} \qquad \text{Eq. 1-2}$$

with h being the Planck constant and p the magnitude of momentum. Detailed descriptions are available in numerous textbooks and the fundamentals will only be outlined briefly. Assuming that $\boldsymbol{k}_i$ describes a vector perpendicular to the incident wave, the relationship to the momentum is given by

$$p = \left[\frac{h}{2\pi}\right] \boldsymbol{k}_i \qquad \text{Eq. 1-3}$$

If the wave is being scattered by the crystalline sample, a scattered wave specified by the vector $\boldsymbol{k}_d$ results. Therefore, the total scattering wave vector $\boldsymbol{\Delta k}$ is given by:

$$\boldsymbol{\Delta k} = \boldsymbol{k}_i - \boldsymbol{k}_d \qquad \text{Eq. 1-4}$$

Connecting the momentum with the de Broglie wavelength, it follows that the length of the wave vector is given by the *reciprocal* of the wavelength. To facilitate constructive interference, the path difference must be an integer multiple of the wavelength.

$$|\Delta \boldsymbol{k}| = n \cdot \lambda, \qquad n \in \mathbb{Z} \qquad \text{Eq. 1-5}$$

Within the elastic scattering approximation, the energy of the incoming wave is equal to the energy of the diffracted wave, $\boldsymbol{k}_\mathrm{i}$ must be equal to $\boldsymbol{k}_\mathrm{d}$. Considering a single crystal, by definition a periodic arrangement of molecules or atoms, that can adequately be described by one building block, called the unit cell. From this construct, the complete crystal can be described only by applying translational symmetry in all three dimensions.

$$\mathbf{a} \cdot \Delta \boldsymbol{k} = |\mathbf{a}| \cdot |\Delta \boldsymbol{k}| \cdot cos(\mathbf{a}, \Delta \boldsymbol{k}) = h \qquad \text{Eq. 1-6}$$

$$\mathbf{b} \cdot \Delta \boldsymbol{k} = |\mathbf{b}| \cdot |\Delta \boldsymbol{k}| \cdot cos(\mathbf{b}, \Delta \boldsymbol{k}) = k \qquad \text{Eq. 1-7}$$

$$\mathbf{c} \cdot \Delta \boldsymbol{k} = |\mathbf{c}| \cdot |\Delta \boldsymbol{k}| \cdot cos(\mathbf{c}, \Delta \boldsymbol{k}) = l \qquad \text{Eq. 1-8}$$

The Laue equations (with Laue indices h, k, l being integer numbers) are conditions for the occurrence of constructive interference in a scattering process, exactly when the change of the wave vector equals a primitive (or reciprocal) lattice vector.

As the scattering vector has units of reciprocal length ($\mathbf{\Delta k} = 2\pi/\lambda$) it is convenient to consider the reciprocal lattice with the corresponding reciprocal lattice vectors $\boldsymbol{a}^*$, $\boldsymbol{b}^*$ and $\boldsymbol{c}^*$ defined by

$$\mathbf{a}^* = \frac{\boldsymbol{b} \times \boldsymbol{c}}{V}, \qquad \mathbf{b}^* = \frac{\boldsymbol{a} \times \boldsymbol{c}}{V}, \qquad \mathbf{c}^* = \frac{\boldsymbol{a} \times \boldsymbol{b}}{V}, \qquad V = (\boldsymbol{a} \times \boldsymbol{b}) \cdot \boldsymbol{c} \qquad \text{Eq. 1-9}$$

with the diffracted wave vector $\boldsymbol{K} = h \cdot \boldsymbol{a}^* + k \cdot \boldsymbol{b}^* + l \cdot \boldsymbol{c}^*$ reducing the Laue conditions to

$$\Delta \boldsymbol{k} = \boldsymbol{K} \qquad \text{Eq. 1-10}$$

and constructive interference occurs if the scattering vector can be described by a reciprocal lattice vector.

W. L. Bragg and W. H. Bragg reduced the Laue equations into an expression without vector representations. Instead of considering the diffraction by every molecule, W. L. Bragg proposed the astonishingly simple formulation where X-rays that are being reflected by planes, interfere with each other.

$$2d \sin\theta = n\lambda, \qquad n \in \mathbb{Z} \tag{Eq. 1-11}$$

Here, n is the diffraction order, λ the wavelength, d the spacing between lattice planes and θ the scattering angle (angle between the incident beam and the plane the scattering occurs on). This formulation allows the concept of resolution to be directly accessible, given as the smallest measured plane distance d, and features relying on distances below that value cannot be reliably resolved. However, with the Bragg equation having an explicit wavelength term it can only be used describing monochromatic X-ray diffraction.

Even though the methodical approach is different for Bragg and Laue they are essentially equivalent in that the Bragg concept of diffraction planes merges perfectly with the Miller indices (Miller, 1839). Miller indices multiplied with the diffraction order yields the Laue indices), a way to characterise reflections by an assignment to their respective diffraction plane that is uniquely defined by h, k and l, the plane intersections with the crystal's primitive vectors (or unit cell edges).

If reflections are measured experimentally, the equations allow the retracing of the crystal orientation relative to the measurement devices' space. Based on the diffraction condition and combined with the crystal orientation, expected reflection positions can be predicted. From the diffraction pattern the unit cell constants and the crystal symmetry is directly accessible by the so-called indexing. This algorithm makes use of all available information e.g. the diffractometer angles ϕ, χ, ω and θ, the detector distance d along with the spatial coordinates x and y, varying the unit cell dimensions a, b, c, α, β, γ to find the smallest possible unit cell adopting highest symmetry and maximising the number of reflections with successfully assigned integer Miller indices. The unique diffraction pattern has its origin only in the symmetry elements of the crystal system and does by no means allow for a precise assignment of the atom distribution inside the crystal, e.g. the target molecular structure. The relative intensity distribution, however, contains all the information about the electron density and therefore indirectly the positions of the atoms as well. It is again the interference, which was shown at the beginning of this chapter, to give rise to the distinct reflection pattern that now uniquely shapes the intensity of every single reflection. All the atoms in the crystal are exposed to the incident beam causes elastic scattering and their spatial arrangement contributes to the resulting intensity of the diffracted beam by constructive and destructive interference. Every reflection hkl is an inherent part of the complete electron density $\rho(\boldsymbol{r})$ of the crystal. When considering all symmetry equivalents, it is unique to the molecular structure and therefore named the structure factor $F(hkl)$.

$$F(hkl) = \int_V \rho(\boldsymbol{r}) \exp\{2\pi i(h\boldsymbol{a}^* + k\boldsymbol{b}^* + l\boldsymbol{c}^*)\boldsymbol{r}\} d\boldsymbol{r} \tag{Eq. 1-12}$$

The structure factor, a superposition of individual scattering processes, being a periodic and continuous signal, therefore belonging to the frequency domain, can be dismantled into individual components. Since the considered object is periodic and diffraction cancels out in all directions except those e.g. specified by integer Miller indices, it involves a summation over all structure factors and therefore it is referred to as Fourier summation (Fourier, 1822) (the cell volume V being a scale factor to keep the units in electrons per unit cell).

$$\rho(\boldsymbol{r}) = \frac{1}{V}\sum_{h}\sum_{k}\sum_{l} F(hkl)\exp\{-2\pi i(h\boldsymbol{a}^{*} + k\boldsymbol{b}^{*} + l\boldsymbol{c}^{*})\} \qquad \text{Eq. 1-13}$$

This electron density expression involves a summation over all *hkl* and to a good approximation the density can be re-constructed from a summation over all observed F_{hkl}.

The atomic form (or scattering) factor is the Fourier transform of an atom's electron density

$$f_j = \int \rho(\boldsymbol{r}_j) \cdot \exp(2\pi i\boldsymbol{s} \cdot \boldsymbol{r}_j)\, d\boldsymbol{r}_j \qquad \text{Eq. 1-14}$$

here, by convention the free electron is considered to be at the nucleus and $\boldsymbol{s}$ denotes the phase difference for an electron in the electron density (or electron cloud). The exponential term showing the resolution or θ dependence. Due to the finite size of the electron cloud, photons scattered at different points in the cloud experience a relative phase change, which makes them interfere with each other. The more expanded the electron density around an atom is, the more contracted the scattering factor will be. The scattering power of the diffuse valence shell is strongest for low angle data while the compact core will scatter up to much higher angles. Normalised scattering factors have been approximated by Gaussian functions and were fitted to a nine-parameter equation by D. Cromer and J. Mann.

$$f^{0}(\sin\theta/\lambda) = \sum_{i=1}^{4} a_i \cdot \exp(-b_i(sin\theta/\lambda)^2) + c \qquad \text{Eq. 1-15}$$

Starting from tabulated coefficients a_i, b_i and c (Johnson & Levy, 1974) scattering factors for virtually all atoms and ions as a function of θ are available. The Thomson- or elastic scattering by a free electron considers an X-ray photon to have insufficient energy to be absorbed by an atom and is either scattered or not. However, the scattering factor contains additional contributions from anomalous dispersion. This is essentially resonance absorption occurring for the scattering by atoms when the X-ray photon energy is slightly larger than the respective X-ray absorption edge, then, the amplitude of both the real (Δf') and imaginary (Δf") dispersion components increases. The atomic scattering factor can then be expressed as the sum of three terms.

$$f(\theta,\lambda) = f^{0}(\theta) + \Delta f'(\lambda) + i\Delta f''(\lambda) \qquad \text{Eq. 1-16}$$

In experimental diffraction studies, this θ dependent decay is much more pronounced. This is mostly due to thermal motion where the atoms describe a normal motion around an equilibrium position. Thermal motion U can be considered as a smearing out of an atoms position, e.g. the convolution of the density with a damping function that depends on the resolution (*sin(θ)/λ*).

$$F(hkl) = \sum_j f_j \cdot \exp\left(2\pi i\left(hx_j + ky_j + lz_j\right)\right) \cdot \exp\left(-2\pi^2 U(\theta)\right) \qquad \text{Eq. 1-17}$$

The thermal motion can be described either as a one parameter isotropic motion (U_{iso}) or as a six-parameter displacement tensor (U_{ij}) to describe an ellipsoid.

$$U = U_{11}h^2\boldsymbol{a}^{*2} + U_{22}k^2\boldsymbol{b}^{*2} + U_{33}l^2\boldsymbol{c}^{*2} + 2U_{23}kl\boldsymbol{b}^*\boldsymbol{c}^* + 2U_{13}hl\boldsymbol{a}^*\boldsymbol{c}^* + 2U_{12}hk\boldsymbol{a}^*\boldsymbol{b}^* \qquad \text{Eq. 1-18}$$

Now, that an expression for $F(hkl)$ is available it can be combined with the experimentally measured intensities. However, as $F(hkl)$ represents a complex number and is proportional to the square root of the intensities, only the amplitude is experimentally accessible while the phase information is lost. Eq. 1–13 can be reformulated to include the measured amplitude (given as $|F(hkl)|$) separating it from the unknown phase (α_{hkl}), which is included as a variable.

$$\rho(\boldsymbol{r}) = \frac{1}{V}\sum_h \sum_k \sum_l |F(hkl)| \exp\left(-2\pi i\left(hx + ky + lz - \alpha_{hkl}\right)\right) \qquad \text{Eq. 1-19}$$

This central problem is known as '*the crystallographic phase problem*' and states that the density cannot be directly reconstructed but has to be modelled. The fundamental strategy is to find the model that represents the best fit to the experimental data by comparing the experimental structure factors F(obs) with the ones calculated from the model F(calc). In later chapters the conversion from the measurable intensity to the structure factor including possible corrections for arising systematic errors will be discussed in detail.

1.2 Structure solution

When waves get diffracted by a crystal, they give rise to distinct diffraction spots and each spot corresponds to a point in the reciprocal lattice and again represents a wave with an amplitude and a phase. When the wave is detected by a photon counting device all phase information is lost and this information needs to be reconstructed. Figure 1 exemplarily shows Bragg diffraction with a plane spacing of d and the points (1-4) are representing atoms at positions between the two planes. The total scattering depends on each individual contribution, the amplitude (proportional to the number of electrons, Z) and the relative phase (0 to 360 degrees, from plane to plane) depending on the relative distance of the atom from the diffracting plane. With the computational power available today, one way to overcome this problem is straightforward: guess the structure! This of course has some severe limitations and requirements and is only useful for small molecules. There are numerous more possibilities to find a way to a structure solution, e.g. Patterson map calculation for inorganic heavy atom structures or molecular replacement in protein crystallography. *SHELXT* (Sheldrick, 2015a) is a recently released program that uses a unique combination of techniques. Here, the data are expanded to $P1$, a Patterson

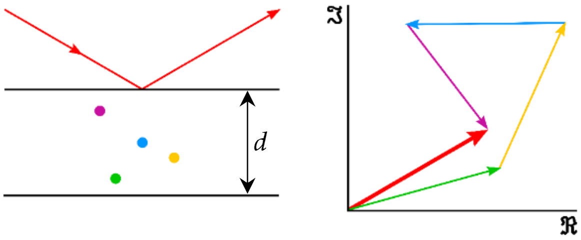

Figure 1
Graphical presentation of the influence of an atoms relative position (coloured dots, left) regarding a Bragg plane (black, left) on the phase change (0 – 360°) and combination of individual contributions (right) to the resulting diffracted beam (red arrows).

map superposition is used to obtain an initial set of phases and the structure is solved using iterative dual-space recycling. The *P*1 phases are then used to determine the space group. However, since the focus is not on structure solution, this topic will not be discussed further and detailed descriptions of different techniques are available in the literature (Patterson, 1949, Karle & Hauptman, 1950, Zachariasen, 1952, Palatinus, 2013, Sheldrick, 2015a).

1.3 Data reduction

The data reduction or data integration is briefly explained exemplary on the basis of the Bruker software *SAINT* (Bruker, 2013). There are plenty of programs using different algorithms; however, they all try to extract all the information found on hundreds of frames and compress the data into one file. After successful crystal system determination and indexing (assignment of *h*, *k* and *l*) the integration routine finds reflections, determines the relevant background (noise, error) and either integrates over the reflection profile by a simple sum method for strong reflections or integrates over a learned profile fitted to weak intensities (ultimately extracting the intensity). The resulting output is a raw list containing all measured reflections and including all necessary information e.g. *h*, *k*, *l*, intensity (I), error ($\sigma(I)$) and direction cosines of the diffracted beam (needed to trace back each reflections path through the crystal sample, chapter 3.2.2).

1.4 Data scaling

The *SADABS* program (Bruker, 2014b), used for inter-frame scaling, absorption correction and error model determination, assumes that the corrected intensity is given by the product of an incident beam scale factor $S(n)$, where n is the frame number, a diffracted beam factor $P(u,v,w)$, where u, v and w are the direction cosines of the diffracted beam relative to crystal-fixed axes, and a spherical crystal factor $Q(\mu r, 2\theta)$, where μ is the linear absorption coefficient and r the effective radius of the crystal:

$$I_{\text{corrected}}=I_{\text{raw}}\cdot S(n)\cdot P(u,v,w)\cdot Q(\mu r, 2\theta) \qquad \text{Eq. 1-20}$$

Similar approximations were used by Kopfmann & Huber (Kopfmann & Huber, 1968, North et al., 1968, Huber & Kopfmann, 1969) and in many subsequent papers and programs. There is one incident beam scale factor $S(n)$ for each frame n, but in *SADABS* the values are interpolated according to the calculated rotation angle of the reflection relative to the rotation angles of the beginning and end of the frame. In addition, a restraint - adjacent frames should have similar scale factors - is applied; this is essential when there are few (perhaps even zero) reflections that have their centres on a particular frame. Thus, the incident beam scale factor $S(n)$ in *SADABS* corrects for crystal decomposition, intensity variations of the X-ray source, changes in the effective volume irradiated (possibly caused by the crystal not being accurately centred), beam inhomogeneity, and absorption by the crystal sample and its support. The plot of $S(n)$ against the frame number n is a useful diagnostic and outlying frames can easily be identified. The diffracted beam factor $P(u,v,w)$ is based on spherical harmonics. Blessing (1995a) also used spherical harmonics but applied them to both the incident and diffracted beams. The multi-scan correction involves refining the incident beam scale factors and spherical harmonic coefficients so that the intensities of equivalent reflections become more equal (Kopfmann & Huber, 1968, North et al., 1968, Blessing, 1995a). This is critically dependent on there being a high multiplicity of observations involving different paths through the crystal, so in general multiple scans about different rotation axes relative to the crystal are required. In *SADABS* the incident beam scale factors and spherical harmonic coefficients are refined in alternate half-cycles, so that each of these full-matrix refinements is linear. This has the advantage that no starting values are required and that each half-cycle converges in one iteration. After each half-cycle the weighted mean intensity of each reflection is calculated using robust/resilient weights as described by Blessing (1997), and the resulting weighted mean intensities are used as observations for fitting the least-squares parameters. Several double cycles are required, but the method is robust and fast. The spherical crystal term $Q(\mu r, 2\theta)$ (Blessing, 1995a) is applied only after the other parameters have been refined to convergence, because it has no effect on the agreement of the equivalent reflections. Since the spherical absorption factor $Q(\mu r, 2\theta)$ is largest at low 2θ and decreases monotonically as 2θ increases, neglecting this term would cause the atomic displacement parameters to become too small or even negative (Katayama, 1986). If the crystal faces have been indexed and their distances from a reference point in the crystal was determined, a numerical absorption correction based on Gaussian integration (Busing & Levy, 1957) may be performed in *SADABS* before the refinement of the other parameters. In such a case, lower-order spherical harmonics can be used in $P(u, v, w)$. For X-ray beams from a sealed tube source, which have been shaped by slits but not focused, this procedure works well, because the assumption that the crystal is completely bathed in a uniform (top-hat profile) beam is valid, and it is even possible to use it to refine the linear absorption coefficient μ. As will be shown later in this thesis, this approach fails for the highly focused microsource beams. After the determination of the scaling parameters, *SADABS* rejects severe outliers and scales the estimated standard deviations of the intensities so that they statistically correspond to the degree of agreement between the corrected intensities of the equivalent reflections. The equation used to scale the reflection standard deviations involves two parameters, K and g. They are refined so that the weighted mean square deviation χ^2 is as close as possible to unity over the full range of intensities. Since there is no resolution-dependent term in this error model, plots of χ^2 against resolution are a particularly effective diagnostic test; in an ideal case χ^2 should be close to unity over the full ranges of intensity and resolution.

$$\sigma^2(I)_{\text{corrected}}=[K\cdot\sigma(I)_{\text{raw}}]^2+(g\cdot\langle I\rangle)^2 \qquad \text{Eq. 1-21}$$

It should be noted that the current versions of *SADABS* and the programs *XDS* (Kabsch, 2010), *AIMLESS* (Evans & Murshudov, 2013) and *HKL-2000* (Borek et al., 2003), which are very widely used for macromolecules, all use the same error model, an example of convergent evolution. This error model is justified by the fact that it results in values of χ^2 that are close to unity throughout the full range of intensity and resolution, except for an occasional small rise at very low resolution that is clearly indicative of residual systematic errors, this can be seen later in Figure 10. It is remarkable that this is achieved by the refinement of only two parameters, K and g. Recent versions of *SADABS* also allow these parameters to be fixed (e.g. at 1 and 0, respectively), refined as overall values for all scans or refined separately for each scan. In this thesis, the default *SADABS* option of refining separate K values for each scan (because they may be influenced by different scan speeds etc.) but only one overall g value was adopted for all routine structure determinations. As we will learn later, this error model is not generally applicable to charge density data and it has been criticised by Henn and Meindl (2010) and Jørgensen et al. (2012).

1.5 Independent atom model

This model's basic assumption is the *atomicity* of crystal structures and describes atoms as spherically symmetric, nucleus-centred radial functions convoluted with their respective displacement from an equilibrium position (thermal motion). The calculated structure factors are of course on an arbitrary scale and a scale factor has to be refined to match the experimental data. Within this framework, it depends on the flexibility of the used program for side conditions to be introduced, e.g. constraints and restraints as well as occupancy factors. Refining an occupancy additionally allows for the distinct ability to describe dynamic or static disorder. The side conditions help to stabilise a model or are used to introduce and apply chemical knowledge to a crystal structure refinement e.g. if severe disorder is to be modelled. There are numerous programs available using this model, which differ only in their flexibility (e.g. the constraints and restraints) and user operability. Concluding, within the IAM approximation, investigations are limited to the connectivity of atoms and the conformation of the molecules including bonding distances / angles and the determination of the absolute structure.

1.6 Figures of merit: Data

$$R_{merge} = \frac{\sum_h \sum_i \left| F_{o,i}^2(h) - \langle F_o^2(h) \rangle \right|}{\sum_h F_o^2(h)} \qquad \text{Eq. 1-22}$$

$$R_{sigma} = \frac{\sum_h \sigma\left(F_o^2(h)\right)}{\sum_h F_o^2(h)} \qquad \text{Eq. 1-23}$$

$$R_{r.i.m.} = \frac{\sum_{hkl} \left(\frac{N}{N-1}\right) \sum_i^N \left| F_{o,i}^2(hkl) - \langle F_o^2(hkl) \rangle \right|}{\sum_h \sum_i^N F_{o,i}^2(hkl)} \qquad \text{Eq. 1-24}$$

$$R_{p.i.m.} = \frac{\sum_{hkl} \left(\frac{1}{N-1}\right) \sum_i^N \left| F_{o,i}^2(hkl) - \langle F_o^2(hkl) \rangle \right|}{\sum_h \sum_i^N F_{o,i}^2(hkl)} \qquad \text{Eq. 1-25}$$

A widely accepted way to judge on the quality of a data set is to check statistical criteria such as the agreement of equivalent reflections R_{merge} (R_{int}, R_{sym} or R_{linear}). Ideally, during data collection, all possible diffraction geometries are sampled, gathering more than one symmetry equivalent observation of an individual (or unique) reflection. This is called *multiplicity* (in the past often referenced to as *redundancy*) of unique reflections and is of fundamental value to minimize the influence of systematic errors. In X-ray crystallography, there is a plethora of possible origins of systematic errors such as blind detector spots, inconstant sample rotation, non-uniform crystal shape etc., which will be discussed in later chapters. The mean significance (or signal to noise) of the data is given as I over $\sigma(I)$ or as the mean accuracy R_{sigma} of equivalent reflections, and low values indicate a low background with strong signal, exactly what is considered to be *good* data. The redundancy-independent merging R-value ($R_{\mathrm{r.i.m.}}$ or R_{meas}) proposed by Weiss (2001) describes the mean precision of individual intensities independent of the multiplicity and the precision indicating merging R-value ($R_{\mathrm{p.i.m.}}$) yields the precision of the average intensity. The problem is that with increasing multiplicity, the general R-value will increase indicating worse data. In contrast, however, high multiplicity denotes a more carefully screening of the crystal and should therefore be indicated by a decrease in *R*. In the calculation of $R_{\text{p.i.m.}}$ and $R_{\text{r.i.m.}}$, the square root term adjusts the common *R*-values to make them independent of the multiplicity.

In 2010, Diederichs (2010) suggested a new indicator to assess the influence of systematic instrument errors for X-ray data. The limiting numerical value of this indicator is given as the maximum signal-to-noise (I/σ) an experimental setup is able to produce. It can be obtained from a scatter plot of I/σ against log(I) for unmerged data, exemplarily shown in Figure 2, which asymptotically approaches the limiting value of I/σ. With the error model employed by the *SADABS* program I/σ is calculated as $1/g$ and the direct consequence is the characteristic shape of the plot.

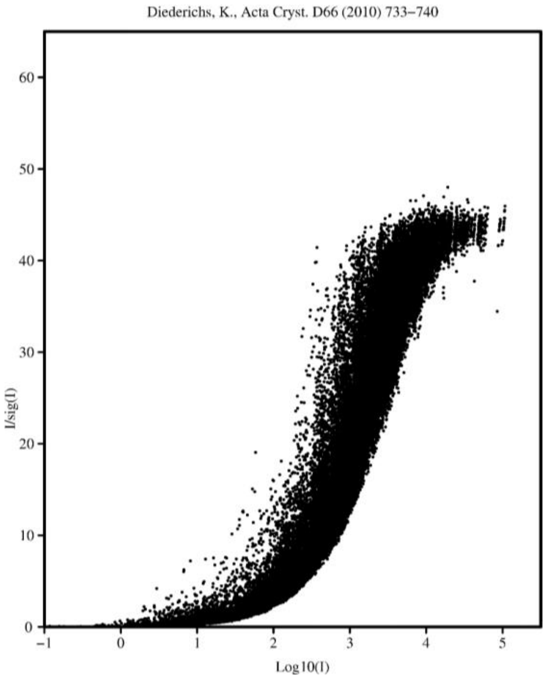

Figure 2
Example for a typical Diederichs plot of I/σ against log(I).

1.7 Figures of merit: Model

From the results of a least-squares minimisation, values can be derived displaying the agreement between the refined model and the measured data (*R*1, *wR*2, *GooF*). These indicators deliver a good estimate of the quality of the model, however, they can only provide information on the goodness of the underlying mathematical fit. Inherently, these values cannot judge on the *reliability* of a derived model, e.g. artefacts or systematic errors present in the data that *are fitted* with the model are completely ignored by these indicators. Problems arise as soon as a model attunes to these errors enabling false conclusions to be drawn. Over the course of the last decades, many indicators have been developed, some persist until the present day. There is no common agreement as to what quality indicator has to be shown in order to prove a model, however, a few largely accepted indicators are presented in the following. The analysis of the difference electron density (or residual density) is one highly useful tool to judge on the quality of a given model. Here, the calculated structure factors F_{calc} are used to supply a phase for the experimentally observed amplitude, giving *model*

$$R1 = \frac{\sum_{hkl}\left||F_o(hkl)| - |F_c(hkl)|\right|}{\sum_{hkl}|F_o(hkl)|} \qquad \text{Eq. 1-26}$$

$$wR2 = \sqrt{\frac{\sum_{hkl} w\{F_o^2(hkl) - F_c^2(hkl)\}^2}{\sum_{hkl} w\{F_o^2(hkl)\}^2}}$$

$$w = 1/[\sigma^2(F_o^2) + (aP)^2 + bP] \qquad \text{Eq. 1-27}$$

$$P = \left[\frac{2}{3}\cdot F_c^2 + \frac{1}{3}\cdot \max(F_o^2, 0)\right]$$

$$GooF = \sqrt{\frac{\sum_{hkl} w\{F_o^2(hkl) - F_c^2(hkl)\}^2}{reflections - parameters}} \qquad \text{Eq. 1-28}$$

phased structure factors F_{obs}. A map of ρ calculated for the difference of the two structure factors highlights features where the deviation between model and data is largest. Such a map is called a difference Fourier map or residual density map ρ_0 and can be considered as a three dimensional representation of the *R*-value highlighting local discrepancies. The appearance of programs allowing a three dimensional representation of real space densities, such as *FRODO*, *O*, *XtalView* and later *Coot*, the Crystallographic Object-Oriented Toolkit (Emsley & Cowtan, 2004, Emsley et al., 2010), had strong impact on the crystallographic community, greatly changing crystal structure determinations. The herein exclusively utilised graphical user interfaces (GUI) *SHELXle* (Hübschle et al., 2011) for *SHELXL* and (Sheldrick, 2015a, b) *MoleCoolQT* for (Hübschle & Dittrich, 2011) *XD2006* (Volkov et al., 2006) are progeny of *Coot*.

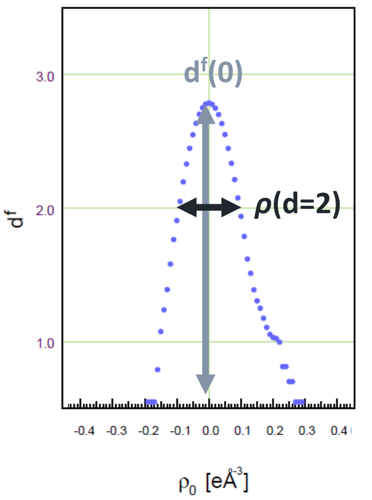

Figure 3
Plot of the residual density ρ_0 against its fractal dimension d^f.

Meindl and Henn (Meindl & Henn, 2008) developed an elegant indicator that is essentially a compressed graphical descriptor for features in the residual density. It is an evaluation of the fractal dimension of the residual density distribution on a finite grid using a line-counting algorithm (was found to be faster and more efficient than a box-counting algorithm). This descriptor is visualised as a plot of the residual density against its fractal dimension (Figure 3). If only Gaussian noise with a mean of zero and no model inadequacies are present, the resulting distribution is of parabolic shape. The parabola of a given difference Fourier density is characterised by the terms *flatness* and *featurelessness*. *flatness* gives a measure for the noise in a given set of data the parabola's width represents the noise level (disregarding any shoulders). The height of the parabola is determined by the fractal dimension of zero difference density $d^f(0)$ and approaches the limiting value of three (the density is a three-dimensional fractal). This indicator is connected to the resolution of the data and the spatial grid scale, data truncation reduces the height of the parabola because it reduces the fractal dimension of the residual density distribution. However, strong noise in the data will produce similar findings, effectively truncating the data. A further great feature lies in the possible separation of noise and structural information. The *featurelessness* tends to show inadequacies on the model side. Such features are revealed by shoulders at either side of the parabola. In Figure 3, a small shoulder is visible at the positive residual density level, indicating features present in the data, which the current model is incapable to describe. On the negative density level, no such feature is visible. Their occurrence indicates a model that shows features that are not backed up by the data. A quantification of the total amount of residual density is given by the descriptor e_{gross}, defined as:

$$e_{gross} = \frac{1}{2}\int_V |\rho_0(\boldsymbol{r})| d^3r \qquad \text{Eq. 1-29}$$

To good approximation, this quantity is available as a summation over a finite grid and can be understood as a global measure for accumulated residuals, regardless of their origin.

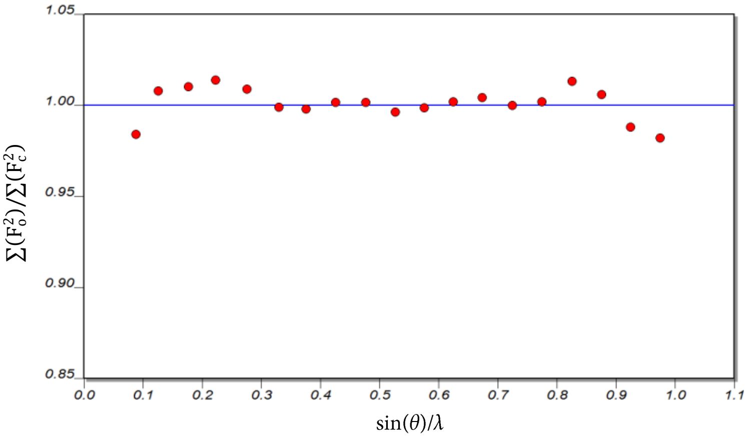

Figure 4
Resolution dependent distribution of the agreement of observed and calculated structure factors.

A further measure for the quality of a density model is the ratio, usually called *K*, of the observed and calculated structure factors dependent on the resolution (Figure 4). Suitable resolution ranges are determined and the structure factors are divided into bins accordingly, resulting in a characteristic plot (Zavodnik et al., 1999, Zhurov et al., 2008). The ideal distribution is close to unity over the full resolution range. It is widely accepted that a model must not show any deviation larger than 5 %. Reasons for severe *underestimations* of the low resolution data (e.g. $\sum F_o^2/\sum F_c^2 < 1$) was found to have its origin in a detector saturation due to highly intense reflections that do not occur at higher resolutions (Wolf et al., 2014a). Deviations from unity in high resolution areas are attributed to systematic resolution dependent errors such as thermal diffuse scattering or inadequacies during data reduction. The interested reader is referred to a recent publication by Niepötter et al. (2015). Of course, the analysis of variance for reflections employed in a refinement is not limited to the resolution dependence. In *SHELXL* an additional ranking according to intensities (F_c/F_c(max) ranging from 0 to 1) is given and similar to the resolution dependent distribution, this *K* value should always be close to unity. K_{weak} refers to the *bin* containing the weak reflections, e.g. where $F_c/F_c(\text{max}) \approx 0$. An increased K_{weak} usually indicates twinning but it can as well be useful in the determination of systematic errors, especially when twinning can be excluded.

CHAPTER 2:

INTRODUCTION TO EXPERIMENTAL CHARGE DENSITY INVESTIGATIONS

2 Charge density investigations

In 1964 Hohenberg and Kohn (1964) confirmed that the electron density $\rho(r)$ is the fundamental property that characterises the ground state energy of a system. Upon knowledge of $\rho(r)$ a diverse range of properties, in principle, is available. An experimental electron density can be reconstructed in the form of nuclear-centred multipolar expansions using real spherical harmonics. This aspherical atomic density description was introduced by Stewart (Stewart, 1972, 1973) and the first software implementation was provided by Hansen & Coppens (Hansen & Coppens, 1978, Volkov & Coppens, 2001). In contrast to a routine independent atom model (IAM) refinement, where nine designated atomic parameters are intended to model *the molecular structure*, an aspherical electron density description requires an additional set of up to 25 parameters:

$$\rho(r) = P_{core}\rho_{core}(r) + P_{val}\kappa^3\rho_{val}(\kappa, r) + \sum_{l=0}^{l_{max}} \kappa_l'^3 R_l(\kappa_l', r) \sum_{m=0}^{l} P_{lm\pm} d_{lm\pm}(\Omega) \qquad \text{Eq. 2-1}$$

In this formalism, the electron density $\rho(r)$ is divided into a core, a spherical valence shell and an aspherical valence component forming atomic-like densities or so-called pseudoatoms. In this expression r is the distance from the pseudoatom centre and Ω represents the angular coordinates. ρ_{core} and ρ_{val} are spherically averaged and one-electron normalised densities obtained from Hartree-Fock calculations, P_{core} and P_{val} are the corresponding population parameter. Throughout this thesis, a *frozen-core* approach was followed keeping the populations of the core density fixed. The spherical valence density is multiplied with an expansion and contraction parameter κ, that can be optimised during refinement. The third term describes the aspherical deformation density modelled by density normalised spherical harmonics $d_{lm\pm}$. For monopoles the value of the respective population parameter essentially denotes an electron population resulting in a direct connectivity between the monopole of an atom to the *charge* of that particular atom. For the non-spherical functions, the populations indicate an electron shift from negative to positive regions (Coppens, 1997). The population parameters $P_{\mathrm{lm}\pm}$ of the spherical harmonics and κ_l' are dimensionless adjustment coefficients for the single Slater-type radial functions R_l.

$$R_l(\kappa_l', r) = (\kappa_l'\,\alpha_l)^3 \frac{(\kappa_l'\,\alpha_l\, r)}{[n(l)+2]!} \exp(-\kappa_l'\,\alpha_l\, r) \qquad \text{Eq. 2-2}$$

The α_l values are estimated from single-ζ (zeta, determines the function width, e.g. large ζ give tight, small ζ more diffuse functions) exponents obtained from Hartee-Fock optimised wavefunctions calculated for the valence-orbitals. These values are multiplied with the parameters κ_l' that are optimised during the refinement. Dominiak and Coppens (2006) showed that the best procedure to obtain optimal κ_l' parameters for experimental data is a constrained refinement as one combined value for a given group. In this thesis, core and valence scattering factors were exclusively used that derive from wave functions that were fitted to relativistic Dirac-Fock solutions by Su-Coppens-Macchi and are stored in the *XD2006* (Volkov et al., 2006) SCM bank file (Su & Coppens, 1998, Macchi & Coppens, 2001). The resulting charge density refers to the non-vibrating molecule, as vibration and density are deconvoluted, and it can serve directly for theoretical interpretation and analysis (Hirshfeld, 1976).

2.1 Multipolar refinement strategy

To explain the stringent requirements on the experimental data in charge density refinements Table 1 shows a comparison of possible parameters per atom allowed in *SHELXL* and *XD2006* (Volkov et al., 2006). Though, of course, not all parameters might be desirable to be refined, if at all, the sheer number demonstrates the possible flexibility the multipole model has to offer. Even when the data quality meets the high requirements, the data to parameter ratio usually becomes unreasonable and high correlations between parameters are to be expected (e.g. the *κ* parameter and the respective monopole) if all parameters are refined. The global strategy is to start with a highly restricted model and gradually increase the complexity (Farrugia, 2016). The multipolar model is set on-top an existing IAM model, however, this description only offers adjustable parameters for atomic vibrations and their positions but none for the bonding density. In return, these parameters do not represent the true vibrational behaviour and cause a final calculated difference density map to present a distorted picture of the charge distribution Hirshfeld (1976) and therewith false estimates for the multipolar parameters. To overcome this inherent problem, it is common practise to perform a refinement of the positions of the heavy atoms against data truncated to the highest resolution. To some extent, this will leave density polarisation effects unconsidered, because the valence density is ignored. Therefore, the procedure enables largely bias-free positional parameters. This is equally valid for the atomic motion, yet, in a different manner. The lack of flexibility regarding the bonding density, the U_{ij} parameters are incorrectly retracting the bonding density in order to increase the agreement of model and data. Given that such a refinement was carried out using *SHELXL* the next step would be to start modelling the predominant bonding density using multipoles *only*. After successfully describing the bonding density with a first set of multipoles, the monopoles are introduced and thereafter the strategy is extended including positions and motions, followed by *κ* and hydrogen positions. The default strategy is shown in Table 2. From the final stage, the refinement has to be adjusted to the crystal data individually.

Table 1
Model parameter comparison.

	SHELXL		*XD2006*	
Occupancy	1	*occ*	-	*occ*
Positions	3	*xyz*	3	*xyz*
Thermal motion	6	U_{ij}	6	U_{ij}
	-	-	10	*GC* 3^{rd}
	-	-	15	*GC* 4^{th}
Multipoles	-	-	2	P_v, P_{00}
	-	-	3	$P_{10}, P_{11\pm}$
	-	-	5	$P_{20}, P_{21\pm}, P_{22\pm}$
	-	-	7	$P_{30}, P_{31\pm}, P_{32\pm}, P_{33\pm}$
	-	-	9	$P_{40}, P_{41\pm}, P_{42\pm}, P_{43\pm}, P_{44\pm}$
Total	*10*		*60*#	

\# *κ* and *κ*' are excluded in this summation as their number is determined by the investigated structure.

Table 2
Default *XD2006* refinement strategy. Abbreviations: *D*, dipoles; *Q*, quadrupoles; *O*, octapoles; *H*, hexadecapoles; *M*, monopoles; *xyz*, positional coordinates; xyz-H, hydrogen coordinates; U_{ij}, displacement parameters; κ, spherical expansion parameters; κ', aspherical expansion parameters.

1	Scale factor				
2	-	-	-	*D Q O (H)*	-
3	-	-	*M*	*D Q O (H)*	-
4	*xyz*	U_{ij}	*M*	*D Q O (H)*	-
5	-	-	-	-	*κ*
6	*xyz*	U_{ij}	*M*	*D Q O (H)*	*κ*
7	*xyz*-H	-	-	-	-
8	*xyz*	U_{ij}	*M*	*D Q O (H)*	*κ*
9	-	-	-	-	*κ*'
10	*xyz*	U_{ij}	*M*	*D Q O (H)*	*κ*

2.2 Local symmetry and chemical constraints

One topic of major interest in the field of experimental electron density analysis are chemical constraints (chemcons). In *XD2006*, the multipole parameters of an arbitrary number of atoms can be constraint onto each other essentially decreasing the number of parameters while still allowing to model the deformation density. In the beginning of a charge density investigation, it is wise to constrain the pole populations of as many chemically (more or less) equivalent atoms as possible to keep the refinement robust and stable. The idea behind the chemcons is closely related to the concept of transferability of atomic densities in molecules, similar to *UBDB* (Dominiak et al., 2006) or *INVARIOM* (Dittrich et al., 2004, Dittrich et al., 2013) approaches. The *INVARIOM* database, for example, stores theoretical multipole parameters for geometry optimised molecular fragments. Fitting fragments can be combined with an experimental geometry to obtain a more accurate density description. The question arises as to what extend such a density is still 'experimental'. The transferable densities approach is much faster than a quantum chemical calculation as long as all fragments are available. The resulting density is somewhere in between pure theory and experiment as the positions and atomic motion are refined against the experimental data, the pole parameters, however, are not. Four cases need to be considered: a) unconstrained and b) constrained experimental densities, c) experimental geometries and calculated pseudoatom densities and d) complete theoretical calculations. a) and d) do not need any special attention and belong either in experimentalist's or theoretician's hands. A differentiation between b) and c) is more difficult, not in terms of the involved scientific branches but in the degree of possible acquisition of information. Chemically constrained pseudoatoms will only be able to model a somehow *mean* density, while differences to other atoms and accordingly the density overlap is only dependent on their positions. Concluding, that local differences in regions of interest can hardly be distinguished, for densities obtained either way, given that the assumption of transferable atoms in molecules is valid.

For now, the cautious presumption is made that an unconstrained refinement is the goal in order to justify the expenditure an experimental charge density investigation comes with. This, however, as we will learn later in this thesis, is seldom fully achievable.

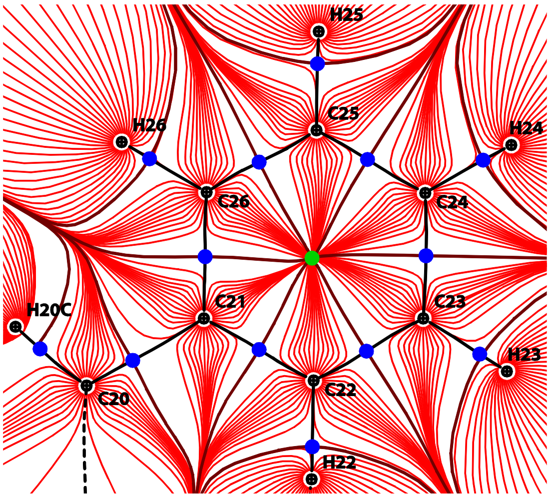

Figure 5
Trajectory plot of the electron density gradient. There are atoms (black crossed dots), bond paths (black lines) with bond critical points (blue dots), ring critical points (green dots) and interatomic zero-flux boundaries (violet paths).

2.3 Quantum theory of atoms in molecules

In the early 1970's, Richard Bader (Bader et al., 1971, Bader & Beddall, 1973, Bader, 1975, 1991) provided a framework to allow for a detailed and unique analysis of the electron density. The term '*quantum chemical topology*' is a better representation for what QTAIM is about (Popelier, 2016). The density (a scalar field) is ultimately modelled because we, as experimentalists, are interested in the underlying properties. An analysis of the topology of the density directly leads to concepts such as atoms, molecules, structure and bonding. Moreover, this framework is valid regardless of the way a density was obtained. It has to be emphasized at this point that this only offers a *concept* of bonding, because a chemical bond is unfortunately not a quantum mechanical observable (Haaland et al., 2004). However, within the QTAIM framework, the concept of atoms and bonding is uniquely defined on the basis of the topology of the electron density and properties can be readily extracted. The first location-dependent derivative of the density shows intriguing features and is called the gradient field $\nabla\rho$ (Figure 5). Stationary points in $\nabla\rho$ are connecting joints of zero-flux trajectories that in total reveals the molecular structure, Bader shaped the terms of critical points and bond paths. The concept of bond paths as a '*linking bridge of density*' between atoms, however, was already introduced by London (1928). Pendas et al. (2007) showed evidence that bond paths of the quantum theory of atoms-in-molecules signal the existence of privileged exchange channels in molecules and addressed a clear meaning to chemistry, however, in the literature their occurrence is discussed contentiously (Farrugia et al., 2006). A critical point indicates an extremum in $\rho(\mathbf{r})$ where $\nabla\rho(\mathbf{r}) = 0$, a point of zero-flux. These points are characterised by the rank m (number of non-zero eigenvalues) and the signature n (algebraic sum of the sign of the eigenvalues) of the corresponding Hessian Matrix $H(\mathbf{r})$. The Hessian is the partial second derivative of the spatial coordinates x, y, z at the point $\mathbf{r}$. The sum of the diagonal terms or the trace of the Hessian matrix is called the Laplacian $\nabla^2\rho(\mathbf{r})$ and is of great importance for the interpretation of the densities properties.

$$H(\boldsymbol{r}) = \begin{pmatrix} \frac{\partial^2\rho}{\partial x^2} & \frac{\partial^2\rho}{\partial x\partial y} & \frac{\partial^2\rho}{\partial x\partial z} \\ \frac{\partial^2\rho}{\partial y\partial x} & \frac{\partial^2\rho}{\partial y^2} & \frac{\partial^2\rho}{\partial y\partial z} \\ \frac{\partial^2\rho}{\partial z\partial x} & \frac{\partial^2\rho}{\partial z\partial y} & \frac{\partial^2\rho}{\partial z^2} \end{pmatrix} \qquad \text{Eq. 2-3}$$

Bader stated that "*with relatively few exceptions, the critical points of charge distributions for molecules at or in the neighbourhood of energetically stable geometrical configurations of the nuclei are all of rank three*", concluding that there are exactly four uniquely defined critical points available, their individual meanings are summarised in Table 3. A local maximum indicates an atomic position (ap) and a local minimum denotes a cage critical point (ccp) formed by at least four atoms. The maximum density trajectory connecting two extrema linked by a saddle point, the bond critical point (bcp), defines a bond path between two atoms. A full set of bond paths completes the molecular graph. A ring critical point (rcp) is found as a minimum density framed by three or more atoms. For every molecular graph the critical points have to satisfy the Poincaré-Hopf relationship (Hopf, 1926, Collard & Hall, 1977) in order to be considered a characteristic and complete set. The expression has its origin in the mathematical field of differential topology and is defined as:

Table 3
Characterisation of QTAIM based critical points.

(3, -3)	local maximum, atomic position (ap)
(3, -1)	saddle point, bond critical point (bcp)
(3, +1)	saddle point ring critical point (rcp)
(3, +3)	local minimum, cage critical point (ccp)

$$n_{ap} - n_{bcp} + n_{rcp} - n_{ccp} = 1 \qquad \text{Eq. 2-4}$$

where the summation of the individual critical point occurrences ($n_{\text{critical point}}$) needs to yield unity. The algorithms employed in the program *XD2006* to retrieve critical points and draw the molecular graph follow an iterative protocol assuring the self-consistency of the final structure by testing if the rule is satisfied.

Bader's approach towards atoms employs a unique density partitioning scheme that considers atomic basins as discrete regions limited by interatomic zero-flux surfaces. An interatomic surface satisfies the zero-flux boundary condition if:

$$\nabla\rho(\mathbf{r}) \cdot \mathbf{n}(\mathbf{r}) = 0 \;\forall\; \mathbf{r} \in \text{surface } S(\mathbf{r}) \qquad \text{Eq. 2-5}$$

where $\nabla\rho(\mathbf{r})$ is the gradient of the electron density and $n(\mathbf{r})$ is the vector normal to the plane at $\mathbf{r}$. This atom definition is only valid and useful because the associated atomic properties coincide with properties predicted by quantum mechanics (Bader, 1990). On the other hand, the obtained topological atoms do not look like the balls and spheres from molecular models we know.

In contrast to the gradient $\nabla\rho(\mathbf{r})$ being able to reveal critical points and e.g. bonding, the Laplacian highlights regions of charge accumulations $\nabla^2\rho(\mathbf{r}) < 0$ or depletions $\nabla^2\rho(\mathbf{r}) > 0$. The knowledge of this quantity at e.g. a bond critical point gives rise to assumptions regarding the nature of that particular bond. A charge concentration is usually found in covalent or charge-shared bonding situations whereas a charge depletion at the bond critical point hints towards a more ionic character. Apart from bond type evaluations, the Laplacian can indicate valence shell charge concentrations, typically found at positions predicted by the valence shell electron pair repulsion (VSEPR) theory and are characterised by a local charge concentration. However, the found regions of high charge concentrations show different forms, usually they resemble more a *banana shape* than the *rabbit ears* known from the Lewis (1916) concept found in most chemistry text books.

2.4 Electrostatic potential and intermolecular interactions

The electrostatic potential $V(\boldsymbol{r})$ is one of the most important property related to the electron density and are connected via the Poisson equation (Coppens, 1997):

$$\nabla^2 V(\boldsymbol{r}) = -4\pi\big(\rho_{nuclear}(\boldsymbol{r}) - \rho(\boldsymbol{r})\big) \qquad \text{Eq. 2-6}$$

where ρ_{nuclear} is the nuclear charge and $\rho(\mathbf{r})$ the electron density. The potential $V(\boldsymbol{r})$ is obtainable by integration over all space ($\boldsymbol{r}'$):

$$V(\boldsymbol{r}) = \int \frac{\big(\rho_{nuclear}(\boldsymbol{r}') - \rho(\boldsymbol{r}')\big)}{|\boldsymbol{r}' - \boldsymbol{r}|} d^3\boldsymbol{r}' \qquad \text{Eq. 2-7}$$

Due to the differences in mass, the electrons are assumed to react instantaneously on positional changes of the pivotal nuclei, making them approximately stationary from the electrons point of view. With this, known as the Born-Oppenheimer approximation, applied, this integral can be transformed and its evaluation greatly simplified. Assuming N nuclei, each nuclei i at position $\boldsymbol{R}_i$ carrying the charge Z_i, the expression can be transformed into:

$$V(\boldsymbol{r}) = \sum_{i=1}^{N} \frac{Z_i}{|\boldsymbol{R}_i - \boldsymbol{r}|} - \int \frac{\rho(\boldsymbol{r}')}{|\boldsymbol{r}' - \boldsymbol{r}|} d^3\boldsymbol{r}' \qquad \text{Eq. 2-8}$$

Within *XD2006* the unperturbed intermolecular electrostatic interaction energies E_{es} between molecules, molecular fragments or atoms can be evaluated by numerical integration using atomic or molecular multipolar moments. Empirically derived atom-atom potentials allow for the approximation of exchange-repulsion $E_{\text{ex-rep}}$ arising from anti-symmetrisation or Pauli requirement and a dispersion term E_{dis} following from the induced charge distribution of different fragments onto each other. There are three different potentials available, yet, two must be excluded right away, as the Lennard-Jones (1931) and the Williams and Cox (1984) potentials are only available for the elements H, C, N and O, leaving the (Spackman, 1986) potentials the only available resource. The total interaction energy E_{tot} can be written as summation over these individual contributions. The approximation of exchange-repulsion and dispersion in this thesis were done using potentials derived by Spackman.

$$E_{tot} = E_{es} + E_{ind} + E_{disp} + E_{ex-rep} \qquad \text{Eq. 2-9}$$

The induction term E_{ind} describes the interaction of two unperturbed density distributions onto each other. For experimental data this term is already included in the derived pseudo-atom (or multipole) parameters, since a crystal packing cannot contain unperturbed molecules. All electrostatic interaction energies calculated during this thesis were obtained using the exact six-dimensional double-basin integration for each atom–atom pair.

$$\begin{aligned} E_{es} = \sum_{a\in A}\sum_{b\in B}\frac{Z_a Z_b}{r_{ab}} + \int_A \rho_A(\boldsymbol{r}_A)V_A^{nuc}\,d\boldsymbol{r}_A + \int_B \rho_B(\boldsymbol{r}_B)V_B^{nuc}\,d\boldsymbol{r}_B \\ + \int_A\int_B \frac{\rho_A(\boldsymbol{r}_A)\rho_B(\boldsymbol{r}_B)}{|\boldsymbol{r}_A-\boldsymbol{r}_B|}\,d\boldsymbol{r}_A d\boldsymbol{r}_B \end{aligned} \qquad \text{Eq. 2-10}$$

In this expression, V_A^{nuc} and V_B^{nuc} are the nuclear potentials of the nuclei A and B, respectively. A typical integration involves 50 radial and 194 angular quadrature points. A so-called Buckingham-type approximation (Volkov et al., 2004) that utilises the multipole moment expansion of the pseudoatom electron density model would be appreciably faster in terms of computation times. Unfortunately, the herein used atom-atom potentials base on a spherical-density / spherical-density term and cannot be used in conjunction with this type of approximation, since an equivalent term is already included and would therefore lead to a systematic overestimation of the respective contribution (e.g. dispersion or exchange-repulsion).

The non-covalent interactions (NCI) descriptor, proposed by Johnson et al. (2010), is a dimensionless quantity based on the electron density distribution $\rho(\boldsymbol{r})$ or more precisely on the reduced density gradient (RDG) $s(\boldsymbol{r})$. In its first stages it was only applied to theoretical densities, the field where it emerged, because the RDG was used for the generalised gradient approach in density functional theory (Becke, 1988). Luckily, the electron density is a quantum mechanical observable that may be obtained from either ab initio calculations or single crystal X-ray diffraction, rendering it particularly comprehensible for both branches of science. Saleh et al. (Saleh et al., 2012b, Saleh et al., 2012a, Saleh et al., 2013) were the first making it applicable to experimental electron densities revealing non-covalent interactions in charge densities derived from the pseudoatom formalism. It can encompass a wide range of intermolecular weak bonding types including the herein relevant CH ⋯ π, π ⋯ π and CH ⋯ HC interactions.

$$s(\boldsymbol{r}) = \frac{|\nabla\rho(\boldsymbol{r})|}{2(3\pi^2)^{1/3}\,\rho(\boldsymbol{r})^{4/3}} \qquad \text{Eq. 2-11}$$

In combination with the sign of the second eigenvalue of the Hessian Matrix $H(\boldsymbol{r})$ it allows for the discrimination of the attractive or the repulsive nature of one particular interaction. Moreover, it enables a ranking of the relative strength of interactions on a qualitative level.

The latest incarnation of density descriptors is the Density Overlapping Regions Indicator (DORI) and it shows appealing properties as a universal indicator, combining intra- and intermolecular interactions. The main advantage distinguishing DORI from other bonding indicators is that it depends only on the electron density, without any approximations that other indicators suffered from. This feature makes it applicable for density analysis regardless of its origin, whether post-Hartree-Fock, density functional theory or experimental approaches. In combination with the quantity $\text{sign}(\lambda_2)\cdot\rho(r)$ the indicator allows for an estimate of the magnitude of a particular interaction.

Experimental densities should in principle yield the most accurate information on intermolecular interactions because they base on a physically observable. However, restrictions and inadequacies in the modelling capabilities or systematic errors during data collection of course influence the resulting experimental accuracy. A balance of orthogonal strategies for obtaining the density seems promising, e.g. theoretical densities calculated on experimental geometries and with the purpose to obtain accurate estimates for the individual terms in the expression for intermolecular interactions.

$$E_{tot} = E_{es} + E_{ind} + E_{disp} + E_{ex-rep} \qquad \text{Eq. 2-12}$$

2.4.1 Pixel CLP Package

'*After twenty-plus years of subjective crystal 'engineering', based on geometrical guesses of interactions between postulated 'synthons', it is now evident that such an approach is never going to work in a reproducible manner*' Gavezzotti (2008). In the PIXEL (Gavezzotti, 2002, 2003) procedure, intermolecular energies are evaluated as numerical integrals over discrete points (pixels) of a theoretical electron density grid of isolated molecular densities. The density expression is obtained on the basis of a gas-phase quantum-mechanical calculation on the experimental geometry using the B3LYP (Becke, 1993, Lee et al., 1988) functional with the Pople triple-ζ polarised 6-311G(d,p) (Hariharan & Pople, 1973, Pietro et al., 1982) basis set using the *GAUSSIAN09* package (Frisch et al., 2010). The energy partitioning follows the very same approach as presented in Eq. 2-11. In the PIXEL formulation, the electrostatic terms are calculated as numerical integrals. Polarisations (induction, E_{ind}, in Eq. 2-11) are approximated as linear dipoles, the dispersion term is included as a function described by London-type forces (inverse sixth power approximation) and repulsion is calculated from the overlapping molecular densities.

2.4.2 Crystal Explorer

CrystalExplorer (Spackman et al., 2012) offers powerful tools for the analysis of crystal structures, with its main selling point being the three-dimensional visualization of properties such as Hirshfeld surfaces, molecular densities, electrostatic potentials and crystal voids that were calculated using the built-in quantum mechanical framework *TONTO* (Jayatilaka & Grimwood, 2003). It is a unique combination of an intuitive GUI that simplifies quantum mechanical calculations and allows for a comprehensive inspection of molecular properties. In the context of this thesis the calculation of crystal voids are of special concern and the interested reader is directed to an excellent article by Spackman and

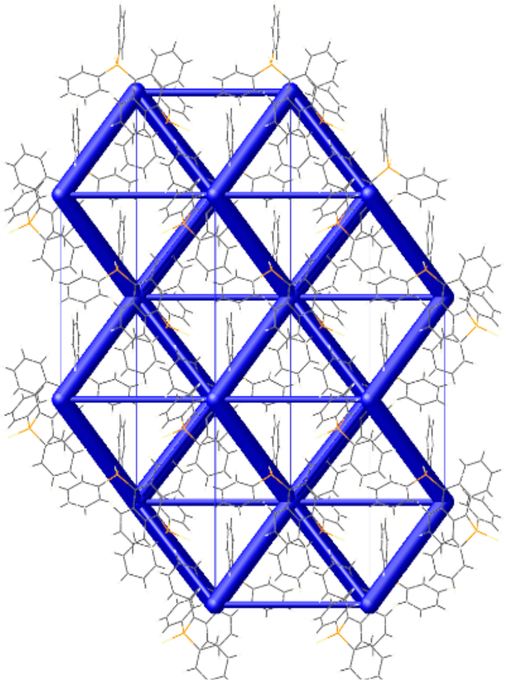

Figure 6
A typical CrystalExplorer representation of an energy framework. The total interaction energy of Bis(diphenylthiophosphoryl)anthracene is depicted along the crystallographic *a*-axis.

Jayatilaka (2009) for further reading. The voids (Turner et al., 2011) are given as regions within the unit cell, where the sum of the promolecule density is less than the specified value of 0.002 e$Å^{-3}$. The promolecule is a term characterised by Hirshfeld (1977) and is defined as the sum of spherically-averaged electron densities centred at the nuclei. The frontier molecular orbital (MO) population analysis performed herein are as well based on the popular B3LYP/6-311G(d,p) level of theory, the HOMO and LUMO orbitals are given as the last occupied and first virtual molecular orbital, respectively. One of the *CrystalExplorer*'s main feature is the visualisation of close intermolecular contacts using the Hirshfeld surface and subsequent generation of fingerprint-plots. These plots, in an elegant way, give a condensed summary of all interactions, essentially unique for every molecule. This concept was followed up in a subsequent release (currently unpublished, only an internal beta test version), however going from interaction distances to energies, producing an intuitive three-dimensional representation of the intermolecular interactions, called the energy framework (Turner et al., 2014, Turner et al., 2015). Based on the experimental geometry, an electron density is calculated on the dispersion and counterpoise corrected B3LYP/6-31G(d,p) level of theory and the obtained monomer densities are used to obtain accurate estimates of the intermolecular interaction energies. The applied energy partitioning scheme is done in a similar fashion to the *PIXEL* approach. The total energy is constructed from individual contributions, E_{es} is the classical electrostatic energy term for the interaction between two charge distributions, the polarisation (called induction E_{ind} in *PIXEL*) term E_{pol} is calculated as a combination of isotropic atomic polarizabilities and local electric fields (computed from the charge distribution) summed over all nuclei (Thakkar & Lupinetti, 2006), E_{dis} is gained using the empirical Grimme (2006) dispersion correction as summation over all atom pairs. The individual contributions are empirically scaled against a large training set giving sensible model energies. The complete energy framework can be calculated and visualised and is able to highlight the individual as well as the total energy contributions. The pairwise intermolecular interaction energies are represented as cylinders joining the molecules, the radii of these cylinders scaled proportional to the strength of the respective interaction.

CHAPTER 3:

A COMPARISON OF A SILVER AND A MOLYBDENUM MICROFOCUS X-RAY SOURCE AND THE EFFECT OF ABSORPTION ON THE DATA QUALITY IN SINGLE CRYSTAL X-RAY DIFFRACTION

3 Quality of Data in Single Crystal X-ray Diffraction

Microfocus sealed-tube X-ray sources have become standard in many laboratories, because of their very low power consumption and minimal maintenance requirements (Coles & Gale, 2012, Schulz et al., 2009). Copper (Cu) *Kα* and molybdenum (Mo) *Kα* microsources are already widely used, but the more recent commercial availability of silver anode microsources raises the question as to when silver (Ag) *Kα* is preferable. The shorter wavelength enables a higher resolution to be achieved and results in a compressed diffraction pattern, which is particularly advantageous when the diffraction geometry is restricted, for example by high-pressure cells (Saouane et al., 2013). The strength of the absorption correlates with the wavelength of the incident beam: a short wavelength is generally less prone to absorption unless it is close to an absorption edge (Hamilton, 1965, Becker & Coppens, 1974a, b). In the case of large, strongly absorbing crystals, it is possible that reduced absorption with the silver anode could more than compensate for the decrease in the absolute scattering power of the crystal (which is proportional to λ^3). The question of the optimal crystal size has been investigated for weakly absorbing crystals by Görbitz (1999). The curved mirror optics used by both Mo and Ag microsources deliver a narrow beam with a slightly anisotropic profile, making accurate sample alignment essential (Arndt, 1990, Coles & Hursthouse, 2004, Storm et al., 2004). The focal spot size of the beam is 110 and 90 mm for Mo *Kα* and Ag *Kα*, respectively (Hasse et al., 2010). This highly focused beam makes a uniform homogeneous sample illumination impossible even for small crystals. In the following, Mo and Ag microsource data are compared for a variety of crystals with significant absorption in typical data collection situations. Although in these tests independent atom model (IAM) refinements were employed, the conclusions should also apply to data collected for charge density studies, as we will see later in this thesis.

3.1 Experimental

Scandium platinate, **1** (Hasse et al., 2010, Harmening et al., 2010), murdochite, **2** (Dubler et al., 1983), sodium tungstate, **3** (Farrugia, 2007), and scandium cobalt carbide, **4** (Rohrmoser et al., 2007, Scherer et al., 2010, Eickerling et al., 2013), were used to represent inorganic compounds and minerals with medium to high absorption coefficients. Small crystals were chosen for this investigation in order to match the highly focused beams of the two microsources. Less strongly absorbing test crystals

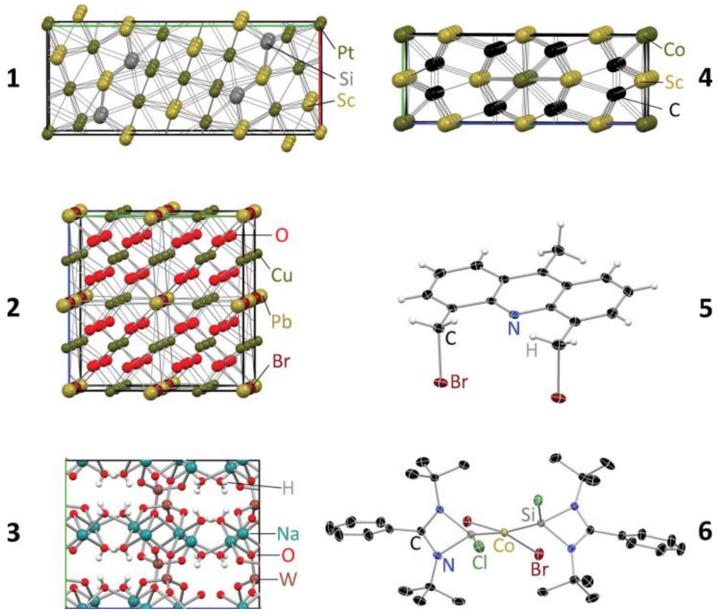

Figure 7
Test Crystals.

included a dibromoacridine derivative, **5** (Visscher, 2016), and an inorganic cobalt complex, **6** (Azhakar et al., 2013). See Figure 7 and Table 4 for detailed information on each sample.

Table 4
Experimental setup and sample characteristics. *r* is the mean crystal radius biased towards the smallest dimension, *μ* is the linear absorption coefficient, Sph. harm. denotes the order of the spherical harmonics employed in the correction and Max. res. is the maximum experimental resolution.

	Space group	Crystal dimensions [mm]	*r* [mm]	Source	μ [mm^{-1}]	$\mu \cdot r$	Sph. harm.	Max. res. [Å]	Reflections: measured/ unique
1	*Pbam*	0.06×0.04×0.02	0.014	Ag	65.25	0.919	8/7	0.33	88135/6527
				Mo	121.02	1.705		0.43	51469/3183
2	$Fm\bar{3}m$	0.12×0.11×0.09	0.049	Ag	20.50	1.009	8/7	0.31	14474/770
				Mo	38.25	1.876		0.43	10420/313
3	*Pbca*	0.11×0.05×0.03	0.021	Ag	10.16	0.214	8/7	0.40	154303/10927
				Mo	18.84	0.397		0.44	84934/8314
4	*Immm*	0.08×0.05×0.05	0.026	Ag	5.02	0.129	8/7	0.33	25448/1590
				Mo	9.78	0.251		0.43	11127/704
5	$P2_1/n$	0.20×0.16×0.15	0.078	Ag	3.16	0.246	6/3	0.79	55453/3161
				Mo	5.90	0.459		0.79	35888/3130
6	$P2_1/n$	0.08×0.06×0.02	0.018	Ag	1.53	0.027	8/5	0.79	62614/8300
				Mo	2.87	0.051		0.79	96806/8338

3.2 Diffractometer setup and data acquisition

All experiments were performed on Bruker SMART APEX II systems based on D8 three-circle goniometers with Incoatec microfocus X-ray sources (IμS) and Incoatec QUAZAR mirror optics (Schulz et al., 2009). The data were collected at 100 K crystal temperature (Mo source: Bruker CRYOFLEX; Ag source: Oxford Cryosystems CRYOSTREAM 700), 50 kV and 600 mA for both machines with an appropriate 0.5° scan strategy for the wavelength in question. Since no radiation damage to the crystals was expected, the same crystals were used to successively collect data on both diffractometers. Differences in scattering power and resolution for the two wavelengths led to differences in the data collection strategy and in the exposure times. Both diffractometers are equipped with Bruker APEX II area detectors that use Fairchild CCD6161 sensors. The only difference is the thickness of the scintillation phosphor, which results in a characteristic quantum yield of 160 e per X-ray photon for Mo *Kα* and 204 e per X-ray photon for Ag *Kα*. The detector on the Ag source uses a slightly thicker scintillation phosphor in order to compensate for the smaller gain caused by the shorter wavelength. A thicker scintillation phosphor increases the sensitivity but also increases the point spread function, which significantly broadens the reflection profiles (Gruner, 2002), as can be seen in Figure 8.

3.2.1 Data processing

Data reduction was performed with *SAINT* version 7.68A (Bruker, 2009a) from the program package *APEX2* version 2.2012.2-0 (Bruker, 2009b). The *SAINT* data reduction program uses either a predetermined or an internally derived and refined box size for the integration steps. The dimensions of this box are expected to be primarily determined by the mosaicity of the crystal, the point spread

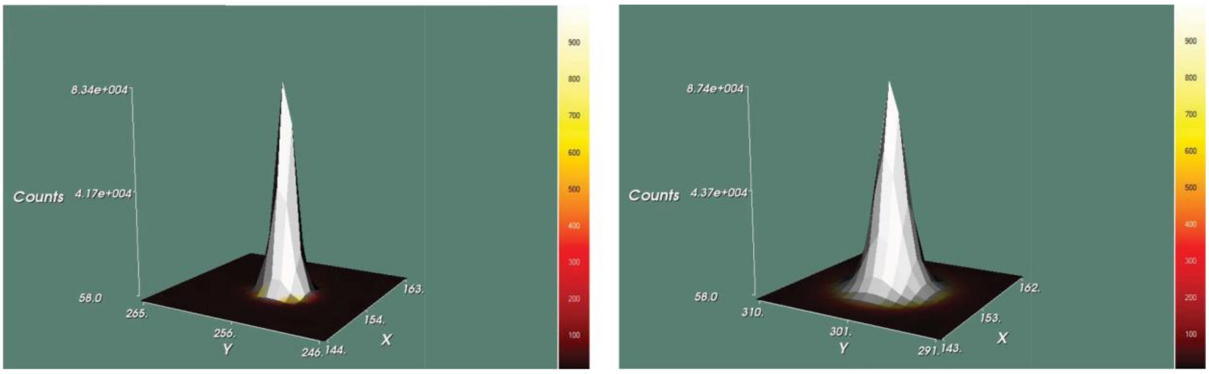

Figure 8
Reflection profiles as recorded by the scintillation phosphor for Mo $K\alpha$ (left) and Ag $K\alpha$ (right). 4×4 binning mode was used for both sources.

function of the detector and, where applicable, the $K\alpha_1/K\alpha_2$ splitting. As the same crystals were used for both sources, no changes in mosaicity were expected. However, in order to minimize systematic errors due to imprecise or improperly determined box sizes, the box size was always determined and refined by *SAINT* using a standard procedure. Data were collected up to a maximum resolution (max.) that was limited either by the scattering power of the sample or by the 2θ limit of the experimental setup. These limits are roughly 0.43 and 0.31 Å for the Mo and Ag sources, respectively, and are solely due to the different wavelengths since both sources were mounted on identical goniometers. The data for each crystal were then integrated to different resolution shells (1.00, 0.83, 0.79, 0.60, 0.43 and max. Å). This was done to facilitate the detection of resolution-dependent differences.

3.2.2 Scaling and absorption corrections

SADABS (version 2014/4) was employed for the incident beam scaling, determination of the spherical harmonic coefficients, outlier rejection and determination of the error model parameters. The current standard *SADABS* option of refining one overall g value and one K for each scan was adopted for the studied crystal structures. Additional tests were required to see if the empirical absorption correction method was a suitable treatment for the highly absorbing crystals, since the numerical correction requires well defined crystal faces. It was almost impossible to index the faces of the tiny crystals of **1** and **4** reliably, so the numerical and empirical absorption corrections were compared for the crystals of **2**, **3** and **5**, since these were larger than the width of the beam and had high linear absorption coefficients μ. It was anticipated that the numerical absorption correction would provide the best correction and that for the empirical correction it might be difficult to estimate the effective radius r for the additional spherical crystal correction. The validation of this correction involved a stepwise increase of the μr value followed by a comparison of the principal mean square atomic displacements of selected atoms with the values obtained by the numerical method. Satisfactory results were achieved when r was chosen so that it is biased towards the smallest crystal dimension; e.g. for a crystal with dimensions $0.1 \times 0.2 \times 0.3\ \text{mm}^3$ and $\mu = 10\ \text{mm}^{-1}$, 0.07 mm would be a good value for r, giving 0.7 for μr.

3.2.3 Structure refinement

All the structures were solved by either Patterson or direct methods with *SHELXS* (Sheldrick, 2008). They were refined by full-matrix least squares against F^2 using *SHELXL-2014/3* with the help of the

SHELXle graphical user interface (Hübschle et al., 2011). All non-H atoms were refined with anisotropic displacement parameters (ADPs). The H atoms were set to idealized positions and refined using a riding model with their isotropic displacement parameters constrained to be 1.5 times the equivalent isotropic displacements of the atoms to which they were attached for methyl H atoms and 1.2 times for all other H atoms. The bromine/chlorine disorder in **2** was treated with EADP/EXYZ constraints in *SHELXL*. In compound **6** the chlorine/ bromine disorder and the rotational disorder of the tertiary butyl group attached to N1 were refined using distance and ADP restraints.

3.3 Results

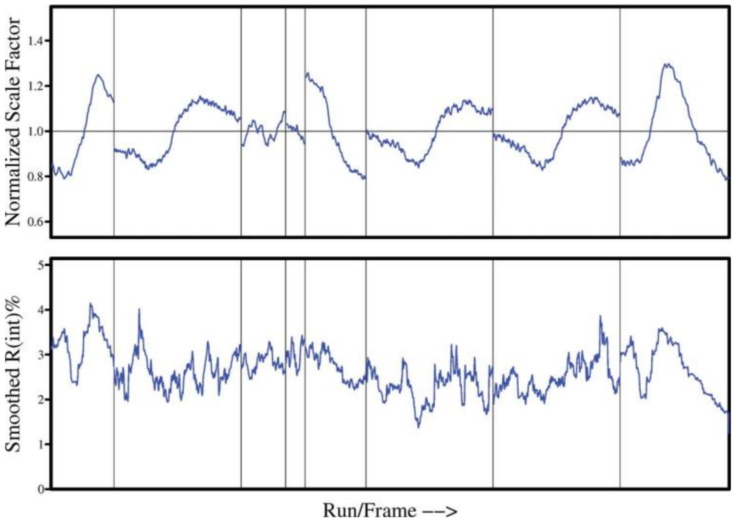

Figure 9
Incident beam scale factor $S(n)$ and merging R_{int} as output by *SADABS* for the strongly absorbing crystal **2** with Ag $K\alpha$ radiation. It should be noted that the smoothing algorithm for the R_{int} plots was changed in *SADABS* 2014/4 to make these plots more informative.

Table 5 shows the quality indicators after scaling and correction. For this table the data were truncated to the highest common resolution, but if the crystal diffracted further with Ag $K\alpha$ than could be achieved with Mo $K\alpha$ and the experimental geometry employed, these Ag $K\alpha$ data are also reported. The data collection strategies were optimized for the wavelength in question, which resulted in only slightly longer total data collection times for Ag $K\alpha$. To some extent, the larger number of reflections recorded per frame for Ag $K\alpha$ and the corresponding reduction in the number of different detector 2θ settings required compensates for the higher Mo $K\alpha$ flux. To reduce the influence of the multiplicity on the quality indicators, the multiplicity-independent $R_{\text{r.i.m.}}$ and $R_{\text{p.i.m.}}$ values (Weiss, 2001) are shown. Except for sample **6**, which gave the weakest diffraction and would probably have benefited from a longer total data collection time with Ag $K\alpha$ radiation, these R-values and $\langle I/\sigma \rangle$ for the merged data are very comparable for the two sources for data to the same resolution. The broader reflection profile for Ag $K\alpha$ (Figure 9) requires the use of slightly larger integration boxes and hence involves a larger contribution from the background noise. However, this appears to have little influence on the data from these relatively strongly diffracting crystals. Table 5 also shows the asymptotic limiting value of I/σ for infinite intensity (calculated by *SADABS* as $1/g$ from its error model) and the average number of reflections collected per second. This is calculated by dividing the total time required for the data collection by the number of reflections measured, which in most of the cases is higher for the Ag $K\alpha$ data. As shown in Figure 9 exemplarily for the strong absorbing compound **2**, the variations in the incident beam correction factor

Table 5
Data quality indicators. Res. is the maximum available resolution, Mult. denotes the multiplicity.

	Source	Res. [Å]	Compl. [%]	Mult.	⟨I/σ⟩	$R_{\mathrm{r.i.m.}}$	$R_{\mathrm{p.i.m.}}$	Exp.	I/σ limit	Refl./s
1	Ag	0.33	97.6	13.06	27.97	0.0718	0.0181	60-120	16.4	0.18
		0.43	99.4	18.93	40.02	0.0619	0.0143		18.1	0.05
		0.83	99.8	12.88	45.42	0.0403	0.0113		21.3	0.04
	Mo	0.43	100	15.92	39.12	0.0491	0.0120	15-90	17.0	0.02
		0.83	100	14.80	40.76	0.0464	0.0125		17.8	0.07
2	Ag	0.31	99.1	18.63	81.63	0.0298	0.0061	5-60	33.6	0.23
		0.43	100	25.27	112.20	0.0255	0.0051		40.1	0.17
		0.83	100	34.14	196.24	0.0214	0.0045		56.5	0.13
	Mo	0.43	100	33.19	125.77	0.0361	0.0071	5-60	29.1	0.09
		0.83	100	30.43	127.70	0.0370	0.0084		27.6	0.04
3	Ag	0.40	99.9	14.10	48.46	0.0301	0.0072	20-120	43.9	1.06
		0.44	99.9	14.87	58.00	0.0282	0.0066		49.3	0.87
		0.83	100	25.96	105.23	0.0247	0.0049		44.8	0.01
	Mo	0.44	99.4	10.15	45.04	0.0316	0.0086	10-60	37.1	0.49
		0.83	100	15.09	81.89	0.0241	0.0062		48.1	0.02
4	Ag	0.33	83.3	13.34	61.51	0.0274	0.0059	20-60	54.9	0.11
		0.43	100	25.58	112.10	0.0247	0.0050		64.7	0.10
		0.83	100	21.39	194.77	0.0160	0.0038		82.5	0.16
	Mo	0.43	99.7	15.73	122.91	0.0208	0.0040	20-60	66.1	0.04
		0.83	100	30.71	215.43	0.0216	0.0037		56.8	0.16
5	Ag	0.79	99.8	17.49	56.22	0.0323	0.0072	10	36.1	1.28
		0.83	100	18.35	60.84	0.0312	0.0068		36.4	0.92
	Mo	0.79	100	11.45	63.01	0.0242	0.0067	10	44.2	0.75
		0.83	100	11.92	67.22	0.0234	0.0064		44.0	0.74
6	Ag	0.79	99.5	7.51	29.94	0.0407	0.0145	30-40	34.4	0.73
		0.83	99.5	7.71	33.01	0.0388	0.0136		38.0	0.68
	Mo	0.79	99.8	11.56	44.49	0.0290	0.0075	30	33.6	0.80
		0.83	99.8	12.43	49.87	0.0279	0.0070		34.4	0.75

$S(n)$ can be substantial, even for Ag $K\alpha$ radiation. Despite this, the $R_{\mathrm{r.i.m.}}$ and $R_{\mathrm{p.i.m.}}$ values after correction (red lines in Figure 10) are low and show little systematic variation with resolution. The corresponding values for Mo $K\alpha$ (blue lines in Figure 10) are similar at higher resolution but increase significantly at low resolutions, indicating that the empirical absorption correction is less effective at correcting for the even higher absorption with molybdenum radiation. The χ^2 plots for the same experiments in Figure 11 again show a more pronounced rise at low resolutions for the molybdenum data;

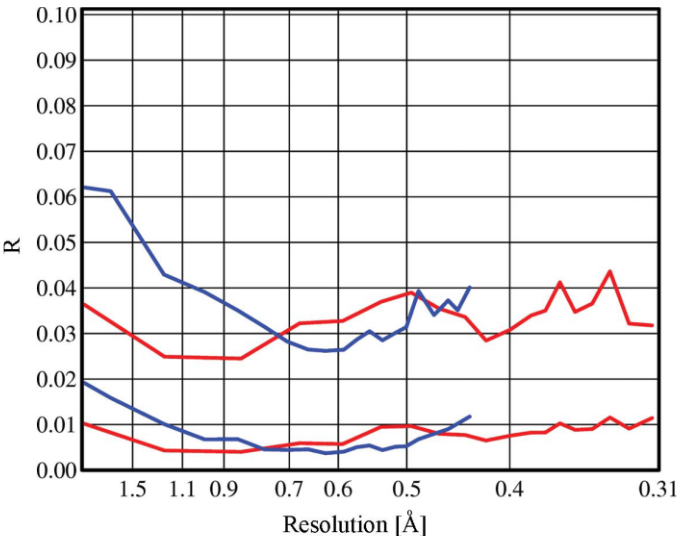

Figure 10
$R_{\mathrm{r.i.m.}}$ (upper curves) and $R_{\mathrm{p.i.m.}}$ (lower curves) after correction as a function of the resolution in Å for Ag (red) and Mo (blue) for the strongly absorbing crystal **2**. This figure was prepared with the *XPREP* (Bruker, 2014) program.

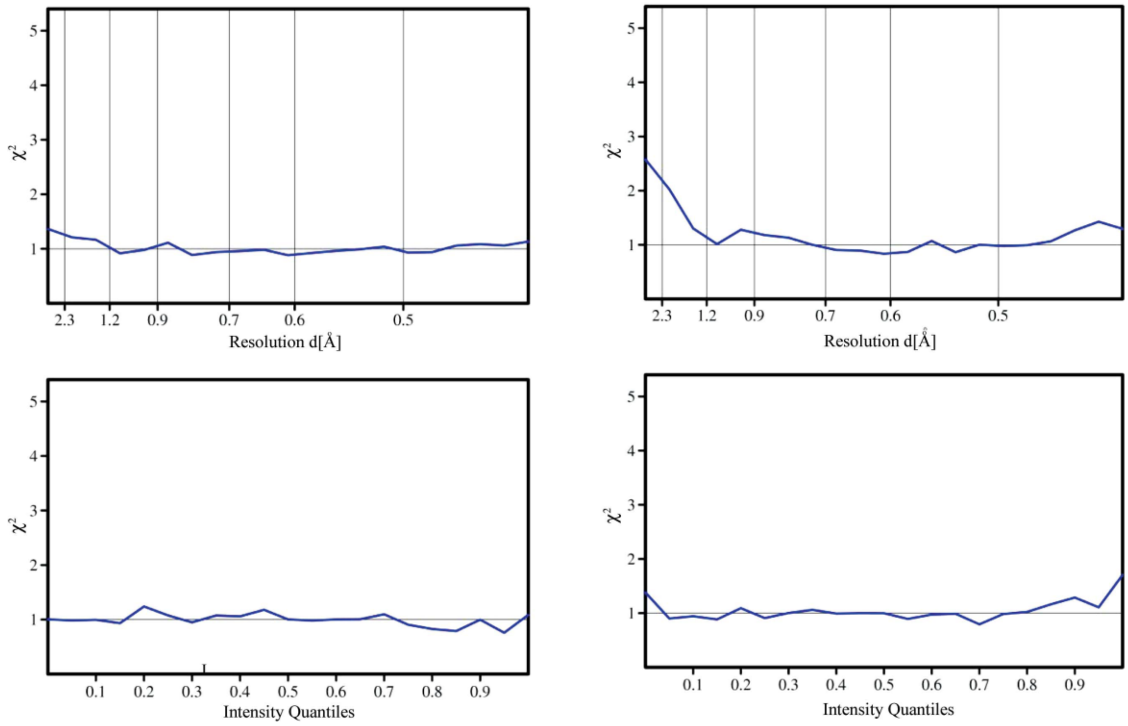

Figure 11

χ^2 after applying corrections and deriving the error model for crystal **2**. Ag (left) and Mo (right) radiation. $\chi^2 = \langle N \sum (I - \langle I \rangle)^2 / (N-1) \sum \sigma^2(I) \rangle$ (N equivalents).

however, these plots also demonstrate that the corrections have been very effective for both sources, even for this highly absorbing sample. Since the error model has not been fitted as a function of the resolution, a flat curve close to a χ^2 of unity for the full resolution range is a particularly good validation of the quality of the corrected data. Convincing χ^2 plots were obtained in all the analyses reported here. Figure 12 shows the Diederichs plot prepared for the Ag $K\alpha$ data to 0.43 Å resolution for sample **4** using *SADABS*. A limiting value greater than 30 for I/σ at infinite intensity is regarded as adequate for synchrotron data and is thus used to indicate that the data are relatively free from systematic errors. With the exception of the highly absorbing sample **1**, the values reported here are all higher than 30. The limiting I/σ values for the unmerged data are relatively constant for the same sample and do not vary much with the resolution threshold, supporting

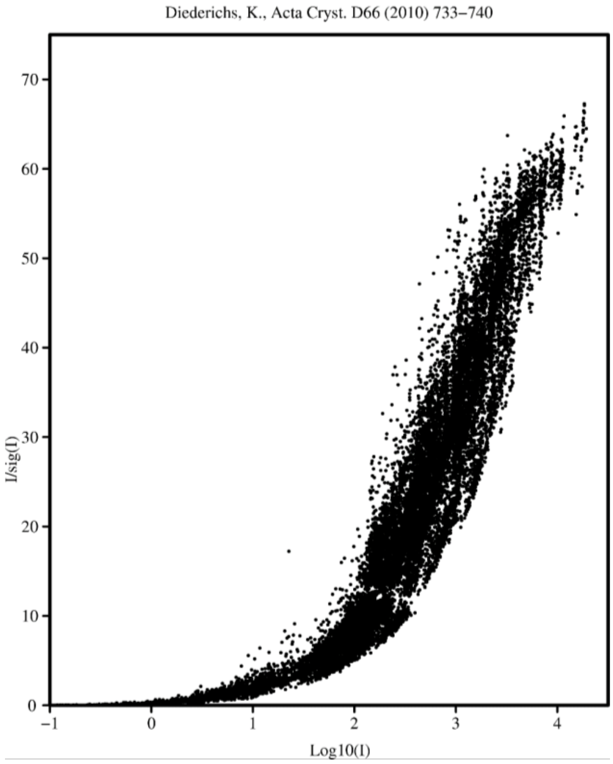
Diederichs, K., Acta Cryst. D66 (2010) 733–740

Figure 12

Diederichs plot of I/σ against $\log(I)$ for sample **4** for Ag $K\alpha$ data to 0.43 Å.

the idea that this is a robust indication of the extent of systematic errors for a given crystal and experimental arrangement. On the other hand, the mean $\langle I/\sigma\rangle$ values for the merged data are clearly correlated with the multiplicity, which tends to decrease at the highest resolution. For the strongly absorbing sample **2**, the merging *R*-values are lower for the Ag $K\alpha$ data, but the opposite is true for the less strongly absorbing sample **6**. Overall the precision of the Ag $K\alpha$ and Mo $K\alpha$ data is comparable.

After the full structure refinement, the *R*1 value calculated using all data, the *wR*2 value (the quantity minimized in the full-matrix least-squares refinement) and the residual electron density $\Delta\rho$ were compared at both the maximum resolution achieved and the standard resolution of 0.83 Å. $\Delta\rho$ was calculated as the difference between the highest and lowest residual density in a weighted difference Fourier map. For crystals **2**, **3** and **5** it proved possible to index the crystal faces and compare the numerical and empirical absorption corrections. However, the attempts to refine the absorption coefficient μ, although this works well for conventional sealed tube sources without focusing optics, were not satisfactory. Especially for the Ag $K\alpha$ data, μ refined to unreasonably small values or even to zero. This problem may be attributed to the use of highly focused beams, the Ag $K\alpha$ source having the most highly focused beam. When the numerical correction is combined with lower-order spherical harmonics (even / odd orders 4 / 1), the merging *R*-values and the *R*1 values for the *SHELXL* refinement (shown in Table 6) were extremely similar to those obtained using no numerical correction but higher-order spherical harmonics (specified in Table 4 on page 25) plus a spherical crystal correction Q($\mu\cdot r$, 2θ). In both cases the incident beam term S(n) is responsible for about half the correction. It is thus debatable whether the numerical correction is

Table 6
Selected quality criteria after structure refinement.

	Res. [Å]	Source	*R*1 (all data)	*wR*2	$\Delta\rho$ [eÅ^{-3}]	Data/ parameter	*R*1#
1	0.83	Ag	0.0133	0.0283	2.64	10.64	–
		Mo	0.0216	0.0665	4.43	10.60	–
	0.43	Ag	0.0219	0.0391	7.34	71.93	–
		Mo	0.0262	0.0678	13.15	70.86	–
2	0.83	Ag	0.0170	0.0566	1.68	5.27	0.0166
		Mo	0.0138	0.0360	1.33	5.27	0.0128
	0.43	Ag	0.0201	0.0469	9.69	28.55	0.0201
		Mo	0.0196	0.0451	7.07	28.45	0.0193
3	0.83	Ag	0.0080	0.0193	0.80	11.87	0.0081
		Mo	0.0094	0.0215	0.98	11.91	0.0092
	0.43	Ag	0.0151	0.0228	4.01	79.87	0.0151
		Mo	0.0172	0.0326	5.34	79.83	0.0165
4	0.83	Ag	0.0129	0.0354	0.77	6.33	–
		Mo	0.0157	0.0408	1.21	6.33	–
	0.43	Ag	0.0099	0.0254	1.25	39.11	–
		Mo	0.0121	0.0327	1.70	39.11	–
5	0.83	Ag	0.0193	0.0470	1.21	14.62	0.0193
		Mo	0.0197	0.0491	1.34	14.52	0.0198
	0.79	Ag	0.0206	0.0488	1.47	16.94	0.0205
		Mo	0.0211	0.0541	1.37	16.77	0.0211
6	0.83	Ag	0.0237	0.0488	0.54	16.00	–
		Mo	0.0252	0.0572	0.63	16.07	–
	0.79	Ag	0.0260	0.0506	0.66	18.55	–
		Mo	0.0278	0.0593	0.65	18.64	–

\# *R*1 values for the refined structure after application of a numerical absorption correction based on the measured crystal faces and the absorption coefficient μ calculated from the known unit-cell contents. The other *R*-values in this table were obtained using the empirical correction.

justified. In practice an effective crystal radius r for the spherical correction Q(μr,2θ) biased towards half the smallest crystal diameter gives an adequate spherical crystal correction. For ten of the twelve combinations of crystal and resolution cut-off shown in Table 6, both $R1$ and $wR2$ were lower for the Ag $K\alpha$ data. The residual density values show a similar trend but are not quite as decisive. The $R1$ and $wR2$ values are significantly lower for Ag (average values $R1$ 0.0178, $wR2$ 0.0398) than for Mo ($R1$ 0.0197, $wR2$ 0.0485). Thus, although the data precision (Table 5) is comparable for the two sources, the Ag data are clearly more accurate (Table 6). These low R factors (three of the $R1$ values for all data are below 1 %) confirm that the empirical corrections have performed remarkably well, despite the unfavourable combination of highly focused beams and relatively high absorption. For the refinement of structures **2** and **4** against data truncated to the standard (*Acta Crystallographica*) requirement of 0.83 Å, the data-to-parameter ratios are low (5.27 and 6.33, respectively). Since the scattering is dominated by the lead (Pb) and bromine (Br) atoms in the case of **2**, the oxygen (O) atoms cannot reliably be refined. However, with data to 0.43 Å the data-to-parameter ratio is 28.55 and there are no problems refining the oxygen atoms. Therefore, it should be standard practice to collect data to the highest possible resolution especially when both heavy and light atoms are present.

3.4 Conclusion

The empirical correction employed in *SADABS* performed remarkably well for strongly absorbing crystals despite the highly focused microsource beams, leading to very low R factors for the refined structures. While the precision of the corrected intensities was comparable for both Ag $K\alpha$ and Mo $K\alpha$ microsources, their accuracy was higher for the silver source because of the reduced absorption. For strongly absorbing crystals the Ag $K\alpha$ microsource data were in general less affected by systematic errors than the Mo $K\alpha$ data. The application of a numerical absorption correction did not improve the results. Clearly, the assumption that the crystal is completely bathed in a uniform X-ray beam is not valid for highly focused X-ray optics. However, when the empirical approach is used it is important to obtain a good estimate of the effective crystal radius for the correction term Q($\mu \cdot r$, 2θ). An estimate of r biased towards half the smallest crystal diameter is an adequate approximation. Due to the remarkable performance of the empirical multi-scan correction method it is advisable to always try to collect a full sphere of data, maximising the number of diffraction pathways and therefore the information on the crystal shape.

CHAPTER 4:

LOW ENERGY CONTAMINATION OF MIRROR-FOCUSED SINGLE CRYSTAL X-RAY DIFFRACTION DATA

4 Low energy contamination

Focusing multilayer mirror optics have become standard for in-house as well as synchrotron X-ray source beam conditioning. The high X-ray flux density and fine focus achieved by reflection on mirror optics facilitate high-performance experiments in-house (Coles & Gale, 2012, Schulz et al., 2009). The beam-focusing device is based on elliptically shaped silicon wafers that are coated with tungsten/carbon multilayers to reflect the X-rays by constructive interference, as suggested by Schuster and Göbel (Schuster & Göbel, 1995, Storm et al., 2004). Two identical mirrors arranged in a 90° side-by-side geometry, as proposed by Montel (1957), enable the originally divergent beam to be focused in two dimensions (Hertlein et al., 2008). Michaelsen et al. (2004) describe the design and fabrication of this type of beam-shaping equipment in more detail. The X-ray optic produces a very high flux density; however, low-energy photons that originate from the continuous X-ray emission spectrum permeate the device by total reflection and cause additional diffraction. Storm et al. (2004) explained this low-energy photon contamination in a technical paper presenting the beam-shaping optics for Mo *Kα* single-crystal diffraction. Later, Macchi et al. (2011) reported the degree of contamination to be in the range of 0.2 – 1.5%. These numbers seem small, but this is certainly not the case for their influence on the reflection data. Even 0.1% of the intensity of a low order reflection added to that of a mid-angle reflection dramatically changes its resulting intensity. Low-angle reflections are completely unaffected, whereas the contamination of high-order reflections is substantially lower than for the aforementioned mid-resolution range. Software-reconstructed images (precession images) calculated directly from the recorded frames by the software package *APEX2* (Bruker, 2014a) clearly show the spectral impurity

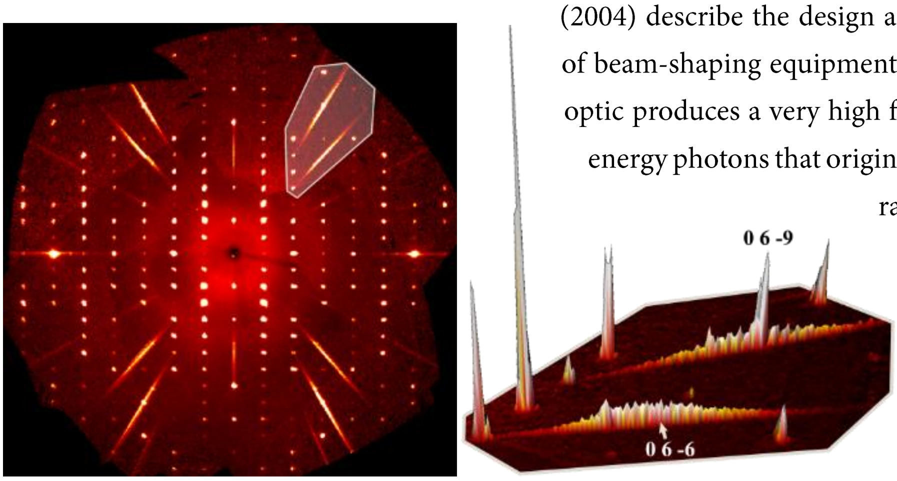

Figure 13
Software-reconstructed precession image of the 0kl diffraction plane calculated from the experimental data of compound 1 (left). Three dimensional representation of the highlighted section (right).

Table 7
Comparison of the significances and the raw intensities of the filtered and the unfiltered data for all investigated compounds. Filter: Aluminium foil, thickness 100 µm.

		XPREP		*SAINT*	
		I/σ	Δ [%]	⟨*I*⟩	Δ [%]
1	no filter	48.11†	3.51	1904.95	16.87
	filter$^{\#}$	46.42		1583.56	
2	no filter	61.12	5.96	288.47	26.47
	filter	57.48		212.11	
3	no filter	36.39	13.38	700.42	15.64
	filter	31.52		590.84	
4	no filter	25.40	19.21	327.04	32.63
	filter	20.52		220.34	
5	no filter	69.57	0.86	7318.76	9.75
	filter	68.97		6605.07	

†: exposure time reduced (from 30 s to 20 s) to avoid detector saturation; #: three aluminium layers were needed to filter the contamination (300 µm).

(Figure 13). Since this diffraction originates from the continuous intensity profile (*Bremsstrahlung*), there is no sharp reflection pattern but blurred streaks radially oriented throughout the image. The peak intensity of a strong reflection hkl is roughly at the $3h\ 3k\ 3l$ position. The only way to produce a primary beam that is free of the low-energy photons is to insert a low-density material foil (Al or Zr) into the beam (Storm et al., 2004). Macchi et al. (2011) investigated this solution in detail and concluded that it is indeed a simple and economical one. There are, however, at least two major drawbacks in following this procedure. Firstly, the filter reduces all intensities. This becomes problematic as soon as the last bit of resolution is crucially needed, for example in charge density investigations or if poorly diffracting crystals are to be probed. In this investigation, the loss of intensity amounts to 1–19% in I/σ, as printed out by the program *XPREP* (Bruker, 2015), or from 10 to 32% in mean raw intensity following the listing file of the data reduction program *SAINT* (Table 7). Of course, the low-energy photons add to the overall intensity, increasing the unfiltered raw intensity even more. Secondly, this solution is, of course, not applicable to already measured data. Re-collection and adjustment of the collection strategy to the new experimental conditions is somewhat time consuming and should be avoided if possible. With the newly introduced single photon counting hybrid pixel array detectors (Wenger et al., 2014, Stalke, 2014), this contamination should no longer be problematic since these detectors are able to discriminate on photon energy. The given energy difference is most likely large enough to set an effective threshold ignoring the low-energy photons. However, this needs to be experimentally validated.

4.1 Empirical correction

The primary effect of the low-energy contamination is that the intensities of the reflections $3h\ 3k\ 3l$ are systematically increased in proportion to the intensity of the reflection hkl. Therefore, the experimentally determined intensity of these reflections can be written as the sum of two components, similar to the λ/2 contamination (Kirschbaum et al., 1997, Macchi et al., 1998):

$$I(3h\ 3k\ 3l)_{\text{measured}} = I(3h\ 3k\ 3l)_{\text{unaffected}} + k_{3\lambda}\ I(hkl) \qquad \text{Eq. 4-1}$$

As $I_{\text{unaffected}}$ is experimentally unavailable, it is replaced by F^2_{calc}, and I_{measured} by F^2_{obs}. Hence, the best value for the contamination coefficient $k_{3\lambda}$ can be determined from a linear regression using all $3h\ 3k\ 3l$ reflections and $k_{3\lambda}$ can afterwards be used for data correction with a routine already implemented in the Bruker program *SADABS* (Krause et al., 2015). In addition, it became apparent that a weighting applied to the linear regression could improve the reliability of the derived correction factor. Strong hkl reflections are the main contaminants and a large contribution of contamination allows for better separation from the intensity variations caused by other sources of error. In the same way, well determined reflections, for example with low $\sigma\left(F^2_{\text{obs}}\right)$, are needed. The weighting scheme $w = F^2_{\text{obs}}(hkl)/\sigma\left(F^2_{\text{obs}}(3h3k3l)\right)$ was applied to compensate for this. Nevertheless, one drawback of this external factor determination is, of course, the dependence on the model. Therefore, a correction incorporated directly into the refinement process with a refined correction factor would be more elegant (Dudka, 2010, Angel, 2015). The contamination can be treated as twinning, where all $3h\ 3k\ 3l$ reflections of a virtual twin domain overlap with the base reflection hkl (Herbst-Irmer & Sheldrick, 1998). This means that F^2_{calc} is calculated as

$$\left[F^2_{calc}(3h\,3k\,3l)\right]^* = (1 - k_{twin})F^2_{calc}(3h\,3k\,3l) + k_{twin}F^2_{calc}(hkl) \qquad \text{Eq. 4-2}$$

It follows that k_{twin} is an alternative measure for the degree of contamination, since $k_{\text{twin}} \cong k_{3\lambda}$, as $k_{\text{twin}} \ll 1$. Another particular advantage of following this protocol is the directly available *s.u.* from the full-matrix least-squares refinement. In *SHELXL* (Sheldrick, 2015b) this procedure is possible using a data file in the HKLF5 format with the appropriate information included. In principle this could be achieved with the TWIN 1/3 0 0 0 1/3 0 0 0 1/3 command, which would not need a special data file. However, non-integer values are not allowed in combination with the TWIN command in *SHELXL-2014/7*.

4.2 Experimental Details

To test the empirical correction developed within this thesis, we collected data on five compounds, **1–5** (see Figure 14 and Table 8), for a routine structure determination and investigated the influence on two charge density data sets of compound **6**. Detailed information of the investigated structures can be found in the appendix A3.

4.2.1 Data collection

All experiments were performed on Bruker SMART APEX II systems based on a D8 three-circle goniometer equipped with a molybdenum Incoatec micro-focus X-ray source (IμS) and an Incoatec QUAZAR mirror optic or a Bruker rotating-anode X-ray source (TXS) and Incoatec HELIOS mirror optics. Two data sets were collected on each crystal at a temperature *T* of 100 K (TXS: Bruker CRYOFLEX; IμS: Oxford Cryosystems Cryostream 700) or room temperature for compound **5**, one with and one without an Al foil inserted into the beam path right behind the mirror optics. The same data collection protocol was used for each respective

Table 8
Test crystals.

	Formula	Space group	X-ray source	*T* [K]	Literature
1	$C_{28}H_{18}N_2$	$C2/c$	IμS	100	Visscher (2016)
2	$C_{12}H_4N_4$	$C2/c$	IμS	100	Wolf (2014)
3	$C_{18}H_{17}CuO_6$	$C2/c$	IμS	100	J. A. Solera-Rojas, M. L. Montero, L. Krause, D. Stalke & L. W. Pineda (unpublished)
4	$C_{34}H_{26}MgN_4O_4$	$P2_1/n$	TXS	100	*Köhne* (unpublished)
5	$C_{11}H_{38}O_2S$	$P2_12_12_1$	IμS	293	*Cook and Moffatt (1968)*, Guzei et al. (2008)
6	$C_{52}H_{38}P_2S_2$	$P\bar{1}$	IμS/TXS	100	(Herbst-Irmer et al., 2013)

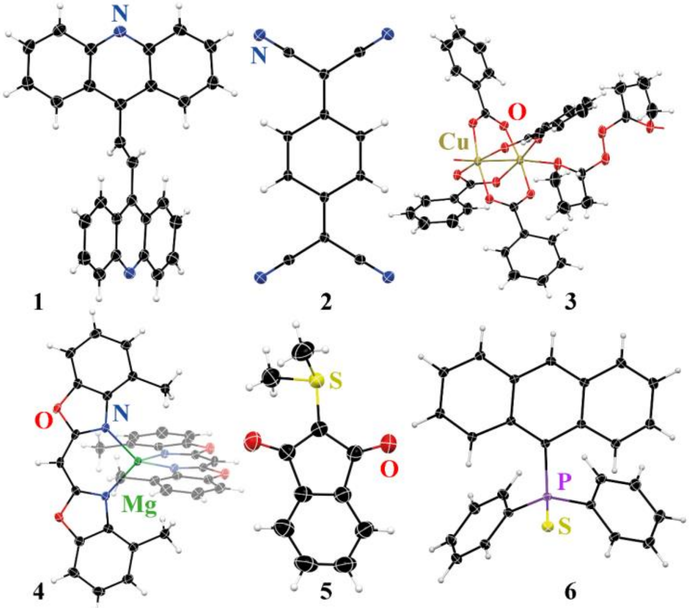

Figure 14
Test crystals.

pair, with the exception of compound **1**, where the data acquisition time was decreased without the Al foil to avoid detector saturation.

4.2.2 Data processing

Data reduction was performed with *SAINT* (Bruker, 2013) from the program package *APEX2* (Bruker, 2014a). *SADABS* (Krause et al., 2015) was employed for the scaling, correction, error model determination and outlier rejection of the data. The two data sets were treated equally throughout the data processing. All structures were solved with *SHELXT* (Sheldrick, 2015a) and refined by full-matrix least-squares against F^2 using *SHELXL-2014/7* (Sheldrick, 2015b) within the *SHELXle* graphical user interface (Hübschle et al., 2011). All non-hydrogen atoms were refined with anisotropic displacement parameters. The hydrogen atoms were set to idealized positions and refined using a riding model. The isotropic displacement parameters of the hydrogen atoms were constrained to 1.5 times the equivalent isotropic displacement of the carbon atom they are attached to for methyl hydrogen atoms and to 1.2 times for all other hydrogen atoms.

4.2.3 Missing reflections

A short remark on missing low order reflections e.g. that are obscured by the beamstop or rejected by the integration program for being overexposed. This means that for some contaminated mid-order reflections the base reflection's intensity is no longer available making the empirical correction impossible. The program *XPREP* is able to generate a theoretical *hkl* from a *SHELXL* parameter file that contains *all* intensities according the given model (Fourier transform of the model). It has to be emphasised that these intensities are entirely theoretical and of course contain model bias. Nevertheless, previously missing intensities are made available and can be used to correct contaminated reflections and these *model based intensities* should prove sufficient to serve as basis, despite their theoretical origin.

4.2.4 Theoretical validation

To visualize the effect of low energy contamination, theoretical *hkl* were generated from the calculated structure factors of compound **1** using the Bruker program *XPREP*. These *hkl* were then artificially contaminated by the addition of a certain fraction of the structure factor of all reflections *hkl* to their corresponding *3h3k3l* reflections (fractions added: 0.2 % and 1.0 %, Table 9).

Table 9

Comparison of the fractal dimension against residual density after artificial addition of contamination to theoretical data. The difference Fourier was calculated using 72x64x64 grid points, a σ-cutoff of zero and a resolution of 0.40 Å.

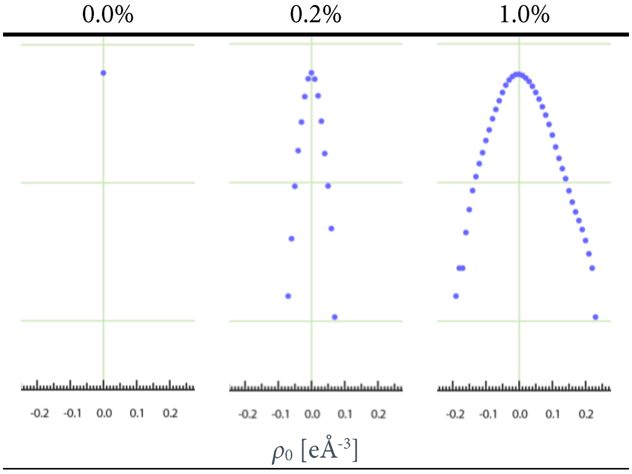

The differences between the model and the given data were calculated. Of course, this only adds a sharp peak of wavelength 3λ while for experimental data the blurred streaks of low energy photons do contaminate as well. However, on a quantitative level this procedure is able to reproduce the features observed for experimental data. Table 10 shows selected indicators representing the quality of the derived model. From this data it is clear that the contamination basically leads to an addition of noise. This is mainly represented by an increasing e_{gross}. In the first place it might be counterintuitive for the $d^{\text{f}}(\rho_0)$ value to increase as well, indicating a more *featureless* residual density *after* the addition of noise (from: 2.7720 to: 2.7909). This can be explained by the fact that any former peaking residual feature is *masked out* by the addition of noise, increasing the overall noise level and therefore indirectly flattening the residual density. A contamination of more than one percent results in a severely broadened curve that seems somewhat exaggerated when compared to actual data showing this percentage of contamination. Here, the *sharp peak* restriction of the utilized contamination model might introduce additional errors, degrading the data faster than experimental findings suggest.

Table 10
Selected quality indicators after artificial addition of contamination to theoretical data.

contamination [%]	**0.0**	**0.2**	**1.0**
$wR(F^2)$	0.0	0.0019	0.0096
$R(F^2)$	0.0	0.0011	0.0054
ρ(peak) [eÅ^{-3}]	0.001	0.074	0.238
ρ(hole) [eÅ^{-3}]	-0.001	-0.074	-0.197
e_{gross} [e]	0.00	13.96	36.88
$d^{\text{f}}(\rho_0)$	2.7720	2.7909	2.7805
$\rho_{\min}(d{=}2)$ [eÅ^{-3}]	-0.0028	-0.0488	-0.1341
$\rho_{\max}(d{=}2)$ [eÅ^{-3}]	0.0028	0.0488	0.1340

Table 11
The *most disagreeable reflections* for the unfiltered data of **1**.

h	k	l	F^2_{obs}	F^2_{calc}	Error / s.u.	F_{calc} / $F_{\text{calc}}(\max)$	Res. [Å]
-6	6	6	485.7	146.58	9.77	0.040	1.38
-6	6	12	282.82	67.90	8.02	0.027	0.94
-6	0	6	142.60	31.00	7.57	0.019	1.88
-5	5	5	76.63	6.14	7.20	0.008	1.66
-3	3	9	469.64	228.05	6.82	0.050	1.31
-7	7	7	430.86	244.10	5.06	0.052	1.18
-15	3	3	30.72	0.79	4.49	0.003	0.85
-8	8	8	41.56	0.95	4.37	0.003	1.03
6	0	0	2755.76	2090.42	4.26	0.152	1.98
8	0	0	218.53	125.37	4.02	0.037	1.48

Table 12
The *most disagreeable reflections* for the filtered data of **1**.

h	k	l	F^2_{obs}	F^2_{calc}	Error / s.u.	F_{calc} / $F_{\text{calc}}(\max)$	Res. [Å]
0	6	6	44.53	0.84	6.07	0.003	1.37
-5	5	5	26.77	5.6	4.37	0.008	1.66
1	1	3	143.82	239.03	4.32	0.051	3.03
-12	10	4	292.2	178.03	4.02	0.044	0.82
7	7	7	219.67	139.07	4.02	0.039	0.84
6	0	2	105.45	59.51	3.72	0.026	1.63
4	2	0	8.69	0.11	3.71	0.001	2.67
-4	0	4	1232.44	966.42	3.69	0.103	2.81
0	4	1	446.49	334.69	3.43	0.061	2.94
4	0	4	20.61	5.29	3.42	0.008	1.66

Error/s.u. is calculated as $\sqrt{\text{w}\Delta^2/\langle \text{w}\Delta^2\rangle}$, where w is given by the weight formula, $\Delta = F^2_{\text{obs}}\text{-}F^2_{\text{calc}}$ and $\langle\ \rangle$ refers to the average over all reflections.

4.3 Results

The most prominent indicator for low-energy contamination apart from the software-reconstructed precession images prior to the refinement is the list of most disagreeable reflections in the *SHELXL* listing file. Table 11 shows this list for the unfiltered data set of compound **1**, displaying mostly 3*h* 3*k* 3*l* reflections with $F^2_{\mathrm{obs}} > F^2_{\mathrm{calc}}$. In the equivalent list for the filtered data (Table 12), no dependency on the indices is recognizable. Table 13 summarizes the superiority of the filtered data set: *R*1 is significantly lower, $K = \langle F^2_{\mathrm{obs}} \rangle / \langle F^2_{\mathrm{calc}} \rangle$ for the group of reflections containing only weak data with $F_{\mathrm{calc}}/F_{\mathrm{calc}}(\mathrm{max}) < 0.006$ is much closer to unity and the bond precision of C – C bonds is improved.

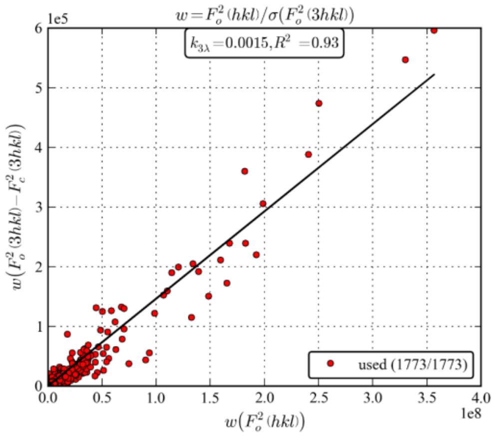

Figure 15
Difference of the observed and calculated structure factors of the 3*h*3*k*3*l* reflection *versus* the observed structure factor of *hkl*.

Considering that only 3.7% of the data are contaminated, this is a significant increase in model quality. Then the two empirical correction methods were applied to the unfiltered data set to test if the results are similar to the quality of the filtered data set. Figure 15 shows a plot for the determination of $k_{3\lambda}$. This correction factor is then used in *SADABS*. As an alternative correction, k_{twin} is refined in *SHELXL*. For both correction methods a striking improvement is detectable (Table 13). The difference between the two methods is negligible. Compared to the filtered data, both corrections perform well. The next question to address is: what influences the correction factor? In general, the additional photons possess a lower energy and are therefore more prone to absorption than the primary beam. Accordingly, it is assumed that there is a strong correlation between the transmission of the crystal sample and the resulting correction factor. Figure 16 shows the results of a screening of roughly 50 crystal structures (see Appendix A4.12) and the relationship between $k_{3\lambda}$ and the

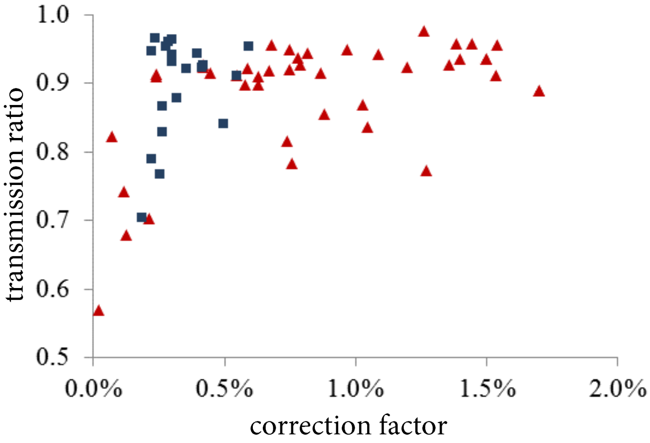

Figure 16
Transmission ratio versus $k_{3\lambda}$ for a collection of different structures. Data collected on the TXS (blue squares) and on the IμS (red triangles).

Table 13
Comparison of the model quality for models derived from unfiltered and filtered data for compound **1**.

Data set	Data used	Data with *R*1 ($F_{\mathrm{obs}} > 4\,\sigma(F_{\mathrm{obs}})$)	bond precision C – C [Å]	*R*1 ($F_{\mathrm{obs}} > 4\,\sigma(F_{\mathrm{obs}})$)	*R*1 (all data)	w*R*2 (all data)	*K*(weak)
No filter, no correction	1697	1547	0.0026	0.0429	0.0463	0.1265	2.442
Filter	1707	1549	0.0020	0.0393	0.0428	0.1105	1.726
$k_{3\lambda} = 0.0123$	1697	1539	0.0021	0.0402	0.0438	0.1108	1.762
$k_{\mathrm{twin}} = 0.0117(7)$	1697	1530	0.0021	0.0396	0.0435	0.1113	1.615
default $k_{3\lambda} = 0.0100$	1697	1539	0.0021	0.0404	0.0440	0.1117	1.756

respective transmission ratio. $k_{3\lambda}$ ranges from nearly 0 to 1.7%. Highly absorbing crystals (transmission ratio below 0.6) do not need any corrections: $k_{3\lambda}$ is close to 0. However, for all other compounds no clear dependency on the transmission is recognisable.

However, $k_{3\lambda}$ seems to be significantly lower for data collected on the TXS compared to IμS data. We normally measure data on low- or medium absorbing crystals of organometallic compounds and therefore assumed a default correction factor value of 0.002 for data collected on the TXS and 0.010 for the IμS. Table 14 lists the results for compounds **2**–**5**. All corrections show an improvement in model quality. The differences between the various corrections are not significant. As shown by Macchi et al. (2011) the influences on the positional and vibrational parameters are subtle, showing a variation in *xyz* and U_{ij} of the two compared models of much less than 3σ. We are able to reproduce these findings since the corresponding models do not differ by more than 3σ. In conclusion, the use of a filter is the physically correct treatment of the contamination, but the results for the empirically corrected data are similar.

Table 14
Comparison of model quality indicators.

Data		Correction factor	Δ(C – C) [Å]	*R*1 (all data)	w*R*2	*K*(weak)#
2	No filter, no correction	–	0.0013	0.0377	0.1074	1.337
	filter	–	0.0010	0.0362	0.0992	0.995
	$k_{3\lambda}$	0.0086	0.0011	0.0360	0.0967	1.006
	k_{twin}	0.0082(5)	0.0011	0.0357	0.0963	1.053
	default	0.0100	0.0011	0.0363	0.0975	0.985
3	No filter, no correction	–	0.0029	0.0342	0.0704	1.574
	filter	–	0.0027	0.0380	0.0681	1.475
	$k_{3\lambda}$	0.0080	0.0026	0.0331	0.0651	1.340
	k_{twin}	0.0076(3)	0.0026	0.0328	0.0650	1.356
	default	0.0100	0.0026	0.0333	0.0650	1.321
4	No filter, no correction	–	0.0016	0.0483	0.1148	1.466
	filter	–	0.0016	0.0499	0.1113	1.648
	$k_{3\lambda}$	0.00613	0.0016	0.0477	0.1102	1.239
	k_{twin}	0.0052(2)	0.0016	0.0475	0.1091	1.205
	default	0.0020	0.0016	0.0479	0.1118	1.393
5	No filter, no correction	–	0.0024	0.0262	0.0680	1.049
	filter	–	0.0024	0.0261	0.0674	1.005
	$k_{3\lambda}$	0.0016	0.0024	0.0257	0.0669	1.033
	k_{twin}	0.0018(2)	0.0024	0.0256	0.0668	1.031
	default	0.0020	0.0024	0.0257	0.0669	1.031

#*K*(weak) = F_o / F_c, for reflections with F_c / F_c(max) ≈ 0

For a charge density investigation, a much higher level of accuracy and resolution is needed compared to routine structure determination, the importance of accurately measured data for charge density studies cannot be emphasized enough (Destro et al., 2004, Wolf et al., 2014a, Zhurov et al., 2008). The resolution of the data should be as high as possible, so that the attenuation of the beam could be a problem. Programs using (Hansen & Coppens, 1978) multipole model such as *XD2006* (Volkov et al., 2006) or *MoPro* (Guillot et al., 2001) are, of course, not intended for a twin refinement. Therefore, the correction via a twin refinement is not an option for this type of investigation but must be applied during the scaling of the data. One could expect that the contamination is even more severe than for routine structures as there are normally very strong low-order reflections and a large quantity of much weaker high-order data. For compound **6**, two data sets were recorded, one on the TXS and the second on the IµS, both without a filter, and full charge density refinements were carried out with the program *XD2006*.

Table 15

Comparison of selected parameters.

Source	IµS		TXS	
Correction	**None**	$k_{3\lambda} = 0.0043$	**None**	$k_{3\lambda} = 0.0015$
$R(F^2)$ all data	0.0154	0.0146	0.0155	0.0152
P1 – C1 [Å]	1.82658(18)	1.82668(15)	1.82687(14)	1.82684(13)
$\Delta\rho_{\mathrm{max}}$ [eÅ^{-3}]	0.303	0.299	0.199	0.208
$\Delta\rho_{\mathrm{min}}$ [eÅ^{-3}]	-0.245	-0.230	-0.211	-0.209
e_{gross} [e]	29.1	25.6	28.6	27.4
$d^f(\rho_0)$	2.6825	2.6890	2.6126	2.6111
ρ_{min} $(d=2)$ [eÅ^{-3}]	-0.0990	-0.0890	-0.0931	-0.0896
ρ_{min} $(d=2)$ [eÅ^{-3}]	0.0984	0.0875	0.0904	0.0862

Additionally, a residual density analysis (Meindl & Henn, 2008) was performed. The plot, shown in Figure 17, of the fractal dimension versus the residual density is a common tool to judge the flatness and featurelessness of the residuals after a refinement. Table 15 shows a comparison of selected quality indicating parameters for the final models, refined against corrected and uncorrected data. As for the routine structure determinations, $k_{3\lambda}$ is much smaller for the data collected on the TXS. Accordingly, so are the improvements achieved by the correction. The $R(F^2)$ value drops by 5% for the IµS data, while the improvement is negligible for the TXS data. The same is valid for the model precision, but for both data sets the residual density becomes cleaner, though less for the TXS (data not shown). The overall noise level is lower, displaying significant features (see Figure 18). For both data sets the residual density becomes significantly flatter. The e_{gross} (Meindl & Henn, 2008), is decreased by more than three electrons for the IµS and one for the TXS data. Hence, a correction for IµS data seems to be absolutely necessary, while the effect is minor for TXS data. In this particular example the effect on the refined parameters is not significantly above 3σ, but there might be other cases where the improvement of the noise level is crucial for the correct interpretation of the structure.

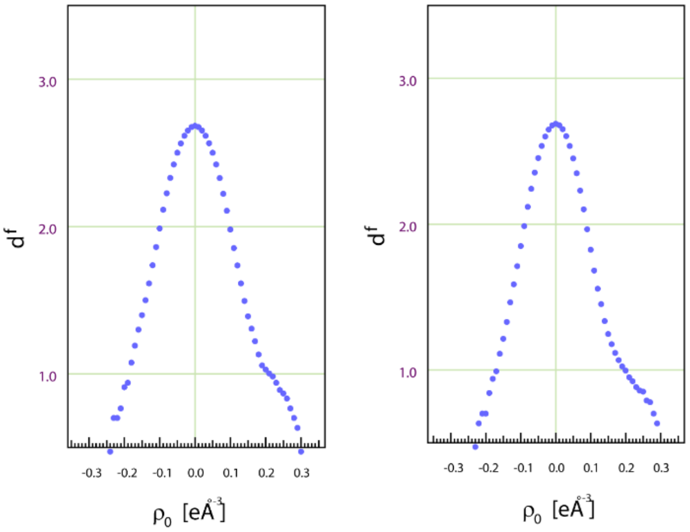

Figure 17

Plot of the fractal dimension d^f versus the residual density ρ_0 for the IµS data of compound **6**. (left) No correction, no filter; (right) $k_{3\lambda}$. The difference Fourier map was calculated using 108 × 125 × 180 grid points, a σ cutoff of zero and a resolution of 0.445 Å.

4.4 Conclusion

In this chapter, a straightforward correction for low energy contamination is demonstrated, applicable to already measured data, for which the resulting model quality is almost equivalent to those derived from filtered data. It reduces the impact of systematic errors and, in particular, considerably improves the final model. The application of an empirical correction is feasible and straightforward as it can be directly incorporated into the least-squares refinement. Both empirical methods and the filter insertion are able to increase the precision significantly, but the filter is, of course, physically correct by avoidance of contamination. Yet, an increase in model accuracy is visible after the application of either correction. There is no case where an application of the suggested correction method leads to inferior model quality indicators. For routine crystal structure determination, we were able to show that an overall setup-dependent correction factor, equivalent to the λ/2 correction factor for graphite beam monochromatisation, is sufficient. This enables a high-throughput solution, as it allows a default value entered in *SADABS*. In charge density modelling, where extremely accurate data are required, we recommend a dedicated correction factor determination from the multipole model. The data correction significantly reduces noise and improves the resulting model, as a residual density analysis shows.

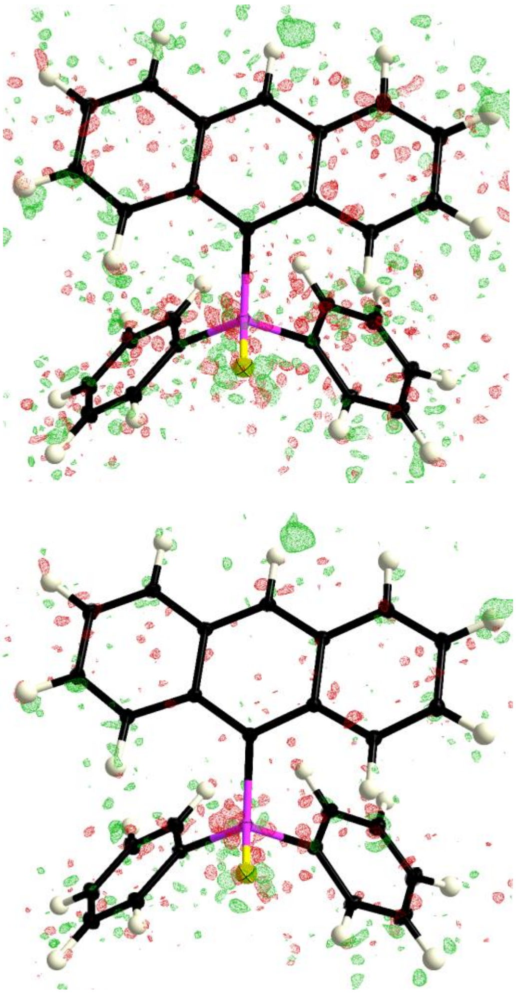

Figure 18
Comparison of the residual density for the models derived from high resolution IµS data of **6**, with either empirically corrected or uncorrected contamination. (top) No correction, no filter; (bottom) $k_{3\lambda}$ (*SADABS*). Map level: 0.08 eÅ^{-3}.

CHAPTER 5:

DETECTING CHARGE DENSITY DATA

5 Collecting charge density data – A tough job for detectors

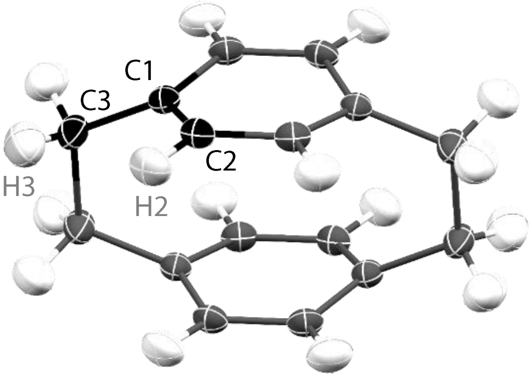

Figure 19
Structure of [2,2]-paracyclophane, carbon atoms are depicted in black/grey and the hydrogen atoms in white/light grey. Contents of the asymmetric unit in black/light grey.

Paracyclophane is a comparably compact system, only consisting of carbon and hydrogen atoms (Figure 19). In the high temperature phase, above 45.2 K (Wolf et al., 2014b, Wolf et al., 2015), it adopts the highly symmetric space group $P4_2/mnm$ and has only 5 atoms in the asymmetric unit. With the diffraction power of this system being limited to carbon and hydrogen, the scattering amplitude rapidly decreases at higher angles, readily approaching zero after a resolution of 0.5 Å for Ag *Kα* radiation at 100 K sample temperature. To counteract this, a large specimen is usually chosen to avoid exposure times exceeding two to three minutes at the highest diffraction angles. Large, as specified in chapter 4, means that the crystal dimensions explicitly exceed the width of the incident beam. However, large crystals give rise to highly intense low angle reflections imposing considerable demands to the dynamic detection range. Generally, the information on the diffuse bonding density is mainly determined by these low order reflections and severe overexposure, e.g. wrong intensity determination, can easily render a complete set of data useless. This is mainly because there are so few inner shell reflections compared to the higher resolution regimes, that missing reflections or wrong intensities have such a high impact. The combination of all the mentioned special properties render paracyclophane a perfectly suited test candidate for the performance of X-ray detection devices and was suggested as such by Wolf et al. (2014a).

5.1 Bruker APEX II

Figure 20
Bruker APEX II CCD Detector.

Main aspects of this detector were already discussed in chapter 3, however, a short summary of features and discussion on arising problems is given for convenience. The APEX II is a scintillating CCD (charge coupled device) detector and the stopping of the X-rays is performed by a layer of a phosphorescent material that also converts impinging photons into visible light. The conversion rate depends on the scintillation material (higher Z elements increase the stopping power) and the layer thickness. Since the light has to travel through the phosphor to reach the CCD, the once compact bundle of light will spread, thus diluting the spatial resolution with increasing layer thickness. A CCD camera then detects the light and converts the signal into an electric charge. This photo-generated charge is transferred pixel by pixel to the readout amplifier that converts the charge into a voltage, thus requiring a significant read-out time. For the APEX II, the counter relies on a 16bit well depth allowing a dynamic range of 1:65 535 counts per image, and that is exactly is the crux. It was shown in preceding theses (Wolf, 2014, Hey, 2013) that this count-rate limitation is insufficient for the collection of charge density data even for home-sources. The sample size needed to achieve high resolutions causes severe overexposure in the low resolution range that is not simply improvable by a decrease of the exposure time.

5.2 Dectris Pilatus3 R CdTe 300K

In late 2015, the Stalke group was offered the opportunity to get hands on experience with a CdTe300K. It is the newest incarnation of an already heavily tested detector, updated with a cadmium telluride (CdTe) sensor for high quantum efficiency at lab-system X-ray energies (e.g. Mo, 17.4 keV; Ag, 22.1 keV; In, 24.1 keV). The sensor consists of a layer of CdTe with a thickness of 1000 μm in contrast to monolithic silicon sensors whose X-ray stopping power would be insufficient (Dectris, 2016). The sensing layer is bump-bonded pixel-by-pixel to the application specific integrated circuit (ASIC) (Figure 22). This parallel architecture enables for quick read-out times, but constraints pixels to sizes significantly larger than for CCDs.

Figure 21
Dectris PILATUS3 R CdTe 300K.

In hybrid pixel array (or area) detectors (HPAD), the incoming X-rays are directly converted into an electronic signal. This hybrid photon counting technology (HPC) or direct conversion guarantees an excellent spatial resolution and a point spread function of only one pixel. The hybrid pixels consist of directly connected sensor and readout parts, so virtually every pixel is an independent detector. Concerning the dynamic range, the Pilatus3 has a 20bit counter depth, which corresponds to 1 048 576 single events. In single-photon counting mode, an incoming X-ray produces a charge at the sensor that is registered as a certain voltage and triggers a comparator. Here the voltage is compared with a user defined threshold and if it exceeds this, an in-pixel counter is incremented and the pixel is reset ready for the next input. The detectors' dynamic range is being set uniquely by the counter depth for the single-photon counting mode. Usually the energy threshold is set to values larger than the read-noise of the typical pixel electronics and this leads to these detectors being advertised as 'noise free'. However, all on-chip computations take time rendering the pixel 'inactive' during that period and thereby limiting the detectors count rate. This is called the 'dead-time' for processing a single photon and can lead to paralysation. In the case of pulse pile-up during dead-time, the counting of the second pulse is lost. To overcome this limitation, a technology called instant retriggering was implemented. A pre-set interval is started after every successful count and on expiry of the interval the counting circuit is

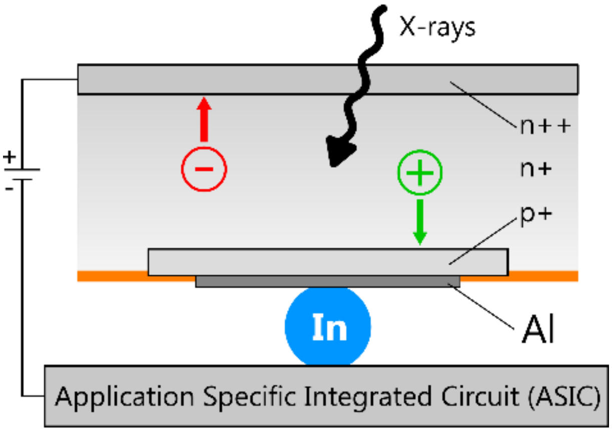

Figure 22
Illustration for the principle of direct X-ray detection. The impinging photon creates a charge in the sensor pixel that is directly detected as voltage in the read-out pixel (ASIC). The two pixels are bump-bonded by Indium balls.

retriggered (Dectris, 2015). The threshold allows the detector to ignore a certain energy range, of which an application would be the suppression of X-ray fluorescence and thereby reduction of the background. Thresholding is a post-processing step, so the user can decide to prioritise background reduction or accurate photon counting. However, the threshold has further consequences concerning the pixels. That is, if an X-ray directly hits the detector in between two pixels, the resulting charge is shared between these pixels. Depending on the threshold, the photon might be counted twice or is missed entirely. This is called the *charge-sharing* noise and becomes increasingly significant with the signal being on the magnitude of a pixel, i.e. for small reflections. Usually, the threshold is set to half the wavelength of the incoming photons to avoid double counting.

5.3 Bruker PHOTON II

The PHOTON II is a charge-integrating pixel area detector (CPAD). The underlying technology consists of a scintillation phosphor, photon/light conversion and subsequent detection by a CMOS chip (converting the light into a charge). The resulting charge is therefore dependent on the energy of the incident photon. In contrast to single-photon counting devices, the charge is collected, integrated and saved for later readout. Generally, there is no instantaneous count-rate limitation, however, they do suffer from *full-well* saturation. Since the complete charge is stored, the limiting well-depth is reached considerably faster in contrast to operation in photon-counting mode where only an integrated counter is incremented. Therefore, the dynamic range is handled differently and is only abstractly related to photons since a charge is stored together with the noise (read-out and dark current) and accumulate towards the well-depth. This limitation is counteracted by high frame rates. The PHOTON II operates in shutterless mode and a complete read-out cycle takes 13 ms (the detector operates at 70 Hz). Every pixel is read-out 70 times per second increasing the effective maximum count rate per second. A further benefit from high frame rates is the possibility to perform the so-called adaptive-oversampling. If a long exposure time is chosen for a particular frame, the pixels are read non-destructively and the accumulation of charge is monitored over a certain period of time. This can be thought of in the same manner as *correlated* measurements greatly reducing noise for shuttered operation. Long exposure periods are making a CPAD virtually noise free and give rise to the term: *single photon sensitivity*. Due to the CMOS technology, the full-well saturation affects only single reflections and no contamination of adjacent reflections is to be expected. From the three dimensional point of view, the detected intensity gets a clear cut allowing for easy identification and omission by the integration routine. Of course, these reflections have to be re-collected at lower exposure times.

Figure 23
Detector used in this investigation: Bruker PHOTON II.

5.4 Experimental details

Table 16
Local coordinate systems and symmetry constraints used for the charge density model of paracyclophane.

Atom	Atom/Axis 1	Atom/Axis 2	R/L	symmetry
C1	C3/X	DUM0[$]/Y	R	*m* ⊥z
C2	H2/Z	C1/X	R	*mm*2 ǁ z
C3	C1/X	DUM0[$]/Y	R	*m* ⊥z
H2	C2/Z	C1/Y	R	*cyl* ǁ z
H3	C3/Z	C1/Y	R	*cyl* ǁ z

[$]DUM0 has the fractional coordinates (0.5, 0.5, z) to allow C3 and C1 adopting mirror symmetry. R/L indicating a right (R) or left (L) handed orientation.

Indium data was as well collected in Karlsruhe using a D8-Venture equipped with an Excillum Metal-Jet and a Bruker PHOTON II detector. The source was operating at 120 kV and the metal target was a molten indium rich alloy (consisting of 21% indium, gallium and tin). The focussing mirrors were specifically designed to suppress the contamination of the permeating gallium radiation. An empirical correction in a similar fashion to the low-energy contamination discussed herein is as well possible. The data was collected on a freshly crystallised paracyclophane sample and was later processed in Göttingen.

A Pilatus3 R CdTe 300K detector was successfully incorporated into our Ag IμS enclosure by F. Engelhardt and was controlled by the Bruker *APEX2* software. In order to have all goniometer information ready while keeping a changing-back effort as low as possible, an APEX II detector was connected to the software collecting only ‘dark’ frames but registering goniometer angles and other required data, while the Pilatus recorded the actual diffraction and being externally triggered by the software. It was then possible to combine the information and convert the recorded image into Bruker frame format.

A further data set was collected at Rigaku in Houston, Texas, using a 1.2 kW MicroMax-007 microfocus rotating-anode with a Ag target. The Ag $K\alpha$ radiation was focussed using VariMax multilayer mirror optics. This data was processed with the *CrysAlis Pro* (Agilent, 2014) software. The frames were later converted into Bruker frame format and were integrated with *SAINT* in order to achieve a better general comparability. However, it was not possible to attain similar results and consequently this endeavour was not considered appropriate.

All other data was processed individually within the flexibilities of *SAINT* (8.30C or 8.37A) ensure that the special demands of every detector are factored in. The PHOTON II and Pilatus data were integrated using the newly implemented *PLANEBG* algorithm for the determination of the background, as, in contrast to APEX II data, there is no significant noise. The Pilatus data did show problems with the automatic integration box size adjustment and was kept at fixed values. The same scaling and correction protocol was employed for the final data and thereafter a rather conservative and highly constrained multipolar model refinement of paracyclophane was carried out. The local coordinate systems were set up to allow for the maximum possible symmetry (Table 16). The data was truncated to 0.5 Å, because beyond that point the data quality rapidly decreases and in all models the $I/\sigma(I)$ cut off was set to zero. This limiting truncation is justified by the fact that the main goal of this investigation is to judge on data quality concerning the detector, not the source and a resolution of 0.5 Å is readily achievable with all employed sources. Multipoles at carbon atoms were refined up to the hexadecapole

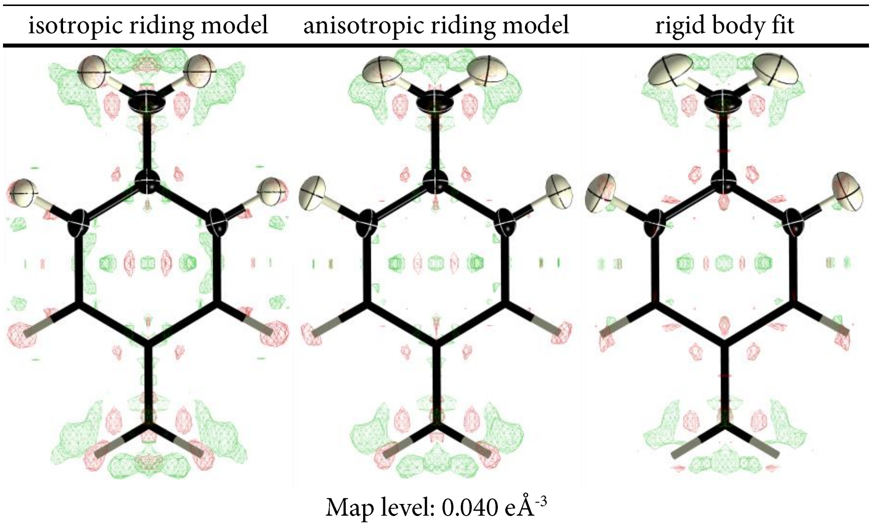

Figure 24
Residual density map for the three different hydrogen descriptions: the top half shows the full ADP, while the bottom part (symmetry equivalent) with omitted ADP revealing the underlying difference density. The riding model and rigid body fit ADP were calculated by the *SHADE3* server (Madsen, 2006).

level, while for hydrogen atoms only the monopole and the bond directed dipole were modelled. The expansion-contraction parameters of the multipole formalism (spherical-valence shell: κ, deformation functions κ') were refined for carbon and kept fixed for hydrogen atoms. The values were set to 1.1 and 1.18 for κ and κ', respectively, as suggested by Volkov et al. (2001) based on their empirical studies. For all data sets severe anharmonic motion of the bridging carbon atom C3 was visible. In the course of this comparison it was concluded as the best option to allow the model this additional flexibility and third order Gram-Charlier parameters were introduced.

However, in order to be able to sensibly model the anharmonicity, a proper description for the vibration of the attached hydrogen has to be found. Collecting neutron data would exceed the scope of this comparison and would not really add valuable information to this topic. The isotropic riding model approximation, achieved by considering only the pivotal atom's motion, was too restricted and insufficient. A more sophisticated estimation of the hydrogen ADP can be achieved by the TLS (Translation, Libration and their correlation, called the S-matrix) fitting routine e.g. the combined neutron/rigid-body formalism implemented in the *SHADE* server (Madsen, 2006) or the segmented rigid-body formalism using the APD-Toolkit (Lübben et al., 2014). The *SHADE* estimation is based on a combination of an internal and an external motion. The external motion is estimated from a rigid body motion using the TLS formalism, analysed by the *THMA11* program (Schomaker & Trueblood, 1968, 1998). The internal part is taken from a database consisting of displacement parameters derived from neutron diffraction experiments. The problem is that paracyclophane only has three non-hydrogen atoms in the asymmetric unit, e.g. three unique sets of anisotropic motions to perform the TLS fit on, which is unfortunately insufficient for this routine. Instead, the ADPs are estimated based on the pivotal atom's motion leading to an anisotropic riding model, giving a slight benefit over the isotropic description. The derived ADPs were calculated by the *SHADE3* server, transferred to *XD2006* and kept fixed during multipole refinement (Figure 24). An improvement was instantly visible in the difference density as well as all dependent quality indicators, highlighting the necessity of an appropriate description of the hydrogen atom motion for this particular compound. In order to make the rigid body fit routine work, the crystallographic symmetry was reduced from the tetragonal $P4_2/mnm$ to the monoclinic setup $P2_1/n$ that offers eight non-hydrogen atoms in the asymmetric unit. After this expansion, the completeness and multiplicity up to a resolution of 0.5 Å was still close to 100% and well above three, respectively (and for all investigated data sets). A check of these values is crucial as the modelled parameters are more than tripled compared to the tetragonal setup. Finally, this procedure allowed for the successful estimation of the paracyclophane hydrogen atoms ADP following the TLS formalism and the according calculations were performed by the *SHADE3* server.

The carbon – hydrogen bond distances were set to tabulated mean values experimentally determined from neutron diffraction.

Concerning the application of a weighting scheme to the data it has to be mentioned that all efforts made in the direction of finding sensible parameters were unsuccessful. As stated in the XD manual, there is no experimental validation that a weighting scheme originally set up for IAM models would stand for charge density analysis. Apart from that, the process of finding an appropriate weighting involves severe trial and error and was therefore considered as too vague to be reasonably incorporated into this comparison. The models were refined using experimental weights, the individual reflections were weighted according to the errors determined by the integration routine. This has the further benefit that the influence of the error model determination can be held to a minimum, the error model determination during data scaling was switched off. However, it has direct consequences regarding certain quality indicators (Goof), more on that particular manner later. It has to be emphasised that the data collection was not performed on the exact same crystals. Systematics in the final error should therefore only depend on the crystal (size, shape, mosaicity), source (brilliance, beam stability), detector (individual corrections for oblique angle, Lorentz profile e.t.c.) and the integration software (*SAINT*, Bruker or *CrysAlis*, Rigaku). The influence of the size and the shape of the sample should only affect absorption processes and anisotropic sample illumination. Paracyclophane only consists of carbon and hydrogen atoms, the wavelength used was Ag *Kα* and absorption effects should not cause any errors. The same holds true for the error introduced by an anisotropic sample illumination as all X-ray sources utilised in this investigation had mirror focused primary beams and all crystal samples exceeded the beam sizes. We have already learned in a previous chapter that the multi-scan absorption correction is indeed astonishingly good at correcting data for this particular matter and it is therefore assumed that varying sample sizes do not introduce bias towards a larger specimen. However, the influence of the sample quality remains an issue as differing mosaicity not only influences reflection profiles, thus integration performance, but also the maximum resolution up to which diffraction is achievable. During crystal screening it was made sure that the reflection profiles were sharp and clean and the maximum resolution must have exceeded 0.5 Å. However, changes in mosaicity were not measured individually. Therefore, an uncertainty or negative bias for some samples might remain to some extent. The impact on the results, however, is considered low.

5.5 Results

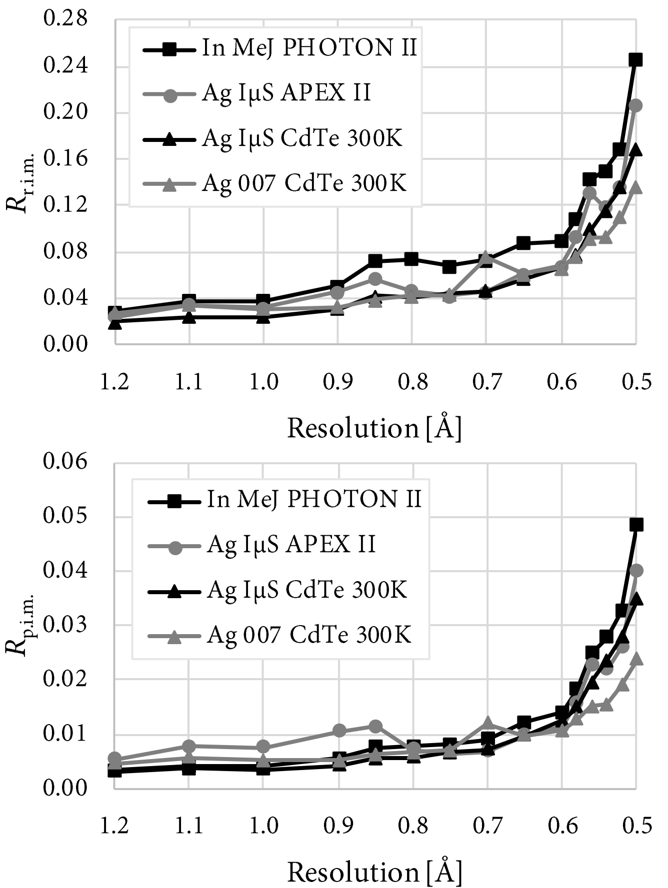

Figure 25
Course of the $R_{\text{r.i.m.}}$ (top) and $R_{\text{p.i.m.}}$ (bottom) against resolution for the investigated systems, truncated to 0.5 Å.

Figure 25 depicts the courses of the redundancy independent and the precision indicating *R* merge value for the investigated systems. In the mid-order region (1.0 to 0.6 Å), the agreement of the data seems to depend more on the detector than on the source, whereas the high resolution data profits from a higher photon flux. This is indicated for the systems equipped with a CdTe 300K by the lower high resolution (< 0.6 Å) *R*-value for the 007 compared to the IμS. One encouraging finding is that, even though processed with different software, the results are in good agreement. For the APEX II and the PHOTON II comparable paired data was unfortunately unavailable. Therefore, only the qualitative statement that the MeJ/PHOTON II combination shows the least agreement of all studied combinations for the mid to high resolution data. No statement can be made about the origin, e.g. if it was the detectors performance or a limitation in diffraction that lead to lower agreement. The most developed of all quality indicators the *R*-value is showing the mathematical agreement of a model and the underlying data and, despite its inadequacies, for this very reason it is used throughout this comparison. The models are refined against the squared structure factors F^2, thus the *R*-value of interest is calculated against F^2 and is therefore called $R(F^2)$, not to be confused with the *R*2 (see chapter 1.7). The goodness of fit (GooF), is a very helpful indicator and tells about the reliability of the estimated standard deviations (*esd*) of the model parameters (not to be confused with the errors of the intensities). It can be seen as a multiplier for the *esd* and the crystallographer usually modifies the weighting scheme to yield a GooF value of unity. Due to the established experimental weighting of the reflections during the refinement, the absolute values for the GooF are substantially larger than unity, this can be addressed to the integration routine to a large extend. Nevertheless, their relative values as well tell about the quality of the data. The difference density $\Delta\rho$ (or residual density ρ_0), representing the balance of the difference Fourier map, yields complementary information to the *R*-value as it shows not the mean but the worst inconsistencies between model and data.

The derived *properties* of interest were selected in order to provide additional sensible information. Herein compared are values of the density at the C1 – C3 bond critical point, selected for being the less precisely determined bond throughout all candidates (Figure 26). This point is considered as representative for all other bonds by showing a lower boundary that is achievable with the underlying data quality. In the course of this investigation it turned out that all the models were able to produce remarkably appealing Henn-Meindl plots, Figure 27 is depicted again as a reminder for the meanings of the discussed properties. The residual density analysis was consequently reduced to the e_{gross} value. This quantity is calculated as a summation over all features present in the residual density (e.g. summation of the absolute height of *all* local peaks and holes yielding one *global* value) and is therefore indirectly capable of showing the amount of accumulated noise in the data. Additionally, the flattest and most featureless data will show the lowest e_{gross}.

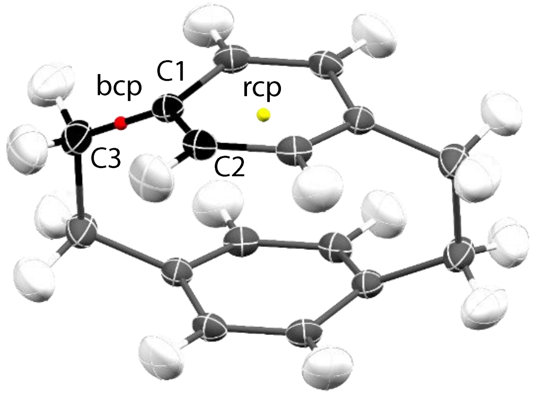

Figure 26
Location of the C1 – C3 bond critical point (bcp, red dot) and of a ring critical point (rcp, yellow dot).

Selected quality indicators are summarised in Table 17. It seems to be a *fruitful* combination if the *overexposure prone* APEX II detector and the comparably low diffracted photon flux of the Ag IμS team-up. It is remarkable that this combination is able to produce the lowest R-value of all investigated combinations, however, R-values have to be considered carefully. It is readily visible, why the crystallographic community is sceptical about the significance of the R-value as the final judgement tool in crystal structure determinations as well as charge density investigations. Here, the R-value is comparably low, yet, the majority of the other, complementary indicators show a different picture. The residual density, especially the e_{gross}, is significantly worse with 5.541 whereas for all other combinations the values are in good agreement between 3.695 to 3.827, this holds as well regarding the $\rho(d=2)$ values.

Table 17
Selected quality indicators and properties of the models derived from different experimental setups.

Detector	Pilatus3 R CdTe 300K	APEX II	Pilatus3 R CdTe 300K	PHOTON II
Source	007	IμS	IμS	Metal-Jet
*K*α	Ag	Ag	*Ag*	In
Software	*CrysAlis*[#]	*SAINT*	*SAINT*	*SAINT*
$R(F^2)$	0.0213	0.0170	0.0152	0.0215
Data	1260	1208	1231	1228
GooF	3.015	2.086	2.748	4.550
$\Delta\rho$	0.156	0.232	0.168	0.157
e_{gross}	3.766	5.541	3.695	3.827
$\rho(d=2)$	0.0879	0.1230	0.0848	0.0892
$d^f(0)$	2.6745	2.7226	2.7223	2.7165
ρ(bcp)	1.684(6)	1.687(6)	1.720(5)	1.698(6)
$-\nabla^2\rho$(bcp)	-11.662(13)	-12.620(15)	-13.250(11)	-12.295(14)
ρ(rcp)	0.177(1)	0.162(1)	0.180(1)	0.186(1)
$-\nabla^2\rho$(rcp)	3.146(1)	3.404(1)	3.343(1)	3.285(1)

[#] Integration with *SAINT* showed no improvement over *CrysAlis*.

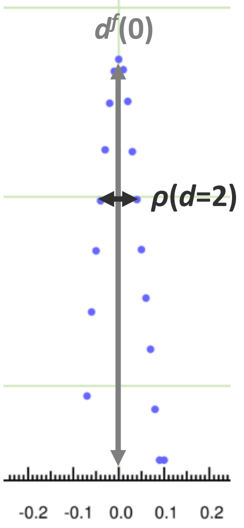

Figure 27
Plot of the fractal dimension d^f versus residual density ρ_0.

Table 18
Residual density map for the four different experimental setups: the top half shows the full ADP, while the bottom part (symmetry equivalent) with omitted ADP revealing the underlying difference density. The hydrogen ADP were calculated (rigid body fit) by the *SHADE3* server (Madsen, 2006).

<table>
<tr><th>Ag IµS APEX II</th><th>Ag 007 CdTe300K</th><th>Ag IµS CdTe300K</th><th>In MeJ PHOTON II</th></tr>
<tr><td>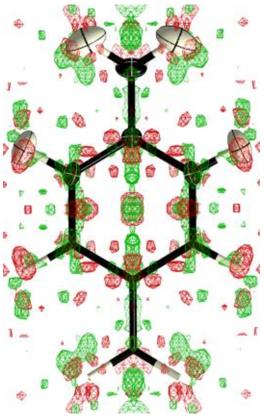</td><td>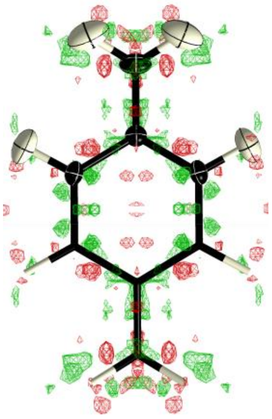</td><td>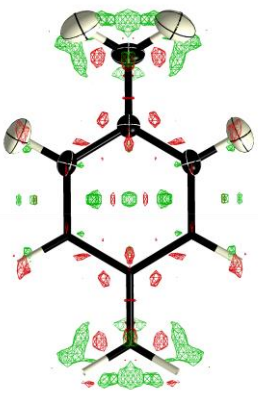</td><td>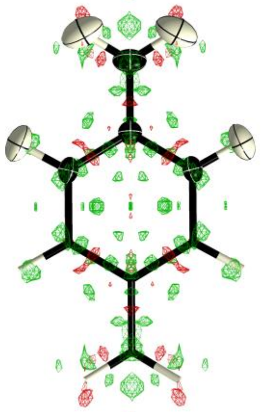</td></tr>
<tr><td colspan="4">Residual density map level: 0.040 eÅ^{-3}</td></tr>
</table>

A comparable observation is made for the CdTe300K data from the 007 rotating anode. The combination shows a high $R(F^2)$ while all other quality indicators certify a rather good performance. A finding is that the CdTe 300K detector is able to handle the high photon flux delivered by the 007 rotating anode, that are dramatically more photons when compared to a micro-focus sealed tube. The values of the density at the bond critical point are in good agreement for all the data, the Laplacian $-\nabla^2\rho$ shows a comparable trend (the *esd* are largely underestimated as stated in the *XD2006* manual, this will be of particular interest in chapter 6). The derived *esd* of the density at the ring critical point, however, does not seem to be of any meaningful value. Yet again, all the models are on a comparable scale.

The residual density maps shown in Table 18 clearly highlight the very same features for all data, whereby the IµS/APEX II data clearly exceeds the others in the noise level. Apart from that, it can be seen that generally all data are of such high quality that model deficiencies are becoming the limiting factor. The only valid conclusion must be that both studied detectors, the Dectris Pilatus3 R CdTe 300K and the Bruker PHOTON II, are able to deliver single crystal X-ray data well suited for charge density determinations and on-par data quality. The main differences come from the underlying technology; the CdTe 300K has readout dead-times, count-rate saturation and charge-sharing. However, it has to be mentioned that even though these disadvantages are visible, no systematics could be seen in the data leading to the assumption that the calibration is able to handle these problems satisfactorily. The PHOTON II does not show these effects; however, since being a charge-integrating detector, it suffers from full-well saturation and dark current noise. Concluding that both detectors are having weaknesses that have to receive attention during data collection.

CHAPTER 6:

VALIDATION OF CHARGE-DENSITY REFINEMENT STRATEGIES

6 Validation of charge-density models – When do we overfit?

Although in 2005 Coppens (2005) wrote that *Charge Densities Come of Age*, experimental charge density studies still depend strongly on the amount and the quality of the measured data. However, even after 100 years the procedure itself did stay virtually unaltered. The routines got faster, the models more sophisticated, the corrections more reliable and the data gained resolution and quality, but minimizing residuals between a parameterized model and a target set of data will always stay prone to its inherent problem of overfitting. Yet, there is no published investigation on the question whether the refinement of all meaningful parameters might lead to an overfitting of the data. In X-ray crystallography, the atomic positions are determined quite reliably by the core electrons and are modelled by three parameters. The information of the atomic motion, albeit harder to acquire from the deconvolution of density and vibration, is described by six (or more) parameters. Here, the underlying problem is well over-determined (for small molecules). In the multipole model, the valence density, e.g. the bonding electrons or lone pairs, are to be modelled by up to 25 parameters. This unavoidably leads to an increasing gap between parameters and available information, making over-parametrisation inevitable at some point.

The information describing the valence density is found in the low order data ($\sin(\theta)/\lambda < 0.5$), but to be able to derive proper coordinates and thermal displacements, or in other words to properly de-convolute the density from the thermal motion, high resolution data are needed. An inherent problem when trying to model experimental charge density following the Hansen & Coppens formalism is that the largest number of parameters is effectively refined against the least amount of information. However, this is invisible to the user as there is only *one model* that is refined against *one set* of data.

6.1 Cross-validation

In conclusion, adding more parameters might result in a significant drop in the *R*-value by adding flexibility to the fitting function without any real improvement. The model is over-parametrised and some parameters are irrelevant to the fit. A statistical method that can help to detect such over-interpretation of data is cross-validation. The concept was successfully adapted to macromolecular structure determination by Brünger (1992, 1997) to overcome problems the community encountered. Due to the fact that for macromolecular molecules (e.g. proteins) the available data rarely exceeds a resolution of $\sin(\theta)/\lambda > 0.5$ and the model building will become non trivial, as a large number of parameters relies on a limited number of information. Again, over-parametrisation (over-parametrisation, over-interpretation and overfitting are used analogously throughout this thesis) must lead to a more or less pronounced drop in the employed evaluation factor (e.g. the $R1$ or equivalent value). However, at a certain point, there is no more information left in the data and the additional flexibility the model gained by the introduction of parameters leads to the fitting of noise.

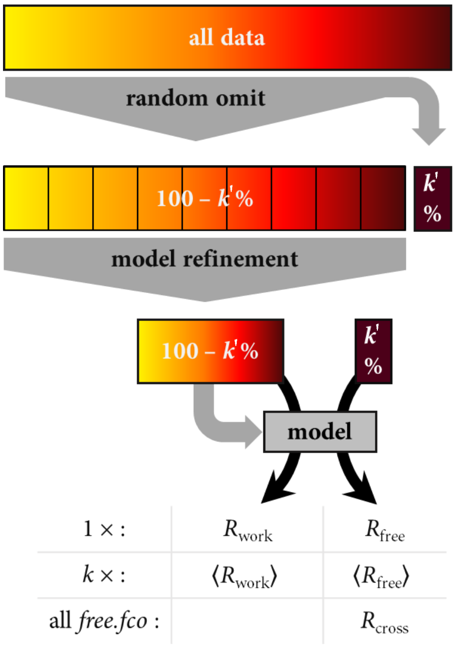

Figure 28
Workflow of the cross-validation protocol. k models are calculated against k different $(100 - k'\%,\ k' = 100/k)$ data sets. For the derived models the R-values are as well calculated for the free data (k'%).

The idea of cross-validation is to find this point precisely and it is appealingly simple. The data are divided into complementary subsets and a certain fraction (e.g. 5 %, *free* set, R_{free}) of the data is completely ignored in the model building procedure (e.g. 95 %, *work* set, R_{work}) and once finished, the evaluation factor is calculated against the omitted subset of data (the 5 %, yielding an R_{free}), see Figure 28. The R-value is the property that is minimised, e.g. the agreement of model and data. In statistics, this is solved by k-fold cross-validation. This means that a given data set is divided into k subsets. One subset is used as *free* set, while the other k-1 sets are combined and used to derive the model, this procedure is repeated k times. Hence, all data were used for model building and once for validation, but no model ever saw the complete set of data. From the k different refinements, the mean R_{free} values can be calculated where their variance is closely related to the number of reflections in the particular set. A final refinement is then of course carried out against all data. The fundamental assumption to this procedure is that the individual observations (reflections) are independent. In a non-centrosymmetric space group, the *Friedel* mates are *dependent* observations, the sets are biased and the derived models are no longer *independent* of the validation procedure. To avoid this special issue, it is essential to make sure that the *Friedel* mates are either in the *working*– or in the *free* set. For centrosymmetric space groups this special consideration is not neccessary because their *Friedel* mates are already merged for the use with *XD2006*.

As in charge density refinements the changes in the R-values and especially the differences in the R-values are small, their individual variation is too large to significantly allow for a conclusion. The number n of reflections in the validation set is crucial: If the number is too small, the standard deviation of R_{free} grows large. The error of the R_{free} value is approximately given by $R_{free}/\sqrt{(2n)}$ (Tickle et al., 2000), with n being the number of reflections in the *free* set. If n is large, the completeness of the *working* set is low and therefore the data omission might lead to biased models. Since this substantial drawback, a newly proposed $R_{complete}$ (Lübben & Grüne, 2015) that considers all *free* sets of all k refinements is used instead. A similar method was already used to validate the weighting of restraints (Paul et al., 2011, Zarychta et al., 2011), but it can also be used to judge, for example, the local symmetry. Herein, the model/data differences for all k models and their respective *free* sets (each contain n independent *free* reflections) of data are jointly used to calculate the R_{cross}.

$$R_{cross} = \frac{\sum_k \sum_n |F_o^2 - F_c^2|}{\sum_k \sum_n F_o^2} \qquad \text{Eq. 6-1}$$

In contrast to the well-established R_{free} (or $R_{complete}$) concept the method developed herein is not about absolute R_{cross} values, but in the progress of the R_{cross} along the refinement strategy. As emphasized in the previous Chapters, a high quality and of course complete set of reflection data is needed to unequivocally find *the* model that describes the associated density. Under these circumstances, how can we dare to leave out a certain fraction of the crucially needed data? And, is there any bias introduced by leaving out data, e.g., are the *k*-models still consistent with the *complete*-model? The purpose of cross-validation can be considered as *validation-only*, in other words, it is not only a check for overfitting but as well a test for the robustness of the derived model. The size of the *free* fraction shows considerable variation according to the structure (cell dimensions, number of reflections, etc.) and has to be considered individually. However, a protocol consisting of 20 *work* sets (*free* set size of 5%) turned out to be a reasonable starting point and seems a good compromise between computational cost and bias. An unbiased *work*-model is assumed when the following criteria are fulfilled:

- Reasonable data to parameter ratio after the *free*-set exclusion
- Reasonable parameter distribution for the *work*-models (will be discussed in detail)
- Histogram of compliant[#] *work*-model parameters show a normal distribution ([#]available if the *XD2006* significance allows a distribution to show normality, problematic parameters are: *x*, *y*, *z*, U_{ij}, 4th and 5th order Gram-Charlier).

Experimental data will always contain noise to a certain extend and as soon as the refined parameters begin to model that noise the agreement factor (R_{work}) improves, but there will hardly be any improvement in the R_{free}, calculated against the left-out subset of data. That is because this information is not present in the left out fraction, here, the model fits less, and it is over-parameterised. As long as *both* factors improve, the model can be considered to improve as well, as the addition of parameters must lead to a decrease in the evaluation factor, but only sensible parameters will also decrease the R_{free}. The naming for the two fractions of data varies in the literature; *training*- or *working*-set entitles the model building (larger) part of data and *validation*-, *free*- or *testing*-set are the most common expressions for the smaller, left-out fraction used to calculate the R_{free} value only. The transfer of this concept to the field of charge density needs a bit of adjustment. Different regions in reciprocal space affect different parameters: the multipoles describe the valence density, whereas the positional and vibrational parameters are mostly determined by the high resolution data. A calculation of R_{work} and R_{free} truncated at $\sin(\theta)/\lambda = 0.5$ is an important instrument to show if newly introduced parameters behave as expected. The values below and above this truncation limit yield R_{low} and R_{high}, respectively. They display valuable information on the model especially suited for the stepwise build-up, e.g., for a refinement of initially introduced multipoles a significant decrease in R_{low} is expected, whereas the same for R_{high} would be highly suspicious.

6.2 The method

In this thesis, a modular script (*XDRfree*) has been developed (using the Python programming language) that is capable of setting up the folder structure and performing all necessary calculations requiring only very little user input. The required input files are an IAM model (*SHELXL start.res* file), the *XD2006* strategy-, input- and data files (*xd[01 - 99].mas*, *xd.inp*, *xd.hkl*). There are a few requirements regarding the strategy. The script should run through all demanded steps *flawlessly*, meaning only a robust or mature strategy is to be validated. A stepwise addition of parameters, following the suggestions made in the *XD2006* manual is highly recommended, as, apart from convergence issues, a smaller stepping (e.g. smaller groups of parameters) supports the successful recognition of an over-parametrisation along with the possibility to actually find parameters that are likely to contribute to the overfitting of the data.

6.2.1 Starting model

It was widely accepted that random shifts must be applied to all parameters to make the initial model 'forget' the information of the full data. In *XDRfree,* this is realised by feeding *SHELXL* the *WIGL* command to apply random shifts to the positional and vibrational parameters, of course within defined boundaries. Recently, Lübben and Grüne (2015) have elaborately demonstrated that such effort is no longer needed as the model rapidly and entirely adapts to partially truncated data by refining until quasi convergence. However, they did show this particularly for the IAM. Therefore, an '*if desired*' option to shake the parameters for the starting model generation is offered for the multipole model.

Within the IAM model, the positions of the heavy atoms are refined against data truncated to the highest resolution in order to leave the valence density unconsidered and thereby enable bias free positional parameters. The opposite is the case in the tracing of the hydrogen atoms, data truncated to low resolutions effect supports the assignment. This is explained with *a*) the hydrogen atoms do not show any significant contribution to the structure factors at resolutions larger than 0.5 $\sin(\theta)/\lambda$ and *b*) the bonding density *erroneously* modelled by the IAM flattens the overall residual density allowing the hydrogen atoms to emerge from the Fourier map, facilitating their assignment. Here, it is assumed that the local density maxima are good estimators for the *direction* from the pivot atom towards the actual hydrogen atom position. Unless neutron data are available, the bond length has to be reset to tabulated values (Allen & Bruno, 2010), however, it is still possible and advisable to find the best direction initially.

In the course of this thesis it was found over and over again that it is absolutely crucial to start from best possible parameters, e.g. having unsatisfying atomic motions, the refinement of monopoles – one of the very first steps of density modelling – is problematic. This can be explained with the correlation between the monopole and the atomic motion as both functions are spherical and centred at one atom. Starting from the best available local minimum assures robustness to the overall refinement as bad estimates for the motion directly result in poor pole populations. It was found that the best overall results can be achieved when starting from a *fully restricted* model. By applying chemical constraints to as many atoms as possible and assuming the highest reasonable local symmetry in order to reduce the number of refined multipole populations. E.g. for the compounds investigated in this context, *mm2* symmetry was adopted for all aromatic, likewise *3m* symmetry for terminal methyl groups. This high symmetry can later be re-evaluated and adjusted or reduced if reasonable. Thus, the general protocol of the R_{free} routine is as follows:

1. *SHELXL* (Sheldrick, 2015b) starting model generation:
    - Random shifts applied to x,y,z and U_{ij} values (if desired)
    - Refinement of heavy atom positions (high resolution)
    - Hydrogen atom assignment, Q-peak search cycles (low resolution, fixed heavy atom parameters)

2. In *XD2006* (Volkov et al., 2006) the full MM refinement is performed:
    - Stepwise refinement against the *work* sets (R_{work})
    - Zero cycle structure factor calculation against the *free* sets (R_{free})
3. Calculation of R_{cross} using all *free* structure factors
4. Step-wise visualization of R_{work} and R_{cross}

6.2.2 Is there more to learn from the *k* refinements?

The distribution of each refined parameter can be investigated and compared to the value *pval* and its estimated standard deviation *esd* obtained from the least-squares refinement against the *complete* set of data. Model bias due to the omission of data can then be easily identified in the early stages of the refinement and is indicated by outliers. However, it is not limited to reveal model bias. As specific terms will be used frequently from now on, a short summary on their meaning is given. R_{work} and R_{cross} reference the R-value calculated from the *working* and the *free* sets of data, respectively. It has to be emphasised that the R_{work} is the mean value of all R-values calculated for all k *working* sets, whereas R_{cross} is calculated as *one* value from a combined file containing *all* the needed information of the *free* data sets. In regard to truncated data (to either low or high resolutions), the terms R_{low} and R_{high} are used, respectively. In these cases, both the R_{work} and the R_{cross} are considered equally. The use of k different refinements has the advantage that k sets of refined parameters are available. The *esd* means the least-squares estimated standard deviation of the determined parameter *pval* that was calculated against a *complete* set of data. Whereas the *std* is used to describe the standard deviation of the distribution of the parameters derived from the individual *working* sets of data with *mean* indicating their mean value. *pwork* is the value of one particular parameter derived for one working set.

If all k refinements would be independent of each other, we should find a normal distribution with the mean value *mean* that is identical to *pval* and a standard deviation *std* of the distribution that equals the *esd* multiplied by a correction factor that can be derived by use of Cochran's theorem (Cochran & Wishart, 1934). But as each refinement uses $\frac{k-1}{k} \cdot N$ reflections of the total N data, the refinements are not independent and therefore the *std* usually is found smaller than expected, e.g. smaller than *esd*. As reversal conclusion, *std* > *esd* indicates problems in the refinement. After refinement with no clear indication of overfitting, the distribution of topological parameters like the density ρ, the Laplacian $-\Delta^2\rho$ and ellipticity ϵ at the bond critical points can as well be checked for consistency. Using the same arguments as above, we can estimate lower limits for standard uncertainties of these values that either are not calculated or are substantially underestimated, e.g. there are severe limitations to the calculation of errors on ρ and $\nabla^2\rho$, as only the contributions from the multipole populations are taken into account, the contributions from symmetry-generated atoms, κ parameters or coordinates are neglected (Volkov et al., 2006).

In the following, an assumption is made that over-parametrisation is a *local* problem, meaning that even though the model represents an over-interpretation of the data, there are more fixed and more loose parameters in the model. The full-matrix least-squares routine of *XD2006* enables the calculation and estimation of errors for all of the refined parameters. Through the *work* refinements, it is possible to actually validate the *esd*. How do the parameters perform? Do they follow the *complete* refinement and concentrate within the suggested error around the value? From the distribution of each parameter (from the *work* sets) the *std* is directly available and a comparison between the *complete* and the *work* refinements becomes feasible for every parameter involved in the refinement. In a charge density investigation, the target model should not only be capable of describing the density perfectly but it must also be robust to ensure the assumption is that the derived *esd* are reliable. Robust in terms of convergence and vulnerability towards false minima.

Each *work* refinement is considered as only minimally perturbed in contrast to the *complete* refinement due to data omission. Therefore, the values derived from all the *work* refinements should display a normal distribution for every parameter. Even though the individual values are derived from *dependent* models (most data are identical) their distribution should be normal. Again, the *reference* refers to the set of parameter values that are derived from the refinement against *all* data with its *esd* determined from the covariance matrix; the *mean* corresponds to the average of the distribution of values regarding all *work* refinements together with their *std* from the distribution. A plotting routine was established to enable a fast inspection of all individual parameters. In Figure 29, the *pval* value and its respective *esd* are displayed as a Gaussian (grey), so is the *mean* value with its *std* (red), grey lines mark relevant multiples of the *esd.* The Shapiro and Wilk (1965) test on statistical significance can be performed to check the null-hypothesis that the given sample comes from a normal distribution. This test is chosen because of its high statistical power, especially in the audition of small sample sizes (possible sample size: 3 – 5000, reasonable range for *k*: 10 - 50), rendering it well suited for the present problem. The Shapiro-Wilk test is highly sensitive to outliers; this can be exploited to find most disagreeing reflections. If such a case is present, the *outlying* set separates from the others by the fact that it is *not* affected by that particular reflection, all the other sets certainly are. The *free .fco* file calculated for that set now contains all the information needed to identify the reflection, e.g. using the program *DRK-Plot* (Zavodnik et al., 1999, Zhurov et al., 2008). A range of scenarios has to be addressed:

1. *std* exceeds *esd*, *mean* and *reference* in good agreement:
    - parameter not unambiguously determined
    - local symmetry constraint not fulfilled
    - problematic chemical constraint
    - over-interpretation

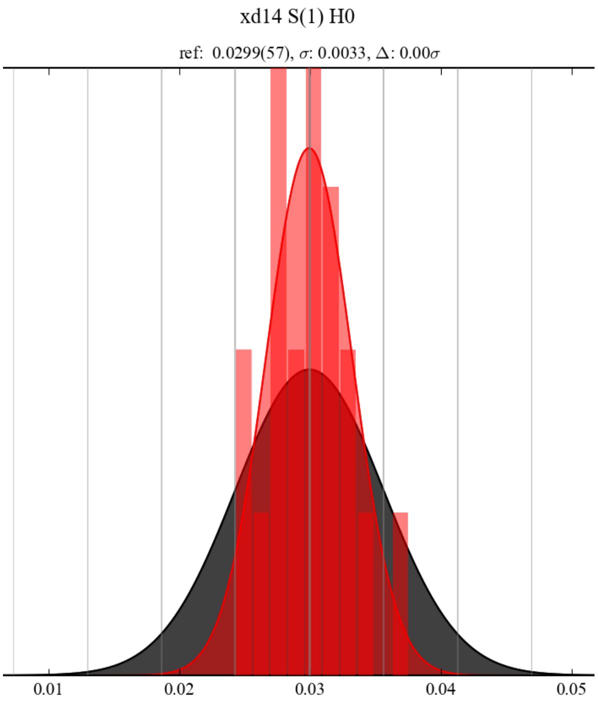

Figure 29
Typical plot of the refined parameter (center of grey Gaussian) and the estimated error from covariance matrix (grey Gaussian) compared to the distribution of the parameter from the *work* refinements (red bar plot) and their standard deviation (red Gaussian).

2. *std* and *esd* are in good agreement, *mean* and *reference* differ significantly
    - wrong chemical constraints
    - wrong local coordinates (e.g. switched systems *R*/*L*)
3. *std* exceeds *esd*, *mean* and *reference* differ significantly
    - more than one equivalent local minima
    - parameter is ambiguously determined
4. *w*-value less than desired alpha level
    - outlier (set)
    - limited significance prohibits normal distribution
    - more than one equivalent global minima

Within this cross-validation, it is possible to detect an over-interpretation of the data, evident in a principle ambiguity of the parameterised density. The parameters derived from the minimization of the discrepancy of a given data and a model yield of course no unique set of model parameters. There will be a *minimal* set of parameters able to model and sufficiently describe a certain density. Additional flexibility by an increasing number of parameters will lead to a redistribution of the individual parameter populations, yet the overall described density will stay the same. Such over-parametrisation will remain hidden from the cross-validation protocol as it is only able to detect whenever *pwork* and *pval* disagree by more than three times *esd*.

6.2.3 Can overfitting be visualized?

The idea presented in the following based on the assumption that overfitted parameters are imprecisely determined and therefore lead to higher variations in the electron density described by them. A density cube at a relevant isosurface level will not be able to show that variation, as the model parameters do not directly reflect this uncertainty. A detour involving a set of density cubes calculated for all work sets allow the calculation of the standard deviation of each grid point.

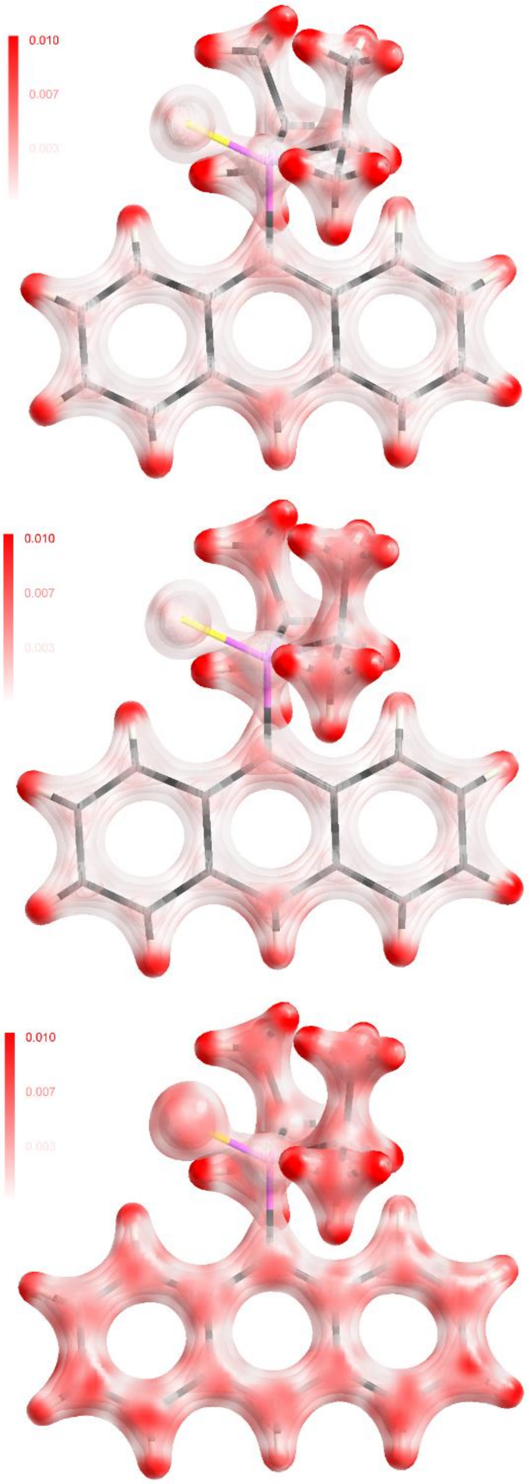

Figure 30
The indicative power of the *error* cube demonstrated on *i*Pr$_2$SPAnH (example in 6.3). A model where all reasonable symmetry- and chemical constraints are applied (top) compared to an intermediate stage where symmetry and chemical constraints are released only for the six isopropyl carbon atoms (center) and to a completely unrestricted model (bottom). Isolevels: 1, 1.5, 2, 2.5, 3, 3.5, the standard deviation of the density is capped at 0.01.

A color-coded overlay (e.g. transparent to red) of such an *error*-cube on a density cube (calculated from the *full* model) is able to highlight regions of higher uncertainties (Figure 30). A routine implemented in *XDRfree* can calculate this type of cube and *MolecoolQT*/*MOLISO* (Hübschle & Dittrich, 2011) or any other program that reads *.grd* files (*gaussian09* cube format) can plot them. This *error*-cube is related to the $\sigma(\rho)$-cube whose calculation is implemented in *XD2006*, however, it shows additional features not covered hitherto.

As the hydrogen atom positions are by far the least precisely determined parameters, their density will probably show severe features in the corresponding error cube. Nevertheless, the calculation of this type of visual inspection allows for excellent tailoring of potential refinement strategies, e.g. allowing the maximum flexibility in the region to be interpreted. Similar to the constrained-periphery vs. flexible-core strategy followed by Kratzert (2013) in the modelling of a hexasilabenzene, the presented tool is able to show ambiguous regions and aid finding the balance between flexibility and over-parametrisation.

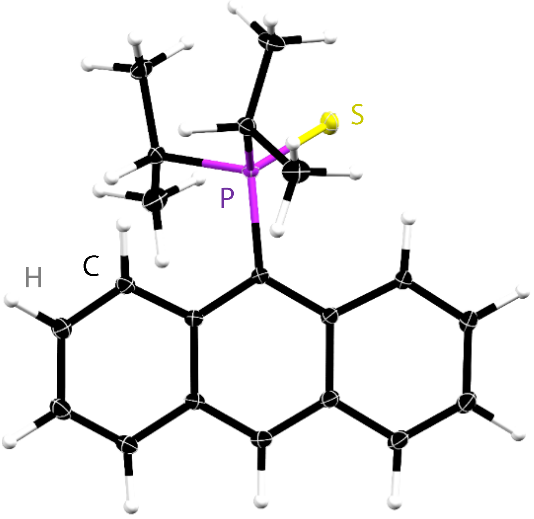

Figure 31
Structure of *i*Pr$_2$SPAnH.

Table 19
Multipole refinement strategy for *i*Pr$_2$SPAnH. Abbreviations: *D*, dipoles; *Q*, quadrupoles; *O*, octapoles; *H*, hexadecapoles; *M*, monopoles; *xyz*, positional coordinates; *xyz*(H), hydrogen coordinates; *U*2, displacement parameters; *U*3, 3rd order Gram-Charlier parameters; κ, spherical expansion parameters; κ', aspherical expansion parameters. *d*/*p*, data to parameter ratio (*d*: 18435); d_l/m, low-order data to multipole parameter ratio ($\sin(\theta)/\lambda < 0.5$, d_l: 1740).

#	position	motion	mono- / multipoles	$\kappa^{(\prime)}$	*d*/*p*	d_l/mp
1	-	-	-	-	-	-
2	-	-	*D Q O H*(S,P)	-	307.3	29.5
3	-	-	*M D Q O H*(S,P)	-	259.7	24.5
4	-	*U*2	*M D Q O H*(S,P)	-	90.8	24.5
5	*xyz*	*U*2	*M D Q O H*(S,P)	-	68.5	24.5
6	*xyz*(H)	-	-	-	24.9	-
7	*xyz*	*U*2	*M D Q O H*(S,P)	-	68.5	24.5
8		-	-	κ	-	-
9	*xyz*	*U*2	*M D Q O H*(S,P)	κ	66.3	21.8
10	-	-	-	κ'	-	-
11	*xyz*	*U*2	*M D Q O H*(S,P)	κ	66.3	21.8
12	*xyz*	*U*2	*M D Q O H*(S,P,C)	κ	61.5	17.1
13	*xyz*	*U*2	*M D Q O H*(S,P,C)†	κ	55.9	13.2
14	*xyz*	*U*2	*M D Q O H*(S,P,C) †	κ	36.1	5.7
15	*xyz*	*U*2	*M D Q O H*(S,P,C) †	κ	23.9	3.1

†Symmetry reduction for all C_{Ar} from *mm*2 || *z* to *m*⊥*x* (in anthracene plane).

6.3 Proof of concept

The data of di(*iso*-propyl)thiophosphoryl-anthracene (*i*Pr$_2$SPAnH, Figure 31) was collected by D. Kratzert on a fixed χ Bruker D8 Ultra diffractometer equipped with a Bruker Turbo X-ray Source (TXS) and Helios optics as beam shaping device. Data was collected at a detector distance of 50 mm and in 0.3° ω-scan mode with correlated exposure to reduce background noise and overexposed frames were recollected at 1/8th of the requested exposure time. All data were re-processed with the newest versions of *SAINT* and *SADABS*, structure solution and subsequent model building done with *SHELXT* and *SHELXL* within the *SHELXle* GUI, respectively.

The XD2006 refinement strategy is depicted in Table 19, in the first step all the carbon – hydrogen distances were set to experimental mean values derived from neutron diffraction experiments for similar compounds (Allen & Bruno, 2010). The radial screening parameters *κ* sulfur (*So long sulphur*, 2009), phosphorus and chemically equivalent groups of carbon were refined freely, however, all *κ*' for one particular group were refined as constrained to one single value as suggested by Dominiak and Coppens (2006) for sulfur (e.g. refining only one *κ* parameter for dipoles, quadrupoles, octupoles and hexadecapoles). An optimisation of the single slater-type radial function parameters *n*(*l*) as suggested did, however, not improve the model and was discarded.

The local coordinate systems were defined so that the highest possible symmetry could be used. This led to cylindrical symmetry for hydrogen and sulfur atoms, mirror- for methine and three-fold symmetry for methyl carbon atoms. For the anthracene carbon atoms even *mm*2 symmetry was adopted. The pole population of chemically equivalent atoms were constrained to be identical. Hydrogen atom poles were restricted to the monopole and a bond directed dipole and the pole populations of chemically equivalent hydrogen were constraint onto each other. The carbon multipole expansion was restricted to octupoles, this was later released (step 12). Sulfur and phosphorus were refined without restrictions to the multipole expansion. The data to parameter ratios, especially the *effective* low-order to multipole ratio, presented in Table 19 impressively demonstrate what the loosening of local symmetry- and chemical constraints means. The *effective* multipole ratio drops from 13.2 in step 13 to 5.7 with the release of the chemical constraints in step 14 and ends with the really low value of 3.1 after loosening of the local symmetry constraints in the last step. The two main questions were:

- Can the local symmetry constraints be released without overfitting and does it add useful information?
- Can the chemical constraints be released without overfitting and does this add useful information?

The course of the refinement is depicted in Figure 32, Figure 33 and Figure 34. Refinement of the multipole populations

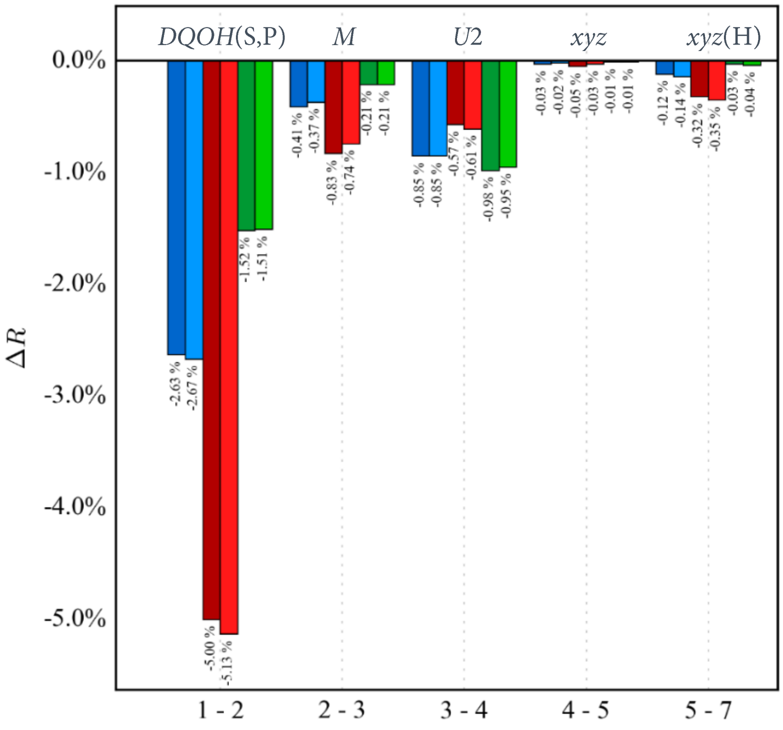

Figure 32
Course of the refinement of *i*Pr$_2$SPAnH, this illustration continues with Figure 33 on the next page.

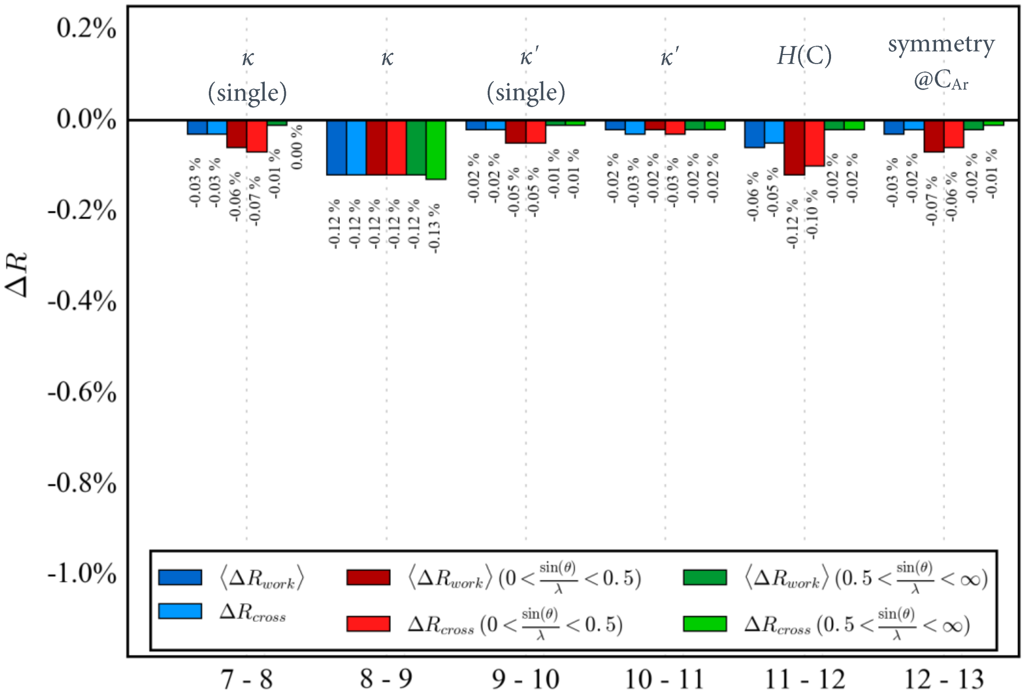

Figure 33
Continuation of the refinement of *i*Pr_2SPAnH. Depicted is the refinement of: κ (8, 9), κ' (10, 11), introduction of carbon atoms hexadecapoles (12) and symmetry expansion (13). The course of the refinement is continued in Figure 34.

improves R_{work} and also R_{cross} significantly. Both values show an improvement larger for the low order data compared to the high order, which is in good agreement with expectations. The subsequent introduction of the monopoles displays a similar picture. Next, the re-adjustment of the displacement parameters does not show any sign of overfitting and are affecting both low order and high order reflections, a change in position changes the core as well as the valence density. It is clearly visible that the atomic motion benefits from the multipolar description of the bonding density. The addition of the positional parameters for the non-hydrogen atoms does not need readjustment to the same extend, here, indicating better starting parameters. With the density modelled, a new adjustment of the hydrogen positions in step 6 and the models response in step 7 leads to a drop in the low resolution R-value, that is again in good agreement with expectations.

The exclusive refinement of the scaling parameters κ in step 8 shows major impact on the low resolution data, as it scales the multipoles. The model's response in step 9 shows is more balanced. κ' shows qualitatively a similar picture, yet, less pronounced. Both adjustments lead to reasonable values and improved the agreement. The introduction of hexadecapoles to the carbon atoms took place in accordance to the individual

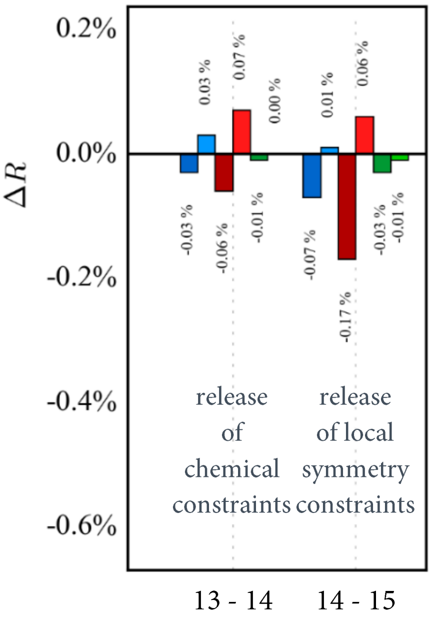

Figure 34
The last steps of the refinement of *i*Pr_2SPAnH, overfitting is directly visible for the release of the chemical constraints (13 - 14) and the full expansion of the symmetry (14 - 15).

applied symmetry constraints and shows an improvement for the low order data. The same is found for the expansion from *mm*2 || *z* to *m* ⊥ *x* (in the plane) symmetry for the anthracene carbon atoms.

After the release of the chemical constraints in step 14, the data-to-parameter ratio is roughly 36 and the model should be considered as being well determined. However, severe overfitting is indicated by a drop of R_{work} and an increase in R_{cross}. Since the multipoles are concerned the impact is more pronounced for the low resolution data. The full expansion of the symmetry in step 15 adds to the overfitting. For both steps it is clearly visible that the information modelled by the newly introduced parameters is not reflected in the *free* data. Finally, it was concluded to stay with the more restricted model obtained after step 13.

6.3.1 Distribution of the refined parameters

To ensure that there is no model bias due to the omission of reflections the distribution of parameters derived from the 20 different refinements is considered. This check is usually performed for step 11 where the refinement of a *basic* model is completed. In the present case, no outlying parameters were found and hereby the assumption of bias-free models could be confirmed. However in the first runs, 1 out of the 330 refined parameters of the final refinement (step 13) differed by more than three times the *esd* from *pval* (Figure 35). It turned out that the chemically constrained C_{methyl} had their local coordinate systems pointing towards different hydrogen atoms, violating the assumption of identical pole populations. This was corrected and no parameter showed a deviation from the suggested values by more than three times the suggested *esd* (see 6.3.3 Error detection).

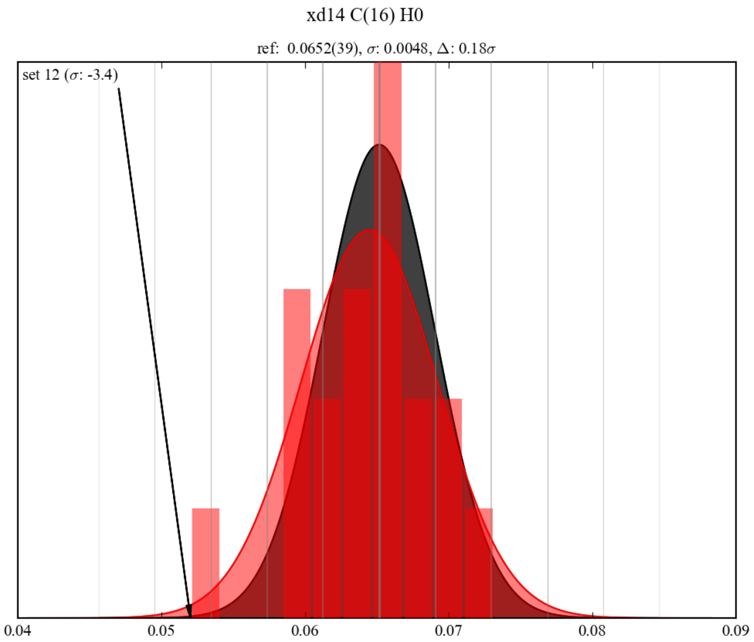

Figure 35
Example distribution for an outlying parameter. The value derived from the refinement against all data *pval* with the estimated standard uncertainty *esd* is depicted in grey, while the distribution of the value with *mean* and standard deviation *std* of the refinements against the 20 different work sets is given in red.

Table 20
Properties at selected bond critical points, comparing the final refinement (step 13) with the overfitted model (step 15), e.g. without local symmetry and chemical constraints.

bond	property	*pval*	*esd*	*mean*	*std*	$\frac{mean - pval}{std}$	$\frac{std}{esd}$
P1 – S1	ρ	1.123	0.003	1.122	0.003	-0.183	1.0
		1.126	0.003	1.126	0.003	-0.033	1.0
	$\nabla^2\rho$	-4.804	0.007	-4.804	0.081	-0.057	11.6
		-4.934	0.007	-4.935	0.086	-0.129	12.4
	ε	0.030	0.000	0.035	0.006	0.000	0.0
		0.050	0.000	0.048	0.009	0.000	0.0
P1 – C15	ρ	1.165	0.003	1.165	0.002	0.083	0.7
		1.172	0.004	1.172	0.004	-0.062	1.0
	$\nabla^2\rho$	-9.731	0.008	-9.722	0.060	1.187	7.4
		-9.873	0.011	-9.850	0.088	2.264	8.0
	ε	0.030	0.000	0.033	0.006	0.000	0.0
		0.060	0.000	0.064	0.007	0.000	0.0
C1 – C2	ρ	1.973	0.006	1.972	0.004	-0.108	0.7
		1.959	0.007	1.959	0.004	0.071	0.5
	$\nabla^2\rho$	-14.511	0.018	-14.510	0.139	0.033	7.8
		-14.228	0.023	-14.228	0.157	0.022	6.8
	ε	0.180	0.000	0.178	0.005	0.000	0.0
		0.190	0.000	0.193	0.006	0.000	0.0
C2 – C7	ρ	1.999	0.003	1.999	0.002	0.050	0.8
		2.012	0.008	2.011	0.004	-0.100	0.5
	$\nabla^2\rho$	-16.171	0.011	-16.159	0.112	1.045	10.2
		-16.587	0.028	-16.557	0.142	1.064	5.1
	ε	0.180	0.000	0.176	0.005	0.000	0.0
		0.190	0.000	0.188	0.006	0.000	0.0

6.3.2 Distribution of the properties at the bond critical points

With this refinement strategy the distribution of the properties at the bond critical points are to be evaluated. The calculations of errors on the density ρ and the Laplacian $\nabla^2\rho$ in *XD2006* have severe limitations as already mentioned. For the ellipticity ε no errors are available at all and an estimation of these errors would be useful. The distribution of k refinements can be used and as previously described the standard deviation derived from the distribution can be considered as a lower limit of the error. Table 20 shows a list of the properties at selected bond critical points comparing the final refinement (step 13) with the refinement not using any local symmetry or chemical constraints (step15). The following observations can be made:

- For all properties the differences between *pval* and *mean* is insignificant $\left(\left|\frac{mean - pval}{std}\right| < 3\right)$
- For the density ρ, the *esd* for the refinement against all data is slightly larger than the *std* of the distribution of the 20 refinements (*std*/*esd* ≤ 1). The *esd* is in the range of 0.003 – 0.007 or 0.2 – 0.4% of ρ, and much lower compared to values reported in the literature. In an investigation using 13 different data sets of oxalic acid (Kaminski et al., 2014) the distribution has a standard deviation in the range of 0.03 – 0.06 or 1.5 – 2.5 %. The deviations from the reported values might be due to differences in the treatment of data (e.g. herein no σ cut off was applied), the data to parameter ratio (resolution) and the data quality.

- For the Laplacian $\nabla^2\rho$ the *esd* is much smaller than the distribution's *std*, *std*/*esd* > 7.4 and the *std* are between 0.06 – 0.16 or 0.6 – 1.1% of *pval*. In the above mentioned investigation the standard deviation was between 1 and 7 or 6% and 28 %.
- For the ellipticity ε, *XD2006* does not give an estimate for the error, the *std* of the distribution is between 0.006 and 0.009. Kaminski et al. (2014) reported values between 0.01 and 0.04.

Comparing the two refinements, most properties are very similar, however, this must not necessarily be the case for different compounds. For the presented compound, the differences between the final and the overfitted model are merely subtle and would most likely not lead to misinterpretations. For other compounds this must not necessarily be the case and the model can be validated regarding the question if differences in parameters or properties actually are worth discussing. In conclusion, it was demonstrated that even in such a well-determined model overfitting can be detected and avoided, greatly reducing the chance of misinterpretation.

6.3.3 Error detection

The following examples illustrate how the presented routine can significantly support finding errors in an underlying strategy. Due to crystallographic symmetry, atoms on special positions need certain constraints in order to be properly refined. While in IAM programs like *SHELXL* these constraints are generated automatically, they have to be set manually in *XD2006*. The compound in question is once again paracyclophane and crystallises in space group $P\bar{4}_2/mnm$, the atoms C1 and C3 are located on a crystallographic mirror plane posing certain restrictions to each atom's respective parameters (Figure 36). With unset Gram-Charlier coefficient constraints for C3 on special positions, the impact on the *R*-value is invisible, but this error could be straightforwardly identified by inspection of the distribution of *pwork* of the *k* refinements (Figure 37), visible by the sheer amount of refined values that differ by more than three times the *esd*. The suggested deviation (grey) and the actual distribution (red) show no correlation at all. Of course, such an error imposes considerable convergence issues that help identifying the problem, yet, the distribution plot directly marks the problematic parameters. Moreover, much subtler errors that are not easily detectable otherwise can be found.

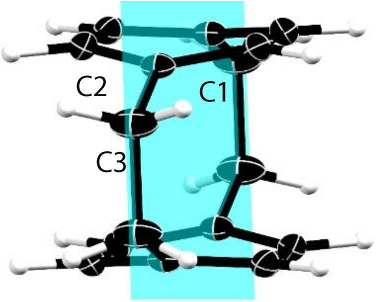

Figure 36
Structure of paracyclophane, a crystallographic mirror plane (blue) cuts directly through C1 and C3.

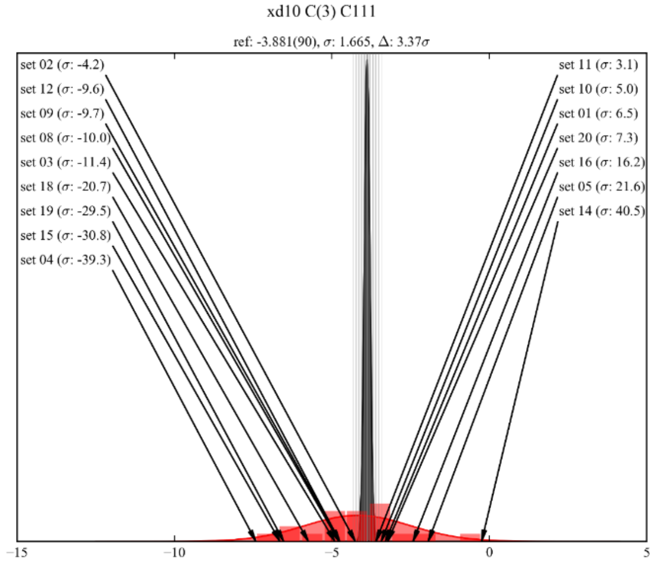

Figure 37
Distribution for the Gram-Charlier coefficient C111 that was refined freely by mistake and should have been constrained to C222 due to the crystallographic mirror symmetry.

6.3.4 Chemical Constraints

Recently, the charge density distribution of a silylone modelled by Niepötter from the Stalke group was published (Niepötter et al., 2014). In this structure, a silicon atom is coordinated by two identical cAACs (cyclic alkyl amino carbines). We found that the two silicon carbon bonds differ a lot both in the bond lengths and in the bond ellipticities. Therefore, it was anticipated that a release of chemical constraints is necessary for a proper modelling of this structure. However, unexpectedly, only the release of the local symmetry constraints of the silicon atom proved necessary. In contrast, the release of the chemical constraints of the two carbene ligands showed severe signs of overfitting. In the course of this thesis, this finding became more of a general experience than an exception. For all investigated compounds, overfitting was observed right after the release of the chemical constraints. Concluding that chemical constraints are indeed an important feature to stabilise a multipole refinement at least for data sets limited to resolutions of 0.45 Å and endorses the initial statement that it might be advisable to keep this stabilisation even in the final stages of a multipole refinement.

6.3.5 Outlier detection

Another example demonstrates the detection of disagreeable reflections. In the parameter distribution plots, all outliers with $|pval - pwork| > 3\ esd$ (Figure 38, top) belong to only three different test sets. Careful inspection of these *free* set's data revealed that two of these three sets each contain one supposedly strong low order reflection with $F_o \ll F_c$ (Figure 39). The two low-order reflections turned out to be severely overexposed, yet, they managed to bypass all applied outlier rejection routines (*SAINT*, *SADABS*). An omission of these two reflections lowers the inner shell completeness but essentially improves the model, as indicated by a far more reasonable parameter distribution (Figure 38, bottom). In this case, omission turned out to be the adequate handling of the problematic data. However, this can by no means be considered a general result. It will always remain a fine line between the errors associated to data omission and the errors induced by wrong-intensities. Leaving out data should always be the last step on a long journey of trial and error.

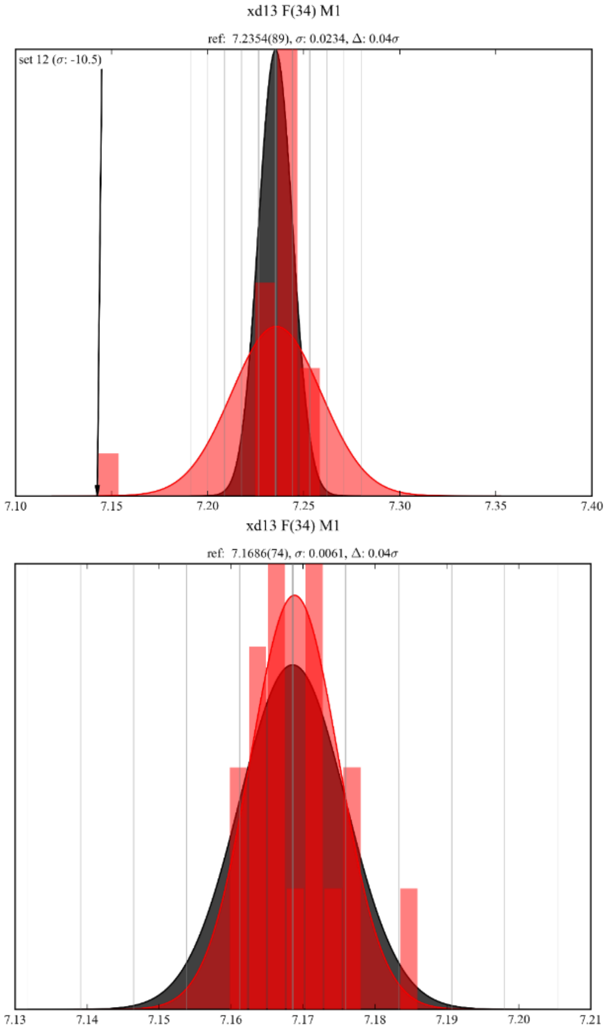

Figure 38
Distribution of the monopole population of atom F34 using all data (top) and after omission of the two outlying reflections (bottom).

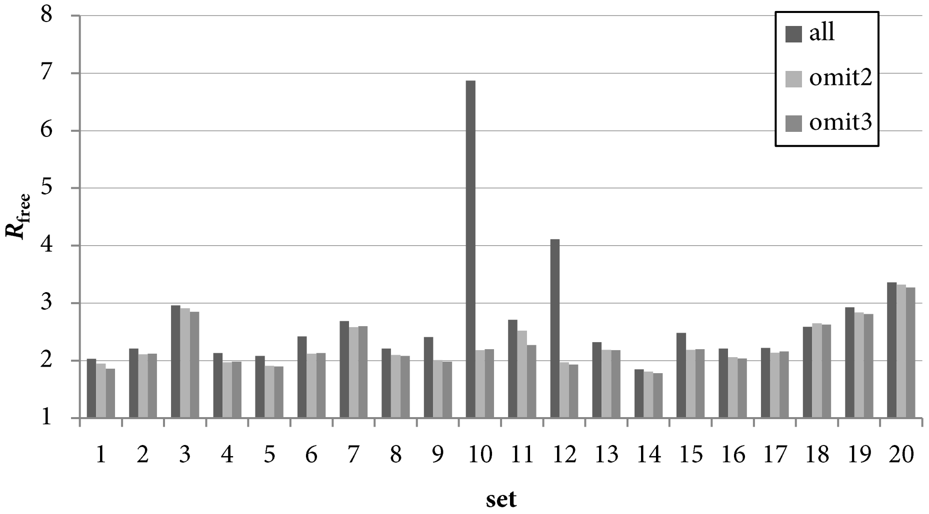

Figure 39
Plot of the individual R_{free} values for all *free* sets including either all data or sets with omitted reflections.

6.3.6 A validation tool for reasonable refinements?

As we already learned in the previous chapter, the data collected on paracyclophane was of marvellous quality, regardless of source or detection device. Model deficiencies turned out to be the bottleneck rather than systematic errors or noisy data. Even after the estimation of anisotropic hydrogen atoms features remained visible related to those atoms. Now after finding a sensible model for the anharmonic motion of the bridging carbon atom C3, can cross-validation help to find an unrestricted and completely refined anisotropic description for the two hydrogen atoms. It is of course one ambitious endeavour to push the deconvolution of thermal motion and the electron density model to its limits, yet, it is a worthy validation of the procedure. As support, anisotropic displacement parameters estimated by the *SHADE3* server have been consulted. A new ten step strategy was set up (Appendix A6.1), the multipoles were restricted to the octupole level for the carbon atoms. The hydrogen atoms were refined using a monopole and a bond directed dipole. For the carbon atoms, the maximum possible local symmetry was adopted, leading to *mm*2 symmetry for C2 and especially *m*/z for C1 and C3, as these two atoms are located on a crystallographic mirror plane restricting the available poles, vibrations and coordinates. The necessary constraints were set up accordingly. Gram-Charlier parameters were introduced to C3 and afterwards, the anisotropic motion for both hydrogen atoms were refined without any constraints and together with all other already introduced parameters, except for κ and of course κ'. A special remark to the screening parameters; according to Volkov et al. (2001) the hydrogen screening parameter were set to 1.1 and 1.18 for κ and κ', respectively. Using the suggested κ' values for the three carbon atoms (C1: 0.87, C2: 0.92 and C3: 0.96) turned out to give good results, an unrestricted refinement led to unreasonable large values. The final refinement was performed against all data (σ cut-off set to zero and the resolution was truncated to $\sin(\theta)/\lambda < 1.0$) leaving 1231 reflections and 74 refined parameters (data to parameter ratio: 16.64). The effective data to parameter ratio for the multipoles shows a different picture, here the data are limited to 178 observations that are used to model 32 parameters, a ratio of only 5.56 clearly suggests to not add further multipoles. Except for the last step,

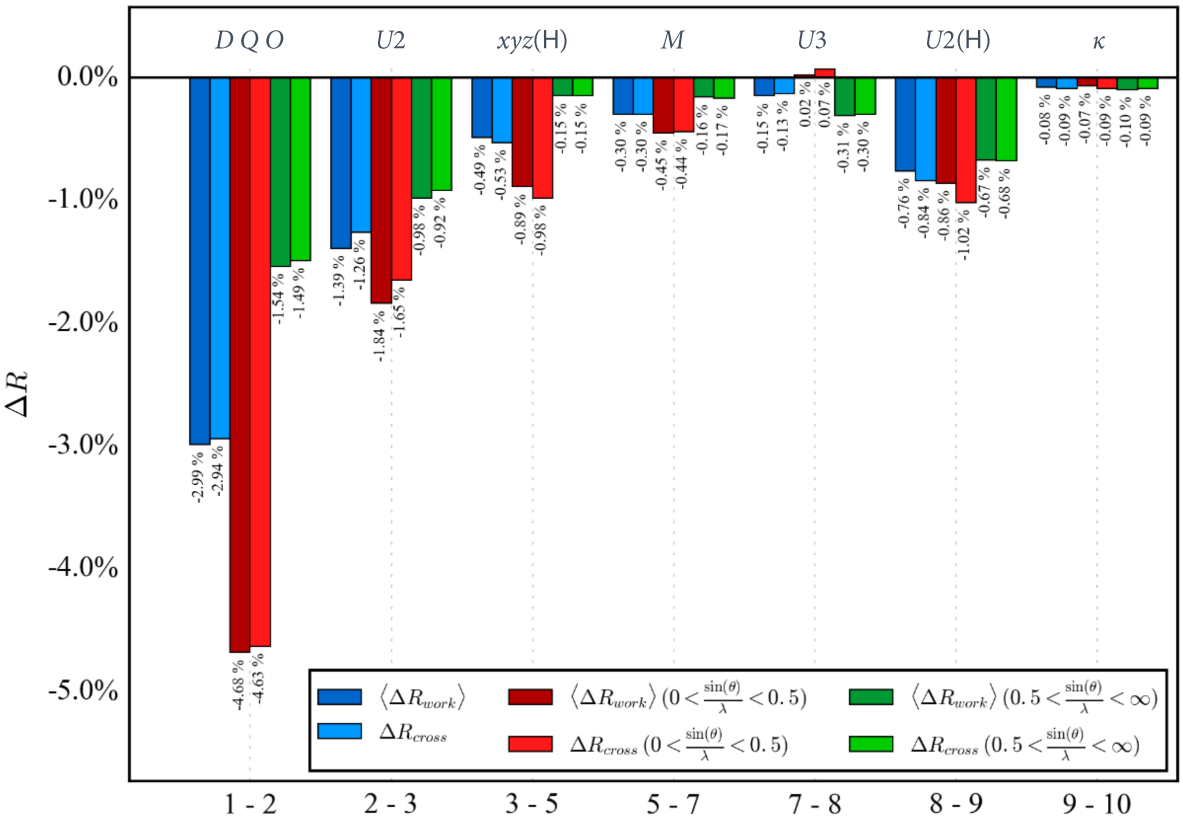

Figure 40

Progression of the refinement of paracyclophane. *M*: monopole, *D*: dipole, *Q*: quadrupole, *O*: octupole, *κ*: Kappa parameter, *U*2: anisotropic motion, *U*2(H): anisotropic motion for hydrogen atoms, *U*3: 3rd order Gram-Charlier and *xyz*/*xyz*(H): positional parameters for non-hydrogen and hydrogen atoms, respectively.

the refinement readily converged with the criterion of allowing a maximum *shift*/*esd* of 10^{-10}. The problematic last step included all parameters, however, a large correlation of 90 % was observed between certain C3 parameters (monopole/κ and dipole) and the H3 monopole and dipole. Here, the joint refinement was given priority over an exclusion of the *κ* parameter.

The validation using cross-validation impressively shows the different impact of the parameters, e.g. the introduction of the anharmonic motion (*U*3) in step 8 at C3 effects the high resolution data most (Figure 40). In step 9, the hydrogen atoms description is expanded to an anisotropic motion and the impact on the agreement is clearly visible. Here, the unexpected decrease of high resolution *R*-values can be explained with a more appropriate model after introduction of the anisotropic description that in return is affecting the anharmonic parameters of C3. A similar explanation can be found for the last step (10) when the three κ parameters are refined. They show a behaviour that is comparable to the slightly inflated displacement parameters in IAM as a result of retracted bonding density due to inadequate modelling capabilities.

Surprisingly, the distribution of the parameters for all five atoms were in good agreement with the least-squares *esd*, not a single outlying parameter was noticed. Concluding that a resilient model was successfully found. See appendix A6.6 for the according model quality indicators.

The positive effect of the anisotropic description is less pronounced for the aromatic H2. Here, the smaller vibrational amplitudes showing only slight deviation from an isotropic description render the

Table 21
Residual density map for the four different hydrogen descriptions, top half shows the full ADP, bottom part (symmetry equivalent) has the ADP omitted to give view to the underlying difference density. The riding model and rigid body fit ADP were calculated by the SHADE3 server (Madsen, 2006).

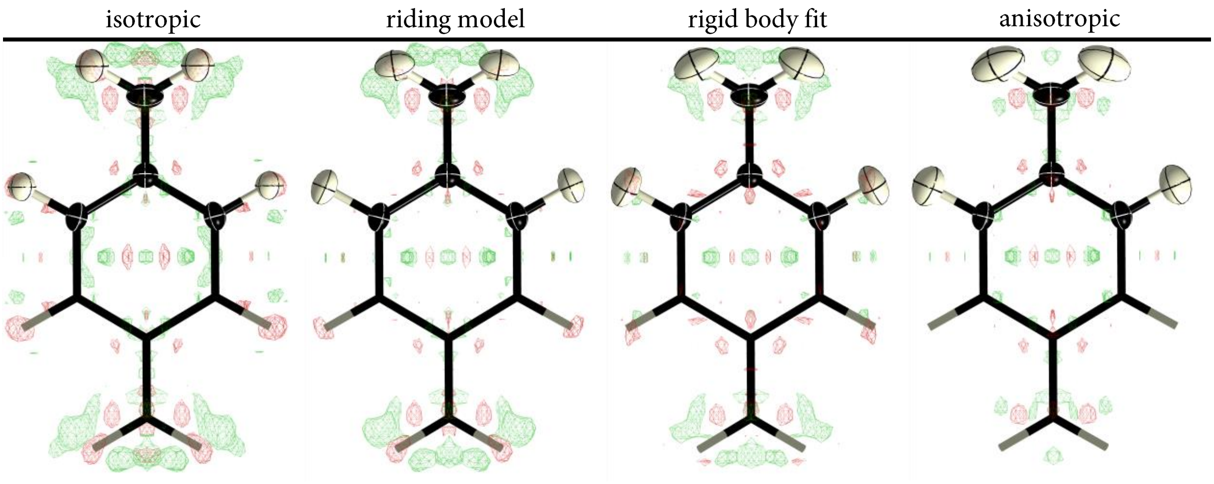

Map level: 0.040 eÅ^{-3}

riding model approximation more appropriate. For the heavily liberating H3, however, the limited modelling capabilities are not able to yield satisfying results and the additional freedom improves the overall description and leads to a reasonable model for the hydrogen motion. A qualitative comparison between the rigid-body ADP and the unrestricted refinement shows a good agreement, although the refined ADP is significantly larger (Table 21).

6.4 Conclusion

The presented method of cross-validation is a useful tool in a multipole refinement. Although the number of data in a high resolution data set is high enough to achieve a global data to parameter ratio larger than 10 to 20 even if all possible multipole parameters up to the hexadecapole level are refined, it must be considered that not all reflections contribute to the modelling of the multipole parameters. The information about the valence density is mainly incorporated in relatively few low order reflections. Therefore, the simple global data to parameter ratio is not a sufficient condition in order to decide about the possible number of parameters. For a reasonable refinement not only the normal *R*-values must decrease, but also the R_{cross} value. After an investigation of several structures following this approach the following general aspects can be formulated:

- The best start is using the highest possible symmetry, defined by the adjacent atoms.
- Lowering of symmetry constraints is not naturally accompanied by significant model improvements. In most cases, it is enough to release these constraints only for a limited number of atoms.
- Release of the chemical constraints for all atoms substantially shows an over-interpretation of the data. This was found for all investigated structures, advocating the idea behind databases for multipole populations and corroborating the assumption of the transferability of these parameters e.g. following an *INVARIOM* (Dittrich et al., 2004) or *UBDB* (Dominiak et al., 2006) approach.

In conclusion, this tool is intended to validate a strategy (or final model), reveal weaknesses and allow for tailoring and fine-tuning that guarantees the highest model flexibility in the regions of interest while the peripheral parts of the structure are kept as fixed as needed. In addition, the test of parameter distributions provides auxiliary error detection tools. Model inaccuracies related to the crystallographic symmetry as well as the local symmetry are directly highlighted. Erroneous low order reflections that might strongly bias the derived parameters can easily be detected. Moreover, the *k* different refinements also provide an estimate for standard deviations of topological properties that were unavailable hitherto.

CHAPTER 7:

SPANPS – THE RADIANT POLYMORPH

7 SPAnPS – the radiant polymorph

The following journey tries to find answers to the ongoing question concerning the solid-state fluorescence of *trans*-9,10-bis(diphenylthiophosphoryle)anthracene co-crystallised with toluene (*trans*-SPAnPS@toluene) and is the result of a process of constant learning, setbacks and adaptations of complementary techniques. First, a general overview is given, while in the following subchapters specific findings are discussed in more detail. The story started with a high-resolution data set recorded in 2007 and a multipole model that raised more questions than it answered, more on that later. This chapter makes extensive use of crystal data obtained by either G. Schwab or N. Finkelmeier and in this work, the focus is not on the synthesis of the particular compounds. Herein, general findings from previous investigations are gathered, re-evaluated and combined with new ideas and computational approaches in the hope of finding answers to the cause of the solid-state fluorescence behaviour of *trans*-SPAnPS@toluene.

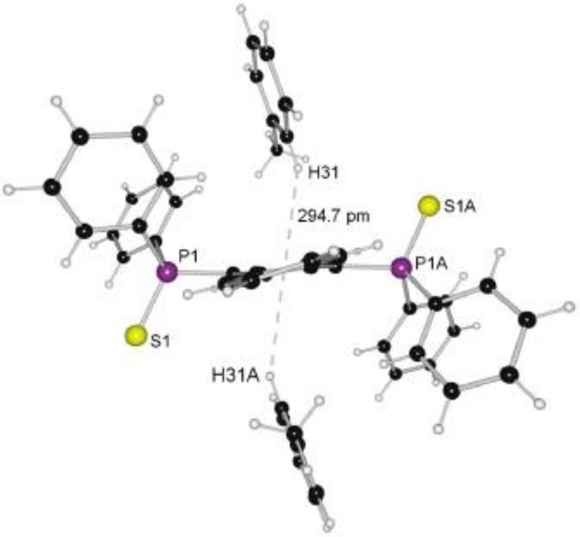

Figure 41
Crystal structure of *trans*-SPAnPS@toluene, showing the short contact between anthracene and toluene. Picture taken from the original publication (Fei et al., 2003).

7.1 A short history of SPAnPS

In 2003, Fei et al. (2003) published an article on the fluorescence properties of the substituted anthracene $(Ph_2P{=}S)_2C_{14}H_8$ (Figure 41). What they found, was a remarkable solid-state fluorescence, whose origin seemed to be exclusively related to intercalation or co-crystallisation of toluene, because in solution, the compound was non-emissive. The loss of toluene from the crystal framework upon vacuum drying was directly indicated by the vanishing of the fluorescence. A new exposure to toluene readily restored the emission. It was concluded that an exciplex (for: **exci**ted com**plex**; accordingly, excimer: **exci**ted di**mer**) formation changes the electronic states of energy and allows the excited system to relax via the fluorescence route. This is in good agreement with the emission spectra that clearly show a redshift compared to a further fluorescent anthracene derivative that comes without an exciplex formation (Fei et al., 2003).

The orientation of the two $Ph_2P{=}S$ moieties shape a cradle facilitating the formation of a T-shaped exciplex upon excitation. This degree of preorganization might be able to minimize the required formation energy, as the reversible exciplex formation / de-aggregation was proposed to be selective towards toluene. They found that benzene was not able to recover the fluorescence after addition to dried *trans*-SPAnPS@toluene powder; however, no explanation for that observation could be given.

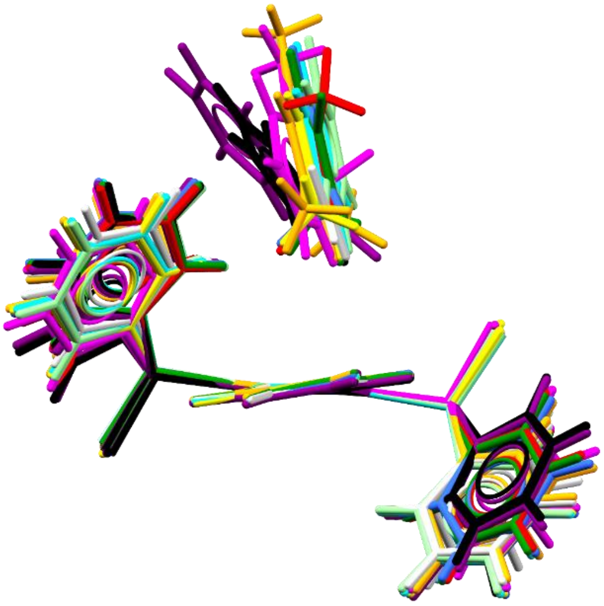

Figure 42
Overlay of all currently known *trans* oriented SPAnPS co-crystals.

The selectivity towards toluene was contradicted as G. Schwab went on with the investigation of this compound. During his diploma thesis, he managed to prepare a wide range of co-crystals with the variation of guest molecules restricted to toluene congeners. All currently known SPAnPS co-crystals that are adopting the *trans* conformation are depicted in Figure 42 (see Table 22). The overlay straightforwardly demonstrates the impressive structural similarities; all these structures have the cradled sulfur – phenyl motif in common, signifying that all these guests fit into the *trans* pocket and are showing approximately the same (guest) C – H ··· π (anthracene) distances, despite their different positions or arrangements. All depicted entrants show solid-state fluorescence upon UV-light exposure, hinting towards an exciplex formation. There was no dedicated detailed investigation on how the intensity of the fluorescence varies with changing partners, only a check on emission wavelength while exposition to UV-light was performed which gave similar results for all guests. The problematics behind reliable relative solid-state emission intensities will be a topic later in this chapter. An investigation on possible guest specific emission shifts was not encompassed herein. Nevertheless, the results indicated that the *type* of guest is only of subordinate importance for the fluorescence behaviour, as long as it fits into the pocket (e.g. aromatic systems).

For getting insight into the mechanisms upon loss of solvent and especially on the remnants, the crystalline powder was of special interest. A thermogravimetric analysis was performed in order to get experimental validation that the toluene is actually released when the co-crystals are being subjected to heat. Moreover, the results can show that the co-crystal stays intact until the very point, where it loses the fluorescence property indicated by the appropriate change in mass. The preparation was straightforward, freshly crystallised SPAnPS@toluene was filtered and desiccated. During the drying process of the crystals special care was taken that the resulting microcrystalline powder was still showing strong fluorescence emission.

Table 22
Hitherto known forms of *trans*-SPAnPS co-crystals and their respective space groups. SSF: solid-state fluorescence emission.

conformation	solvent	space group	SSF
trans[1]	toluene	$P2_1/n$	+
trans[2]	bromobenzene	$P2_1/n$	+
trans[2]	*p*-chlorotoluene	$P2_1/n$	+
trans[2]	iodobenzene	$P2_1/n$	+
trans[2]	*o*-xylene	$P2_1/n$	+
trans[2]	*m*-xylene	$P2_1/n$	+
trans[2]	*p*-xylene	$P2_1/n$	+
trans[2]	styrene	$P2_1/n$	+
trans[2]	benzene	$P\bar{1}$	+
trans[2]	phenyl-acetylene	$P\bar{1}$	+
trans[3]	toluene	$P\bar{1}$	+

1: Fei et al. (2003), 2: Schwab (2004, 2008), 3: Current work

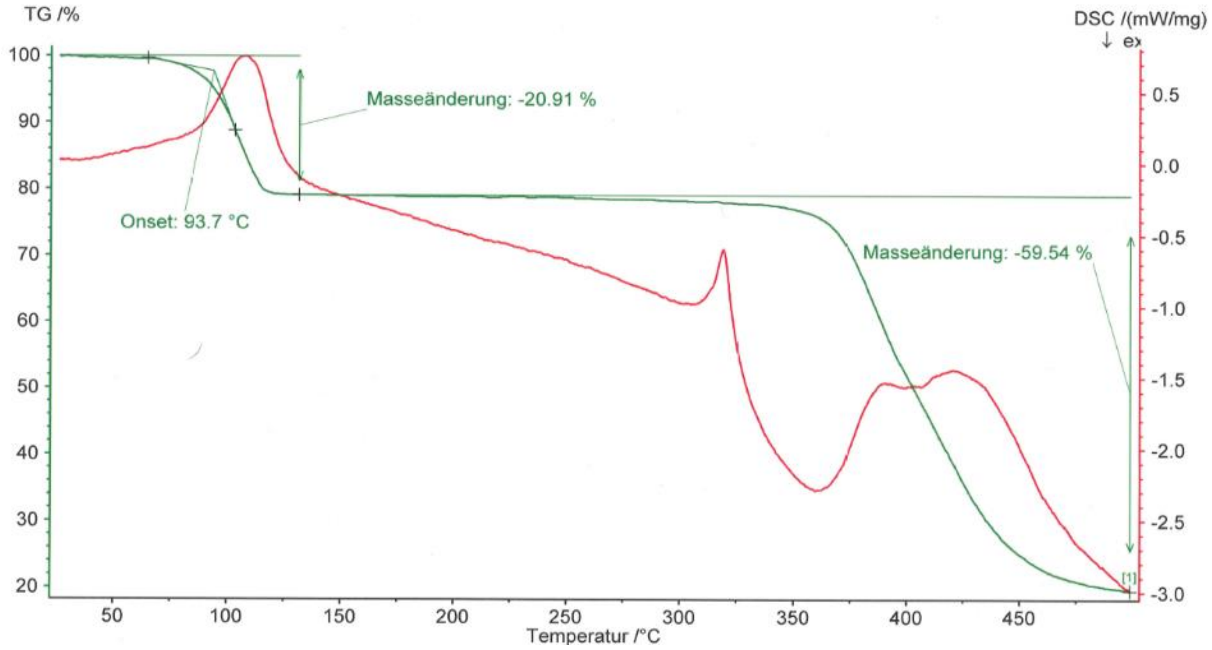

Figure 44
Thermogravimetric analysis (green) and differential scanning calorimetry (red) of *trans*-SPAnPS@Toluene.

Figure 44 shows the resulting TGA thermal curve for *trans*-SPAnPS@toluene. The change in mass upon heating to roughly 100°C is in good agreement with the toluene boiling point and the amount of toluene in the crystal structure, 20.91% to 23.00%, respectively. After the evaporation of toluene, the compound is stable to about 250°C and beyond that temperature the disintegration begins slowly. This was a necessary preliminary examination to the investigation of the dried non-fluorescent solid by means of solid-state NMR techniques corroborated by powder X-ray diffraction (PXRD).

The prepared co-crystals, for this purpose, were checked by means of single crystal X-ray diffraction and the structure was unequivocally determined as *trans*-SPAnPS@toluene in the space group $P2_1/n$. Crystals were packed in a sealed Schlenk flask under argon atmosphere and were successfully shipped to the UK. However, at some point in-between a phase change occurred yielding previously unknown co-crystals suitable for single crystal X-ray diffraction. The new form crystallises in the space group $C2/m$ (Figure 43) and adopts an arrangement comparable to the structure of *cis*-SPAnPS@phenylacetylene co-crystals already known from G. Schwab's diploma thesis. Similar to the phenylacetylene analogue, this new co-crystal does not exhibit strong solid-state fluorescence upon excitation with UV-light. A powder diffraction study carried out by A.-C. Pöppler in collaboration

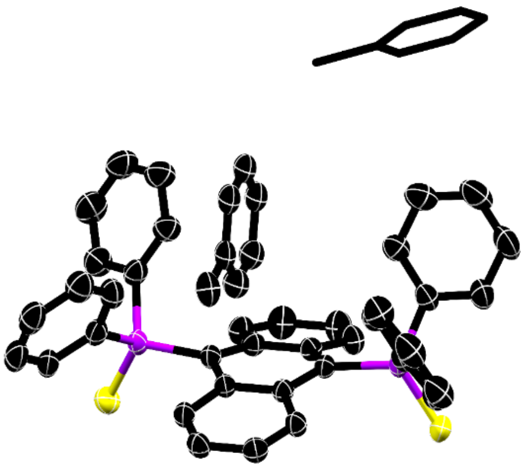

Figure 43
cis-SPAnPS@toluene crystallizes in the space group $C2/m$. The heavily disordered peripheral toluene is depicted as capped-sticks; the hydrogen atoms were omitted for clarity.

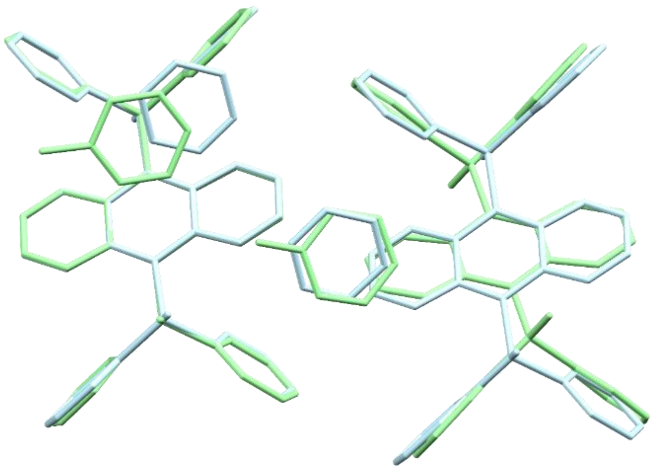

Figure 45
Overlay of the molecular arrangement of SPAnPS@benzene ($P\bar{1}$, light blue) and SPAnPS@toluene ($P\bar{1}$, light green). For the disordered toluene on the left only one position is shown.

with the University of Warwick on a ground sample was able to show that roughly 5 % of the powder adopted another, yet unknown, polymorph (Appendix A7.1). Suitable crystals large enough for single crystal X-ray determination were found in the sample (not the complete sample was ground to fine powder) that could readily be identified, extracted and characterized. The data exposed a new arrangement of the *trans* oriented SPAnPS@toluene in the space group $P\bar{1}$ with two half anthracene fragments and one and a half toluene (disordered) in the asymmetric unit, showing an anthracene to toluene ratio of 2/3. The crystal packing of the new polymorph is similar, albeit not completely superimposable onto that of the already known *trans*-SPAnPS@benzene, that, in contrast to the findings of Fei et al., was confirmed by G. Schwab to show intense solid-state fluorescence. However, it crystallizes in the space group $P\bar{1}$, the compound studied by Fei et al. was *trans*-SPAnPS@toluene in the space group $P2_1/n$. In this low-symmetry *trans*-SPAnPS@toluene arrangement, the guest molecules do not show a preferential orientation in close proximity to the anthracene π-system. Nevertheless, the crystalline system gives rise to solid-state fluorescence upon UV-light exposure. In Figure 45 an overlay of the molecular arrangements is depicted, clearly revealing a similar packing motif, superimposable by only slight adjustments. On a subsequent shipment of again unequivocally identified *trans*-SPAnPS@toluene in $P2_1/n$, the new polymorph emerged from the powder to approximately 95 %.

The emergence of these new polymorphs gave rise to the assumption that the different phases of the SPAnPS co-crystals are only metastable and readily interchangeable upon loss of the guest molecule. The less volatile anthracene moiety remains as loosely bound framework and through slight rearrangements, new polymorphs can be formed. The question arises as to what extend these co-crystals are interchangeable into one another. The respective experiments, similar to that performed by Fei et al. (2003), are presented in the following.

7.2 Role of the space group on the acceptance of guests

Crystalline SPAnPS@benzene in a small excessive amount of benzene was provided in a Schlenk flask and the fluorescence emission of the compound was verified. The excessive benzene was removed under reduced pressure and the remaining crystalline solid was dried with high temperature supply until the solid lost its fluorescence property. The extinguished light emission was accompanied by a colour change with the former bright yellow solid altering to an orange colour. Subsequent addition of a small amount of benzene restored the fluorescence emission of the solid almost immediately, however, after the addition of toluene to the dried orange solid the formation of fluorescent crystals was significantly slower. Yet within seconds, new crystals were forming that again showed solid-state fluorescence emission. This procedure could be repeated *ad libitum*. Here, the observation was made that smaller crystallites began to show fluorescence in the first place with the larger specimens still being orange. However, these darkened blocks also started to show fluorescence without prior dilution indicating characteristics of a sponge. Freshly formed crystals were extracted and suitable specimens were studied by means of X-ray diffraction experiments. Both intercalation compounds (toluene and benzene) now adopted the *trans* $P\bar{1}$ polymorph, hinting towards a precursor theory, where the arrangement of the remaining solvent-free SPAnPS matrix facilitates the formation of the $P\bar{1}$ rather than the $P2_1/n$ polymorph.

The observations made by Fei et al. (2003) that the fluorescence emission of *trans*-SPAnPS@toluene in $P2_1/n$ is lost after drying and that it is not restorable upon exposition to benzene might have its origin in the differing arrangements in the crystalline solid. SPAnPS@toluene crystallises in the centrosymmetric space group $P2_1/c$, however, the benzene co-crystal in the space group $P\bar{1}$. In comparison, they show distinct variations in the spatial arrangement of the anthracene moieties, that might severely hinder the exchange and inclusion of the other guest molecule, respectively, as they might not be able to permeate the other respective molecular arrangement. Similar experiments were performed and *trans*-SPAnPS@toluene in the space group $P2_1/n$ was presented in a Schlenk flask. The crystals were dried until no fluorescence was visible and on subsequent addition of toluene, the emission could readily be restored. Crystals were extracted and the structure was validated to still be $P2_1/n$ by means of X-ray diffraction. Exposition of benzene to the dried solid did not directly yield a light emitting crystalline solid. However, after roughly 60 minutes small fluorescing crystallites were emerging. It was not possible to monitor the crystal formation e.g. if a precursor-like matrix assisted rearrangement or completely new crystallisation took place. The freshly formed specimen were determined as *trans*-SPAnPS@benzene adopting the space group $P\bar{1}$. Addition of toluene to a dried solid of this compound, however, yielded the *trans*-SPAnPS@toluene $P\bar{1}$ polymorph and not the previously determined structure in $P2_1/n$. Concluding, *trans*-SPAnPS@benzene cannot adopt a stable crystalline arrangement in that particular space group. A closer look at the corresponding basic crystal structure parameters like volume, density, voids and lattice energies can shed light on that question. Crystal voids are empty spaces in the crystal structure and are herein calculated using the program *CrystalExplorer*

Table 23
Selected crystal related properties of the two polymorphs of *trans*-SPAnPS@toluene and the benzene co-crystal. Further compounds are shown for comparison. The crystal voids were calculated with the program *CrystalExplorer* (Spackman et al., 2012), the lattice energy was calculated using the *PIXEL* program (Gavezzotti, 2003, Schwab, 2008).

conf.	guest	space group	void [Å^3]	vol. [Å^3]	void/vol.	density [g/cm^3]	lattice energy
cis	-	$P2_1$	216.96	1546.72	0.14	1.311	-205.4
cis	toluene	$C2/m$	271.62	3868.50	0.07[†]	1.207	–[#]
trans	toluene	$P2_1/n$	221.16	2074.97	0.11	1.272	-116.2
trans	toluene	$P\bar{1}$	264.58	2011.50	0.13[†]	1.236	–[#]
trans	benzene	$P\bar{1}$	107.34	983.96	0.11	1.294	-111.6

[#] The unit cell contains more than 2 symmetry inequivalent molecules.

[†] The structure shows severe guest molecule disorder.

(Spackman et al., 2012). These structural parameters are compared for the toluene, benzene and the solvent free structures of SPAnPS. The data depicted in Table 23 show that crystal density and the void volume per unit cell are remarkably similar for the co-crystals *trans*-SPAnPS@toluene in $P2_1/n$ and *trans*-SPAnPS@benzene. Furthermore, these findings were underlined by *Pixel* calculations of the corresponding lattice energies. The two new polymorph show severe disorder and thus, calculations yielding an acceptable accuracy are unfortunately unavailable. It is striking that a much lower lattice energy was calculated for the guest free polymorph. However, this coincides with the experimental finding that the crystals that precipitate in a flask at room temperature do not directly show fluorescence and can be identified as exactly this solvent free compound, whereas lower temperatures support the formation of the respective co-crystal. Concluding that the solvent free compound can be identified as the thermodynamic and the respective co-crystal as the kinetic product. Regarding the toluene guest molecule, the co-crystal adopting the space group $P2_1/n$ seems to be thermodynamically more stable than the $P\bar{1}$ polymorph. This might explain why it was the only known structure containing toluene for such a long time, as long crystallisation periods facilitate the formation of that particular structural motif over the other polymorph. In the previous chapters, we have acquired the knowledge of the chronological order of events, in the following certain underlying aspects will be introduced and discussed in more detail.

7.3 Processes connected to the packing

It is striking that the *cis* conformation exhibits either severe disorder (visible in the *cis* oriented co-crystals) or a substantially lower packing density and significant higher lattice energy in the solvent free motif. This hints towards the restricted intramolecular vibration (RIV) explanation approach in recent literature for aggregation-induced emission (AIE). Here, a tight intermolecular stacking is thought to ensure high solid-state fluorescence quantum efficiency by prohibition of vibrational motion (Li et al., 2016). Owing to the complexity of the processes in the solid-state, this aspect as well as related topics will be discussed in detail later in this chapter. However, there is at least one example in the *trans* configuration (*trans*-SPAnPS@toluene in $P\bar{1}$) exhibiting disorder while showing intense solid-state fluorescence, and disorder is a striking sign of packing flexibility, see Table 24 for an overview of the currently known SPAnPS structures.

Table 24
Hitherto known forms of SPAnPS co-crystals and their respective space groups. SSF: solid-state fluorescence emission.

conformation	solvent	space group	SSF
cis[3]	-	$P2_1$	-
cis[3]	dichloro-methane	$P2_1/c$	-
cis[3]	acetone	$P2_1/c$	-
cis[3]	acetonitrile	$P6_3/m$	-
cis[4]	toluene	$C2/m$	-
cis[2]	anisole	$C2/m$	-
cis[2]	phenyl-acetylene	$C2/m$	-
cis[2]	benzyl alcohol	$C2/m$	-
cis[2]	benzonitrile	$P\bar{1}$	-
cis[4]	ethyl acetate	$P\bar{1}$	-
trans[1]	toluene	$P2_1/n$	+
trans[2]	bromobenzene	$P2_1/n$	+
trans[2]	*p*-chlorotoluene	$P2_1/n$	+
trans[2]	iodobenzene	$P2_1/n$	+
trans[2]	*o*-xylene	$P2_1/n$	+
trans[2]	*m*-xylene	$P2_1/n$	+
trans[2]	*p*-xylene	$P2_1/n$	+
trans[2]	styrene	$P2_1/n$	+
trans[2]	benzene	$P\bar{1}$	+
trans[2]	phenyl-acetylene	$P\bar{1}$	+
trans[4]	toluene	$P\bar{1}$	+

1: Fei et al. (2003), 2: Schwab (2004, 2008), 3: Finkelmeier (2013), 4: Current work

Finkelmeier (2013) carried out systematic investigations on a wide variety of anthracene derivatives, with the focus mainly on the structural motif. The interesting quantities related to SPAnPS were found in the *bending* and *twisting* of the anthracene moiety. However, with the findings directly applied to the SPAnPS co-crystals, the problem is that these quantities are in direct connection to the conformation of the SPAnPS moiety. Concluding, all *bent* structures are *cis* conformers, while all candidates showing a significant *twist* result from a *trans* arrangement. Yet, the conclusion drawn at the end of the chapter '*whether the direct interaction of solvent molecules with the fluorophore or the conformation of the SPAnPS molecule resulting from the intercalation of solvent were the vital factors for strong emission*' is highly interesting and still unanswered.

Since the appearance of a special publication by Langhals in 1989, the nouns used in discussions on supramolecular arrangements might have changed, the debate about the role of packing still actively goes on. '*We think that strong interactions of the chromophores are […] also responsible for the fluorescence quenching via the coupling of electronic excitation to lattice vibrations*' is the primary statement of the publication by Langhals that was used to explain the aggregation-caused quenching (ACQ) for all types of fluorophores that exhibited intense fluorescence emission in solution, whereas the solid material is non-emissive. That explanation got widely accepted in the literature as in radiationless relaxation processes vibronic couplings, electron-phonon couplings and internal conversions play crucial roles (Quina, 1982). Weak chromophore interactions are hardly influenced by lattice vibrations but for strong interactions the electronic excitation can flow into lattice vibrations via the coupling, and non-emissive internal conversion (IC) is therefore required (Langhals et al., 1989).

This general concept is accepted until today. However, it is still only vaguely defined as recent publications show, reporting on non-luminescent crystals explained by enhanced non-emissive deactivation channels such as exciton/excimer/exciplex formation, vibronic interactions and other non-radiative decay processes in aggregated states (Shimizu & Hiyama, 2010). In this context, exciton (an excited molecule, e.g. *one* excited chromophore in the crystal lattice is called an exciton) and excimer are used to explain excited states from which energy can be transferred without the need for a transfer of charge. From these considerations, a scientific field emerged, dedicated to the investigation of intermolecular interactions of guest molecule inclusions that effectively prohibit aggregation-caused quenching. In general, conformational aspects were used to the same extend in order to hinder alternative solid-state relaxation pathways and effectively predict the resulting nature of the fluorescence emission. Since the early publications, many researchers attempted to overcome the problem of fluorophore aggregation in order to develop strongly emitting candidates for high-level applications. One popular way to prevent aggregate formation is the introduction of sterically demanding substituents directly to the fluorophore moiety (Ooyama et al., 2005). The application of strategies, which prevent close-packing lead to a wide range of different luminescent solid-state structures (Hong et al., 2009, Shimizu et al., 2009, Tang et al., 2009, Jayanty & Radhakrishnan, 2004, Ozdemir et al., 2009).

In general, it was shown that the fluorescence intensity could be enhanced by minimizing intermolecular interactions through steric hindrance. In a recent publication, Yokota et al. (2012) were able to demonstrate that from a group of analogue compounds the bulkiest derivative showed the most intense fluorescence. In the same publication, the emission of another bulky candidate, however, was relatively weak. A direct explanation to this contradiction could not be found and it was attributed to the complex emission mechanism. It was concluded that the whole process is not only driven by intermolecular interactions and hereby packing effects are the dominating terms but also the electronic structure of the participating molecules must add significant contributions (Yokota et al., 2012). Yet, another group was successful in relating the fluorescence properties, not only the intensity but also the shift of emission wavelength, to intermolecular stacking modes of extended electronic systems. Face-to-face geometries of anthracene fluorophores were deemed responsible for a bathochromic emission shift in combination with longer fluorescence lifetimes (Dong et al., 2012). Unfortunately, for the many examples given in the literature that show the applicability of either concept, there is a good chance of finding contradicting results for another compound.

Interestingly, many exceptions to these two conventional ideas of emission quenching in solid-states have been published until today. In these exceptions, strong luminescence is observed for long-range ordered solids whereas only faint luminescence emission is visible in solution. This quenching in solution is often attributed to a dominant non-radiative decay by free intramolecular rotation in comparison to the restricted motions possible in the crystal (He et al., 2009). In recent literature (Araki & Mutai, 2016), this is referred to as enhanced emission in the solid-state due to a blockage of radiationless decay channels by restriction of intramolecular rotations (RIR) (Mutai et al., 2014). Intramolecular effects on fluorescence enhancement are explained by the conformational changes of chromophores and effects on fluorescence changes by intermolecular interactions are correlated with the aggregation morphology such as face-to-face and T-shape aggregation. Parallel stacking with a strong intermolecular interaction is thought to induce non-radiative deactivation process (Levitus et al., 2001), contrasted by head-to-tail J-aggregates, which increase fluorescence efficiency (Gruszecki, 1991). Generally, this property is called aggregation-induced emission enhancement (AIEE) for molecules that were already fluorescent in solution. Aggregation-induced emission (AIE) is used for non-fluorescent diluted samples that exhibit strong solid-state emission. Compounds bearing this feature have received attention as promising materials for optoelectronic applications (An et al., 2002, Feng et al., 2010, Kamino et al., 2013, Hong et al., 2009, Liu et al., 2009, Luo et al., 2001). There is a recent review on this matter with the suitable name *Aggregation-induced emission: the whole is more brilliant than the parts* (Mei et al., 2014), concluding the restricted intramolecular motion as the main contributor to the aggregation induced emission.

We have already learned that *trans*-SPAnPS@toluene (in $P2_1/n$) does show exactly this behaviour, as Fei et al. (2003) could show that the fluorescence is dramatically increased upon crystallisation. He et al. (2009) have studied the solid-state photo-physical properties of four 9,10-distyrylanthracene derivatives that possess a typical aggregation-induced emission. All four compounds show solid-state emission and adopt a *trans* conformation of the vinylene moiety relative to the anthracene. Moreover, they related the degree of asymmetry of the molecule to the presence of considerable packing forces and concluded that more distorted conformations limit effective conjugation resulting in hypsochromically shifted emissions (He et al., 2009). Their findings are in good agreement and should be comparable to the herein investigated SPAnPS co-crystals that show a *trans* orientation, they addressed the relationship between the crystal structure and AIE properties to the restricted intramolecular torsion between the 9,10-

anthrylene core and the vinylene moiety. This explains the observation made by Fei et al. that *trans*-SPAnPS@toluene (in $P2_1/n$) is non-emissive in solution and shows strong solid-state emission. This should be applicable to the same extent to the remaining co-crystals of SPAnPS. However, this explanation is unfortunately not sufficient, as it cannot explain the occurrence of the known non-emissive *cis* oriented solid-state structures.

In a short chapter of the diploma thesis of G. Schwab, experiments were performed regarding the influence of temperature on the fluorescence emission. Results that were unfortunately not published at that time and have not been pursued further. Here, it was experimentally observed that the *cis*-SPAnPS@phenylacetylene as well as the dried *trans*-SPAnPS@toluene ($P2_1/n$), both non-emissive at ambient temperature, do exhibit fluorescence emission below -135°C. Regarding the cis co-crystal, a possible temperature dependent phase change could be directly refuted experimentally, as the low temperature phase was found to show *cis* conformation (Schwab, 2004).

Concluding that, while all compounds that exhibit solid-state fluorescence at ambient temperatures have the *trans* conformation in common, the *cis* conformers only show solid-state fluorescence upon cooling.

7.4 Intermolecular attractions – insights from NMR

Albeit being limited to a qualitative understanding, systematic investigations of the non-covalent interactions as well as steric and topological properties of the anthracene derivatives may give useful insights into the underlying processes that lead to the observed solid-state fluorescence. New and complementary aspects were added to the discussion based on the first results of solid-state NMR investigations on the *trans*-SPAnPS@toluene that were performed in collaboration with A.-C. Pöppler in the work group of Prof. S. Brown at Warwick University. Due to the limited variety of hydrogen atoms in the compound, there are only aromatic carbon atoms and one methyl group, the peak assignment is non-trivial. Here, only measurements at the high field 850 MHz spectrometer of the UK 850 MHz Solid-State NMR Facility were able to produce reasonable line separations. In general, solid-state NMR experiments are often supported by quantum mechanical calculations, as the calculations can support the interpretation and facilitate the assignment of these frequently non-trivial solid-state NMR spectra. In the present case, the investigation was coupled with periodic boundary condition density calculations using the GIPAW (*CASTEP*) approach (Pickard & Mauri, 2001, Clark et al., 2005, Yates et al., 2007), that relies on a first-principles quantum mechanical description and uses the density-functional theory with a plane-wave basis set and a pseudopotential formalism.

The initial idea was to shed light on the processes that take place upon heating, e.g. to monitor the transition between the fluorescent toluene co-crystal and the solvent free, non-fluorescent compound *in-situ*. However, the problem encountered was that the sample chamber e.g. the rotor itself, is a sealed system and vaporized solvent cannot be released. Therefore, no complete change is observable and a mixture was detected making the interpretation of the now overlapping spectra of two or more compounds even more difficult.

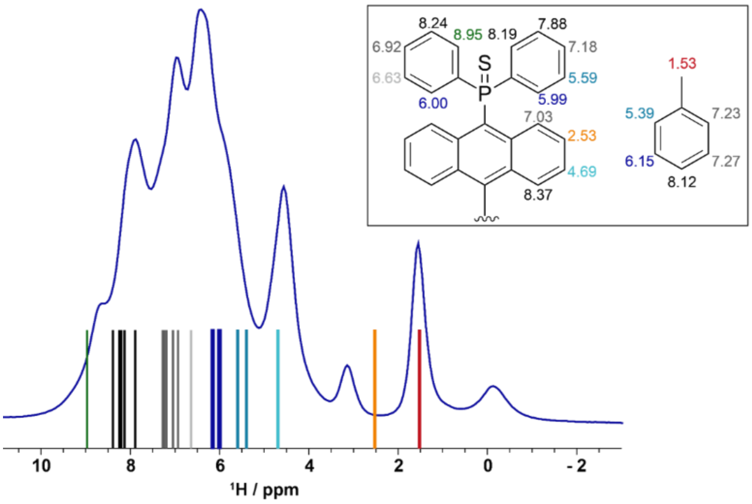

Figure 46
CASTEP based solid-state NMR chemical shift assignment. ^{1}H Solid-state NMR spectrum, calculated shifts as colour coded overlay. Inset: Calculated ^{1}H NMR shifts.

On the other hand, the chemical shift tendencies that the NMR revealed drew a new picture of the important interactions in the solids-state. The chemical shift, a measure for the local electron density distribution at a nucleus, is able to highlight deviant cores. E.g. aromatic hydrogen atoms are expected to show a chemical shift of around 8 ppm, however, those participating in strong interactions are indicated by significant shifts. It is assumed that a large shift towards lower ppm is evident for a C – H ··· π type of interaction. The ^{1}H NMR spectrum (Figure 46) clearly shows that the hydrogen atom of the toluene pointing directly onto the anthracene moiety (X-ray: H22, 5.39 ppm) is strongly shifted to lower ppm, followed by one meta hydrogen atom of the phosphorus bound phenyl group (X-ray: H12, 5.59 ppm). This is in good agreement with the assumption of significant host/guest interactions for the *trans*-SPAnPS@toluene compound. However, the strongest shift is experienced by the outwardly oriented hydrogen atoms of the anthracene moiety (H4 and H5) and is larger than for that particular toluene hydrogen atom pointing directly onto the fluorophore. The two anthracene hydrogen atoms (corresponding atom in the X-ray structure: H4, 2.53 ppm and H5, 4.69 ppm) are significantly shifted from their expected range to lower ppm indicating even stronger interactions than found for the host/guest connection. It has to be emphasised that the NMR investigations gave rise to a completely new view on the intermolecular interactions that take place in the solid-state. Prior to these findings, it was anticipated that the host/guest interactions play the major role in this system.

In order to investigate the role of the host/guest as well as intermolecular interactions and especially their influence on the density a detailed charge density investigation is presented that was performed on the *trans*-SPAnPS@toluene ($P2_1/n$) co-crystal (see chapter 9 for experimental details). The NMR chemical shifts backed-up with calculations in combination with topological features from the experimental charge density e.g. non-covalent interactions and interaction energies on the basis of the multipole model, might be able to give a more complete picture of the forces acting in solid-state form of SPAnPS (Koritsanszky & Coppens, 2001, Stalke, 2011, Flierler & Stalke, 2012).

In the topology of the density a surprisingly large number of intermolecular C – H ··· π interactions in the form of intermolecular bond paths connecting either C ··· C, H ··· C or even H ··· H were found. Nevertheless, the individual paths can be considered as C – H ··· π interactions. Bond paths provide valuable structural information by indicating which atom show exchange interactions in a given system (Bader, 2009, Pendas et al., 2007). These intermolecular paths were not limited to the host/guest

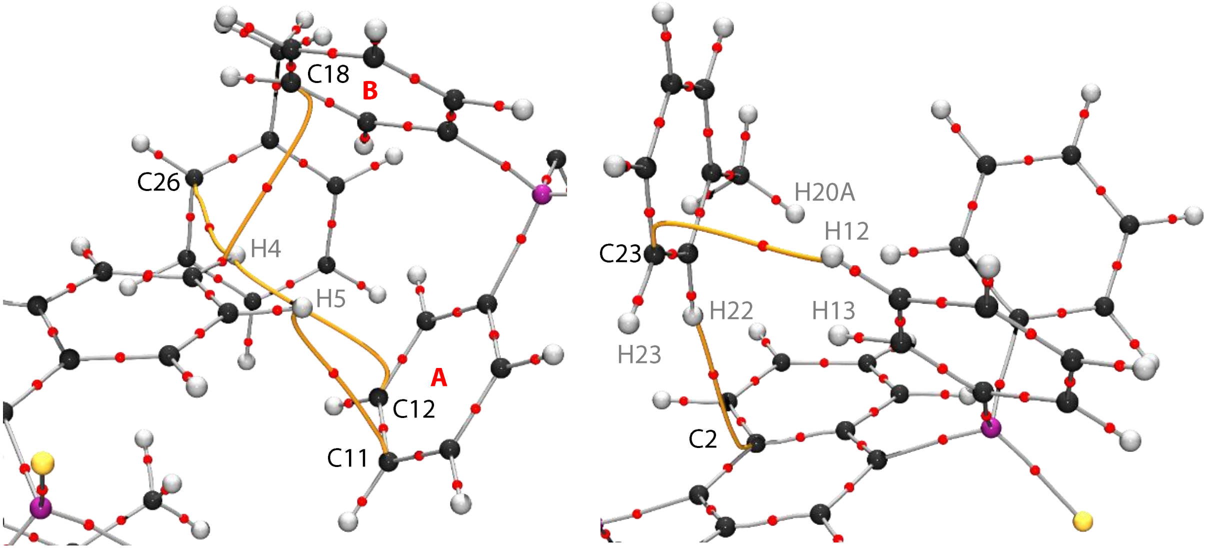

Figure 47
Molecular graph of SPAnPS@toluene. Intramolecular bond paths are depicted in grey, intermolecular bond paths in orange and the bond critical points marked as red dots.

interactions, as NMR already suggested. The most shifted anthracene hydrogen atom shows numerous bond paths to adjacent aromatic systems. The values of the electron density, Laplacian and properties derived thereof are given in Table 25.

Table 25
Properties at the bond critical point for selected hydrogen atoms. Kinetic (G), potential (V) energy densities estimated according to G, V, E are in Hartrees A^{-3}.

pair	ρ	$\nabla^2\rho$	G	G/ρ	V	E
H4 – C12	0.03	0.36	0.02	0.59	-0.01	0.01
H4 – C18	0.05	0.55	0.03	0.64	-0.02	0.01
H4 – C26	0.03	0.34	0.02	0.56	-0.01	0.01
H5 – C11	0.04	0.47	0.03	0.61	-0.02	0.01
H12 – C23	0.03	0.27	0.01	0.56	-0.01	0.00
H22 – C2	0.04	0.51	0.03	0.63	-0.02	0.01

The low-density concentration at these points indicates the closed-shell nature of the interactions and is in agreement with values reported in comparable literature (Wolstenholme & Cameron, 2006, Wolstenholme et al., 2007). Moreover, they show the typical curved paths that are commonly reported for weak closed shell interactions involving π electron density (Figure 47). In the context of bond critical points, the cross-validation using *XDRfree* were able to give an estimate of the reliability of the corresponding properties, e.g., the density and the Laplacian. Figure 48 shows the distribution for the bond critical point connecting H22 (toluene) and C2 (anthracene). The figure demonstrates a good reproducibility, which can be

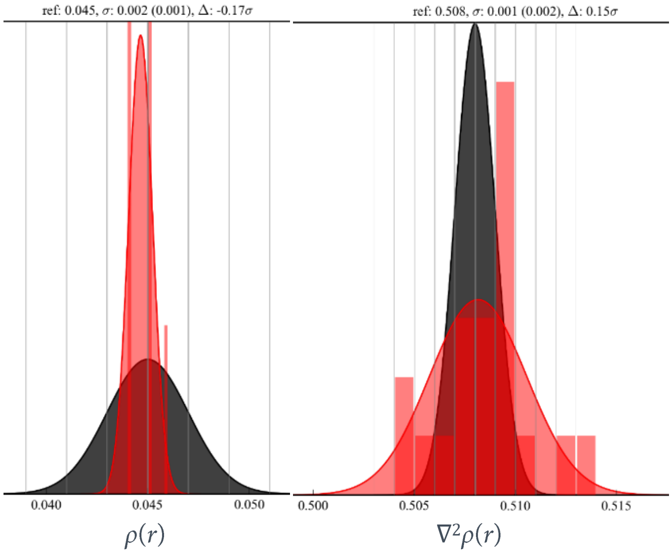

Figure 48
Distribution of $\rho(r)$ and $\nabla^2\rho(r)$ at the bond critical point of H22 and C2. Due to the applied chemical constraints and/or limitations in the calculation of errors in *XD2006* no other least-squares *esd* is available.

considered as a measure for the reliability of the density description. The Laplacian is found to show a broader distribution, that still shows impressive precision provided that the least-squares *esd* is highly underestimated. For the other bond critical points, unfortunately, no *esd* were available at all as *XD2006* does not give an estimate for the error if a chemically constraint atom participates in the derived property. Yet, the distributions show a similarly robust behaviour. Concerning the derivation of the kinetic and potential energy density (Abramov, 1997) from topological properties at the bond critical point, a recent publication conceded that these indicators are inherently unreliable and provide only limited information beyond less demanding interatomic distance considerations (Spackman, 2015).

Table 26
Comparison of the interaction energies between the anthracene moiety and selected hydrogen atom of the toluene. ER: exchange-repulsion; D: dispersion; EL: electrostatic; T: total interaction energy in kJ/mol.

	distance[#]	**ER**	**D**	**EL**	**T**
H22[†]	2.622	11.32	-4.84	-5.48	0.99
H23[†]	3.655	0.69	-1.08	-0.21	-0.59
H20A[†]	3.309	1.97	-1.54	-0.30	0.13
H20B[†]	3.039	4.21	-2.63	-1.44	0.14
H12[‡]	2.949	2.67	-1.60	-2.23	-1.17
H13[‡]	2.572	9.53	-3.46	-3.56	2.51

[#]The distance is calculated between the atom and the mean anthracene plane and is given in Å; [†]toluene hydrogen – anthracene interaction; [‡]anthracene hydrogen – toluene interaction.

The significance of the bond paths is underlined by inter fragment energy calculations performed by the *XDPROP* module within the *XD2006* program. Here, the pair wise energy calculations are not limited to complete molecules but especially allow the evaluation between single atoms and/or molecular fragments. In the following, the calculations between the hydrogen atoms in question and *reasonable* partners e.g. anthracene or phenyl moieties are presented. Regarding H22, the partner in question is the anthracene. Therefore, the corresponding energies are discussed for the four hydrogen atoms that point towards the anthracene π-system, namely H22, H23 and two methyl hydrogen atoms H20A and H20B. The corresponding inter-fragment energies are presented in Table 26. It is directly visible that the pure distance only gives crude estimations for interactions; the overall shortest distance shows repulsive interaction in total. The pure distances should be discussed with caution as far as interactions are concerned. Further, it can be seen that the electrostatic contribution to the interaction energy between H22 and the anthracene moiety is by far the strongest. However, the sum of the attractive contributions is not enough to compensate for the exchange-repulsion energy. This is only the case for the weakly interacting H23. The nature of the hydrogen atom (aromatic or aliphatic) does not seem to have an influence on the displayed interaction energies. The phenyl anthracene interactions give a more pronounced picture. Here, the hydrogen atoms H12 and H13 are directed towards the toluene and thus of interest. It was shown already that only for H12 a direct connection concerning the density is given in a bond path, however, both hydrogen atoms show large electrostatic and dispersion forces towards the toluene. Yet, only for H12 the attractive forces have a higher weight than the repulsion. Thus, concluding that for the toluene/anthracene interaction the NMR results could qualitatively be reproduced by evaluation of the individual interactions using the experimental density.

Table 27
Comparison of the interaction energies between the anthracene hydrogen atoms H4/H5 and nearest toluene and phenyl groups (for A and B see Figure 47). ER: exchange-repulsion; D: dispersion; EL: electrostatic; T: total interaction energy in kJ/mol, the distance is given in Å.

		distance#	ER	D	EL	T
H4	toluene†	3.172	4.60	-2.55	-2.85	-0.81
H4	phenyl† A	3.617	3.76	-1.88	-1.22	0.66
H4	phenyl† B	3.777	6.75	-2.47	-1.70	2.58
H5	toluene‡	4.486	0.23	-0.49	-0.34	-0.61
H5	phenyl† A	2.741	10.04	-4.08	-4.09	1.86
H5	phenyl† B	3.260	2.99	-1.94	-2.30	-1.25

#The distance is calculated between the atom and the mean phenyl or toluene plane; †symmetry operation: 1/2-x, 1/2+y, 3/2-z; ‡symmetry operation: 1-x, 1-y, 1-z.

The anthracene hydrogen atoms H4 and H5 show a comparable, yet less distinct picture (Table 27). There are indeed significant electrostatic and dispersion forces that might explain large NRM shifts. However, the overall interaction reveals itself as mostly repulsive due to very large exchange-repulsion atom-atom potential terms. Overall, the results presented so far for the interactions using XD2006 do not yield an unambiguous picture. On the one hand, bond paths were successfully found between the fragments/atoms, their occurrence is in good agreement with the solid-state NMR results. On the other hand, the total interaction energies were not able to qualitatively confirm the trends observed with NMR. Of course, NMR can indicate close proximities but it cannot identify the attractive or repulsive nature of a particular intermolecular interactions. Furthermore, the exchange-repulsion term grows exceptionally large e.g. in the case of H22, despite its strong electrostatic interaction, the overall energy is of repulsive nature. In summary, no qualitative agreement could be found and the experimental charge density investigation could not fully clarify the understanding of the origin for the fluorescence. For further investigations, quantum mechanical calculations on the crystal geometry might give complementary insights and allows for a more general picture.

7.5 Interaction energies – a computational approach

The majority of host/guest structures that are not showing fluorescence crystallises in the space group *C*2/*m* and herewith adopt the *cis* conformation. The crystallographic mirror plane cuts the anthracene moiety along C9 ··· C10 in half and, similar to the *trans* conformation, the guest molecules are cradled in a pocket formed by both $Ph_2P{=}S$ moieties in this case. In contrast to the *trans* conformation, the guests do not show fixation to the same extend and all structures are exhibiting disorder. Albeit the distances between the hosts and the guests are astonishingly similar, with the mean distance in *cis* even being slightly shorter and the values accumulating around 2.7 Å, compared to 2.9 Å in the *trans* arrangement. The major difference between the two arrangements is that in *cis* oriented co-crystals that crystallise in *C*2/*m* the inclusion of guest molecules pushes the fluorophores together (Figure 49, top and see again Table 24) strengthening their interaction in particular, whereas for the trans arrangement the guests act more like a buffer between the anthracene moieties. The lateral spacing of the bent fluorophores in the *cis* arrangement is identical for all three co-crystals (*cis*-SPAnPS@[benzylalcohol, toluene and phenyleacetylene]) and amounts to 3.4 Å (Figure 49, bottom). The interaction energies were evaluated with the *PIXEL* method as well as with the *CrystalExplorer* program (Spackman et al., 2012). Both programs use a comparable concept for the calculation of pair-wise interaction energies and rely on ab-initio densities derived from the experimental geometry, yet, the evaluation of the energies follows different approaches. The arising orthogonality is therefore used to support the reliability of the results since in some cases the crystal symmetry and/or disorder really adds to the complexity of the system. It is equally valid for the co-crystals that there are two designated guest positions (X and Y in Figure 49, bottom),

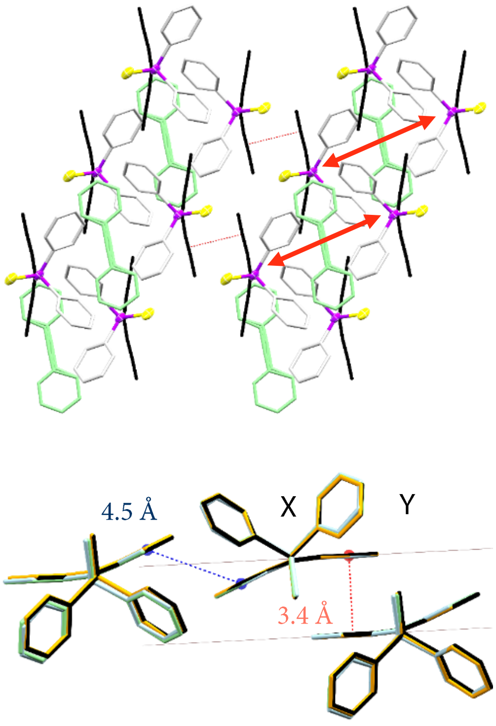

Figure 49
Top: View along the crystallographic b axis onto the crystal structure of SPAnPS@phenylacetylene; Colorcode: anthracene moiety (black), phenyl groups (grey), phosphorus (lilac), sulfur (yellow), phenylacetylene (light green, disordered by inversion). Bottom: Overlay of cis-SPAnPS@(benzylalcohol: black, toluene: orange, phenyleacetylene: light-green).

Table 28
Calculation of interaction energies for selected molecular pairs of three *cis*-oriented co-crystals adopting the space group *C*2/*m*.

Guest	distance$^{\#}$ (face/back) [Å]	CE (face)	PX (face)	CE (back)	PX (back)
PhAc	6.78 / 8.88	-83.8	-82.3	-54.2	-54.5
BzAlc	6.81 / 8.56	-88.6	-87.7	-58.9	-56.6
Tol	6.78 / 8.61	-88.7	-86.1	-58.4	-57.1

CE: CrystalExplorer, PX: *PIXEL*, face: face-to-face stacked pair, back: back-to-back stacked pair. PhAc: phenylacetylene, BzAlc: benzylalcohol, Tol: toluene.
$^{\#}$The distance is different from the direct lateral spacing given in the text, here it is the distance between the respective fragment centres.

one rather fixed position stacked on top of the anthracene and framed by phenyl groups and one more loosely bound position in the periphery. Both positions give rise to disorder due to voids in the crystal packing motif.

The calculated pair-wise energies show good agreement among the three co-crystals (Table 28) and the by far strongest interactions include the anthracene moiety. The combination of the face-face and the back-back interaction arranges as an intermolecular π-stacked chain through the crystal system. As expected from literature for immediately adjacent aromatic systems, the total energy term is largely dominated by attractive dispersion forces. The face-to-face stacking motif is the strongest intermolecular interaction energy found during this investigation, with total attractive energies of approximately -86 kJ/mol at a direct anthracene-anthracene distance of 3.4 Å (red dashed line in Figure 49, distances: 3.40 Å [benzyl alcohol], 3.43 Å [toluene] and 3.41 Å [phenylacetylene]). The lateral back-to-back spacing is longer and roughly 4.5 Å (blue dashed line in Figure 49, distances: 4.36 Å [benzyl alcohol], 4.44 Å [toluene] and 4.63 Å [phenylacetylene]). The interactions between the host and the respective guest could not yet be determined in a satisfactory manner and are not shown in this work. This is due to the case that all cradled guests are disordered by inversion and the fragments in peripheral position are as well disordered. An explanation for the finding of disorder can be given directly from interaction considerations. The cradled guests might be able to obtain two energetically comparable or even similar positions, hence disorder by inversion. For the peripheral positions such a straightforward answer cannot be given. It must be differentiated between disorder due to the absence of any strong interaction and the disorder by occupation of equivalent positions. Here, the conclusion is that the two strongest attractive interactions involve the stacking of the anthracene moiety and the direction of the interaction is along the crystallographic *a*-*c* axis angle bisector. This corroborates the assumption of a radiationless process that leads to a non-emissive excitation decay in these compounds.

However, these findings were directly questioned by a structural motif synthesised by T. Schillmöller from our workgroup. The compound of concern is an *asymmetric* anthracene derivative that consists of one $Ph_2P{=}S$ moiety and an ethyl group counterpart. It co-crystallises with toluene in the space group $P\bar{1}$ and shows intense solid-state fluorescence. Contrary to expectations, the crystal structure comes with a tight lateral spacing of the anthracene moieties of 3.5 Å (Figure 68) giving rise to strong pairwise interaction energy of -66.1 kJ/mol. The major difference is the packing motif, in contrast to the stacking network found for the cis-SPAnPS compounds; the stacking follows more of a dimeric motif without continuous interaction overlap.

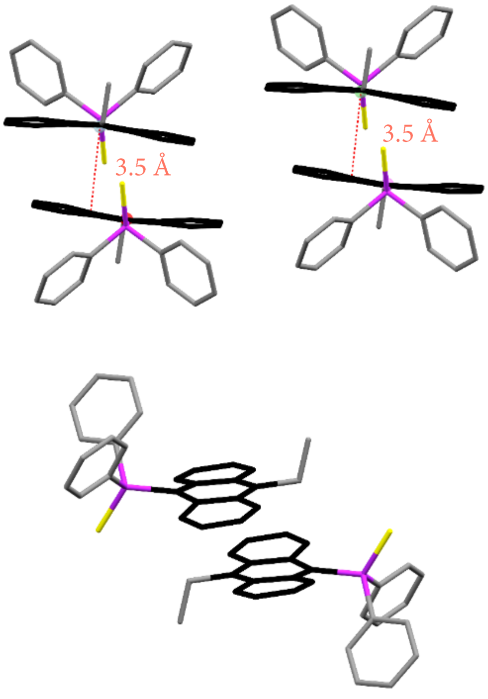

Figure 50
Top: View along the anthracene moiety of $Ph_2SPAnEt$@toluene; Colorcode: anthracene moiety (black), phenyl/ethyl groups (grey), phosphorus (lilac), sulfur (yellow), toluene was omitted for clarity, bottom: Depicted is the dimeric interaction showing the offset anthracene systems.

In the present case, the appearance reminds to be closely related to the isolated dimers in the literature (Mutai et al., 2005, Park et al., 2009, Dong et al., 2012). Furthermore, the aromatic systems do show some offset (Martinez & Iverson, 2012) that is as well discussed as supporting solid-state emission. These findings corroborate the ongoing discussion on the influence and importance of close aromatic interactions. Moreover, the statement that strong intermolecular π ··· π interactions are principal factors of fluorescence quenching in the solid-state cannot be considered as generally valid, for an effective quenching mechanism it might be crucial that a network of π ··· π is present that spans the crystal. Analogous pair-wise interaction energy calculations were performed for three selected *trans* oriented co-crystals with the guest molecules phenylacetylene ($P\bar{1}$), benzyl alcohol ($P\bar{1}$) and toluene ($P2_1/n$). The resulting energy calculations are summarised in Table 29. From a geometrical point of view, the structural motifs are not directly comparable to the *cis* arrangement, the strongest intermolecular interactions can be assembled into three groups. Host/guest interactions, direct fluorophore and fluorophore/phenyl interactions. In the space group $P2_1/n$, no direct fluorophore interaction is possible due to the crystal packing. In contrast to the $C2/m$ *cis* arrangement, the energies summarised in Table 29 show a more balanced behaviour. There is no prominent interaction in terms of energy. The host/guest interaction is dominant in the $P2_1/n$ toluene structure; for the other two co-crystals this is not the case, here the host/guest interaction is the weakest. This ambiguity hints towards the assumption that the guest is only of minor importance for the solid-state fluorescence as all three compounds show distinct emission. The calculated *CrystalExplorer* and *PIXEL* energies again are in good quantitative agreement, however, anthracene/phenyl interaction energies show a deviation for the space group $P\bar{1}$. Unfortunately, no statement can be given whether the energy calculated

Table 29
The strongest interaction energies in the *trans*-SPAnPS co-crystals for selected structural pairs, from the anthracene point of view. An: closest interaction to an anthracene, only in $P\bar{1}$, Ph: interaction via phenyl groups.

Guest	Pair	Distance [Å]	CE [kJ/mol]	PX [kJ/mol]
PhAc [$P\bar{1}$]	Guest	6.03	-35.6	-34.4
	An	9.70	-42.2	-41.1
	Ph	13.08	-38.6	-24.4
Tol [$P2_1/n$]	Guest	4.92	-37.3	-39.2
	Ph	10.54	-35.9	-32.1
BzAlc [$P\bar{1}$]	Guest	5.05	-32.0	-30.7
	An	9.86	-39.5	-39.1
	Ph	12.84	-38.9	-25.7

CE: CrystalExplorer, PX: *PIXEL*. PhAc: phenylacetylene, BzAlc: benzyl alcohol, Tol: toluene.

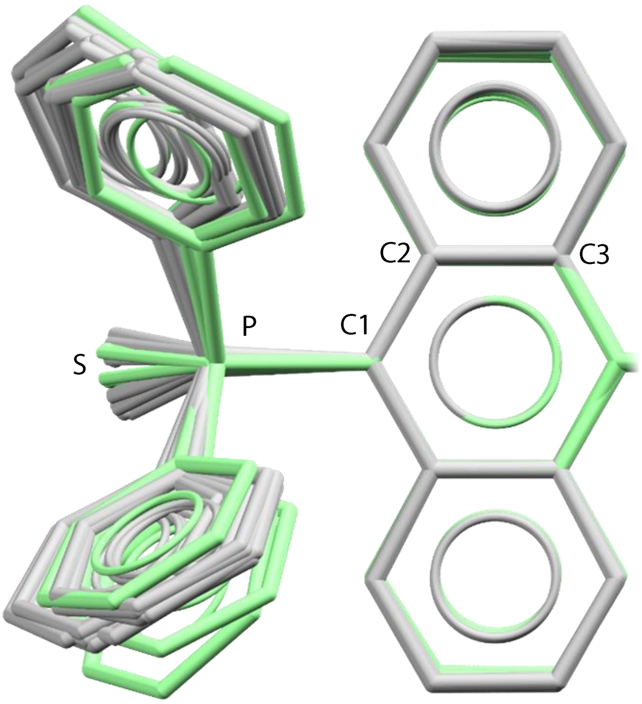

Figure 51
Overlay of SPAnPS co-crystals in the *trans* (grey) and in *cis* (light green) conformation. Anchor points of the structural overlay: C1, C2 and C3.

by the *PIXEL* program is underestimated or if *CrystalExplorer* is overestimating the corresponding energy.

Mutai et al. (2005) reported the reversible on-off switching of the solid-state fluorescence emission of a terpyridine. They addressed the change in emission to a packing induced change in the twist angle between the pyridine moieties. The question was if similar findings are valid for SPAnPS co-crystals, moreover if such an indication is found for the phenyl rings regarding the anthracene. However, the arrangement of the peripheral phenyl groups is found to be remarkably similar between all SPAnPS co-crystals, depicted as overlay in Figure 51. It has to be emphasised that the argumentation in the literature largely focusses on planar arrangements of adjacent π-systems, a motif that is not realisable in the SPAnPS system. Moreover, the phosphoryl bridge, in contrast to a carbon – carbon single bond, is unlikely to promote conjugation of π density (Kocher et al., 2004).

7.5.1 A more complete picture of the packing

On the last pages the consistency of the different experimental approaches (NMR, XRD) was validated and could be successfully verified. However, the focus was on individual contributions and interactions of particular molecular pairs exhibiting distinct motifs or between fragments that show strong interactions. In the solid-state, there are various additional factors that affect luminescent properties. Here, the intermolecular interactions of the excited fluorophore with surrounding molecules are thought to provide additional pathways for radiationless energy dissipation. A three dimensional molecular packing and intermolecular contact analysis, the energy frameworks (see chapter 2.4.2), can give a more general impression of the crystal packing especially regarding the nature of the underlying forces. The global intermolecular attractions that keep the crystals tightly packed might yield valuable insights regarding mechanical properties such as material stiffness, that in turn has influence on the elastic constants of a crystal and therefore on corresponding phonons. In the beginning of this chapter the exciton - phonon coupling was discussed as a possible source for the quenching of fluorescence by non-radiative decay. A visible consequence of such a strong exciton - phonon interaction is a broad multi-phonon phonon side band (PSB) in emission spectra (Pieper & Freiberg, 2014). Phonons are collective vibrational modes (standing waves) in periodic lattices in which all the lattice particles simultaneously participate. The idealized exciton states in deformable lattices interact with the local vibrations of the molecular units as well as with the collective phonons of the surroundings, leading to a dissipation of excitation energy as well as to vibronic spectral structures (Pieper & Freiberg, 2014). When more than one optically active molecule is present, an excited fluorophore may transfer all or part of its energy to a nearby molecule and the *energy transfer* can take place non-radiatively. The excited fluorophore, then called the *sensitizer*, emits a photon that is absorbed by the *activator* before it can leave the crystal. The interaction may be either an exchange interaction (overlap of the wavefunctions), an electric dipole or magnetic multipolar interaction. In the *phonon-assisted* energy transfer the energy difference between the emission of the sensitizer and absorption of the activator is made up for by the absorption or creation of one or more phonons. The amount of energy can excite simultaneously a few high energy vibrations and radiative process is no longer possible. Usually this non-radiative process is called multi phonon emission. The phonon-assisted energy transfer rate generally increases with temperature, which is in good agreement with the experimental finding that cooled SPAnPS fluorophores show solid-state emission regardless of their co-crystal or packing.

In qualitative terms it is assumed that the rate of excited-state energy transfer is determined by exchange and dipole - dipole interactions, which are associated with the models proposed by Dexter (1953) and Förster (1949). The energy transfer is based on approximations that are difficult to separate when they are competing at short distances, however, it is known that Förster energy transfer dominates at long distances and that Dexter energy transfer is effective only with significant orbital overlap (Kitai, 1993). In the case of polar molecules the electron-phonon coupling is mediated mainly by the dipole - dipole interaction (Renge, 1992). Mutai et al. (2008) found that the directions of the dipole moment of the excited and ground states of emitting species were remarkably different and they concluded that this could be the reason for a change in the luminescence energy. These findings are especially interesting in the SPAnPS co-crystal case. In the *cis* configuration both sulfur atoms point into the same spatial direction give rise to a dipole moment that must be substantially larger than for the centrosymmetric *trans* configuration. The idea was that the larger dipole moment enables stronger intermolecular energy exchange that opens non-radiative relaxation pathways, either by exciton - phonon coupling or direct dipole-dipole interaction (Obata et al., 1999).

More recent theoretical analysis indicates a connection between intermolecular interaction- and coupling strength and suggest that the emission wavelength is sensitive to the mode of intermolecular interaction with nearest molecules; i.e.,

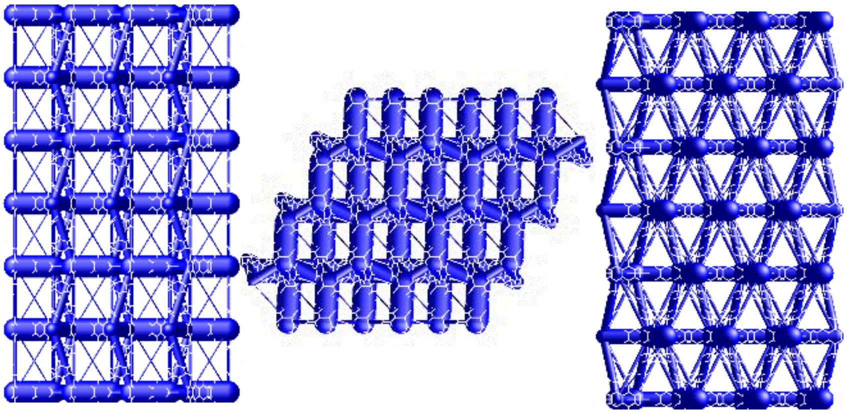

Figure 52
Energy frameworks corresponding to the total interaction energy in *cis*-SPAnPS@benzylalcohol along the crystallographic axis a (left), b (center) and c (right). The large tubes indicate the strong interaction between adjacent anthracene moieties. The tube size is set to 25, no energy cut-off applied.

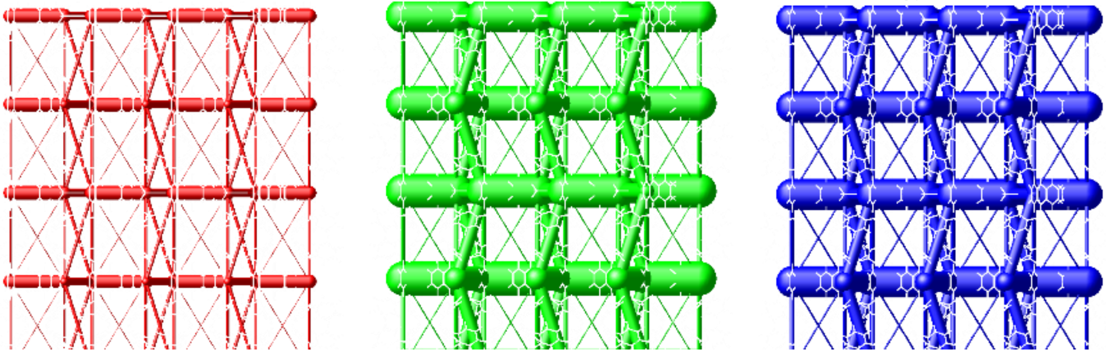

Figure 53
Energy frameworks for *cis*-SPAnPS@benzylalcohol along the crystallographic *a*-axis. The electrostatic, dispersion, and total energies are colored red (left), green (center), and blue (right), respectively, with cylinder thickness proportional to the magnitude of the interaction energy. The tube size is set to 25, no energy cut-off applied.

hypsochromic shifts result from side-to-side interactions and bathochromic shifts from face-to-face interactions (Shigemitsu et al., 2014). There are numerous publications presenting results confirming that the mode of molecular arrangement and conformation is an effective tool for controlling luminescent properties by various mechanisms of the packing-to-luminescence transduction (Araki & Mutai, 2016).

The energy frameworks calculated and visualised by the *CrystalExplorer* program (Spackman et al., 2012) impressively show the strong interaction between adjacent face-to-face stacked anthracene moieties in the *C*2/*m* packing motif that some of the *cis* conformers are adopting (Figure 52). As discussed previously, this motif is remarkable as it can be considered as stand-alone, as no other packing, whether in *cis* nor in *trans* configuration and regardless of space group, is capable of producing such strong interactions between the fluorophores. The framework is able to uncover the dispersion term as the dominating contribution to this π - π interaction, demonstrating the polarizability of the anthracene

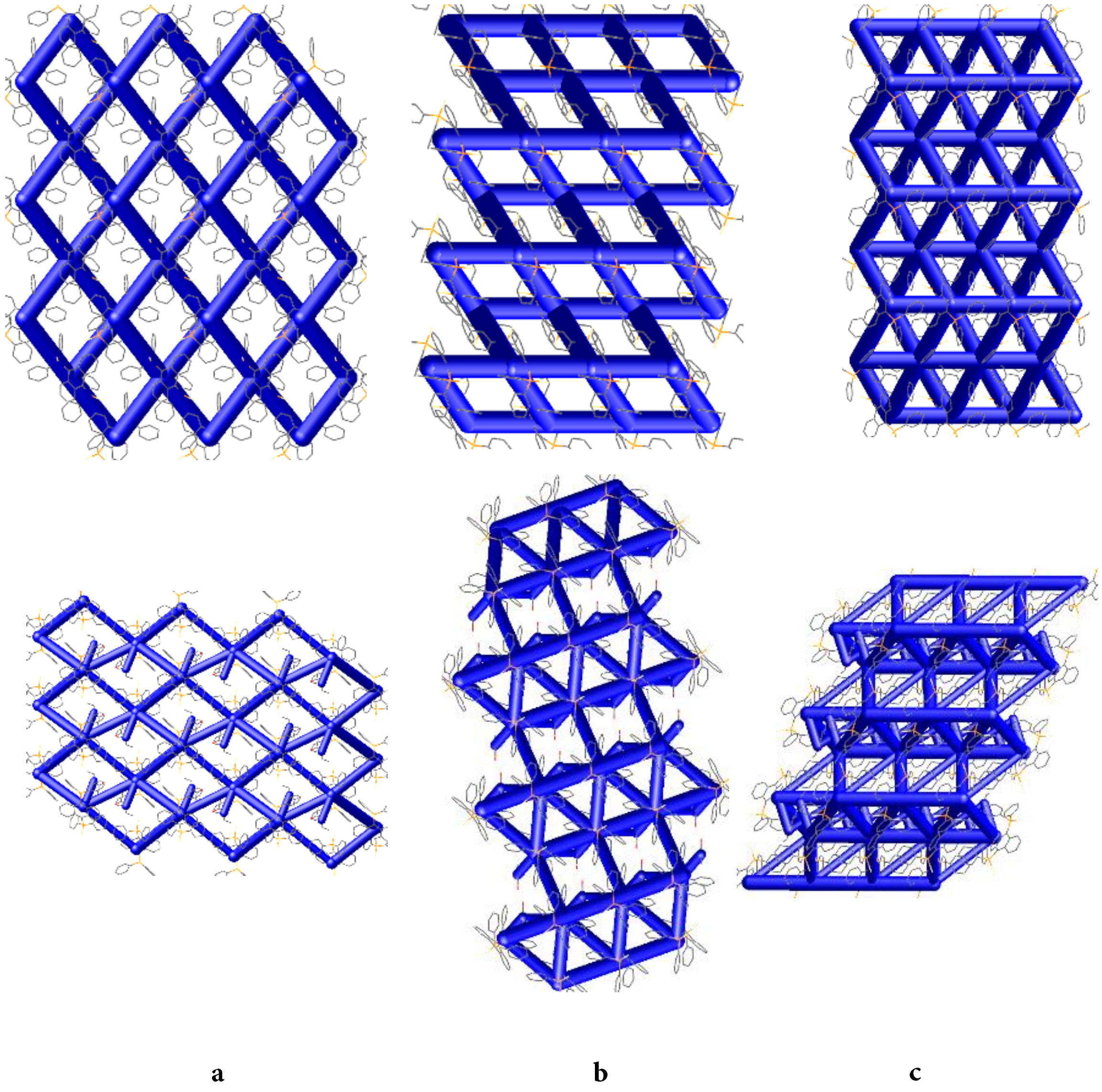

Figure 54

Energy framework for solvent free ($P2_1$, top) over the ethylacetate ($P\bar{1}$, bottom) along the crystallographic *a*, *b* and *c* axes. The tube size is set to 25, energy cut-off is set to 20 kJ/mol to clarify the view and highlight strong interactions.

moiety (Figure 53). The already mentioned preferred direction of the interaction, the face-to-face and back-to-back stacking, is intriguingly visualised by the colonnade motif. The specific interaction energies were already discussed in this chapter.

In contrast to the colonnade motif with one preferred direction of strong interaction, no such pronounced orientation is visible for the remaining *cis* co-crystals that do not crystallise in the $C2/m$ space group. Here, the framework shows a more even or isotropic distribution of pairwise interactions that reflects the considerations on the more balanced interaction energies. The systematic comparison of the remaining *cis* conformers reveals a remarkable similarity between the arrangement of the free compound ($P2_1$) and the ethylacetate co-crystal ($P\bar{1}$). The two compounds show a comparable energy framework, yet due to the guest inclusion the co-crystal gives a more distorted picture (Figure 54).

In the solvent free packing motif, a high degree of isotropy is visible leading to almost isoenergetic interactions to molecular partners of the first coordination shell. The direct orthogonal interactions are remarkably similar with the corresponding total energies of -47.0 kJ\mol, -49.1 kJ/mol and -49.3 kJ/mol, despite its large differences in coordination motifs (Figure 55). The two stronger interactions correspond to a lock-and-key motif that is essentially identical, the slightly weaker can be addressed to an offset on-top stacking motif with phenyl/anthracene being the corresponding interactions (indicated by a red line in Figure 55). With the intercalation of guest molecules, the symmetric picture changes slightly. Due to the inclusion, the fluorophores are forced apart, hereby weakening their interactions, yet, new anthracene/guest interactions are formed that compensate for the loss.

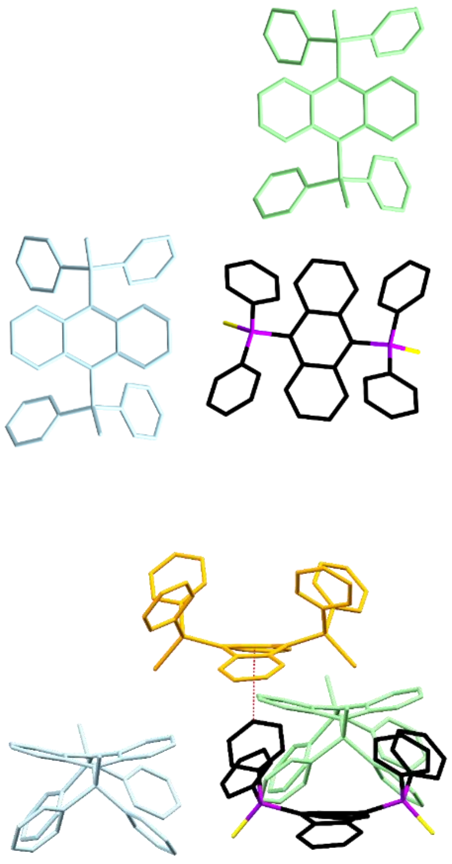

Figure 55
Stacking motif of the solvent free SPAnPS, top: two orthogonal interactions, in green: -49.3 kJ/mol and blue: -49.1 kJ/mol; bottom: on-top interaction depicted in orange: -47.0 kJ/mol.

However, this significant change in coordination motif does not seem to have an equally large impact on the corresponding energies. The new guest interaction is roughly between -11 kJ/mol and -20 kJ/mol with the corresponding anthracene/anthracene interaction being reduced to -25 to -35 kJ/mol, yielding in total a comparable total energy. The top stacked anthracenes interaction is reduced to -42.6 kJ/mol. This particular coordination motif interestingly stayed nearly untouched by the guest inclusion. The anthracene/anthracene interaction energy, albeit being significantly smaller compared to the $C2/m$ case, is again dominated by dispersion forces and sums up to -49.3 kJ/mol (free $P2_1$), -42.6 kJ/mol (ethylacetate, $P\bar{1}$), -42.2 kJ/mol (acetone, $P2_1/c$). The energies are quantitatively on a comparable scale and the reduction of the framework symmetry leads to a slight weakening of the anthracene/anthracene interaction. The same holds for the individual energetic contributions. A similar trend as with the toluene co-crystal can be seen for the *cis* conformer concerning the long range order in the crystals when comparing the solvent free ($P2_1$), the ethylacetate co-crystal ($P\bar{1}$) and the e.g. *cis* toluene ($C2/m$), despite them having different guests. The inclusion of the ethylacetate can be considered as an intermediate phase (Figure 56). In contrast to the toluene, phenylacetylene or benzyl alcohol guest molecules that lead to the crystallisation in the space group $C2/m$, ethylacetate is not found in the anthracene/phenyl cradle but in the periphery. On these positions (X and Y in Figure 56) the guest effectively prohibits the formation of the strong π-stacked interaction as found for $C2/m$. Here, the energy frameworks are able corroborate the picture of the unique flexibility of the SPAnPS moiety towards the inclusion of guest molecules.

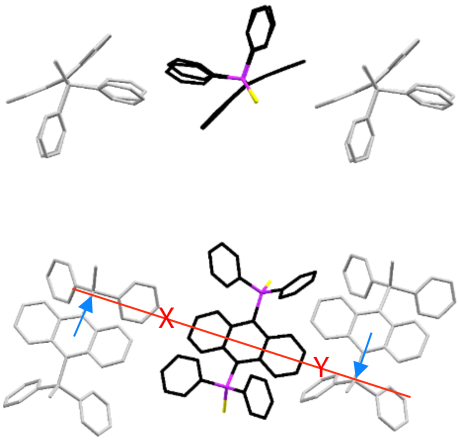

Figure 56
Top: side-view on the anthracene moiety highlighting the similarities between the $C2/m$ packing (see Figure 49 on page 87) and the $P\bar{1}$ ethylacetate. Bottom: possible re-arrangement (blue arrows, red line) to convert the ethylacetate $P\bar{1}$ molecular packing to the π-stacked motif similar to the *cis* co-crystals in $C2/m$.

The *trans* conformers show comparable results, there is a pronounced isotropicity in the three dimensional network, not showing any two dimensional layers or preferential directions (Figure 57). Despite the different orientation of the pillars, the two co-crystals show remarkable similarities. Along all three crystallographic axis, there is striking inter-structural recognition value, especially when considering the different space groups. These similarities underline the possible dynamics that lead to the formation of a wide variety of co-crystals. Along all three crystallographic axes, the higher symmetric *trans*-SPAnPS@toluene ($P2_1/n$) network shows unexpected similarities to the solvent free *cis*-SPAnPS ($P2_1$).

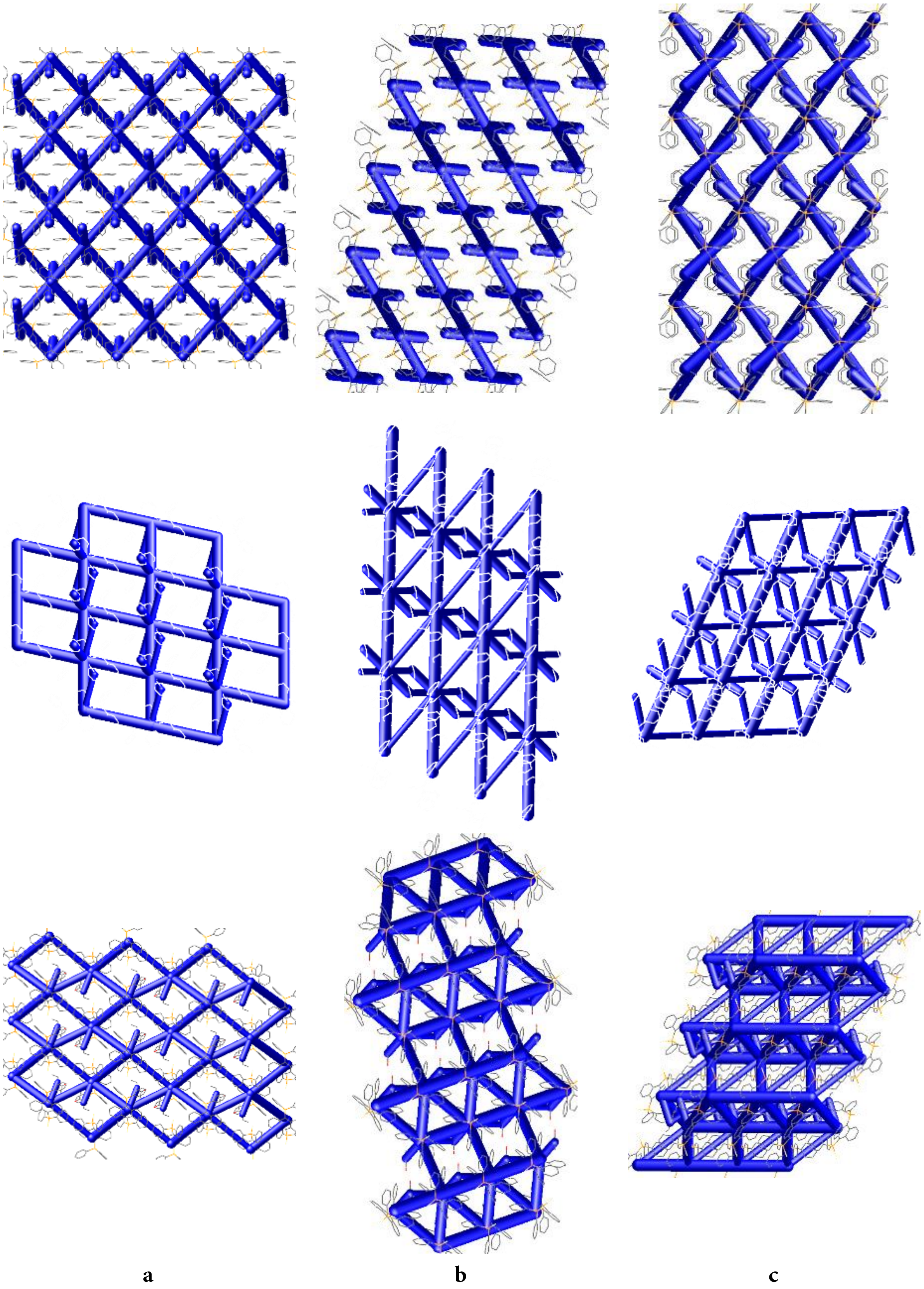

Figure 57
Energy frameworks depicted (columns) for *trans*-SPAnPS@toluene ($P2_1/n$, top), *trans*-SPAnPS@benzene ($P\bar{1}$, middle) and *cis*-SPAnPS@ethylacetate ($P\bar{1}$, bottom), view along the crystallographic (rows) *a* (left), *b* (center) and *c* (right) axis. The tube size is set to 25 (arbitrary units), energy cut-off is set to 20 kJ/mol to clarify the view and highlight strong interactions.

This is most pronounced along the the *a*-axis, yet along *b* and *c* the similarities in the zig-zag shape are visible. Energy frameworks impressively show that there is more to crystals than just the packing, emphasising on the dispersion forces to be the universal glue of organic matter (Dunitz & Gavezzotti, 2009). This sub chapter illustrates that intermolecular interactions are forming a particularly complex system. The framework analysis reveals that there is a three dimensional similarity between the polymorphs and co-crystals of SPAnPS that is not dependent on the molecular arrangement, space group symmetry or guest molecule inclusion.

In this chapter, it was initially discussed that the emerging dipole moment for the *cis* conformers might have an influence on the interaction framework and thereby be able to reveal preferential phonon directions. In a recent publication structure-property correlations were derived directly from the graphical representation of the energy framework, the finding of different melting points of isostructural polymorphs was addressed to the existence of specific strong interactions (Jha et al., 2016). In a similar fashion, it was anticipated that the frameworks could help in a potential matching of the packing motif to the elastic properties of the crystal structure. Unfortunately, there is no indication that would justify such an endeavour. Apart from revealing the striking similarities regarding the forces that keep the crystals packed, the frameworks were not able of drawing a clear picture towards the *cis*/*trans* solid-state fluorescence ambiguity. Nonetheless, the intra- and intermolecular interactions in crystalline systems may be considered to be the only possible interactions and it should be possible to reasonably postulate the source of a radiationless decay (Scott et al., 2004). A very recent publication concluded that the methodologies required to understand the underlying processes for complex systems are still in an immature stage (Shigemitsu et al., 2014). With modern ab initio quantum chemical methods the determination of a large set of properties with chemical accuracies is possible. Predictions of excited-state properties such as fluorescence are, however, challenging tasks. Reliable post-Hartree–Fock multi-configurational wave function approaches such as configuration interaction (CI) (Nakatsuji, 1997), coupled-clusters (CC), (Stanton & Bartlett, 1993) or the many-body perturbation program CAS-PT2 (Pulay, 2011) are computationally expensive and can hardly be applied directly to systems of reasonable size. The approach of time-dependent density functional theory (TD-DFT) is emerging as a promising alternative for the evaluation of excited-state geometries and properties. Results have been confirmed to be comparable to the more computationally demanding wavefunction-based methods (Gonzalez et al., 2012, Jacquemin et al., 2010). Here, the finite cluster ONIOM (Chiba et al., 2007) approach might be able to shed light on the relevance of particular intermolecular interactions on fluorescence properties, by monitoring fragment–fragment interactions at varying cluster sizes (Shigemitsu et al., 2014). In this recent publication, intermolecular dimer interactions were analysed by means of time dependent density functional theory that revealed their significance on the fluorescence emission spectra. The authors were able to confirm intermolecular hydrogen bonds to induce bathochromic shifts whereas chromophore stacking interactions induce blue shifts (Shigemitsu et al., 2014). Recent developments were able to shed light on underlying mechanisms of AIE (Hong et al., 2011, Hu et al., 2014), however, none of which is directly applicable to the herein studied co-crystalline compounds.

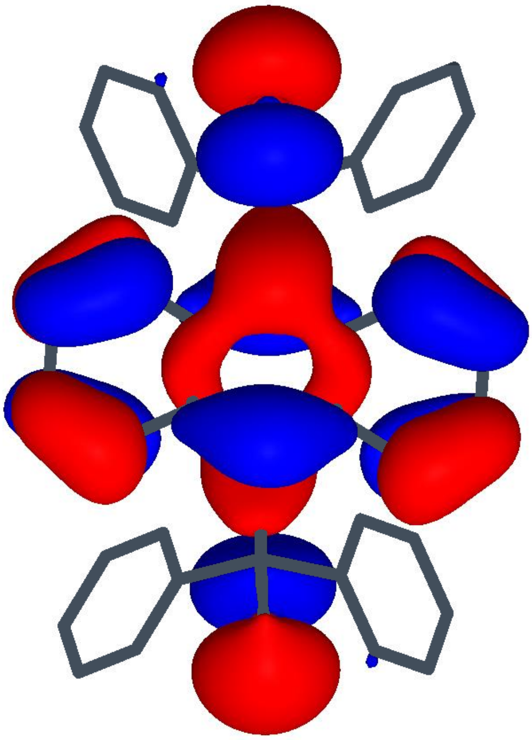

Figure 58
HOMO of the trans-SPAnPS@toluene ($P2_1/n$) co-crystal.

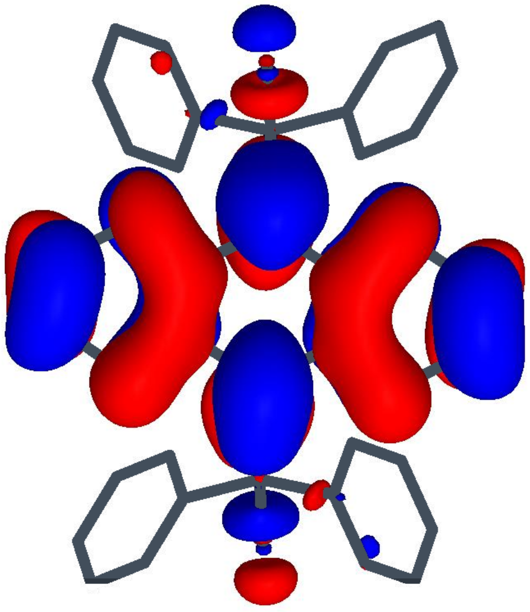

Figure 59
LUMO of the trans-SPAnPS@toluene ($P2_1/n$) co-crystal.

7.5.2 HOMO/LUMO considerations

One interesting property that needs to be addressed in the *cis* orientation of the diphenylthiophosphoryle groups is related to geometrical considerations. Up to the time of writing this thesis, there is no symmetrically substituted anthracene derivative exhibiting the *cis* conformation that shows solid-state fluorescence at room temperature. An explanation to this might be in the symmetry of the molecules, especially the symmetry of the highest occupied molecular orbital (HOMO) and the lowest unoccupied molecular orbital (LUMO).

The probability of absorption or emission of a photon depends on the nature of the wavefunction of the initial and final state. The transition probability is commonly described by the transition strength (Kitai, 1993). To a first approximation, the transition strength is determined by selection rules that define whether a transition is allowed or not allowed. More strictly speaking if the overlap of the two functions can be non-zero. The most satisfactory and complete quantum mechanical description is based on time-dependent wave mechanics; here the transition from the ground state G to another excited state E is described by the transition dipole moment μ_{GE}. The transition dipole moment is proportional to the transition probability (given as $|\mu_{GE}|^2$) and it will be non-zero whenever the symmetry of the ground state is different from the excited state. We anticipated already that the anthracene moiety is probably responsible for the photon absorption and it will therefore play a role in the HOMO - LUMO (corresponding to the π – π* transition) transition geometry. In all *trans* oriented polymorphs, whether $P\bar{1}$ or $P2_1/n$, the HOMO manifests almost identical and centrosymmetrical (Figure 58). The LUMO (Figure 59), on the other hand, shows more of a mirror symmetry that is clearly non-centrosymmetric (Figure 59).

For processes involving one photon the direct product of the participating symmetries must contain the totally symmetric representation (Quina, 1982).

The selection rule for symmetry allowed processes in centrosymmetric molecules is therefore *u* ↔ *g*, e.g. a change of parity must occur. Upon absorption of a photon, the transition from the HOMO to the LUMO should therefore follow a symmetry allowed process.

In contrast, the *cis* conformers (Figure 60 and Figure 61) cannot show a centrosymmetric geometry of the HOMO. However, the anthracene moiety might be considered as quasi-centrosymmetric, albeit being slightly deformed and of course leaving the sulfur contribution unconsidered. A recent publication found strong deviations from the parity selection rule for an investigated nominally non-centrosymmetrical molecule that exhibited properties that were expected only for symmetrical systems (Makarov et al., 2013). They found the π-conjugation structure, which is mostly responsible for optical electronic transitions, remains in the quasi-symmetrical system.

If the π-system of the *cis*-SPAnPS structures can as well be considered quasi-centrosymmetric, the transition from the distorted HOMO to the LUMO (mirror symmetric, *g*) might therefore be less likely due to a smaller orbital overlap. Of course, these are only crude considerations, yet, the findings are intriguing and serve well as explanation on why the *cis* configuration, in contrast to the *trans* arrangement, does not show strong solid-state fluorescence regardless of space group, molecular arrangement, guest inclusion or packing. However, these findings only hold for the herein studied compounds and its polymorphs/co-crystals. Moreover, this cannot explain why *all* conformers show fluorescence upon cooling. Temperature dependent absorption and emission spectra might help to further elucidate this experimental finding and clarify if different mechanisms take place in the cold phase, as this should give rise to a significant shift in either the absorption or the emission spectra.

The finding that all *cis* oriented compounds inherently show a significant bending of the anthracene

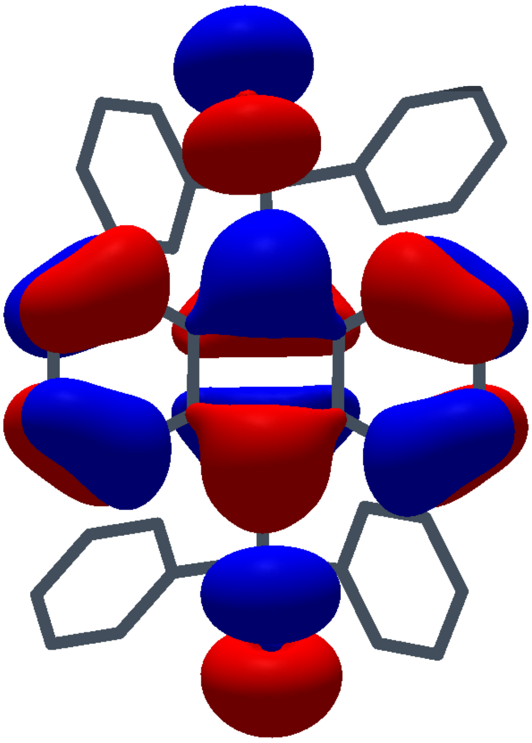

Figure 60
HOMO of the solvent free *cis*-SPAnPS ($P2_1$) polymorph.

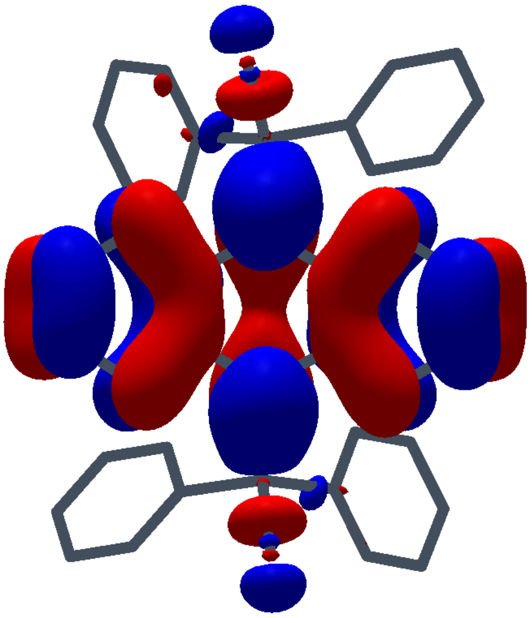

Figure 61
LUMO of the solvent free *cis*-SPAnPS ($P2_1$) polymorph.

moiety, contrasted by the twisted *trans* geometry facilitates further ideas. An appealing explanation for the temperature dependence might be found in a more flexible bend geometry that gives rise to radiationless pathways through vibronic coupling upon excitation. This pathway might not be realisable in the more rigid twisted *trans* geometry or at low temperatures. Here, UV/vis spectra might give valuable insights as the proposed vibrational relaxation should show to distinct absorption bands.

Thus, the conclusion is made that a rationale could be suggested for the long ongoing question about the nature of the solid-state fluorescence. It is, however, more a process of constant exclusion than a straightforward answer and might merely be disproven by the occurrence of a strong fluorescing symmetrically substituted *cis* conformer.

7.6 An experimental protocol towards the comparability of fluorescence intensities

To take full benefit of the ideas developed herein, reliable relative fluorescence emission intensities of the co-crystals are crucially needed. Especially, to make way for further investigations elucidating the processes that lead to the observed fluorescence quenching or enhancement in related systems. Addressing the comparability between the fluorescence emission intensity, herein a protocol for data acquisition was developed and applied preliminarily in collaboration with T. Schillmöller. The solid-state structure of a selection of handpicked single crystals of sizes between 0.04 mm^3 and 0.35 mm^3 is determined by means of X-ray diffraction. The specimen size is chosen to a) be manageable without a microscope, b) show detectable fluorescence and c) yield reasonable diffraction data. Regarding the diffraction experiment, it proved to be sufficient (for *trans*-SPAnPS@benzene, $P\bar{1}$) to collect three subsequent runs with the ϕ angle incremented by 60° in the an ω scan mode (scan width: 50°, ω increment: 0.5°, detector distance: 50 mm and exposure time: 0.25 s per frame at room temperature) to collect data that was successfully integrated (*SAINT*), scaled (*SADABS*) and solved (*SHELXT*). In future investigations, it might prove sufficient to further cut down the measurement time and to collect data sufficient for unit cell determinations. It has to be emphasised that the X-ray data collection is not only used to as weight determination but to unambiguously identify the polymorph. Subsequently, the crystals faces were indexed within the *APEX3* software to get an accurate measure for the crystal size. In combination with the crystal density (experimental, from diffraction) the exact weight can be determined. The crystal was placed on top of the quartz glass that is used to seal the sample chamber. The fluorescence measurements were performed with a Horiba Jobin-Yvon Fluoromax-4 spectrometer equipped with a 150 W xenon arc lamp and a Czerny-Turner excitation monochromator (Lakowicz, 2006). Emission was detected

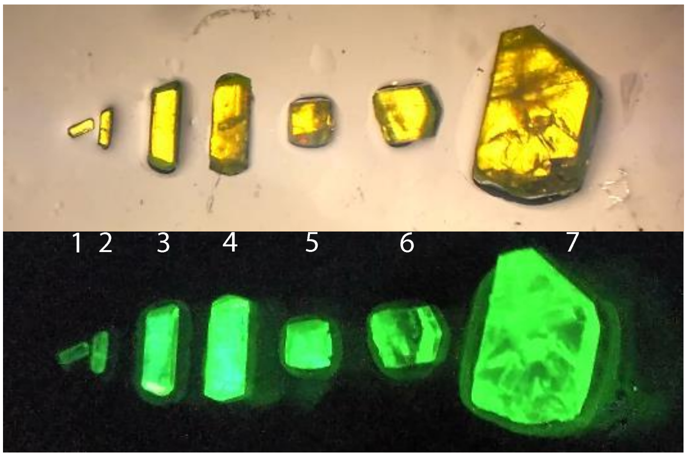

Figure 62
Test crystals of *trans*-SPAnPS@benzene, only the specimen 1, 2, 3 and 5 were suitable for single crystal X-ray determinations.

by a photomultiplier in a perpendicular experimental setup. The data was processed with the *FluorEssence* Software (Horiba, 2008).

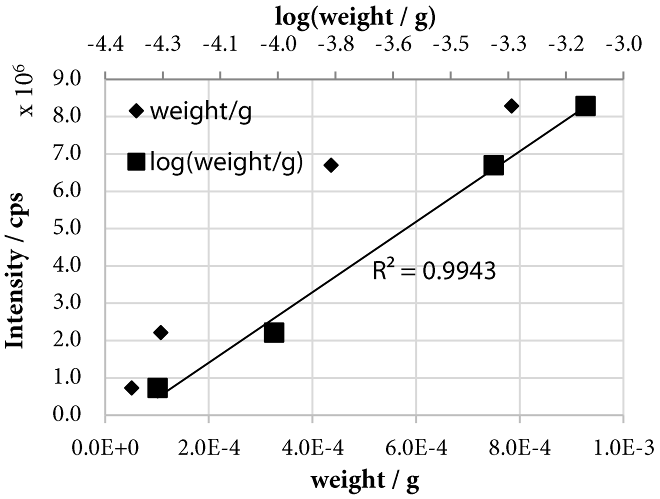

Figure 63
Course of the fluorescence intensity with varying crystal size.

In future experiments, it might turn out to be appropriate to use even smaller specimen and to mount the crystal using a microscope. Following this protocol, the first results obtained suggest that there is an intensity dependence of the specimen size. Figure 63 shows the expected exponential course of a plot of the crystal weight against the fluorescence intensity, similar to the concentration quenching in the liquid-state. Future investigations are needed in order to increase the reliability and to define an operability range by finding optimal crystal sizes (Figure 62). The first tests using *trans*-SPAnPS@benzene clearly demonstrate at least one drawback. The crystals showed anisotropic luminescence (appendix A7.5), complicating the sample alignment. Yet, the procedure can easily be extended to investigations regarding fluorescence quantum yields using an integrating sphere. Here, the diffusion effect achieved by multiple scattering minimises the impact of the wave guiding effect and should allow for highly accurate quantum yield determinations.

Table 30
Properties of the probed crystals. Experimental density (from diffraction): 1.244 g/cm^{-3}, vol: volume, w: weight.

	size [mm]			vol [cm^{-3}]	w [g]	log(w/g)	cps
1	0.20	0.30	0.68	4.08E-5	5.08E-5	-4.29	72690
2	0.26	0.38	0.87	8.60E-5	1.07E-4	-3.97	221430
3	0.44	0.72	1.99	6.30E-4	7.84E-4	-3.11	828800
5	0.50	0.70	1.00	3.50E-4	4.35E-4	-3.36	670020

CHAPTER 8:

SUMMARY AND OUTLOOK

8 Summary and outlook

In the current thesis, the focus was on single crystal X-ray diffraction data quality, the assessment of systematic errors, investigations of experimental charge density distributions, and solid-state fluorescence phenomena. New aspects were discussed and individual solutions were successfully developed and applied to experimental data. The results and possible implications for subsequent investigations will be briefly reiterated in the following chapter.

In the beginning chapters, emphasis was on single crystal X-ray diffraction data quality with a specialised focus on the influence of systematic errors such as absorption of the crystal sample (Chapter 3), low-energy contamination during the shaping of the X-ray beam (Chapter 4), and limitations in the detection of diffracted photons (Chapter 5).

The beneficial influence of Ag $K\alpha$ radiation on systematic errors caused by absorption was thoroughly corroborated by means of investigations on a variety of different compounds. Here, the remarkable performance of the empirical multi-scan absorption correction was verified even for strongly absorbing samples and the importance of the angular dependent term $Q(\mu \cdot r, 2\theta)$ was validated. A beneficial perspective is given to the experimentalist that it is advisable always to collect a full sphere of data in order to maximise the performance of the empirical multi-scan method. For strongly absorbing specimen, where only small crystals are to be probed, the underlying assumptions that the crystal is completely bathed in a uniform X-ray beam was found to be not valid for highly focused X-ray optics. Hereby, the performance of the numerical correction is strongly weakened.

In chapter 4, two different correction routines were established using the python scripting language. One route is specifically designed for the use with the Bruker program *SADABS*. Here, the degree of contamination is estimated by linear regression and the resulting factor can be used to correct the data empirically. A second presented route exploits a specific refinement algorithm in *SHELXL* to determine the level of contamination. The process of correction factor determination is directly incorporated into the least-squares minimisation procedure. Hereby, an estimate for the reliability of the correction is available as well. A straightforward solution following a *default value for a given system* approach was as well reasonably validated. The benefit to the model quality of the application of the correction routine was successfully demonstrated for a large number of chemically inequivalent compounds.

The subsequent chapter 5 emphasised on the importance of accurately measured data and investigated the performance and suitability of two detectors following different underlying detection techniques. The studied detectors, the Dectris Pilatus3 R CdTe 300K and the Bruker PHOTON II, were shown to be able to yield single crystal X-ray data that is well suited for charge density determinations and on-par data quality.

Chapter 6 emphasised on the fact that even though one hundred years since the very first X-ray diffraction experiments were performed, the fundamental technique is inherently flawed with regard to the reliability of a derived model. In the course of this thesis, the concept of cross-validation was successfully transferred and adopted to the field of charge density investigations. Moreover, the herein developed *python* script takes full benefit of the newly arising possibilities. The visualisation of presumed overfitting at different stages of the refinement is of great assistance towards the validity of a charge density model. Intriguing plots that globally indicate overfitting are available and are automatically generated. Moreover, intuitive measures for the reliability of individual charge density model parameters are presented. Finally, a complete picture for the consistency of the modelled density at given stages of the refinement can be represented three dimensionally that is able to highlight problematic regions. Hereby, the assessment of properties and the verification of estimated standard deviations become feasible. A lower limit for the reliability of hitherto unavailable standard deviations for particular properties can be given as well. The suggested cross-validation protocol is able to yield resilient charge density models and hereby lead to more accurately determined properties.

The last chapter 7 is embarking on the primary goal to find a rationale for the solid-state fluorescence of *trans*-SPAnPS co-crystals and polymorphs. Herein, a variety of orthogonal strategies is combined in order to shed light on the complex mechanisms that take place in the solid. The investigation comprised of single crystal as well as powder X-ray diffraction, neutron diffraction, solid-state NMR techniques, computational chemistry using different levels of theory and the analysis of a combined X-ray/neutron model describing the experimental charge density distribution.

An explanation for the aggregation-induced emission evident from experimental investigations of the SPAnPS system was proposed. Completely new co-crystals were found, successfully investigated and possible ways for phase transitions were given. Here, calculations were able to identify kinetic and thermodynamic co-crystals that are in good agreement with experimental observations during the crystal formation. Intermolecular interaction energies as well as complete packing arrangements were evaluated using the recently emerged energy frameworks. These frameworks were of great help on the way to an understanding of the fluorescence of the studied SPAnPS co-crystals. Moreover, the results show promising characteristics that might turn out beneficial regarding investigations of the electronic or mechanic properties of other compounds. This type of three dimensional molecular packing and intermolecular contact analysis provides a qualitative measure for the structure-property correlations; however, herein it was not possible to derive a clear picture. In the last part, the proposed protocol for the acquisition of comparable fluorescence emission intensities can help regarding comparability and reliability. A rationale for the solid-state fluorescence behaviour of the investigated SPAnPS compounds was suggested in the rigidity of the anthracene system and the symmetry of the frontier orbitals that is in good agreement with experimental observations. However, the results are not able to draw the complete picture of the complex mechanisms of the solid-state fluorescence emission. A possible radiationless pathway opened by the bend conformation found in the *cis* oriented anthracene compounds is still to be examined. Here, UV/vis spectra might yield reasonable insights. Yet, the complementary methods used throughout this chapter can serve as new basis for future investigations.

CHAPTER 9:

EXPERIMENTAL: NEUTRON COUPLED CHARGE DENSITY INVESTIGATION

9 Neutron coupled charge density investigation of *trans*-SPAnPS@toluene ($P2_1/n$)

The refinement of multipole models is considered as an advanced and matured technique (Stalke, 2016, Gatti & Macchi, 2012), therefore details are kept rather short, focussing on the important and non-standard difficulties. The high resolution data was collected on a Bruker TXS rotating anode in late 2007 and was of excellent quality. At first, the data was reprocessed with the latest program versions of *SAINT* and *SADABS*. For the integration process, following the standard protocol turned out to yield acceptable results. The high angle and low angle data were integrated separately, however, jointly processed in *SADABS*. In contrast to routine structure determinations, the error model was determined using fixed values $K = 1.0$ and $g = 0.0$, this is explained with the weighting of data with $\sigma(I)$ usually used as weighting factor. The IAM is incapable of describing the bonding density, yet exactly that information is found in the strong low order reflections that have a large $I/\sigma(I)$. It is therefore advisable to decrease the influence of those reflections during the refinement, e.g. by assigning an error model (*SADABS*). On the other hand, in charge density investigations the low-order information is precisely what is modelled and should therefore not get a lower weight during the refinement. Unfortunately, this comes at the price of strong deviations from unity in the resolution and intensity dependent χ^2 distributions and is due to stronger systematic errors in the low-order data.

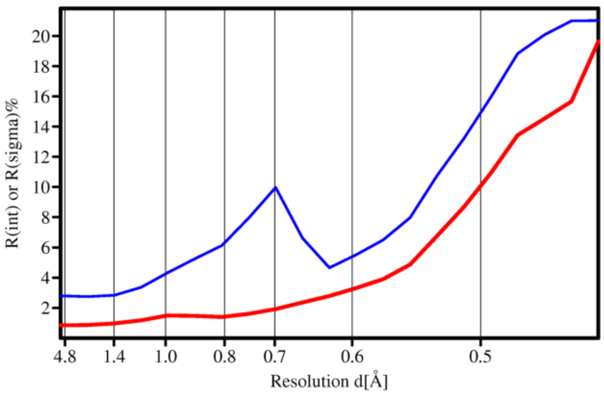

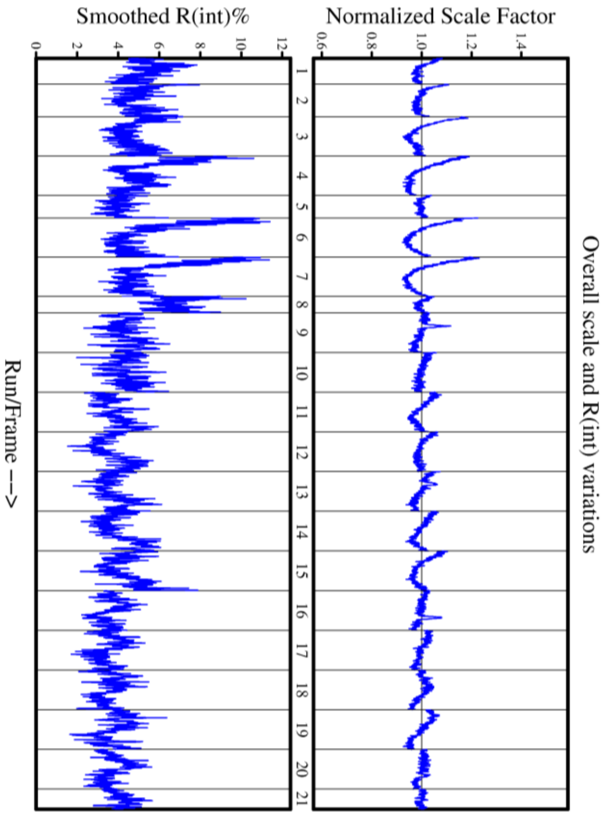

Figure 64
Left: Course of the R_{int} (blue line) and R_{sigma} (red line) against the resolution. Right: Variation of the R_{int} and the scale factor with the frame number.

The effects of a contamination with low energy photons were reliably minimised following the empirical approach as described in chapter 4 by using a correction factor $k_{3\lambda}$ of 0.002. Figure 64 shows the results of the inter-frame scaling and data correction (*SADABS*) and final data quality indicators (*XPREP*). While the initial data for this compounds was already collected in 2007, this structural investigation came back into focus with the open question regarding the SPAnPS system and the availability of beam time at the Spallation Neutron Source (SNS) of the Oakridge National Laboratory

(ORNL) and the collection of neutron data on *trans*-SPAnPS@toluene. Neutron data is crucial in order to investigate the C – H ··· π interactions sensibly that are relevant to this system.

'There is no possibility of deriving hydrogen vibrational parameters from the X-ray intensities' (Hirshfeld, 1976). As discussed in a previous chapter that this, albeit being an absolutely correct statement, is only of limited value since it turned out to be possible to find sensible parameters that indirectly model that motion. Moreover, the motion is in good qualitative agreement with semi-empirically determined motions estimated from combined approaches using rigid-body TLS fitting and transferable experimental neutron data. Hydrogen atoms show low scattering power and intense thermal motion. An insufficient modelling of their displacement parameters manifests in unreliable parameters describing the respective density. Conversely, no reasonable estimate of the charge transfer can be obtained. The electro-neutrality constraint, however, coupled with these uncertainties is most likely seriously affecting the resulting properties. To overcome this limitation, single-crystal neutron diffraction data on SPAnPS@toluene were collected at 100 K on a block shaped crystal with the dimension 1.4 · 0.9 · 0.8 cm on the single-crystal time-of-flight Laue diffractometer TOPAZ at the SNS. Integration was carried out on-site using *Mantid* (Arnold et al., 2014, Schultz et al., 2014, Jørgensen et al., 2014) and incident beam as well as detector efficiency corrections were performed with *ANVRED* (Schultz et al., 1984). The structure was successfully solved by *SHELXT* (Sheldrick, 2015a). Severe extinction was observed caused by the large crystal specimen. Accordingly, a full anisotropic extinction correction was carried out using *GSAS* (Toby, 2001). The hydrogen ADPs used in the multipole refinement were scaled based on a least-squares fit of the U_{ij} between the non-hydrogen atoms of the X-ray model and the hydrogen atoms derived from neutron data using the program *UIJXN* (Blessing, 1995b). The carbon/hydrogen atom distances were set according to the model derived from the neutron data using the *RESET BOND* command.

The multipole modelling was performed against F^2 and the convergence criterion was chosen as $1 \cdot 10^{-6}$, meaning that the maximum shift of any parameter divided by its

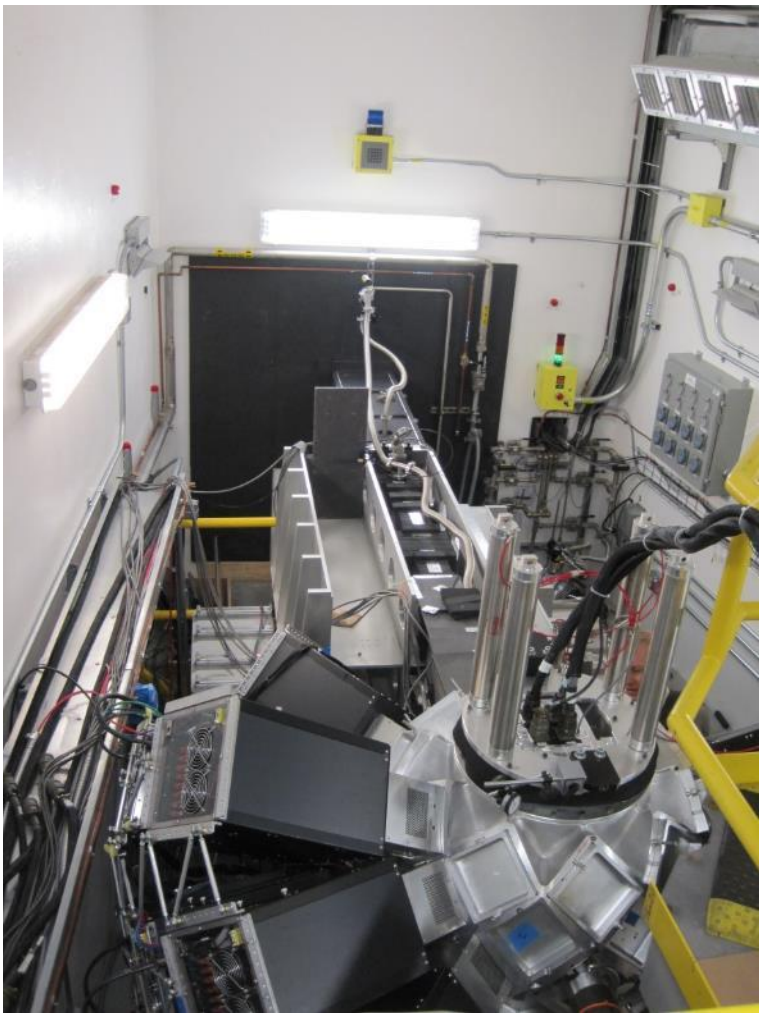

Figure 65
View along the neutron beam path onto the crystal chamber and the attached detectors (black boxes).

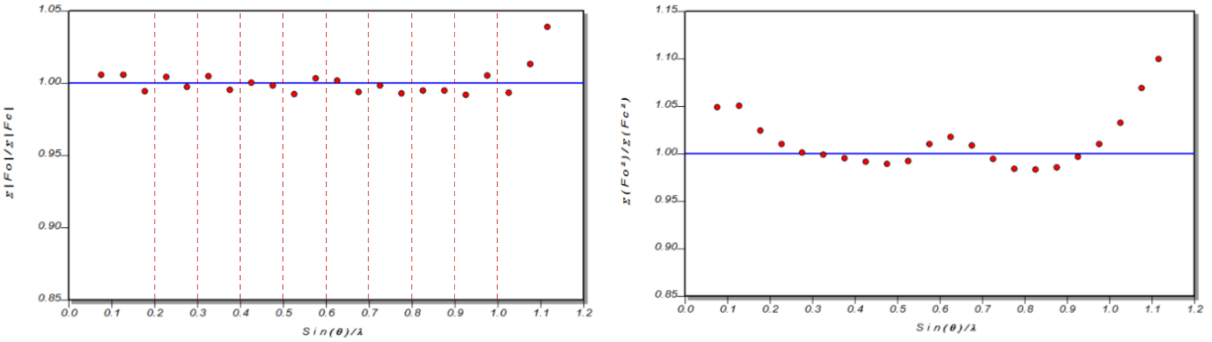

Figure 66
Variation of $\sum F_o^2 / \sum F_c^2$ with respect to the resolution. Left shows the distribution using ten resolution dependent scale factors, right shows the results with one scale factor.

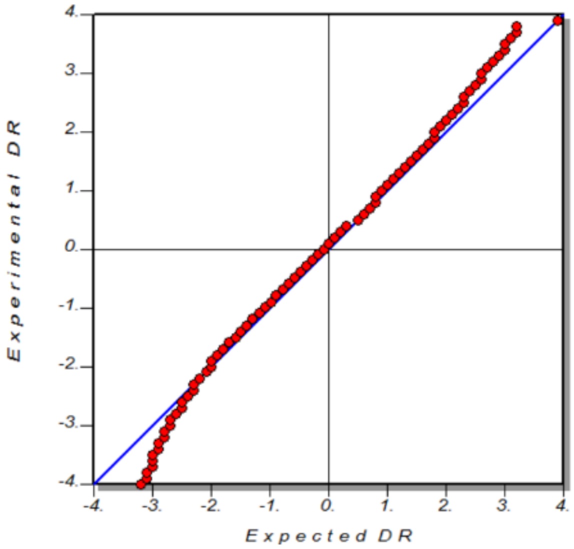

Figure 67
Final normal probability plot, weighting scheme: a = 0. 0152, b = 0.0151.

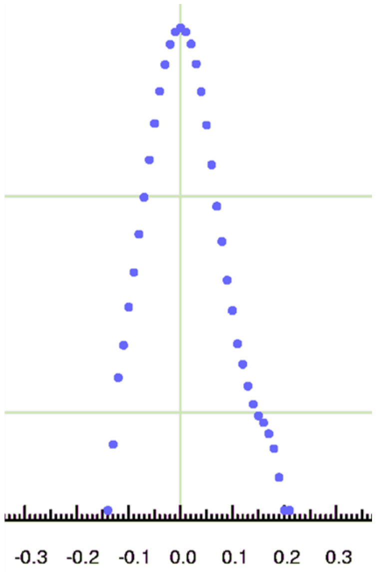

Figure 68
Final fractal dimension plot, showing a flat and almost featureless residual density.

esd must not exceed this value to indicate convergence. In the refinement all data was used that showed positive intensities ($I/\sigma(I) > 0$).

The first refinements showed severe resolution dependence of the data/model agreement, visible in the structure factor plot (Figure 66). It did, however, not exactly follow the distinct *alphorn* shape (see appendix A7.7) that was recently explained by resolution dependent systematic errors such as thermal diffuse scattering (Niepötter et al., 2015).

The refinement with only one scale factor or against empirically corrected data lead to unreasonable net charges for sulfur and phosphorus of -0.105(43), -1.468(110) for one scale factor and -0.110(38), -1.739(97) for the empirically corrected data, respectively. The ten scale factor refinement on the other hand yielded charges of -0.279(32) for sulfur and -0.098(62) for phosphorus, that are in better agreement with chemical expectation. The empirical correction did not seem to cure for this error and the model was refined using ten resolution-dependent scale factors instead. Herein, the normal probability plot is used as a measure for the applied weighting scheme and a satisfactory weighting could be obtained. The final values were found to be 0.01 and 0.01 for the parameters *a* and *b*, respectively. This weighting was as well able to produce a reasonable GooF of 0.9789.

During the refinement, the two heavier elements were problematic and showed severe residual density. The question was to either loosen the constrained symmetry or to introduce Gram-

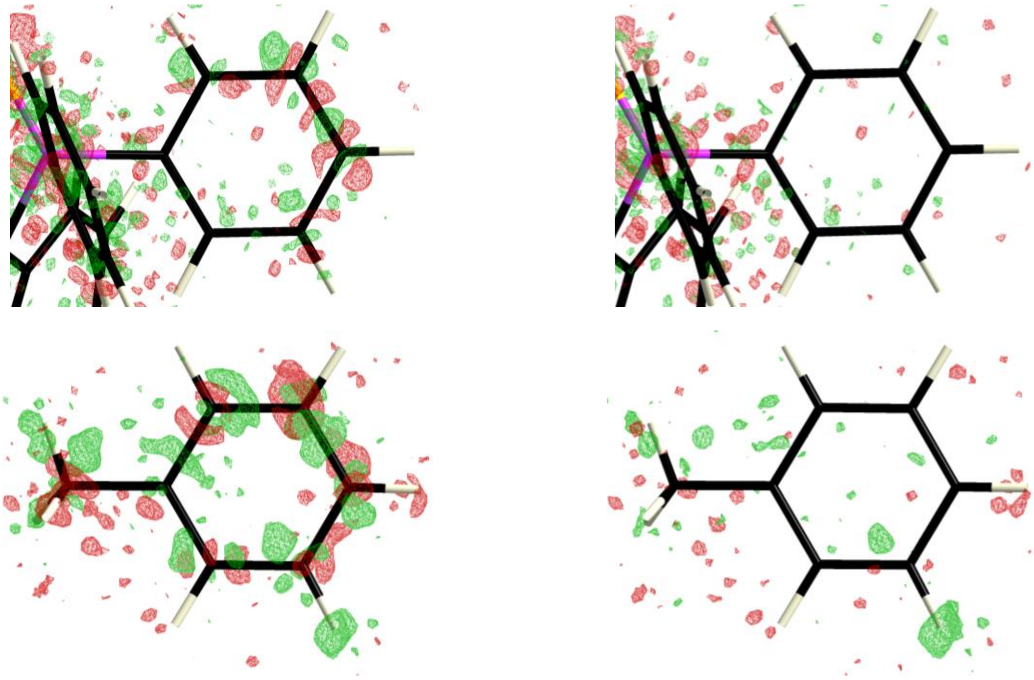

Figure 69
Comparison of the residual density for the phenyl group (top) and the toluene molecule (bottom). Without anharmonic description (left) and with 3rd order Gram-Charlier parameters (right). Map level: 0.09 eÅ^{-3}.

Charlier parameters, as this was the final solution for the structurally similar SPAnH charge density refinement (Herbst-Irmer et al., 2013).

In the course of the investigation, it was found that only the 3rd and 4th order of anharmonic description add the model flexibility needed to sensibly adjust to the data. The sulfur atom needed the 4th order anharmonic description, whereas the phosphorus and the concerned carbon atoms could be restricted to the 3rd order. Additionally, the meta and para carbon atoms of the peripheral phenyl groups showed pronounced signs for anharmonic motion (Figure 69). The toluene is sitting in a pocket, cradled by sulfur and phenyl moieties. This imposes considerable constraints on the degrees of freedom. Hence, the toluene is performing some slight rotary motion, however, not significant enough to be modelled as disorder (Figure 70). The anchor of that motion seems to be C22, forcing C20 into a banana-shape motion. Unfortunately, it was not possible to find a satisfying description apart from allowing the whole toluene fragment to move in an anharmonic fashion, which added 70 parameters to the refinement. More details regarding the validity of the applied model e.g. Kuhs (1992) rule can

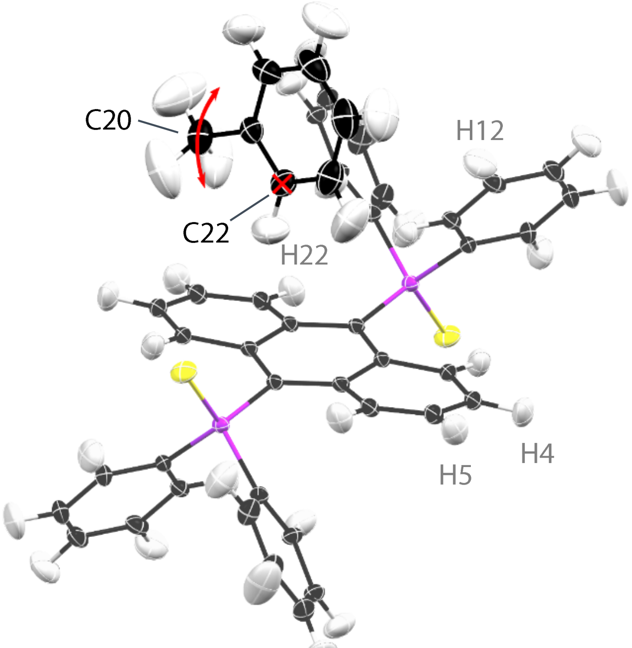

Figure 70
Rotary motion of the toluene guest fragment in the sulfur – phenyl cradle.

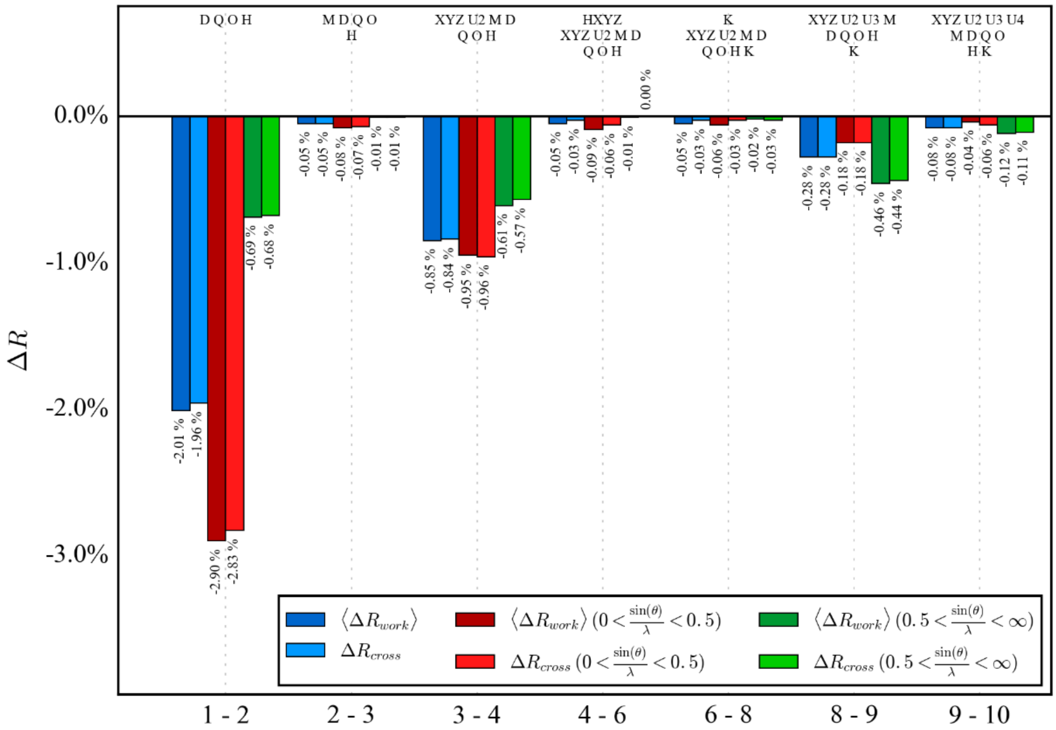

Figure 71

Stepwise progress of the mean R_{work} and R_{cross} showing the overall (blue) and the results calculated against truncated data, here, the low order in red and high order in green.

be found in the appendix (A7.8 and A7.9). It turned out to be utterly necessary to model the toluene completely constrained. The local symmetry is fixed assuming two-fold axis and two mirror planes (*mm*2) for the aromatic carbon atoms and a three-fold symmetry for the methyl carbon atom. The two atoms in *ortho* position and the set of three atoms in meta and para position form two chemically constrained groups.

Loosening of the symmetry constraints brought up severe signs of overfitting. Moreover, the parameter distribution did show severe outliers for a large number of pole parameters. This suggests that the allowance of anharmonic motion is the better description, since the corresponding parameters did not produce any outliers. In contrast, all parameters were well situated within the suggested least-squares estimated standard deviation. The progression of the R_{cross} is depicted in Figure 71. The individual impact of the parameters on the high/low R_{cross} is in good agreement with the considerations discussed in chapter 6 . The introduction of mono- and multipoles in step 2 and 3 shows significant benefit for low resolution data, whereas 3rd and 4th order anharmonic motion influences the high resolution data most. The only problematic step is the transition from 6 to 8, where the radial screening parameter κ is introduced and refined for all non-hydrogen atoms. Following this refinement protocol, it was possible to find a satisfying compromise between model reliability and flexibility. The *XDParPlot* routine from the *XDRfree* script showed not a single parameter exceeding the suggested standard deviation after the final refinement step.

CHAPTER 10:

CRYSTAL STRUCTURE DETERMINATIONS

10 Crystal Structure determinations

Crystal screening and selection was performed on a movable table equipped with a Schlenk line using a polarisation microscope and the X-Temp2 crystal cooling device (Stalke, 1998, Kottke & Stalke, 1993) for temperature sensitive specimen. Air and moisture sensitive samples were taken directly out of the Schlenk flask; crystal manipulation was performed in a drop of perfluorinated polyether oil. The selected crystals were mounted either on the tip of a glass fibre or a MiTeGen Kryoloop. Data collection were carried out on Bruker APEX II Ultra or Quazar diffractometers equipped with Bruker TXS Mo *K*α, Incoatec IµS Mo *Kα* or Incoatec IµS Ag *K*α. All three diffractometers used mirror optics as beam shaping devices. The Bruker *APEX2* (Bruker, 2014a) suite was used for data collection strategy determination according to the crystal symmetry. In the course of data processing, the data reduction was performed using *SAINT* (Bruker, 2013), correction and scaling was done with *SADABS* (Krause et al., 2015)and subsequent structure solution was carried out by *SHELXT* (Sheldrick, 2015a). *SHELXL* (Sheldrick, 2015b) was used within the *SHELXle* GUI (Hübschle et al., 2011) to perform the full-matrix least-squares refinement of the model structures.

10.1 *cis*-SPAnPS@EtOAc ($P\bar{1}$)

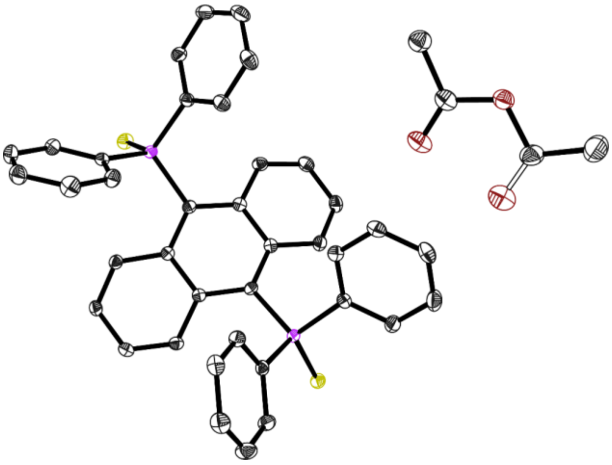

Structure code	cis_SPAnPS_EtOAc_final		$\rho_{calc.}$ [g cm^{-3}]	1.310
Empirical Formula	$C_{42}H_{36}O_2P_2S_2$		μ [mm^{-1}]	0.277
Formula weight [g mol^{-1}]	698.77		F(000)	732
Sample temperature [K]	100(2)		θ range [°]	1.198 to 27.476
Wavelength [Å]	0.71073		Reflections collected	68551
Crystal System	Triclinic		Unique Reflections	7908
Space group	$P\bar{1}$		R_{int} / R_σ	0.0382 / 0.0179
	a = 8.757(2)	α =82.24(2)°	Completeness to θ_{max} [%]	100.0
Unit cell dimensions [Å]	b = 12.628(2)	β = 78.21(2)°	restraints/parameter	721 / 445
	c = 17.413(3)	γ =70.49(3)°	GooF	1.060
Volume [Å^3]	1772.1(7)		*R*1 (all data)	0.0331
Z	2		w*R*2 (all data)	0.0845
Crystal dimensions [mm]	0.12 · 0.10 · 0.09		max. diff. peak / hole [Å^{-3}]	0.468 / 0.300

Currently unpublished results.

10.2 *cis*-SPAnPS@Toluene (*C*2/*m*)

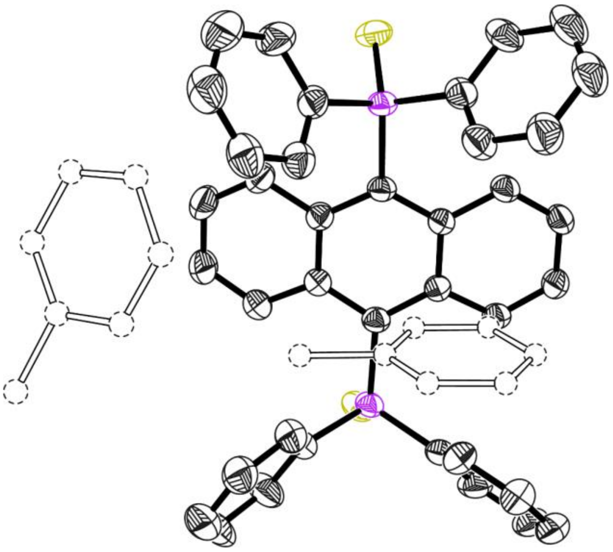

Structure code	exp2454		$\rho_{calc.}$ [g cm^{-3}]	1.286
Empirical Formula	$C_{97}H_{80}P_4S_4$		μ [mm^{-1}]	0.255
Formula weight [g mol^{-1}]	1497.73		F(000)	1572
Sample temperature [K]	293(2) K		θ range [°]	1.660 to 26.812°
Wavelength [Å]	0.71073		Reflections collected	6864
Crystal System	Monoclinic		Unique Reflections	4063
Space group	*C*2/*m*		R_{int} / R_σ	0.0342 / 0.0492
	a = 13.927(3)		Completeness to θ_{max} [%]	99.1
Unit cell dimensions [Å]	b = 24.538(5)	β = 119.69(3)°	restraints/parameter	422 / 274
	c = 13.031(3)		GooF	1.023
Volume [Å^3]	3868.5(17)		R1 (all data)	0.0842
Z	2		wR2 (all data)	0.1978
Crystal dimensions [mm]	0.09 · 0.09 · 0.08		max. diff. peak / hole [Å^{-3}]	0.758 / 0.559

Data measured at the University of Warwick by A-C. Pöppler. This is the first measurement performed on this particular structural motif. Unpublished results.

10.3 *trans*-SPAnPS@Toluene ($P\bar{1}$)

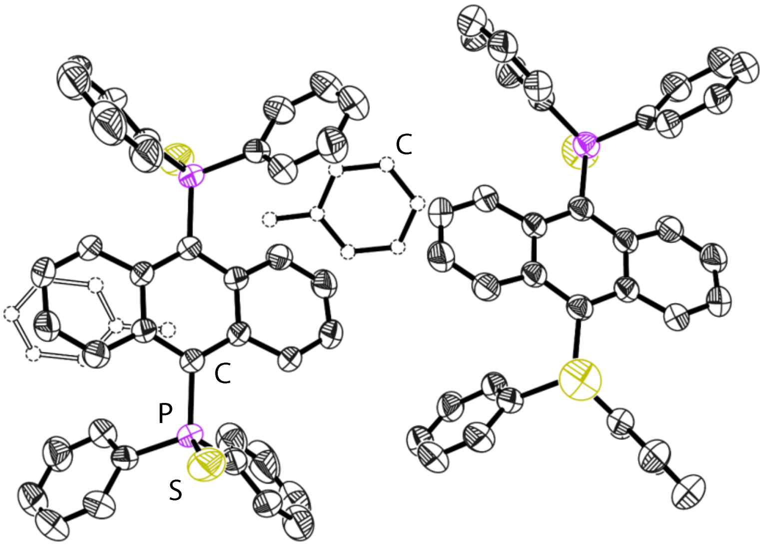

Structure code	trans_spanps_tol_p-1		$\rho_{\text{calc.}}$ [g cm^{-3}]	1.236
Empirical Formula	C48.50 H40 P2 S2		μ [mm^{-1}]	0.245
Formula weight [g mol^{-1}]	748.86		F(000)	786
Sample temperature [K]	293(2)		θ range [°]	1.587 to 26.227
Wavelength [Å]	0.71073		Reflections collected	13583
Crystal System	Triclinic		Unique Reflections	7832
Space group	$P\bar{1}$		R_{int} / R_{σ}	0.0290 / 0.0410
	a = 9.440(2)	α = 70.39(3)°	Completeness to θ_{max} [%]	99.7
Unit cell dimensions [Å]	b = 13.643(3)	β = 88.07(3)°	restraints/parameter	748 / 446
	c = 16.614(3)	γ = 86.47(3)°	GooF	1.076
Volume [Å^3]	2011.6(8)		R1 (all data)	0.0855
Z	2		wR2 (all data)	0.2162
Crystal dimensions [mm]	0.10 · 0.09 · 0.07		max. diff. peak / hole [Å^{-3}]	0.892 / -0.365

A-C. Pöppler measured this data at the University of Warwick. Currently unpublished results.

10.4 Collaboration with Ramachandran Azhakar (Roesky group)

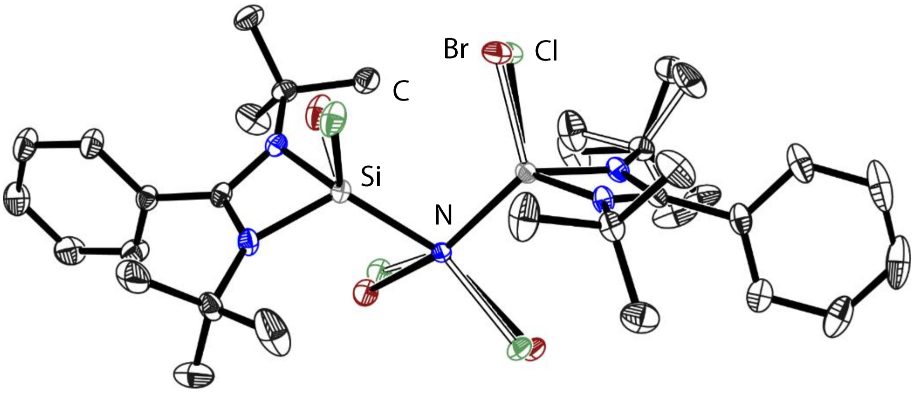

Structure code	p21n_final		$\rho_{calc.}$ [g cm^{-3}]	1.461
Empirical Formula	$C_{30}H_{46}Br_2Cl_2CoN_4Si_2$		μ [mm^{-1}]	1.530
Formula weight [g mol^{-1}]	808.54		F(000)	1652
Sample temperature [K]	100(2)		θ range [°]	1.54 to 25.27
Wavelength [Å]	0.56086		Reflections collected	92551
Crystal System	monoclinic		Unique Reflections	13567
Space group	*P*2$_1$/*n*		R_{int} / R_σ	0.0474 / 0.0308
	a = 18.568(3)		Completeness to θ_{max} [%]	99.7
Unit cell dimensions [Å]	*b* = 9.504(2)	β = 102.95(2)	restraints/parameter	79 / 420
	c = 21.378(3)		GooF	1.047
Volume [Å^3]	3676.6(11)		R1 (all data)	0.0374
Z	4		wR2 (all data)	0.0614
Crystal dimensions [mm]	0.11 · 0.10 · 0.10		max. diff. peak / hole [Å^{-3}]	0.477 / -0.311

Published: Ramachandran Azhakar, Rajendra S. Ghadwal, Herbert W. Roesky, Jakob Hey, Lennard Krause, Dietmar Stalke '*Mixed Valence η^6–Arene Cobalt(I) and Cobalt(II) Complex*' *Dalton Trans.* **2013**, *42*, 10277-10281.

10.5 Collaboration with Sudipta Roy (Roesky group)

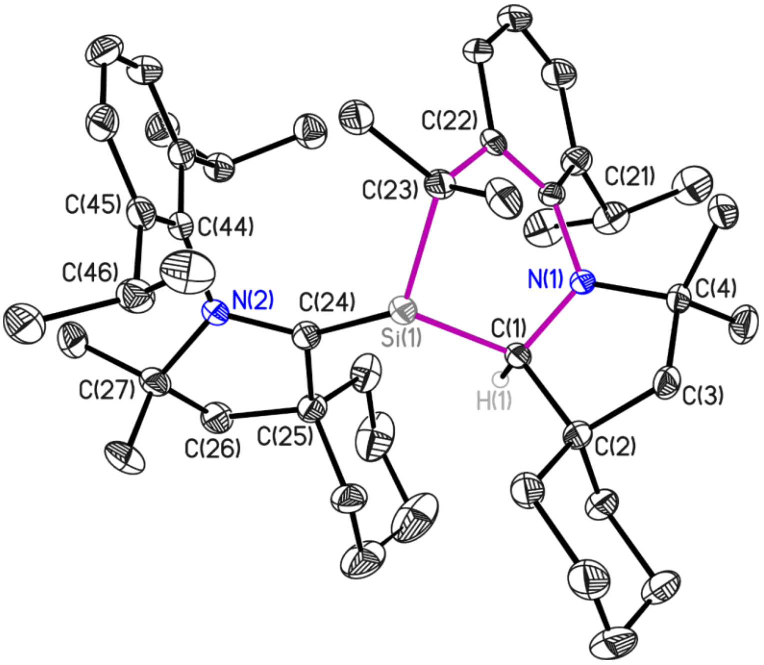

Structure code	P21n_b		$\rho_{calc.}$ [g cm^{-3}]	1.130
Empirical Formula	$C_{40}H_{62}N_2Si$		μ [mm^{-1}]	0.096
Formula weight [g mol^{-1}]	599.00		F(000)	1320
Sample temperature [K]	100(2)		θ range [°]	1.507 to 26.505
Wavelength [Å]	0.71073		Reflections collected	59445
Crystal System	monoclinic		Unique Reflections	7255
Space group	$P2_1/n$		R_{int} / R_σ	0.0857 / 0.0618
	a = 9.273(2)		Completeness to θ_{max} [%]	99.4
Unit cell dimensions [Å]	b = 16.959(2)	β = 90.75(2)	restraints/parameter	0 / 408
	c = 22.383(3)		GooF	1.036
Volume [Å^3]	3519.7(10)		R1 (all data)	0.0908
Z	4		wR2 (all data)	0.1235
Crystal dimensions [mm]	0.04 · 0.10 · 0.12		max. diff. peak / hole [Å^{-3}]	0.294 / -0.328

Published: Sudipta Roy, Kartik Chandra Mondal, Lennard Krause, Peter Stollberg, Regine Herbst-Irmer, Dietmar Stalke, Jann Meyer, A. Claudia Stückl, Bholanath Maity, Debasis Koley, Suresh Kumar Vasa, Sheng Qi Xiang, Rasmus Linser, Herbert W. Roesky '*Electron-Induced Conversion of Silylones to Six-Membered Cyclic Silylenes*' *J. Am. Chem. Soc.* **2014**, *136*, 16776-16779; featured in a Spotlights on Recent *JACS* Publications by Xin Su in *J. Am. Chem. Soc.* **2014**, *136*, 16698-16699.

10.6 Collaboration with Marina Frank (Clever group)

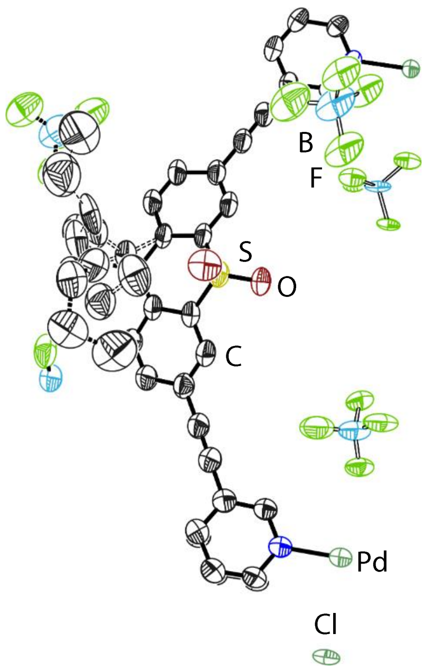

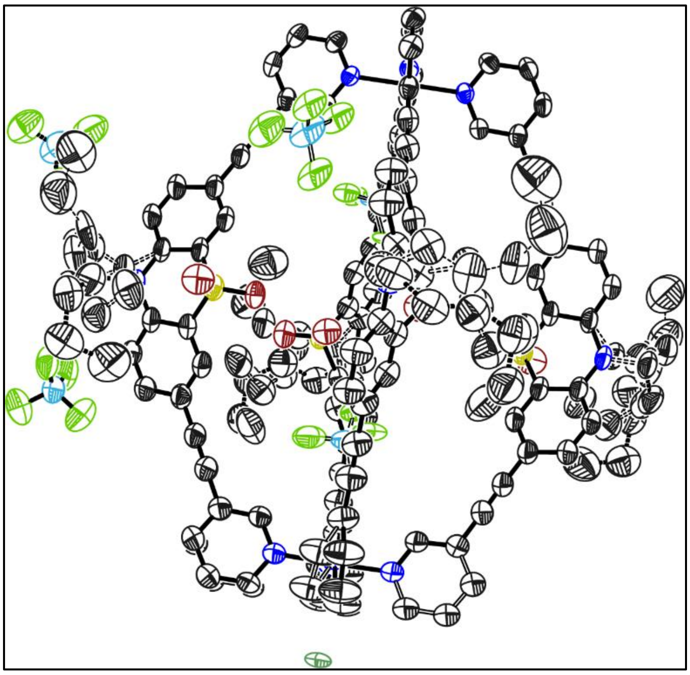

Structure code	final	$\rho_{\mathrm{calc.}}$ [g cm^{-3}]	1.125
Empirical Formula	$C_{64}H_{54}B_{1.75}Cl_{0.25}F_7N_6O_4PdS_2$	μ [mm^{-1}]	0.363
Formula weight [g mol^{-1}]	1302.43	F(000)	5328
Sample temperature [K]	100(2)	θ range [°]	1.126 to 23.837
Wavelength [Å]	0.71073	Reflections collected	166252
Crystal System	tetragonal	Unique Reflections	5937
Space group	*P*4/*nnc*	R_{int} / R_{σ}	0.0583 / 0.0198
	a = 21.991(2)	Completeness to $\theta_{\max}$ [%]	100.0
Unit cell dimensions [Å]	*c* = 31.800(3)	restraints/parameter	1149 / 682
		GooF	1.060
Volume [Å^3]	15379(3)	R1 (all data)	0.1051
Z	8	wR2 (all data)	0.3031
Crystal dimensions [mm]	0.06 · 0.08 · 0.09	max. diff. peak / hole [Å^{-3}]	1.434 / -0.655

Published: Marina Frank, Lennard Krause, Regine Herbst-Irmer, Dietmar Stalke, Guido H. Clever '*Narcissistic self-sorting vs. statistic ligand shuffling within a series of phenothiazine-based coordination cages*' *Dalton Trans.* **2014**, *43*, 4587-4592.

10.7 Collaboration with Muxin Han (Clever group)

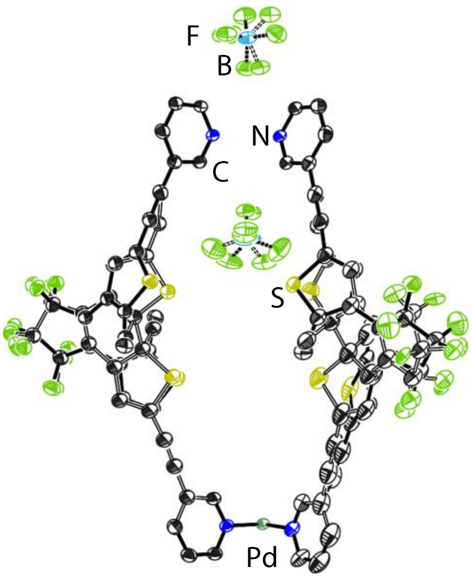

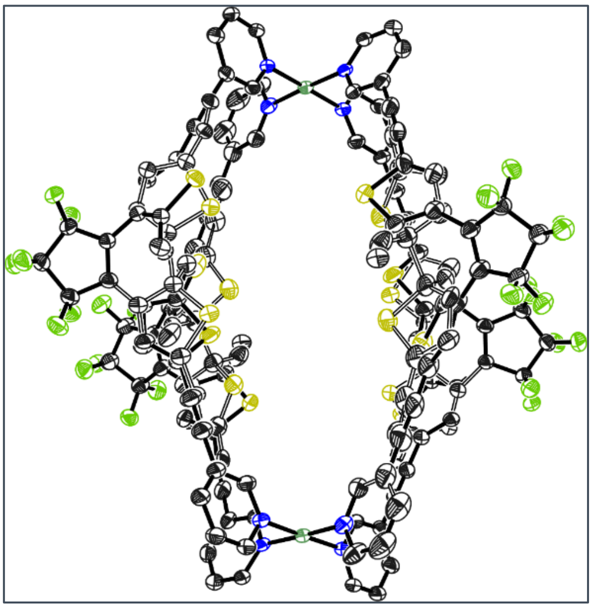

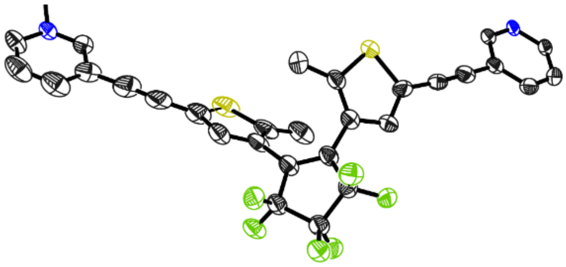

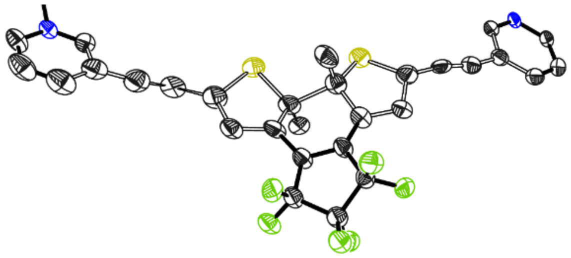

The dichlorobenzene solvent molecules and the boron-tetrafluoride counter ions are omitted for clarity, all counter ions were successfully found in the difference density map. The open:close conformation ratio for the two symmetry independent ligand systems is 95:5 and 65:35, respectively.

Structure code	P-1		$\rho_{calc.}$ [g cm^{-3}]	1.532
Empirical Formula	$C_{100}H_{60}B_2Cl_{14}F_{20}N_4PdS_4$		μ [mm^{-1}]	0.689
Formula weight [g mol^{-1}]	2450.08		F(000)	2452
Sample temperature [K]	100(2)		θ range [°]	1.177 to 26.417
Wavelength [Å]	0.71073		Reflections collected	124148
Crystal System	Triclinic		Unique Reflections	21687
Space group	$P\bar{1}$		R_{int} / R_{σ}	0.0503 / 0.0411
	a = 17.307(1)	α = 116.88(1)°	Completeness to θ_{max} [%]	100.0
Unit cell dimensions [Å]	b = 18.398(2)	β = 90.02(2)°	restraints/parameter	7999 / 2455
	c = 18.707(2)	γ = 91.82(2)°	GooF	1.038
Volume [Å^3]	5309.6(10)		R1 (all data)	0.1109
Z	2		wR2 (all data)	0.2548
Crystal dimensions [mm]	0.11 · 0.10 · 0.09		max. diff. peak / hole [Å^{-3}]	2.712 / -0.886

Currently unpublished results.

10.8 Collaboration with Susanne Löffler (Clever group)

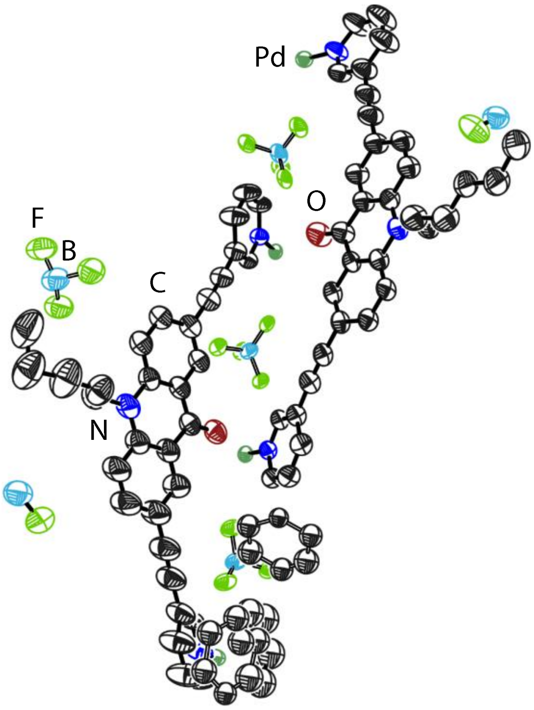

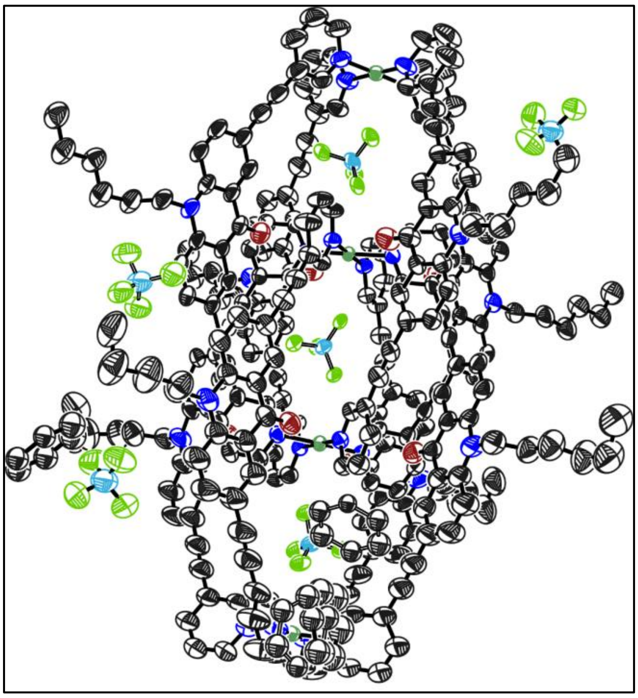

Structure code	AFIX66	$\rho_{calc.}$ [g cm^{-3}]	1.251
Empirical Formula	$C_{354}H_{306}B_8F_{32}N_{24}O_8Pd_4$	μ [mm^{-1}]	0.164
Formula weight [g mol^{-1}]	6144.29	F(000)	6348
Sample temperature [K]	100(2)	θ range [°]	1.136 to 18.161
Wavelength [Å]	0.56086	Reflections collected	143666
Crystal System	tetragonal	Unique Reflections	11745
Space group	*P*4/*n*	R_{int} / R_σ	0.0932 / 0.0479
	a = 22.065(4)	Completeness to θ_{max} [%]	99.9
Unit cell dimensions [Å]	c = 33.491(5)	restraints/parameter	2106 / 1042
		GooF	1.052
Volume [Å^3]	16306(6)	R1 (all data)	0.1559
Z	2	wR2 (all data)	0.3066
Crystal dimensions [mm]	0.09 · 0.10 · 0.12	max. diff. peak / hole [Å^{-3}]	3.220 / -1.070

Published: Susanne Löffler, Jens Lübben, Lennard Krause, Dietmar Stalke, Birger Dittrich, Guido H. Clever '*Triggered Exchange of Anionic for Neutral Guests inside a Cationic Coordination Cage*' *J. Am. Chem. Soc.* **2015**, *137*, 1060-1063.

10.9 Collaboration with Thorben Schulte (Clever group)

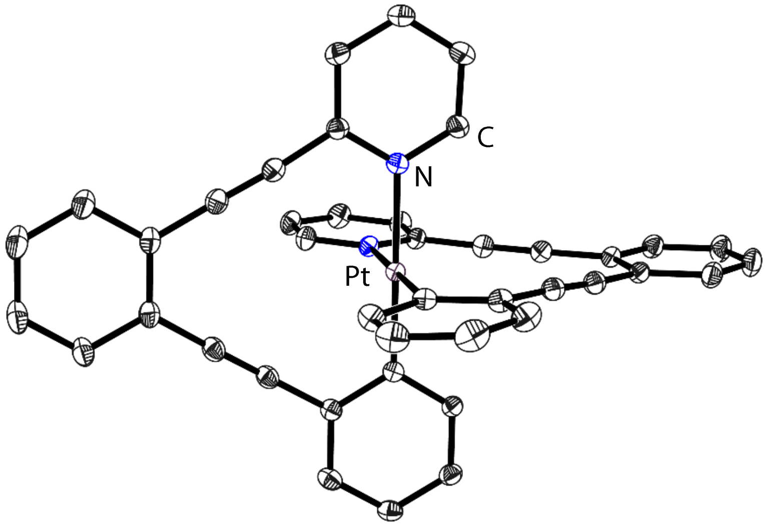

Structure code	P21c_a		$\rho_{calc.}$ [g cm^{-3}]	1.647
Empirical Formula	$C_{42}H_{24}N_2Pt$		μ [mm^{-1}]	4.663
Formula weight [g mol^{-1}]	751.72		F(000)	1472
Sample temperature [K]	100(2)		θ range [°]	1.173 to 36.350
Wavelength [Å]	0.71073		Reflections collected	114524
Crystal System	Monoclinic		Unique Reflections	14542
Space group	$P2_1/c$		R_{int} / R_{σ}	0.0240 / 0.0133
Unit cell dimensions [Å]	a = 17.4922(9)		Completeness to θ_{max} [%]	100.0
	b = 9.2490(5)	β = 97.1260(13)°	restraints/parameter	0 / 406
	c = 18.8813(9)		GooF	1.053
Volume [Å^3]	3031.1(3)		R1 (all data)	0.0204
Z	4		wR2 (all data)	0.0440
Crystal dimensions [mm]	0.122·0.115·0.104		max. diff. peak / hole [Å^{-3}]	1.952 / -0.723

Unpublished results.

10.10 Collaboration with Mavis Montero

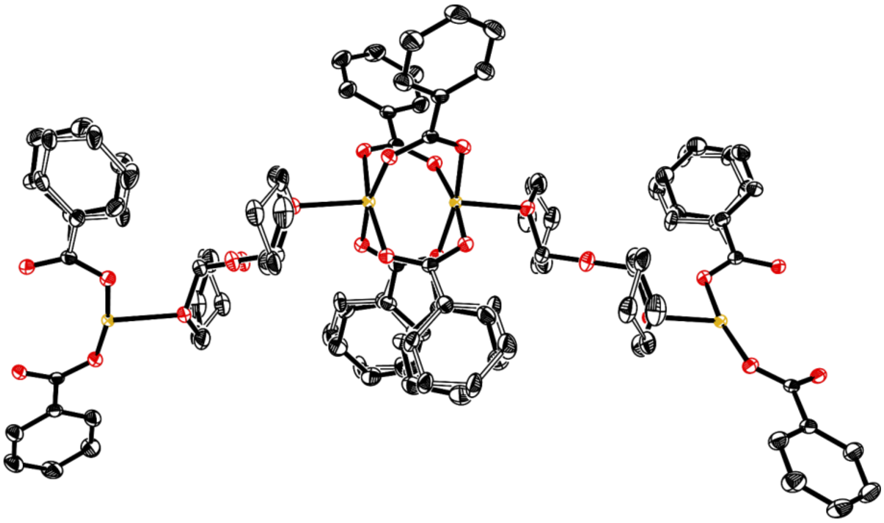

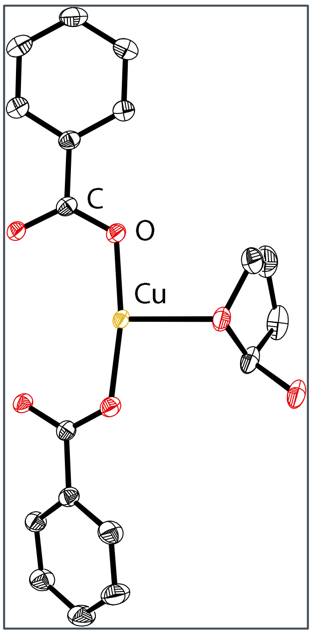

Structure code	final		ρcalc. [g cm-3]	1.538
Empirical Formula	$C_{18}H_{17}CuO_6$		µ [mm-1]	1.318
Formula weight [g mol-1]	392.86		F(000)	1616
Sample temperature [K]	100(2)		θ range [°]	2.143 to 28.426
Wavelength [Å]	0.71073		Reflections collected	29203
Crystal System	Monoclinic		Unique Reflections	4282
Space group	*C*2/*c*		Rint / Rσ	0.0278 / 0.0181
	a = 9.794(2)		Completeness to θ_{max} [%]	100
Unit cell dimensions [Å]	*b* = 19.006(3)	*β* = 94.80(2)°	restraints/parameter	650 / 309
	c = 18.299(2)		GooF	1.033
Volume [Å3]	3394.3(10)		R1 (all data)	0.0332
Z	8		wR2 (all data)	0.0660
Crystal dimensions [mm]	0.120·0.100·0.050		max. diff. peak/hole [eÅ^{-3}]	0.356/-0.294

Unpublished results.

10.11 Collaboration with Markus Scheibel (Schneider group)

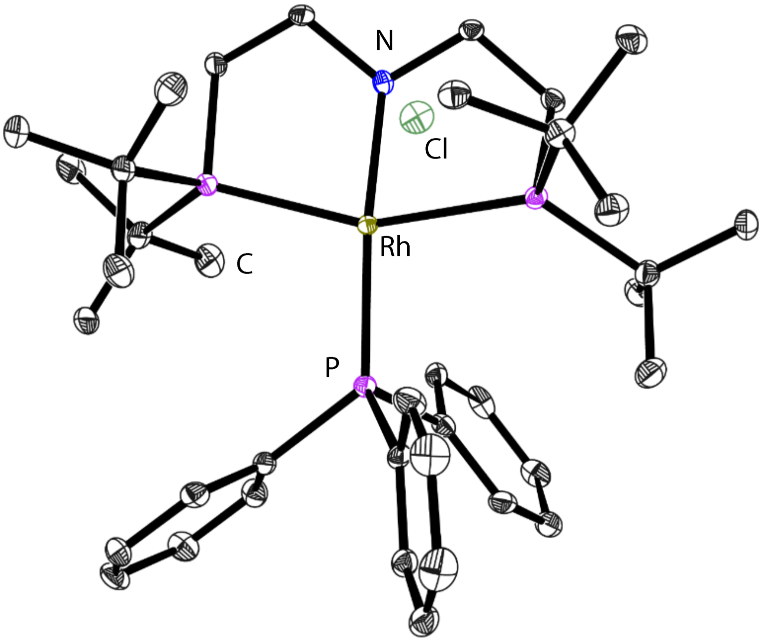

Structure code	p2c_a		$\rho_{calc.}$ [g cm^{-3}]	1.325
Empirical Formula	$C_{38}H_{60}ClNP_3Rh$		μ [mm^{-1}]	0.355
Formula weight [g mol^{-1}]	762.14		F(000)	804
Sample temperature [K]	100(2)		θ range [°]	0.866 to 20.582
Wavelength [Å]	0.56086		Reflections collected	?
Crystal System	triclinic		Unique Reflections	7656
Space group	$P\bar{1}$		R_{int} / R_σ	? / 0.0770
Unit cell dimensions [Å]	a = 10.1464(10)	α = 77.982(10)	Completeness to θ_{max} [%]	98.5
	b = 10.4691(10)	β = 81.91(2)	restraints/parameter	0 / 414
	c = 19.064(2)	γ = 75.721(10)	GooF	1.051
Volume [Å^3]	1911.0(4)		R1 (all data)	0.0676
Z	2		wR2 (all data)	0.0992
Crystal dimensions [mm]	0.05·0.06·0.10		max. diff. peak / hole [Å^{-3}]	0.732 / -0.466

Published: Markus Scheibel, Yanlin Wu, A. Claudia Stückl, Lennard Krause, Elena Carl, Dietmar Stalke, Bas de Bruin, Sven Schneider '*Synthesis and Reactivity of a terminal Nitrido Complex of Rhodium*' *J. Am. Chem. Soc.* **2013**, *135*, 17719-17722.

10.12 Collaboration with Yanlin Wu (Schneider group)

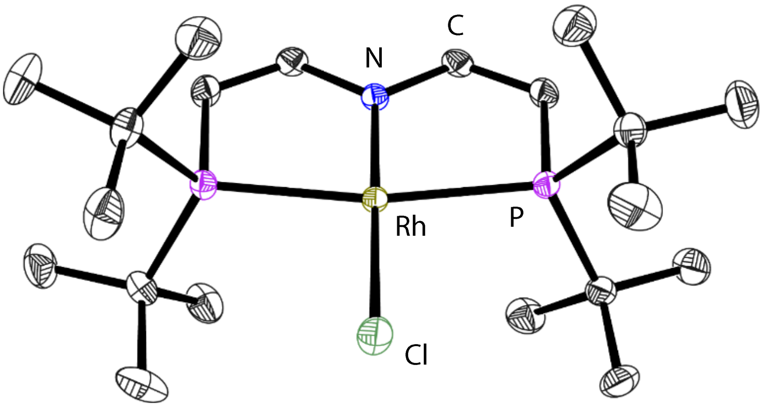

Structure code	p2c_a		$\rho_{calc.}$ [g cm^{-3}]	1.364
Empirical Formula	$C_{20}H_{40}ClNP_2Rh$		μ [mm^{-1}]	0.957
Formula weight [g mol^{-1}]	494.83		F(000)	518
Sample temperature [K]	100(2)		θ range [°]	1.936 to 30.520
Wavelength [Å]	0.71073		Reflections collected	33444
Crystal System	monoclinic		Unique Reflections	3683
Space group	*P*2/*c*		R_{int} / R_σ	0.0267 / 0.0141
	a = 11.452(2)		Completeness to θ_{max} [%]	99.8
Unit cell dimensions [Å]	*b* = 8.527(2)	β = 113.31(2)	restraints/parameter	0 / 122
	c = 13.432(3)		GooF	1.085
Volume [Å^3]	1204.6(5)		R1 (all data)	0.0202
Z	2		wR2 (all data)	0.0481
Crystal dimensions [mm]	0.02 · 0.07 · 0.09		max. diff. peak / hole [Å^{-3}]	0.685 / -0.205

Published: Markus Scheibel, Yanlin Wu, A. Claudia Stückl, Lennard Krause, Elena Carl, Dietmar Stalke, Bas de Bruin, Sven Schneider '*Synthesis and Reactivity of a terminal Nitrido Complex of Rhodium*' *J. Am. Chem. Soc.* **2013**, *135*, 17719-17722.

CHAPTER 11:

APPENDIX

11 Appendix

A3. Quality of Data in Single Crystal X-ray Diffraction

A3.1. *SADABS* diagnostic plots

The following plots are generated from SADABS and show the variation of the normalized scale factor and smoothed R_{int} as a function of the frame number.

1

Ag

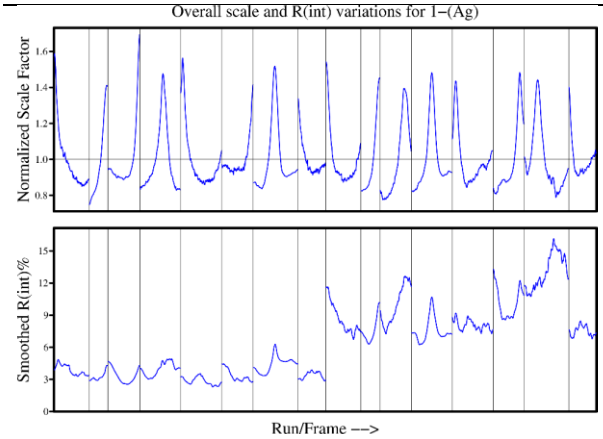

Mo

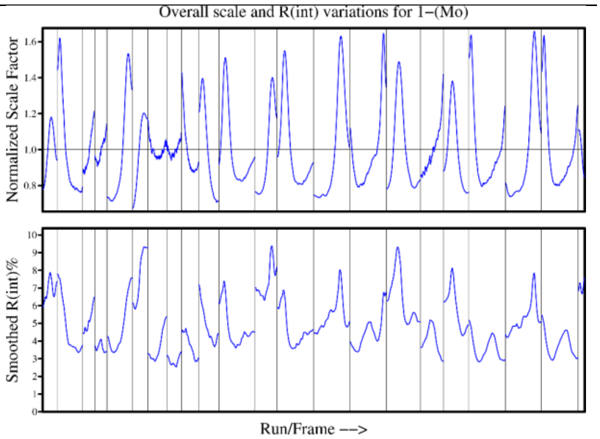

2

Ag

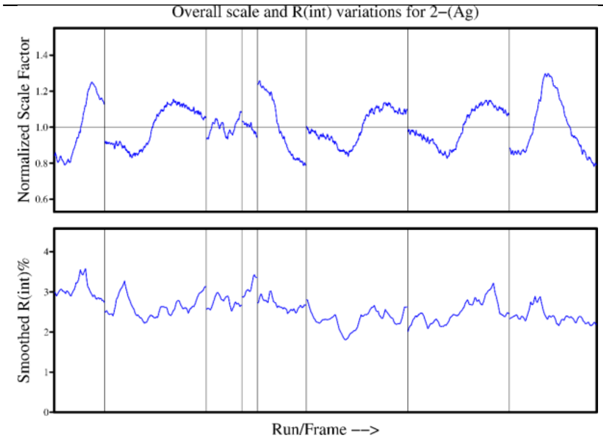

Mo

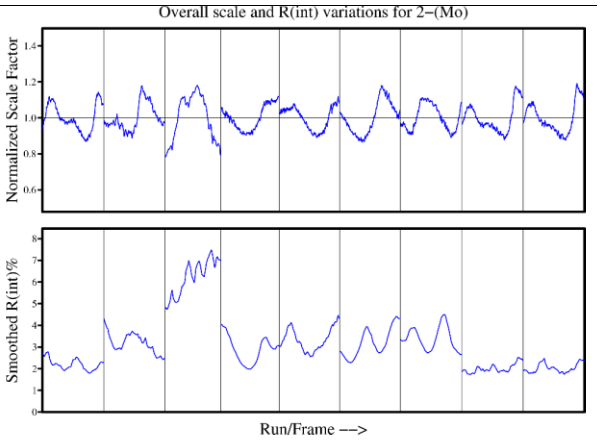

3

Ag

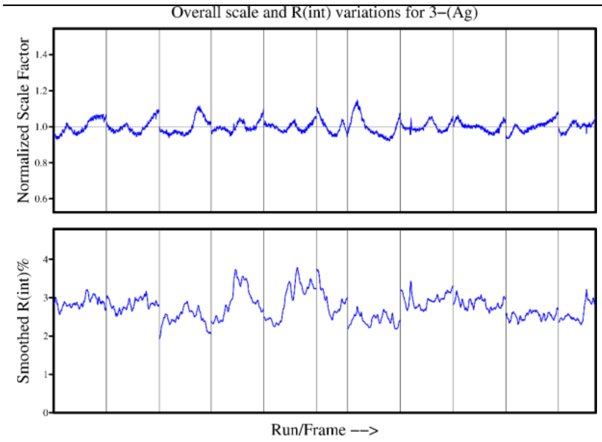
Overall scale and R(int) variations for 3–(Ag)
Normalized Scale Factor
1.4
1.2
1.0
0.8
0.6
Smoothed R(int)%
4
3
2
1
0
Run/Frame —>

Mo

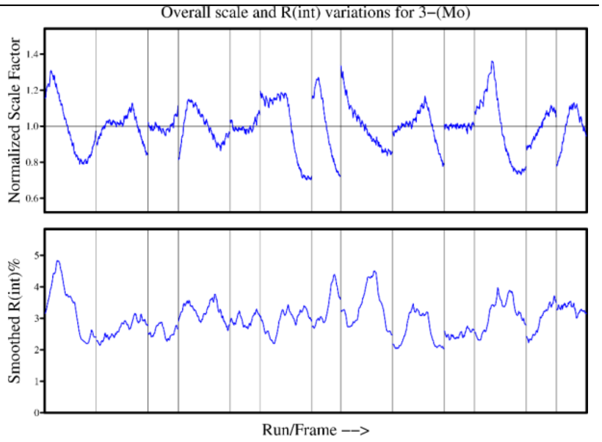
Overall scale and R(int) variations for 3–(Mo)
Normalized Scale Factor
1.4
1.2
1.0
0.8
0.6
Smoothed R(int)%
5
4
3
2
1
0
Run/Frame —>

4

Ag

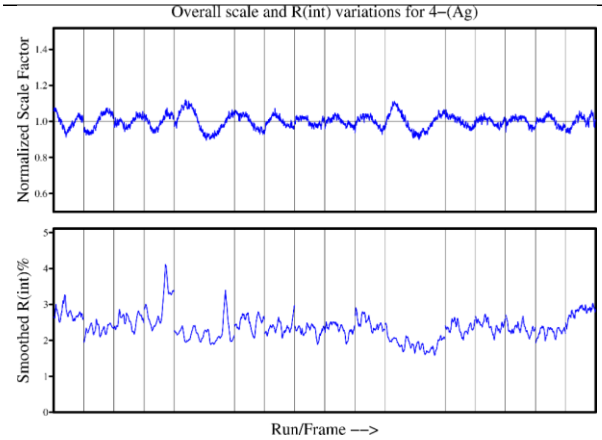
Overall scale and R(int) variations for 4–(Ag)
Normalized Scale Factor
1.4
1.2
1.0
0.8
0.6
Smoothed R(int)%
5
4
3
2
1
0
Run/Frame —>

Mo

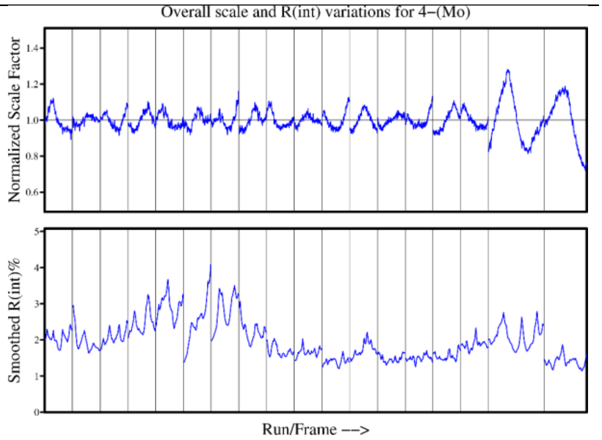
Overall scale and R(int) variations for 4–(Mo)
Normalized Scale Factor
1.4
1.2
1.0
0.8
0.6
Smoothed R(int)%
5
4
3
2
1
0
Run/Frame —>

5

Ag

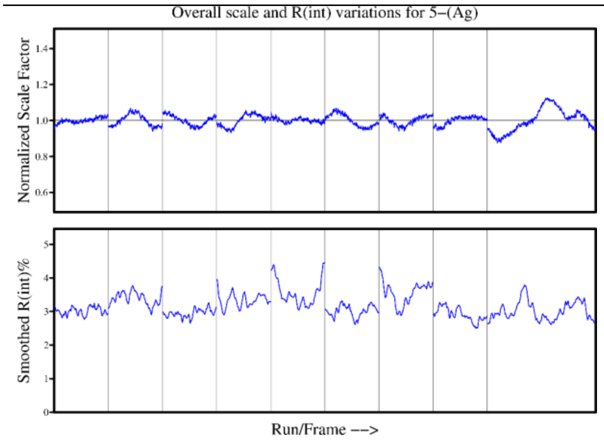
Overall scale and R(int) variations for 5–(Ag)

Mo

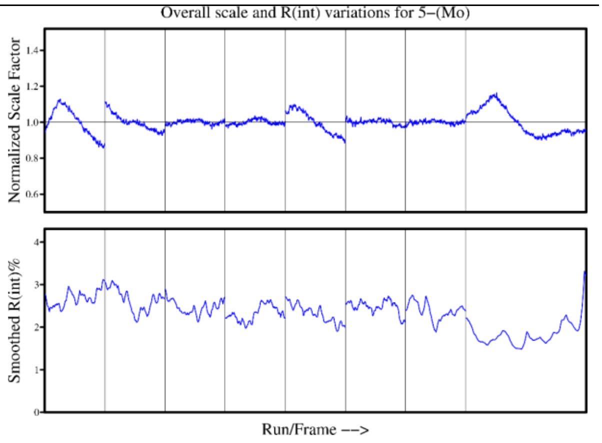
Overall scale and R(int) variations for 5–(Mo)

6

Ag

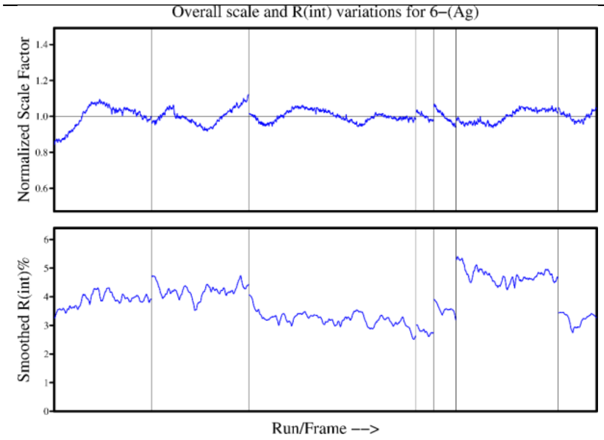
Overall scale and R(int) variations for 6–(Ag)

Mo

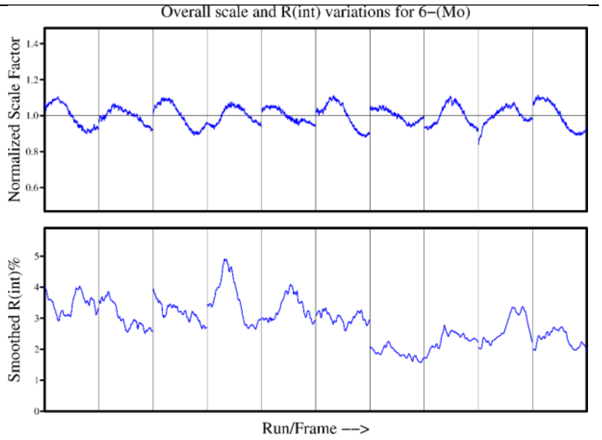
Overall scale and R(int) variations for 6–(Mo)

7

Ag

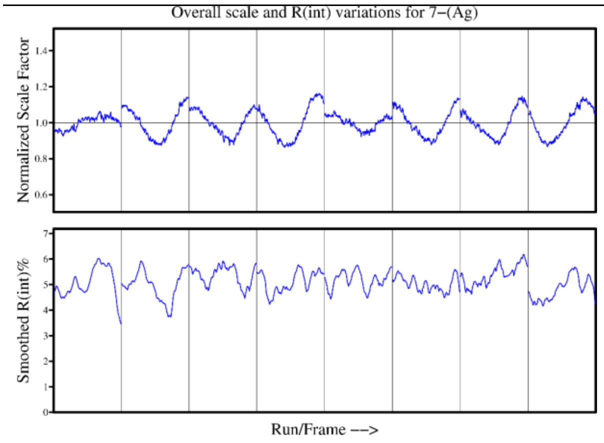

Mo

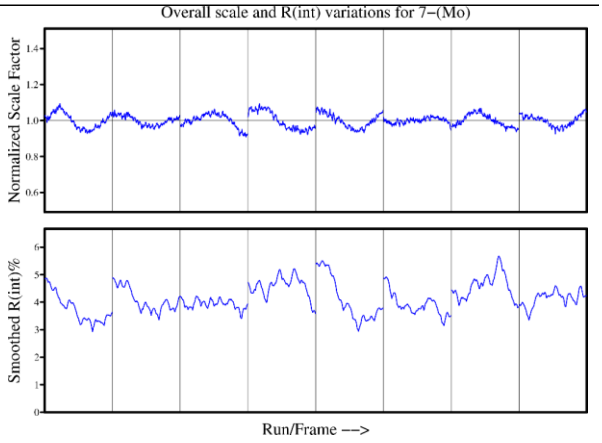

The following Plots are presented as an overlay of the two data sets, one corrected with the numerical (red) and the other with the semi-empirical (blue) absorption correction.

2

Ag

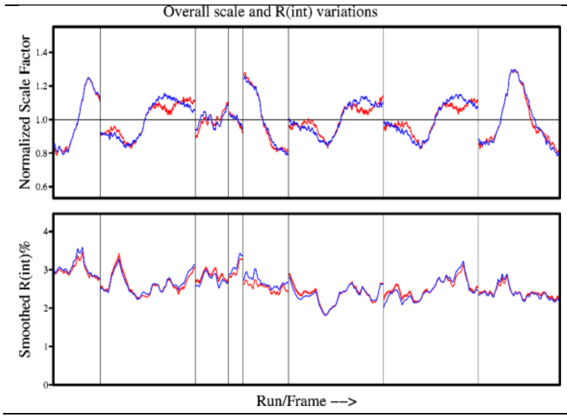

Mo

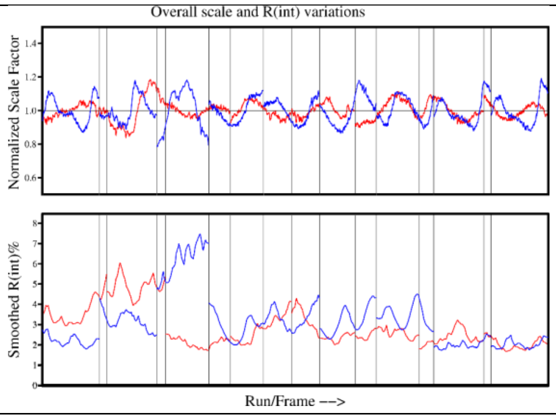

3

Ag

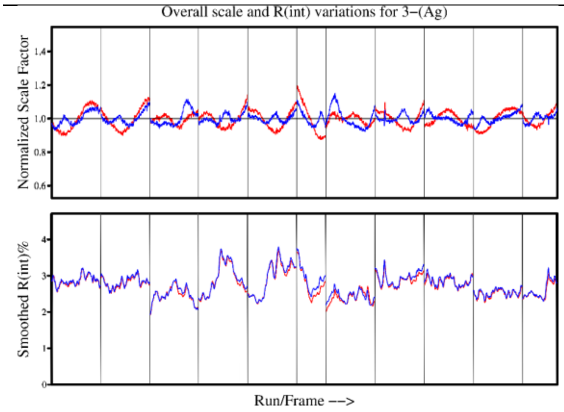
Overall scale and R(int) variations for 3–(Ag)
Normalized Scale Factor
1.4
1.2
1.0
0.8
0.6
Smoothed R(int)%
4
3
2
1
0
Run/Frame –->

Mo

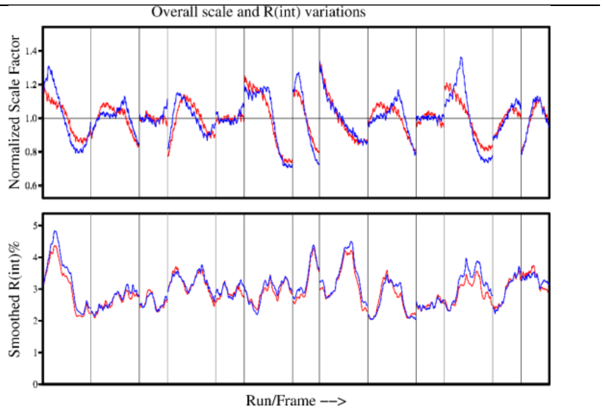
Overall scale and R(int) variations
Normalized Scale Factor
1.4
1.2
1.0
0.8
0.6
Smoothed R(int)%
5
4
3
2
1
0
Run/Frame –->

5

Ag

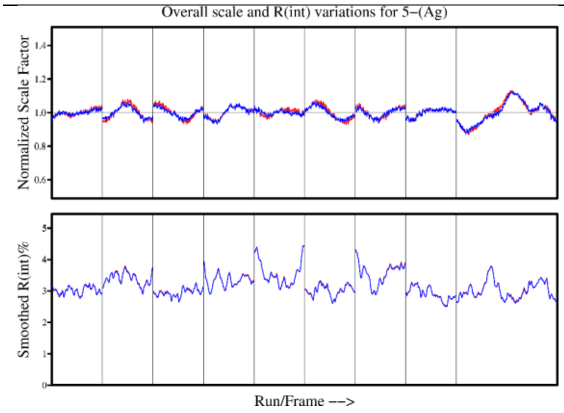
Overall scale and R(int) variations for 5–(Ag)
Normalized Scale Factor
1.4
1.2
1.0
0.8
0.6
Smoothed R(int)%
5
4
3
2
1
0
Run/Frame –->

Mo

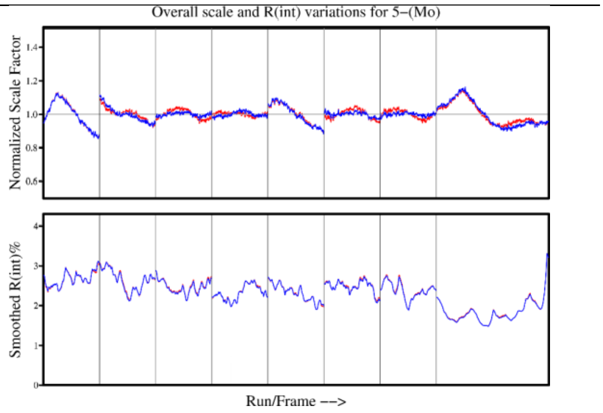
Overall scale and R(int) variations for 5–(Mo)
Normalized Scale Factor
1.4
1.2
1.0
0.8
0.6
Smoothed R(int)%
4
3
2
1
0
Run/Frame –->

A3.2. Significance of the data

In 2010, Kay Diederichs suggested an indicator which is calculated after the data reduction to be used to estimate the systematic instrument error of the x-ray source. The value of this indicator is the highest [I/σ(I)] value the given experimental setup can produce. Diederichs, K. (2010). Acta Crystallogr. Sect. D66, 733-740.

1

Ag	Mo

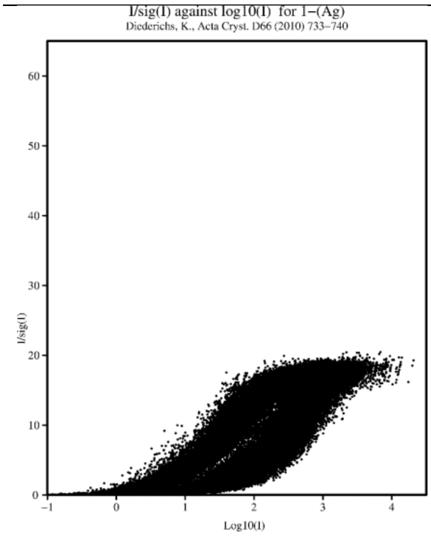

I/sig(I) against log10(I) for 1–(Ag)
Diederichs, K., Acta Cryst. D66 (2010) 733–740

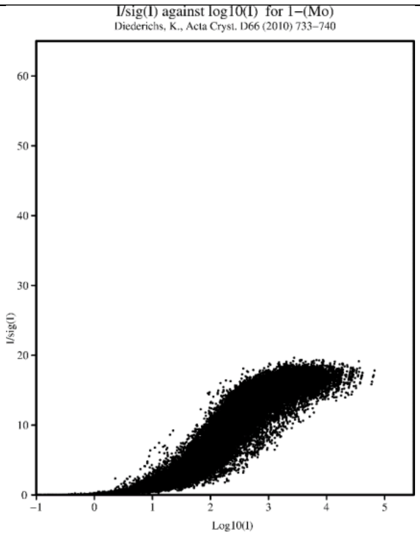

I/sig(I) against log10(I) for 1–(Mo)
Diederichs, K., Acta Cryst. D66 (2010) 733–740

2

Ag	Mo

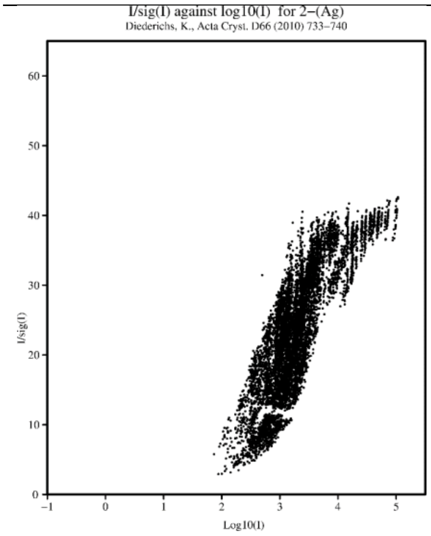

I/sig(I) against log10(I) for 2–(Ag)
Diederichs, K., Acta Cryst. D66 (2010) 733–740

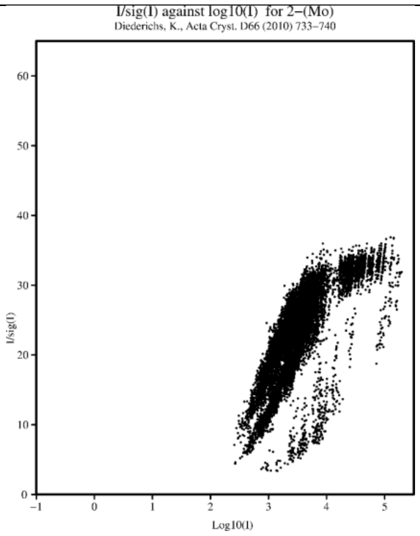

I/sig(I) against log10(I) for 2–(Mo)
Diederichs, K., Acta Cryst. D66 (2010) 733–740

3

Ag

Mo

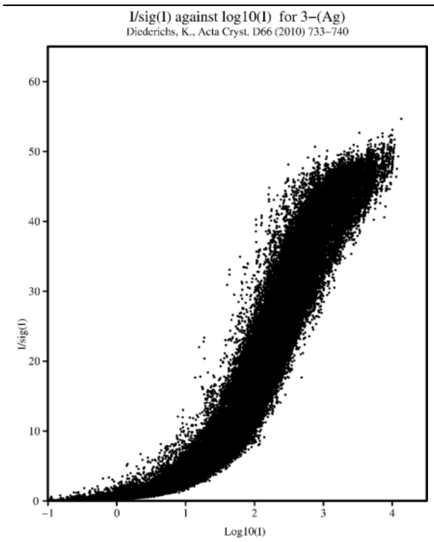
I/sig(I) against log10(I) for 3–(Ag)
Diederichs, K., Acta Cryst. D66 (2010) 733–740
I/sig(I)
Log10(I)
0
10
20
30
40
50
60
–1
0
1
2
3
4

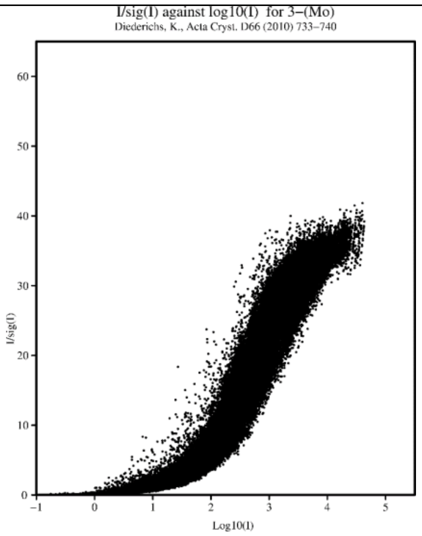
I/sig(I) against log10(I) for 3–(Mo)
Diederichs, K., Acta Cryst. D66 (2010) 733–740
I/sig(I)
Log10(I)
0
10
20
30
40
50
60
–1
0
1
2
3
4
5

4

Ag

Mo

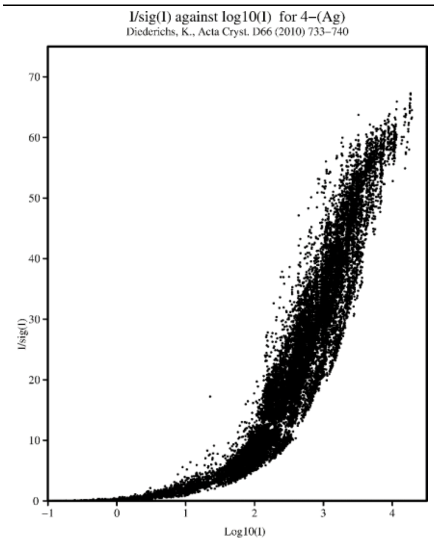
I/sig(I) against log10(I) for 4–(Ag)
Diederichs, K., Acta Cryst. D66 (2010) 733–740
I/sig(I)
Log10(I)
0
10
20
30
40
50
60
70
–1
0
1
2
3
4

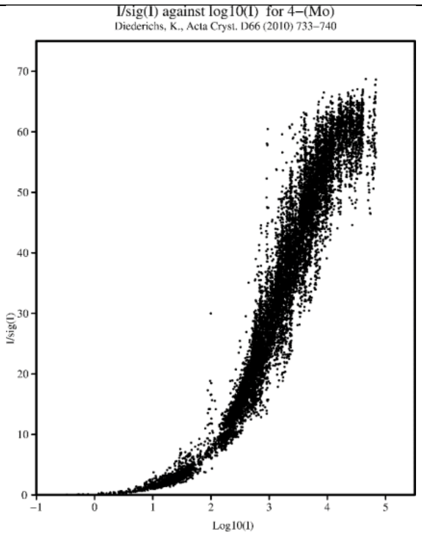
I/sig(I) against log10(I) for 4–(Mo)
Diederichs, K., Acta Cryst. D66 (2010) 733–740
I/sig(I)
Log10(I)
0
10
20
30
40
50
60
70
–1
0
1
2
3
4
5

5

Ag

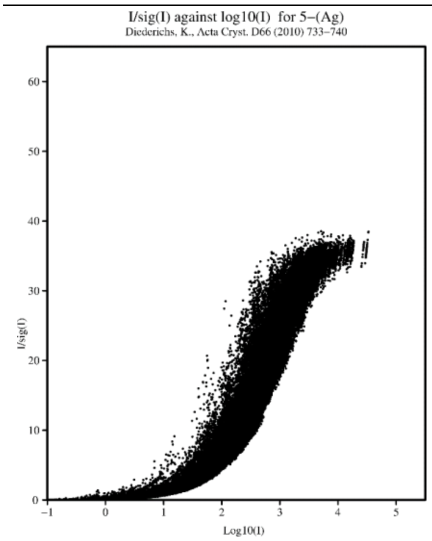
I/sig(I) against log10(I) for 5–(Ag)
Diederichs, K., Acta Cryst. D66 (2010) 733–740
I/sig(I)
Log10(I)
0
10
20
30
40
50
60
−1
0
1
2
3
4
5

Mo

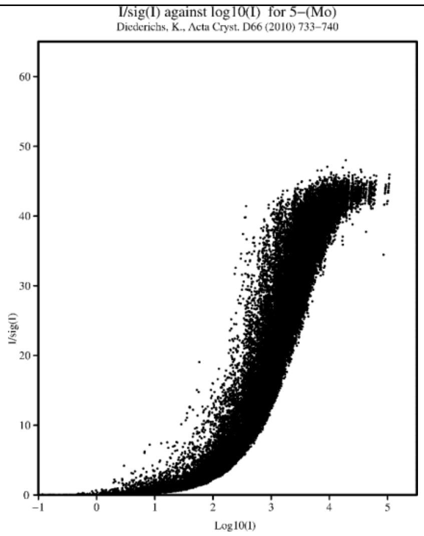
I/sig(I) against log10(I) for 5–(Mo)
Diederichs, K., Acta Cryst. D66 (2010) 733–740
I/sig(I)
Log10(I)
0
10
20
30
40
50
60
−1
0
1
2
3
4
5

6

Ag

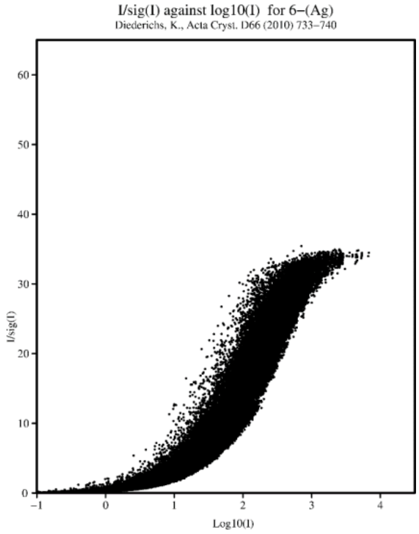
I/sig(I) against log10(I) for 6–(Ag)
Diederichs, K., Acta Cryst. D66 (2010) 733–740
I/sig(I)
Log10(I)
0
10
20
30
40
50
60
−1
0
1
2
3
4

Mo

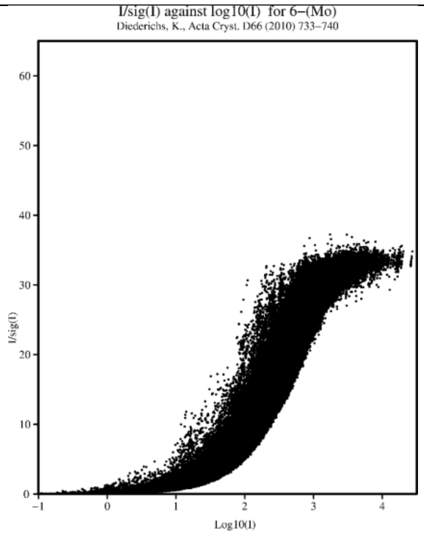
I/sig(I) against log10(I) for 6–(Mo)
Diederichs, K., Acta Cryst. D66 (2010) 733–740
I/sig(I)
Log10(I)
0
10
20
30
40
50
60
−1
0
1
2
3
4

7

Ag

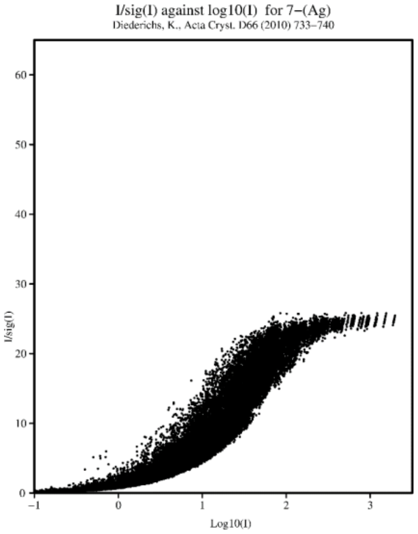

Mo

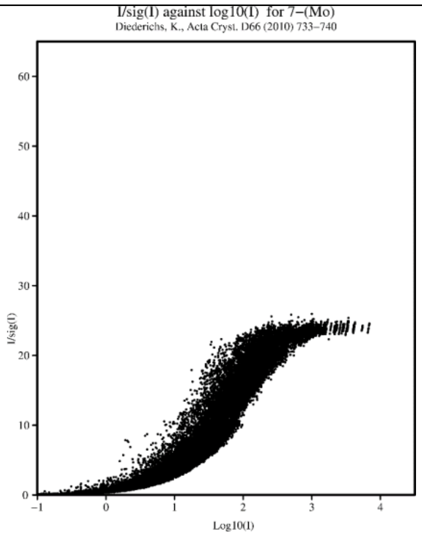

A4. Low energy contamination

A4.1. Selected quality indicators after artificial addition of contamination to theoretical data.

contamination [%]	**0.0**	**0.2**	**1.0**
$wR(F^2)$	0.0	0.0019	0.0096
$R(F^2)$	0.0	0.0011	0.0054
residual density peak	0.001	0.074	0.238
residual density hole	-0.001	-0.074	-0.197
$N(1) - C(1)$ [Å]	1.346758	1.346758	1.346758
e_{gross} $[e]$	0.00	13.96	36.88
$d^f(\rho_0)$:	2.7720	2.7909	2.7805
$\rho_{min}(d = 2)$ $[e\text{Å}^{-3}]$:	-0.0028	-0.0488	-0.1341
$\rho_{max}(d = 2)$ $[e\text{Å}^{-3}]$:	0.0028	0.0488	0.1430

A4.2. Residual densities calculated for the same model against different un-/contaminated data.

contamination: 0.0 %, map Level 0.001 e·A^{-3}

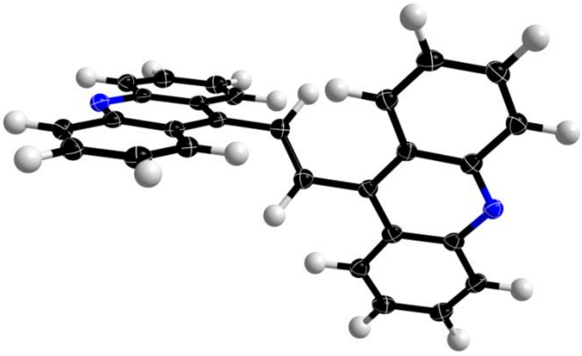

contamination: 0.2 %, map Level 0.048 e·A^{-3}

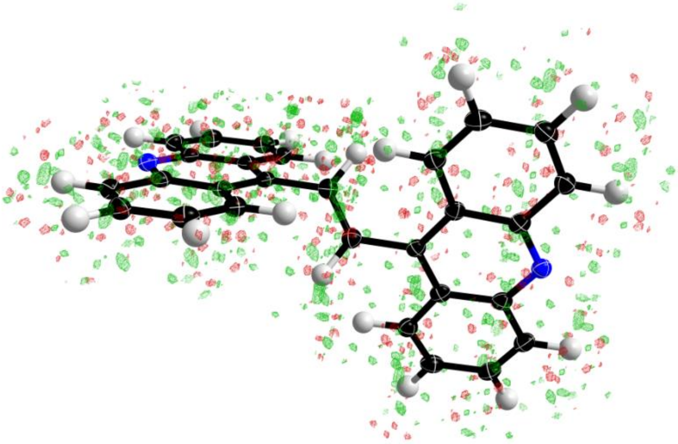

contamination: 1.0 %, map Level 0.137 e·A^{-3}

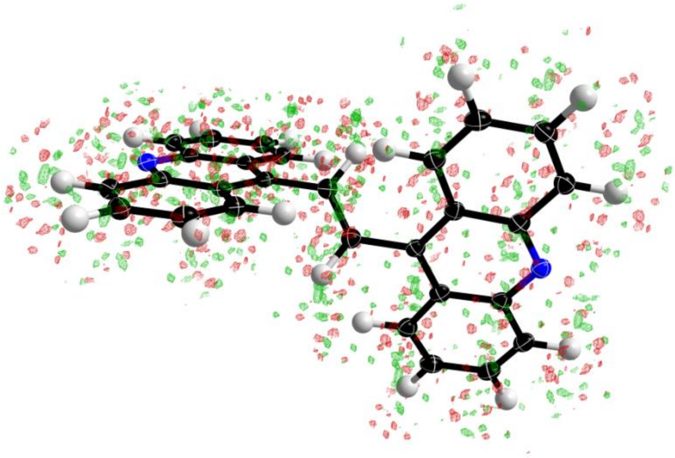

A4.3. plots for $k_{3\lambda}$ determination for structures **1** to **6**

1

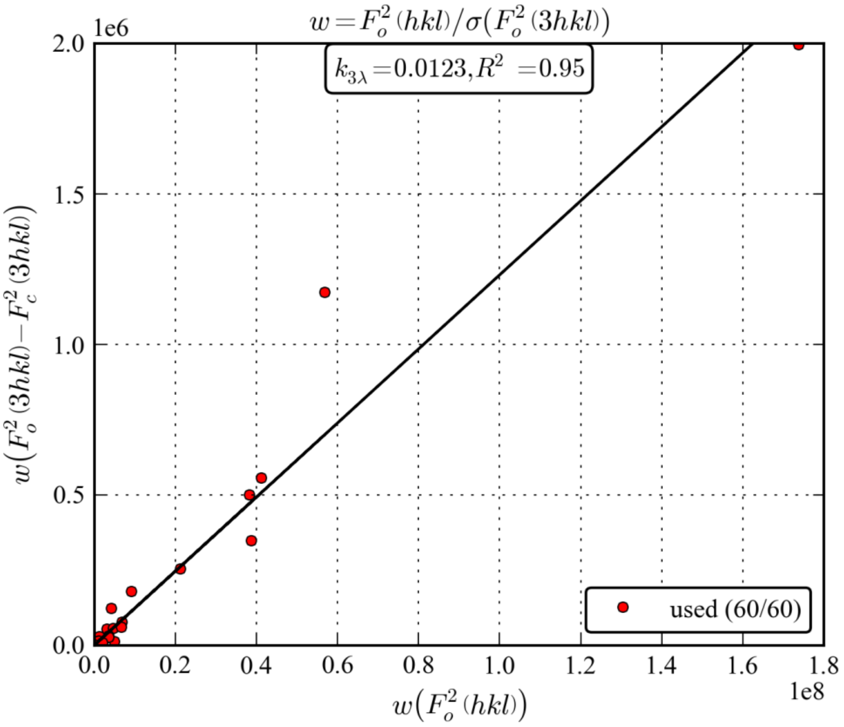

2

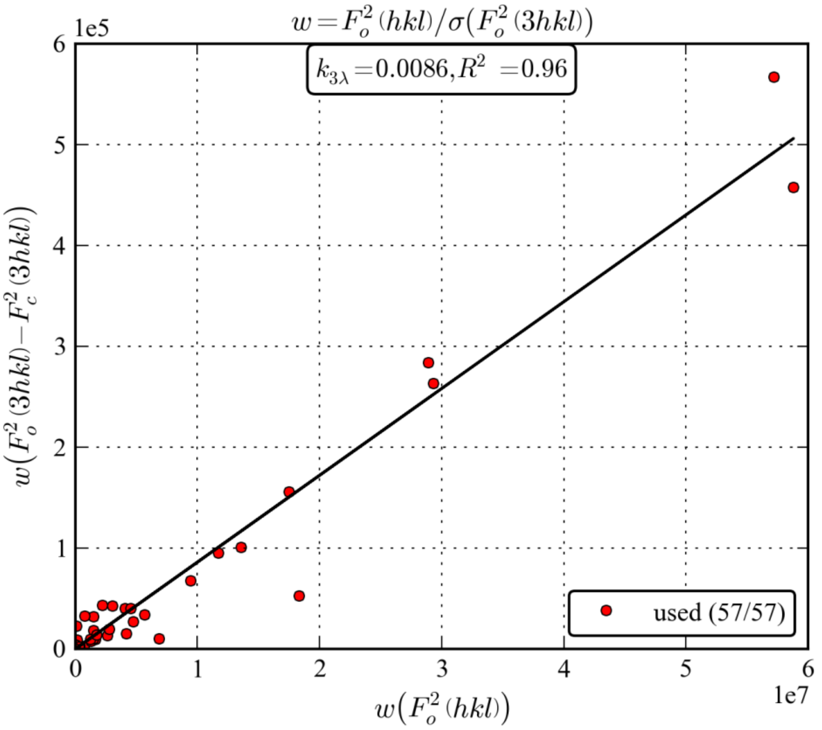

3	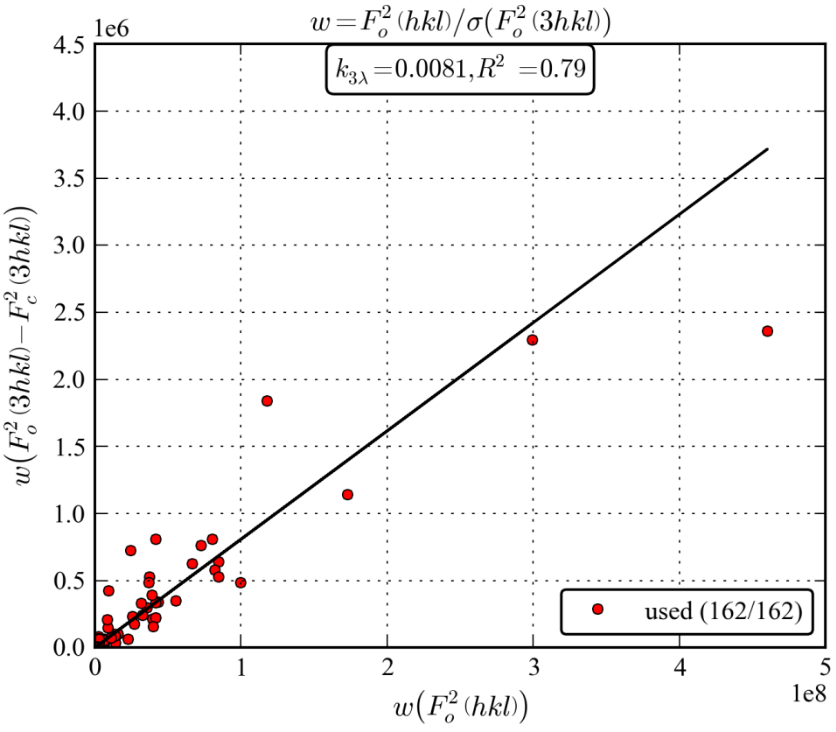$w = F_o^2(hkl)/\sigma(F_o^2(3hkl))$ $k_{3\lambda} = 0.0081, R^2 = 0.79$ 1e6 4.5 4.0 3.5 3.0 2.5 2.0 1.5 1.0 0.5 0.0 0 1 2 3 4 5 1e8 $w(F_o^2(3hkl) - F_c^2(3hkl))$ $w(F_o^2(hkl))$ used (162/162)
4	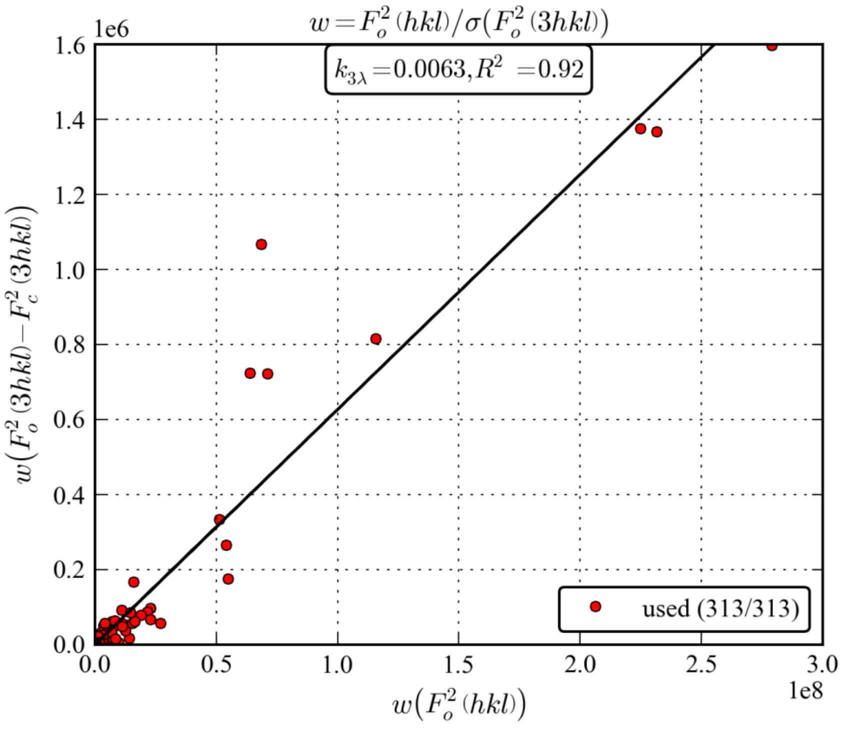$w = F_o^2(hkl)/\sigma(F_o^2(3hkl))$ $k_{3\lambda} = 0.0063, R^2 = 0.92$ 1e6 1.6 1.4 1.2 1.0 0.8 0.6 0.4 0.2 0.0 0.0 0.5 1.0 1.5 2.0 2.5 3.0 1e8 $w(F_o^2(3hkl) - F_c^2(3hkl))$ $w(F_o^2(hkl))$ used (313/313)

5

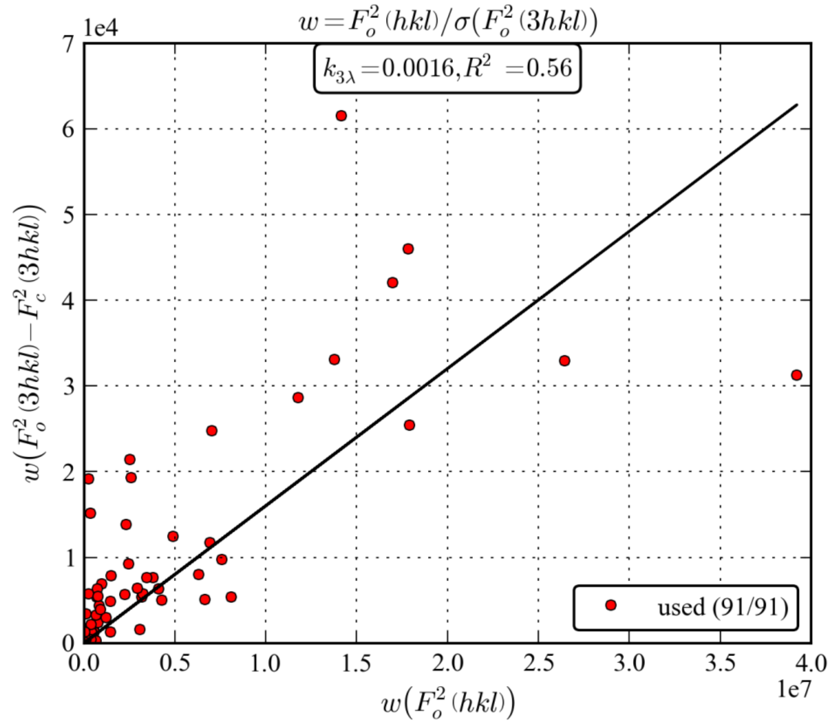
$w = F_o^2(hkl)/\sigma(F_o^2(3hkl))$
$k_{3\lambda} = 0.0016, R^2 = 0.56$
1e4
7
6
5
4
3
2
1
0
$w(F_o^2(3hkl) - F_c^2(3hkl))$
0.0
0.5
1.0
1.5
2.0
2.5
3.0
3.5
4.0
1e7
$w(F_o^2(hkl))$
used (91/91)

6 (IµS)

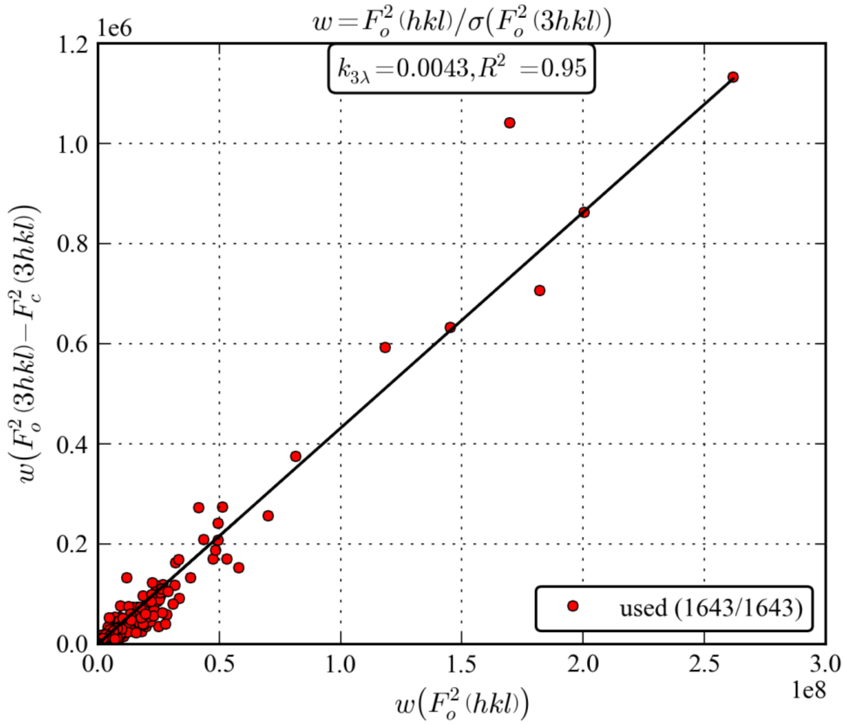
$w = F_o^2(hkl)/\sigma(F_o^2(3hkl))$
$k_{3\lambda} = 0.0043, R^2 = 0.95$
1e6
1.2
1.0
0.8
0.6
0.4
0.2
0.0
$w(F_o^2(3hkl) - F_c^2(3hkl))$
0.0
0.5
1.0
1.5
2.0
2.5
3.0
1e8
$w(F_o^2(hkl))$
used (1643/1643)

6 (TXS)

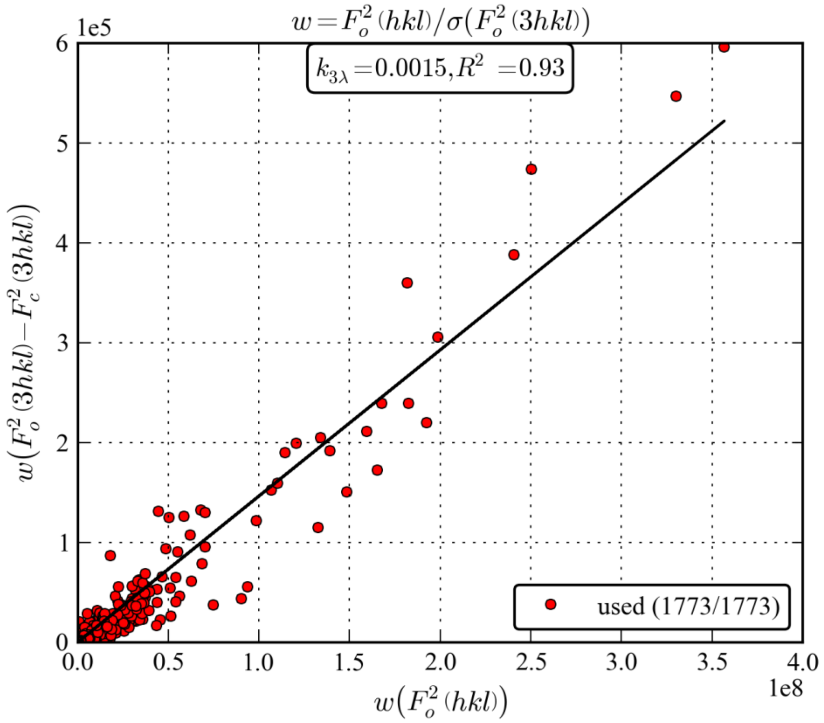
$w = F_o^2(hkl)/\sigma(F_o^2(3hkl))$
$k_{3\lambda} = 0.0015, R^2 = 0.93$
1e5
6
5
4
3
2
1
0
$w(F_o^2(3hkl) - F_c^2(3hkl))$
0.0
0.5
1.0
1.5
2.0
2.5
3.0
3.5
4.0
1e8
$w(F_o^2(hkl))$
used (1773/1773)

A4.4. Crystallographic data for compound 1

Empirical formula	$C_{28}H_{18}N_2$		
Formula weight	382.44		
Temperature [K]	100(2)		
Wavelength [Å]	0.71073		
Crystal system	Monoclinic		
Space group	C2/c		
Z	4		
Density (calculated) [Mg/m^3]	1.383		
Absorption coefficient [mm$^{-1]}$	0.081		
F(000)	800		
Crystal size [mm]	0.320 x 0.250 x 0.100		
Absorption correction	Semi-empirical from equivalents		
Refinement method	Full-matrix least-squares on F^2		
data correction	unfiltered, uncorrected	filtered	corrected (k_{twin})
a [Å]	13.5559(13)	13.5537(16)	13.5559 (13)
b [Å]	12.2134(12)	12.2132(15)	12.2134 (12)
c [Å]	12.6643(12)	12.6619(15)	12.6643 (12)
β [°]	118.8339(17)	118.836(2)	118.8339 (17)
Volume [Å^3]	1836.8(3)	1836.1(4)	1836.8(3)
θ range for data collection [°]	2.392 to 25.500	2.392 to 25.556	2.392 to 25.500
Reflections collected	14302	14259	14302
Independent reflections	1697 [R(int) = 0.0254]	1707 [R(int) = 0.0262]	1697 [R(int) = 0.0253]
Completeness to θ = 25.242°	99.9 %	100.0 %	99.9 %
Max. and min. transmission	0.7452 and 0.7094	0.7452 and 0.7060	0.7452 and 0.7094
Data / restraints / parameters	1697 / 123 / 136	1707 / 123 / 136	1697 / 123 / 137
Goodness-of-fit on F^2	1.115	1.097	1.093
Final R indices [I>2sigma(I)]	R1 = 0.0429 wR2 = 0.1237	R1 = 0.0393 wR2 = 0.1070	R1 = 0.0396 wR2 = 0.1081
R indices (all data)	R1 = 0.0463 wR2 = 0.1265	R1 = 0.0428 wR2 = 0.1105	R1 = 0.0435 wR2 = 0.1113
Largest diff. peak/hole [e·Å^{-3}]	0.239 / -0.199	0.270 / -0.194	0.274 / -0.178

A4.5. Crystallographic data for compound 2

Empirical formula	$C_{12}H_4N_4$		
Formula weight	204.19		
Temperature [K]	100(2)		
Wavelength [Å]	0.71073		
Crystal system	Monoclinic		
Space group	C2/c		
Z	4		
Density (calculated) [Mg/m^3]	1.356		
Absorption coefficient [mm^{-1}]	0.088		
F(000)	416		
Crystal size [mm]	0.180 x 0.130 x 0.060		
Absorption correction	Semi-empirical from equivalents		
Refinement method	Full-matrix least-squares on F^2		
data correction	unfiltered, uncorrected	filtered	corrected (k_{twin})
a [Å]	8.896(2)	8.8840(12)	8.896(2)
b [Å]	6.9130(19)	6.9036(9)	6.9130(19)
c [Å]	16.439(5)	16.421(2)	16.439(5)
β [°]	98.290(3)	98.241(2)	98.290(3)
Volume [$Å^3$]	1000.5(5)	996.7(2)	1000.5(5)
θ range for data collection [°]	2.504 to 30.680	2.507 to 30.728	2.504 to 30.680
Reflections collected	10353	10375	10353
Independent reflections	1543 [R(int) = 0.0153]	1545 [R(int) = 0.0155]	1543 [R(int) = 0.0154]
Completeness to θ = 25.242°	99.9 %	100.0 %	99.9 %
Max. and min. transmission	0.7461 and 0.7182	0.7461 and 0.7184	0.7461 and 0.7182
Data / restraints / parameters	1543 / 0 / 73	1545 / 0 / 73	1543 / 0 / 74
Goodness-of-fit on F^2	1.090	1.084	1.087
Final R indices [I>2sigma(I)]	R1 = 0.0360	R1 = 0.0338	R1 = 0.0338
	wR2 = 0.1059	wR2 = 0.0966	wR2 = 0.0943
R indices (all data)	R1 = 0.0377	R1 = 0.0362	R1 = 0.0357
	wR2 = 0.1075	wR2 = 0.0992	wR2 = 0.0963
Largest diff. peak/hole [$e \cdot Å^{-3}$]	0.469 / -0.164	0.465 / -0.192	0.464 / -0.173

A4.6. Crystallographic data for compound 3

Empirical formula	$C_{18}H_{17}CuO_6$		
Formula weight	392.86		
Temperature [K]	100(2)		
Wavelength [Å]	0.71073		
Crystal system	Monoclinic		
Space group	C2/c		
Z	8		
Density (calculated) [Mg/m^3]	1.538		
Absorption coefficient [mm^{-1}]	1.318		
F(000)	1616		
Crystal size [mm]	0.140 x 0.100 x 0.050		
Absorption correction	Semi-empirical from equivalents		
Refinement method	Full-matrix least-squares on F^2		
data correction	unfiltered, uncorrected	filtered	corrected (k_{twin})
a [Å]	9.7935(7)	9.7936(7)	9.7935(7)
b [Å]	19.0055(13)	18.9973(12)	19.0055(13)
c [Å]	18.2997(13)	18.2982(12)	18.2997(13)
β [°]	94.7996(11)	94.8400(10)	94.7996(11)
Volume [Å^3]	3394.2(4)	3392.3(4)	3394.2(4)
θ range for data collection [°]	2.143 to 28.426	2.144 to 28.332	2.143 to 28.426
Reflections collected	29203	29137	29203
Independent reflections	4282 [R(int) = 0.0282]	4233 [R(int) = 0.0329]	4282 [R(int) = 0.0280]
Completeness to θ = 25.242°	100.0 %	100.0 %	100.0 %
Max. and min. transmission	0.7457 and 0.6951	0.7457 and 0.6935	0.7457 and 0.6951
Data / restraints / parameters	4282 / 652 / 300	4233 / 652 / 300	4282 / 652 / 301
Goodness-of-fit on F^2	1.069	1.034	1.033
Final R indices [I>2sigma(I)]	R1 = 0.0273 wR2 = 0.0676	R1 = 0.0276 wR2 = 0.0642	R1 = 0.0260 wR2 = 0.0619
R indices (all data)	R1 = 0.0342 wR2 = 0.0704	R1 = 0.0380 wR2 = 0.0681	R1 = 0.0328 wR2 = 0.0650
Largest diff. peak/hole [e·Å^{-3}]	0.390 and -0.281	0.338 and -0.294	0.359 and -0.297

A4.7. Crystallographic data for compound 4

Empirical formula	$C_{34}H_{26}MgN_4O_4$		
Formula weight	578.90		
Temperature [K]	100(2)		
Wavelength [Å]	0.71073		
Crystal system	Monoclinic		
Space group	$P2_1/n$		
Z	4		
Density (calculated) [Mg/m^3]	1.361		
Absorption coefficient [mm^{-1}]	0.111		
F(000)	1208		
Crystal size [mm]	0.190 x 0.150 x 0.110		
Absorption correction	Semi-empirical from equivalents		
Refinement method	Full-matrix least-squares on F^2		
data correction	unfiltered, uncorrected	filtered	corrected (k_{twin})
a [Å]	11.3068(12)	11.3182(14)	11.3068(12)
b [Å]	14.9595(16)	14.9745(18)	14.9595(16)
c [Å]	16.7252(17)	16.744(2)	16.7252(17)
β [°]	93.0500(15)	93.044(2)	93.0500(15)
Volume [Å^3]	2825.0(5)	2833.9(6)	2825.0(5)
θ range for data collection [°]	1.828 to 30.615	1.826 to 30.816	1.828 to 30.615
Reflections collected	36155	36495	36155
Independent reflections	8694 [R(int) = 0.0265]	8866 [R(int) = 0.0310]	8694 [R(int) = 0.0264]
Completeness to θ = 25.242°	99.9 %	100.0 %	99.9 %
Max. and min. transmission	0.7461 and 0.6883	0.7461 and 0.6789	0.7461 and 0.6883
Data / restraints / parameters	8694 / 408 / 392	8866 / 408 / 392	8694 / 408 / 393
Goodness-of-fit on F^2	1.030	1.034	1.017
Final R indices [I>2sigma(I)]	R1 = 0.0407 wR2 = 0.1090	R1 = 0.0403 wR2 = 0.1046	R1 = 0.0399 wR2 = 0.1030
R indices (all data)	R1 = 0.0483 wR2 = 0.1149	R1 = 0.0499 wR2 = 0.1112	R1 = 0.0475 wR2 = 0.1091
Largest diff. peak/hole [e·Å^{-3}]	0.533 / -0.250	0.447 / -0.255	0.534 / -0.248

A4.8. Crystallographic data for compound 5

Empirical formula	$C_{11}H_{10}O_2S$		
Formula weight	206.25		
Temperature [K]	293(2)		
Wavelength [Å]	0.71073		
Crystal system	Orthorhombic		
Space group	$P2_12_12_1$		
Z	4		
Density (calculated) [Mg/m^3]	1.381		
Absorption coefficient [mm^{-1}]	0.294		
F(000)	432		
Crystal size [mm]	0.250 x 0.250 x 0.250		
Absorption correction	Semi-empirical from equivalents		
Refinement method	Full-matrix least-squares on F^2		
data correction	unfiltered, uncorrected	filtered	corrected (k_{twin})
a [Å]	5.96330(10)	5.9641(2)	5.96330(10)
b [Å]	9.0417(2)	9.0419(2)	9.0417(2)
c [Å]	18.4007(4)	9.0419(2)	18.4007(4)
Volume [Å^3]	992.14(3)	992.40(5)	992.14(3)
θ range for data collection [°]	2.214 to 28.308	2.213 to 28.283	2.214 to 28.308
Reflections collected	15091	15101	15091
Independent reflections	2456 [R(int) = 0.0199]	2453 [R(int) = 0.0199]	2456 [R(int) = 0.0199]
Completeness to θ = 25.242°	100.0 %	100.0 %	100.0 %
Max. and min. transmission	0.7457 and 0.7096	0.7457 and 0.7124	0.7457 and 0.7096
Data / restraints / parameters	2456 / 0 / 129	2453 / 0 / 129	2456 / 0 / 130
Goodness-of-fit on F^2	1.089	1.105	1.078
Final R indices [I>2sigma(I)]	R1 = 0.0254	R1 = 0.0252	R1 = 0.0249
	wR2 = 0.0674	wR2 = 0.0667	wR2 = 0.0661
R indices (all data)	R1 = 0.0262	R1 = 0.0261	R1 = 0.0256
	wR2 = 0.0680	wR2 = 0.0674	wR2 = 0.0668
Largest diff. peak/hole [e·Å^{-3}]	0.219 and -0.197	0.210 and -0.187	0.218 and -0.184
Absolute structure parameter	0.034(14)	0.049(16)	0.035(15)

A4.9. Crystallographic data for compound 6

Empirical formula	$C_{26}H_{19}PS$	
Formula weight	394.44	
Temperature [K]	100(2)	
Wavelength [Å]	0.71073	
Crystal system	Triclinic	
Space group	$P\bar{1}$	
Z	4	
Density (calculated) [Mg/m^3]	1.328	
Absorption coefficient [mm^{-1}]	0.254	
F(000)	824	
Crystal size [mm]	0.100 x 0.100 x 0.150	
Absorption correction	Semi-empirical from equivalents	
Refinement method	Full-matrix least-squares on F^2	
a [Å]	10.215(2)	
b [Å]	12.322(2)	
c [Å]	17.351(3)	
α [°]	101.57(2)	
β [°]	91.25(2)	
γ [°]	112.02(2)	
Volume [Å^3]	1972.2(7)	
θ range for data collection [°]	1.205 to 52.955	
Reflections collected	272253	
Independent reflections	45758 [R(int) = 0.0149]	
Completeness to θ = 25.242°	99.8 %	
Max. and min. transmission	0.7504 and 0.7163	
Data / restraints / parameters	45758 / 0 / 815	
data correction	unfiltered, uncorrected	corrected ($k_{3\lambda}$)
Goodness-of-fit on F^2	1.67	1.398
Final R indices [I>2sigma(I)]	0.021	0.020
R indices (all data)	0.021	0.020
Largest diff. peak/hole [e·Å^{-3}]	0.291 and -0.208	0.295 and -0.207

A4.10. Systematic Errors

In 2010, Diederichs suggested an indicator which is calculated for the unmerged data after the data reduction to be used to estimate the systematic instrument error of the X-ray source. The value of this indicator is the highest [I/σ(I)] value the given experimental setup can produce.

I/sig(I) against log10(I) for 1_filter
Diederichs, K., Acta Cryst. D66 (2010) 733–740

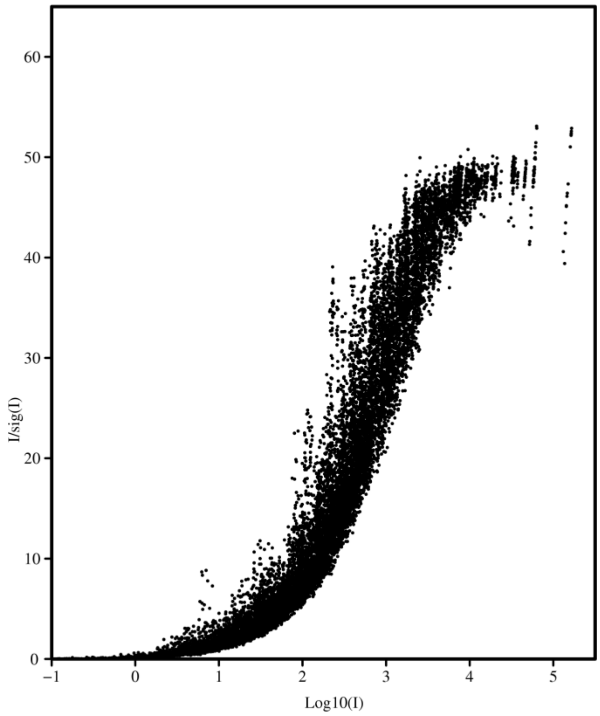

I/sig(I) against log10(I) for 1_no_filter
Diederichs, K., Acta Cryst. D66 (2010) 733–740

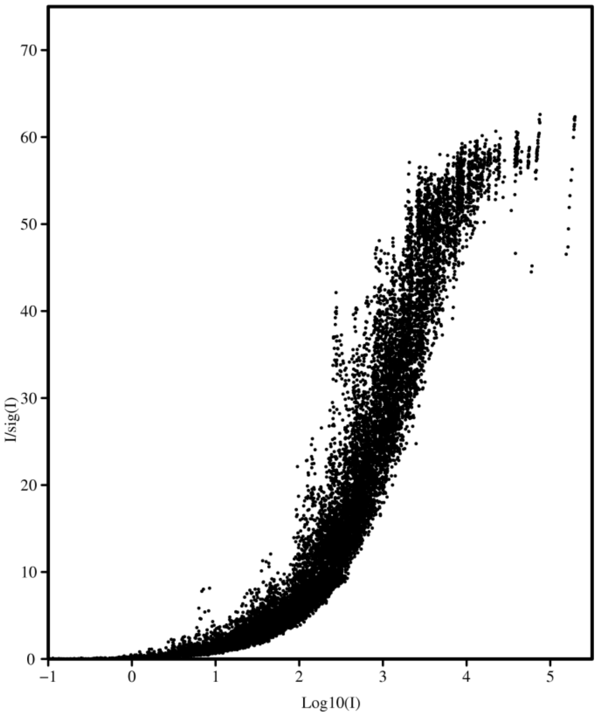

I/sig(I) against log10(I) for 2_filter
Diederichs, K., Acta Cryst. D66 (2010) 733–740

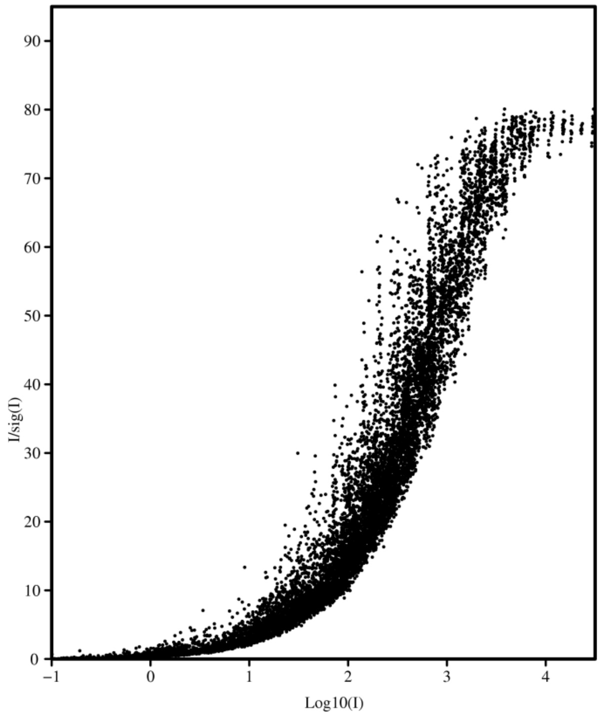

I/sig(I) against log10(I) for 2_no_filter
Diederichs, K., Acta Cryst. D66 (2010) 733–740

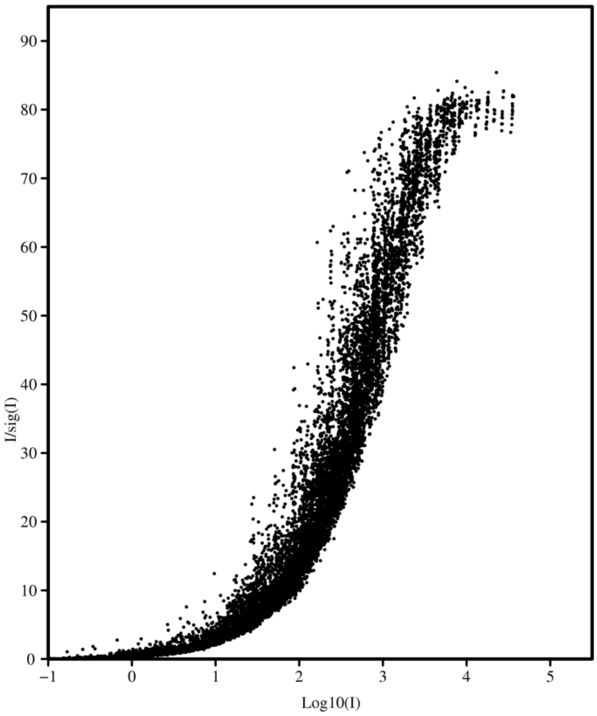

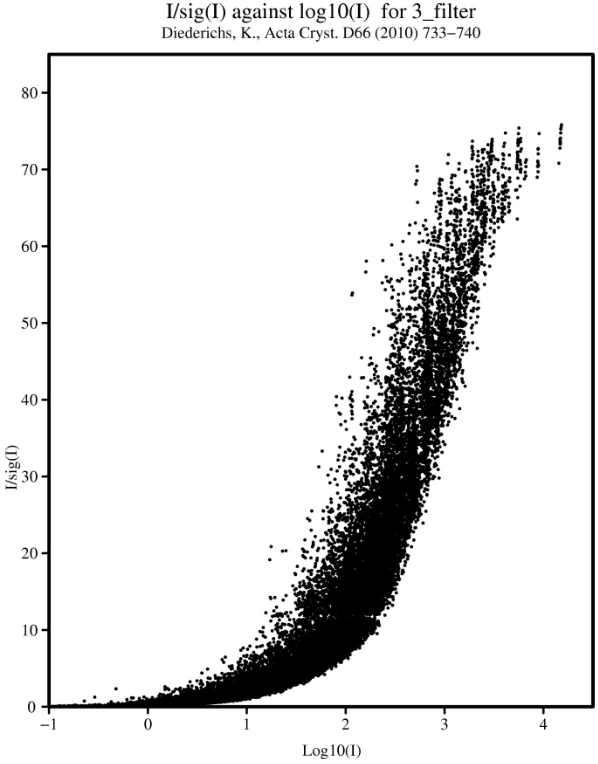
I/sig(I) against log10(I) for 3_filter

Diederichs, K., Acta Cryst. D66 (2010) 733–740

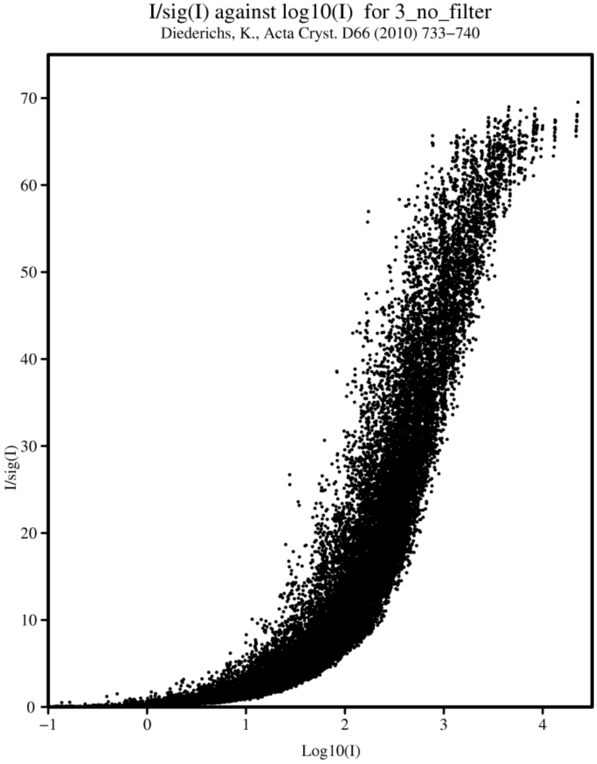
I/sig(I) against log10(I) for 3_no_filter

Diederichs, K., Acta Cryst. D66 (2010) 733–740

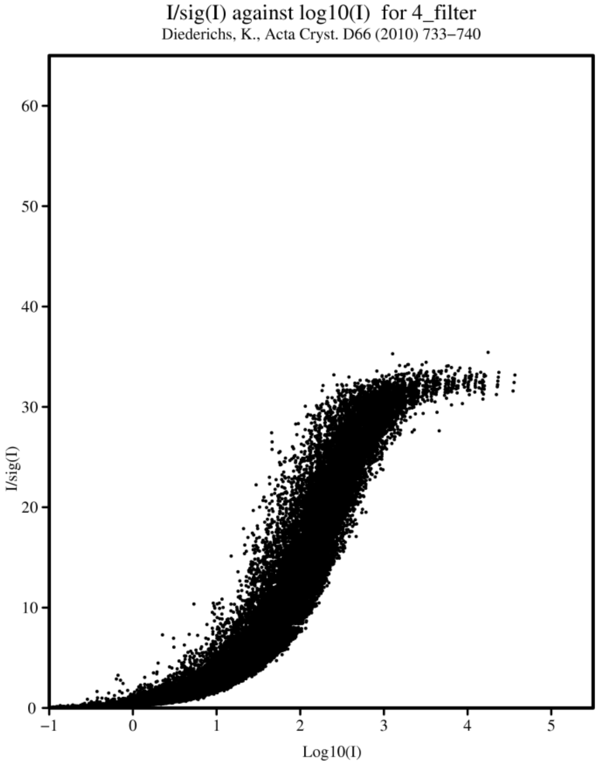
I/sig(I) against log10(I) for 4_filter

Diederichs, K., Acta Cryst. D66 (2010) 733–740

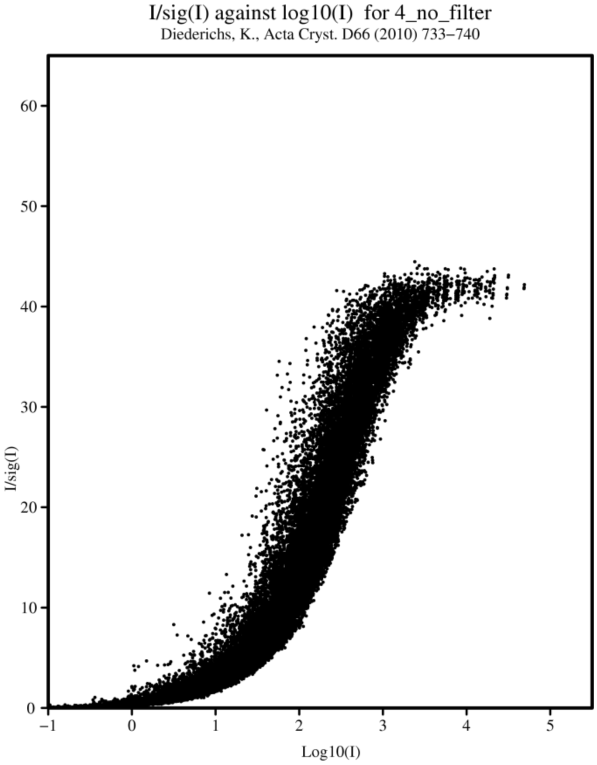
I/sig(I) against log10(I) for 4_no_filter

Diederichs, K., Acta Cryst. D66 (2010) 733–740

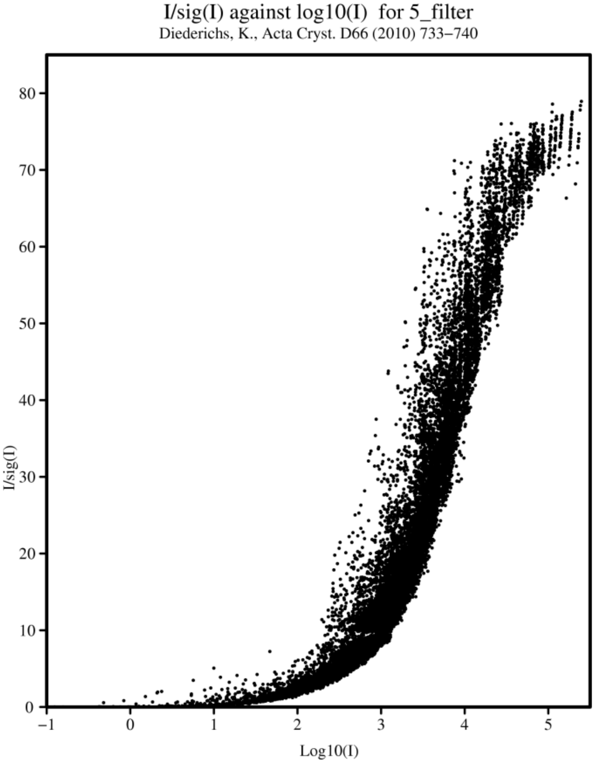

I/sig(I) against log10(I) for 5_filter

Diederichs, K., Acta Cryst. D66 (2010) 733−740

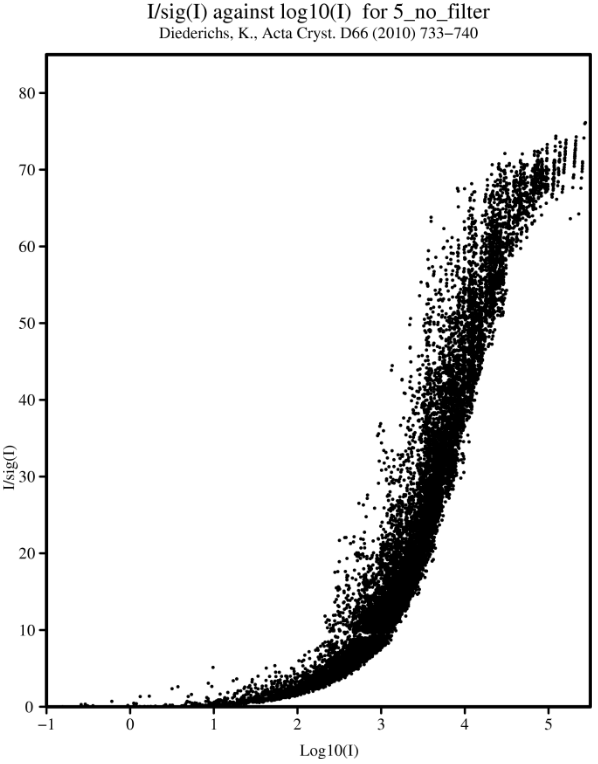

I/sig(I) against log10(I) for 5_no_filter

Diederichs, K., Acta Cryst. D66 (2010) 733−740

A4.11. $k_{3\lambda}$ default values

Comparison of quality indicators for models derived from data individually corrected or corrected with a default value of 1% for selected structures.

Formula Sum	$\Delta(C-C)$ [Å]	$R1$	k
$C_{28}H_{38}N_4$	0.0020	0.0443	0.0075
	0.0020	0.0444	0.0100
$C_{14}H_{23}N_3$	0.0016	0.0417	0.0170
	0.0016	0.0421	0.0100
$C_{15}H_{10}N_2O_2$	0.0016	0.0368	0.0150
	0.0016	0.0374	0.0100
$C_{34}H_{26}MgN_4O_4$	0.0018	0.0412	0.0120
	0.0018	0.0413	0.0100
$C_{70}H_{84}N_4O_2Si_2$	0.0022	0.0430	0.0042
	0.0023	0.0435	0.0100
$C_{16}H_{15}N_3OS$	0.0041	0.0339	0.0079
	0.0041	0.0339	0.0100
$C_{14}H_9N_3S_2$	0.0046	0.0312	0.0075
	0.0046	0.0311	0.0100
$C_{188}H_{152}Al_{10}Cl_{10}N_{20}O_{20}$	0.0029	0.0398	0.0097
	0.0029	0.0398	0.0100
$C_{16}H_{12}AlClN_2S_2$	0.0034	0.0397	0.0136
	0.0034	0.0399	0.0100
$C_{19}H_{31}GeKN_2OS_2$	0.0033	0.0303	0.0063
	0.0033	0.0304	0.0100

A4.12. Transmission-ratio vs. $k_{3\lambda}$

Data for Transmission-ratio versus $k_{3\lambda}$ for a collection of different structures.

Formula sum	**Space group**	***e.s.d*** **(C–C) [Å]**	***R*1**	**w*R*2**	**transm. ratio**	**BASF**	***e.s.d.*** **(BASF)**	**source**
$C_{23}H_{24}O_2$	$C2/c$	0.0017	0.0333	0.0881	0.940561	0.00988	0.00036	IµS
$C_{14}H_{27}N_3$	$C2/c$	0.0036	0.0542	0.1607	0.909787	0.01015	0.00055	IµS
$C_{28}H_{44}Li_2N_6$	$P2_1/n$	0.0019	0.0408	0.1113	0.955869	0.00886	0.00037	IµS
$C_{73}H_{100}Cl_4Li_2O_8S_6Zn_4$	$P\bar{1}$	0.0054	0.0380	0.1012	0.897611	0.00484	0.00022	IµS
$C_{30}H_{17}NO_4$	$P2_1/c$	0.0020	0.0411	0.1056	0.954667	0.01050	0.00041	IµS
$C_{17}H_{14}O_2$	$P2_1/c$	0.0015	0.0387	0.1104	0.956702	0.01092	0.00043	IµS
$C_{12}H_{18}N_2O_6$	$P2_12_12_1$	0.0023	0.0340	0.0879	0.771880	0.01075	0.00049	IµS
$C_{21}H_{16}O$	$Pbca$	0.0000	0.0643	0.1764	0.834809	0.01159	0.00070	IµS
$C_{21}H_{18}O$	$P2_1/n$	0.0017	0.0380	0.0976	0.939370	0.00680	0.00017	IµS
$C_{17}H_{16}N_4$	$P\bar{1}$	0.0017	0.0403	0.1111	0.913504	0.00766	0.00047	IµS
$C_{15}H_{10}N_2O_2$	$P2_1/c$	0.0016	0.0367	0.1006	0.934844	0.01294	0.00041	IµS
$C_{188}H_{152}Al_{10}Cl_{10}N_{20}O_{20}$	$C2/m$	0.0029	0.0393	0.1015	0.947411	0.01064	0.00043	IµS
$C_{16}H_{12}AlClN_2S_2$	$P\bar{1}$	0.0034	0.0396	0.0990	0.925543	0.01511	0.00082	IµS
$C_{15}H_{10}N_2OS$	$P\bar{1}$	0.0017	0.0343	0.0896	0.975204	0.00955	0.00058	IµS
$C_{16}H_{15}N_3OS$	$P2_1$	0.0041	0.0338	0.0848	0.925305	0.00730	0.00038	IµS
$C_{17}H_{14}N_2O_2$	$P\bar{1}$	0.0021	0.0380	0.0979	0.925305	0.00766	0.00036	IµS
$C_{14}H_9N_3S_2$	$P2_1$	0.0046	0.0310	0.0804	0.943252	0.01064	0.00085	IµS
$C_{71}H_{60}N_{12}S_8$	$P\bar{1}$	0.0024	0.0350	0.0880	0.955338	0.00623	0.00037	IµS
$C_{16}H_{16}BrLiN_4$	$P2_1/c$	0.0020	0.0194	0.0510	0.896043	0.00559	0.00033	IµS
$C_{28}H_{38}N_4$	$P2_1/n$	0.0020	0.0446	0.1264	0.918814	0.00642	0.00043	IµS
$C_{70}H_{84}N_4O_2Si_2$	$P2_1/n$	0.0022	0.0425	0.1063	0.925171	0.00355	0.00023	IµS
$C_{19}H_{31}GeKN_2OS_2$	$P2_1/c$	0.0033	0.0302	0.0706	0.908006	0.00532	0.00030	IµS
$C_{25}H_{39}Cl_2N_3Si$	$P2_1/c$	0.0019	0.0305	0.0803	0.910139	0.00339	0.00021	IµS
$C_{22}H_{51}ClN_2Si_6$	$P2_1/c$	0.0030	0.0402	0.1025	0.916723	0.00565	0.00030	IµS
$C_8H_{14}Br_2S_2$	$P2_1/c$	0.0030	0.0223	0.0468	0.781950	0.00784	0.00038	IµS
$C_{91}H_{88}O_{20}$	$P2_1/c$	0.0020	0.0409	0.1190	0.921797	0.00275	0.00010	IµS
$C_{21}H_{18}O$	Cc	0.0033	0.0360	0.0824	0.910408	0.00808	0.00061	IµS
$C_{10}H_6N_2$	$P2_1/n$	0.0018	0.0344	0.0932	0.910408	0.01352	0.00067	IµS
$C_{34}H_{26}MgN_4O_4$	$P2_1/n$	0.0019	0.0416	0.1105	0.922799	0.00903	0.00025	IµS
$C_{21}H_{25}PS$	$P2_1/c$	0.0021	0.0361	0.0876	0.948095	0.00647	0.00028	IµS
$C_{52}H_{82}Cl_2N_8Si_4$	$P2_1/n$	0.0034	0.0373	0.1041	0.844316	0.00628	0.00028	IµS
$C_{67}H_{100}N_8O_6Si_4$	$P2_1/n$	0.0030	0.0423	0.1053	0.919909	0.00718	0.00024	IµS
$C_{14}H_{23}N_3$	$Pbca$	0.0015	0.0410	0.1221	0.919909	0.01393	0.00046	IµS
$C_{22}H_{26}O_8$	$P2_1/n$	0.0012	0.0368	0.1037	0.947192	0.00213	0.00020	TXS
$C_{32}H_{26}BF_{10}NOP$	$C2/c$	0.0010	0.0372	0.1178	0.959487	0.00157	0.00006	TXS
$C_{32}H_{27}BF_{10}NP$	$P2_1/n$	0.0006	0.0367	0.1236	0.964414	0.00158	0.00004	TXS
$C_{20}H_{14}S_2$	$P2_1/n$	0.0030	0.0444	0.1166	0.931303	0.00339	0.00035	TXS
$C_{26}H_{34}N_4$	$P2_1/c$	0.0016	0.0385	0.1109	0.963380	0.00315	0.00025	TXS
$C_{26}H_{34}N_4$	$P2_1/c$	0.0013	0.0417	0.1202	0.942478	0.00323	0.00029	TXS
$C_{10}H_{14}N_2O_5$	$P2_1/c$	0.0018	0.0335	0.0800	0.941524	0.00299	0.00022	TXS
$C_{10}H_{10}S_2$	$P2_1/n$	0.0024	0.0328	0.0826	0.877650	0.00311	0.00025	TXS
$C_{30}H_{28}N_2O_4$	$P\bar{1}$	0.0021	0.0420	0.1032	0.920714	0.00300	0.00022	TXS

$C_{12}H_{11}NO$	$C2/c$	0.0020	0.0383	0.0935	0.952509	0.00419	0.00044	TXS
$C_{24}H_{26}O_6$	$Pbca$	0.0020	0.0397	0.1051	0.827609	0.00271	0.00029	TXS
$C_{42}H_{49}ClN_2OSi$	$P2_1/c$	0.0031	0.0404	0.1259	0.841095	0.00376	0.00029	TXS
$C_{70}H_{84}N_4O_2Si_2$	$P2_1/n$	0.0022	0.0424	0.1066	0.925171	0.00355	0.00023	TXS
$C_{25}H_{39}Cl_2N_3Si$	$P2_1/c$	0.0019	0.0305	0.0804	0.910139	0.00339	0.00021	TXS
$C_{17}H_{19}AlN_2$	$Pbca$	0.0029	0.0446	0.1051	0.788407	0.00280	0.00027	TXS
$C_{24}H_{12}F_{12}O_3$	$C2/c$	0.0030	0.0489	0.1161	0.767404	0.00256	0.00034	TXS
$C_{91}H_{88}O_{20}$	$P2_1/c$	0.0020	0.0411	0.1196	0.921797	0.00276	0.00010	TXS
$C_6H_9BrO_4$	$P2_12_12_1$	0.0030	0.0114	0.0305	0.692555	0.00209	0.00039	TXS
$C_{21}H_{41}N_3Si_3$	$P\bar{1}$	0.0018	0.0303	0.0826	0.958820	0.00187	0.00015	TXS
$H_4Na_2O_6W$	$Pbca$	0.0000	0.0146	0.0329	0.717586	0.00127	0.00006	TXS
C_4CoSc_3	$Immm$	0.0006	0.0118	0.0329	0.821709	0.00073	0.00014	TXS
$C_{13}H_{10}F_3IO_3S$	$P2_1/c$	0.0042	0.0201	0.0473	0.913603	0.00448	0.00035	TXS
$C_{33}H_{41}I_3N_2Pd$	$P2_1/n$	0.0047	0.0229	0.0504	0.908640	0.00242	0.00022	TXS
$C_{26}H_{52}N_2Rb_2Si_4$	$C2/c$	0.0030	0.0303	0.0645	0.741322	0.00117	0.00025	TXS
$C_{12.46}H_{48}K_2N_{5.54}Si_4$	$P2_1/n$	0.0000	0.0218	0.0580	0.912798	0.00243	0.00018	TXS
$C_{18}H_{30}Cs_2O_4$	$Pbca$	0.0038	0.0243	0.0599	0.568556	0.00021	0.00012	TXS
C_5H_8CsN	$Pnma$	0.0030	0.0180	0.0412	0.374883	0.00015	0.00010	TXS
$C_{34}H_{46}N_4O_2Rb_2$	$Pbca$	0.0050	0.0330	0.0858	0.701503	0.00216	0.00037	TXS
$C_{34}H_{26}MgN_4O_4$	$P2_1/n$	0.0016	0.0399	0.1091	0.922530	0.00515	0.00023	TXS
$C_{12}H_4N_4$	$C2/c$	0.0011	0.0338	0.0963	0.962606	0.00816	0.00047	TXS
$C_{18}H_{17}CuO_6$	$C2/c$	0.0026	0.0260	0.0650	0.932144	0.00760	0.00029	TXS
$C_{28}H_{18}N_2$	$C2/c$	0.0021	0.0396	0.1113	0.951959	0.01167	0.00070	TXS
$C_{11}H_{10}O_2S$	$P2_12_12_1$	0.0024	0.0249	0.0668	0.951589	0.00184	0.00023	TXS

A5. Collecting charge density data – A tough job for detectors

A5.1. $R_{\text{r.i.m.}}$ values

Resolution [Å]	Ag 007 CdTe 300K	Ag IμS CdTe 300K	In MeJ PHOTON II	Ag IμS APEX II
2.40	0.0191	0.0076	0.0180	0.0074
2.00	0.0254	0.0129	0.0202	0.0144
1.60	0.0204	0.0158	0.0241	0.0166
1.20	0.0272	0.0194	0.0286	0.0242
1.10	0.0342	0.0241	0.0376	0.0342
1.00	0.0311	0.0241	0.0378	0.0321
0.90	0.0322	0.0312	0.0504	0.0456
0.85	0.0382	0.0417	0.0723	0.0563
0.80	0.0423	0.0411	0.0736	0.0460
0.75	0.0429	0.0438	0.0680	0.0417
0.70	0.0754	0.0467	0.0728	0.0451
0.65	0.0605	0.0566	0.0876	0.0607
0.60	0.0664	0.0664	0.0889	0.0680
0.58	0.0765	0.0772	0.1093	0.0924
0.56	0.0922	0.0998	0.1428	0.1310
0.54	0.0926	0.1159	0.1502	0.1189
0.52	0.1099	0.1355	0.1693	0.1364
0.50	0.1364	0.1686	0.2459	0.2073

A5.2. $R_{\text{p.i.m.}}$ values

Resolution [Å]	Ag 007 CdTe 300K	Ag IμS CdTe 300K	In MeJ PHOTON II	Ag IμS APEX II
2.40	0.0038	0.0016	0.0031	0.0017
2.00	0.0058	0.0027	0.0030	0.0035
1.60	0.0036	0.0030	0.0032	0.0037
1.20	0.0046	0.0031	0.0032	0.0053
1.10	0.0057	0.0036	0.0041	0.0077
1.00	0.0052	0.0035	0.0041	0.0075
0.90	0.0051	0.0042	0.0054	0.0105
0.85	0.0062	0.0055	0.0076	0.0114
0.80	0.0065	0.0057	0.0077	0.0072
0.75	0.0070	0.0066	0.0081	0.0064
0.70	0.0119	0.0072	0.0089	0.0068
0.65	0.0098	0.0098	0.0122	0.0097
0.60	0.0107	0.0124	0.0139	0.0114
0.58	0.0127	0.0149	0.0182	0.0158
0.56	0.0151	0.0194	0.0248	0.0226
0.54	0.0155	0.0235	0.0278	0.0219
0.52	0.0189	0.0278	0.0325	0.0259
0.50	0.0237	0.0347	0.0487	0.0400

A6. Validation of charge-density models

A6.1. Paracyclophane: Refinement strategy

Abbreviations: *D*, dipoles; *Q*, quadrupoles; *O*, octapoles; *H*, hexadecapoles; *M*, monopoles; *xyz*, positional coordinates; *xyz*(H), hydrogen coordinates; *U*2, displacement parameters; *U*3 and *U*4, 3^{rd}- or 4^{th}-order Gram-Charlier parameters; κ, spherical expansion parameters, the aspherical expansion parameters κ' were kept fixed at values suggested by Volkov et al. (2001), C1: 0.87, C2: 0.92 and C3: 0.96 and 1.1 and 1.18 for the hydrogen κ and κ', respectively. *d*: data, *p*: parameter, d_l: data truncated to $\sin(\theta)/\lambda < 0.5$, p_{mp}: mono- and multipole parameter.

step	**refined parameters**						***d***	***p***	***d*/*p***	d_l	p_{mp}	κ	d_l/p_{mp}
01	scalefactor						1231	1	1231.0	178	0	0	-
02	-	-	-	-	*D Q O*	-	1231	28	44.0	178	27	0	6.6
03	-	*U*2	-	*M*	*D Q O*	-	1231	42	29.3	178	27	0	6.6
04	*xyz*(H)	-	-	*M*	*D Q O*	-	178	7	25.4	178	0	0	-
05	*xyz*	*U*2	-	-	-	-	1231	49	25.1	178	27	0	6.6
06	*xyz*(H)	-	-	*M*	*D Q O*	-	178	7	25.4	178	0	0	-
07	*xyz*(H)	*U*2	-	-	-	-	1231	53	23.2	178	32	0	5.6
08	*xyz*	*U*2	*U*3(C3)	*M*	*D Q O*	-	1231	59	20.9	178	32	0	5.6
09	*xyz*	*U*2†	*U*3(C3)	*M*	*D Q O*	-	1231	71	17.3	178	32	0	5.6
10	*xyz*	*U*2†	*U*3(C3)	*M*	*D Q O*	κ	1231	74	16.6	178	32	3	5.1

†*U*2 refined for both hydrogen (H2, H3) atoms.

XDLSM results

Number of data	2112
Rejected based on OBS	0
Rejected based on SIGOBS	0
Rejected based on SINTHL	881
Total number of rejections	881
Included in the refinement	1231
$R(F)$	0.0148
$R(F^2)$	0.0160
$wR(F)$	0.0162
$wR(F^2)$	0.0334
*w*GoF	1.1698
GoF	2.8587
Nref/Nv	16.64

A6.2. Paracyclophane: Absorption correction and data scaling

Equivalent reflections defined by point group 4/*mmm* for scaling and error model, applied odd/even spherical harmonics: 7/8, effective data to parameter ratio for parameter determination 10.54. Established error model 0: K=1, g=0, g_{ini} = 0. Estimated minimum and maximum transmission: 0.9204 - 1.0, additional spherical absorption correction applied with $\mu \cdot r = 0$.

A6.3. Paracyclophane: *XPREP* data statistics

Resolution			#Data	#Theory	%Completeness	Multiplicity	$R_{\mathrm{r.i.m.}}$	$R_{\mathrm{p.i.m.}}$
Inf	-	2.40	23	23	100	20.91	0.0076	0.0016
2.40	-	2.00	11	11	100	30.55	0.0129	0.0027
2.00	-	1.60	27	27	100	28.33	0.0158	0.0030
1.60	-	1.20	68	68	100	37.56	0.0194	0.0031
1.20	-	1.10	30	30	100	47.77	0.0241	0.0036
1.10	-	1.00	51	51	100	50.53	0.0241	0.0035
1.00	-	0.90	65	65	100	54.08	0.0312	0.0042
0.90	-	0.85	45	45	100	56.58	0.0417	0.0055
0.85	-	0.80	61	61	100	50.57	0.0411	0.0057
0.80	-	0.75	70	70	100	46.30	0.0438	0.0066
0.75	-	0.70	95	95	100	41.86	0.0467	0.0072
0.70	-	0.65	123	123	100	35.25	0.0566	0.0098
0.65	-	0.60	168	168	100	28.63	0.0664	0.0124
0.60	-	0.58	86	87	98.85	26.61	0.0772	0.0149
0.58	-	0.56	95	95	100	26.44	0.0998	0.0194
0.56	-	0.54	106	107	99.07	24.04	0.1159	0.0235
0.54	-	0.52	127	127	100	25.14	0.1355	0.0278
0.52	-	0.50	142	143	99.3	23.79	0.1686	0.0347
0.50	-	0.49	85	85	100	24.20	0.2085	0.0422
0.49	-	0.48	83	84	98.81	22.81	0.2124	0.0427
0.48	-	0.47	101	102	99.02	22.50	0.2138	0.0447
0.47	-	0.46	95	98	96.94	22.27	0.2681	0.0558
0.46	-	0.45	117	117	100	21.65	0.2677	0.0566
0.45	-	0.44	128	128	100	21.26	0.3293	0.0708
0.44	-	0.40	611	624	97.92	18.52	0.5688	0.1277
0.50	-	0.40	1220	1238	98.55	20.41	0.3178	0.0682
Inf	-	0.40	2613	2634	99.20	27.68	0.0290	0.0050

A6.4. Paracyclophane: *XDRfree* results

Atom	parm	Ref	esd	Mean	std
KS	KS01	0.978030	0.004465	0.978394	0.001614
KS	KS02	0.974630	0.003795	0.974450	0.001403
KS	KS03	0.969404	0.008216	0.970393	0.002241
C(1)	D1+	-0.024257	0.005254	-0.023216	0.002379
C(1)	D1-	0.008939	0.003986	0.008508	0.001605
C(1)	M1	2.015290	0.018658	2.014708	0.008265
C(1)	O1+	-0.166778	0.004541	-0.166917	0.001640
C(1)	O1-	0.036841	0.004026	0.036528	0.001294
C(1)	O3+	0.052327	0.003962	0.053111	0.001295
C(1)	O3-	0.000736	0.003955	0.000179	0.001415
C(1)	Q0	0.051988	0.004228	0.053499	0.002991
C(1)	Q2+	0.084229	0.003809	0.084240	0.002486
C(1)	Q2-	-0.034532	0.003731	-0.034609	0.001557
C(1)	U11	0.019696	0.000059	0.019693	0.000014

C(1)	U12	-0.003390	0.000055	-0.003382	0.000020
C(1)	U13	-0.000906	0.000037	-0.000908	0.000011
C(1)	U22	0.019696	0.000059	0.019693	0.000014
C(1)	U23	-0.000906	0.000037	-0.000908	0.000011
C(1)	U33	0.022253	0.000087	0.022250	0.000033
C(1)	X	0.372158	0.000017	0.372158	0.000004
C(1)	Y	0.372158	0.000017	0.372158	0.000004
C(1)	Z	0.347171	0.000022	0.347173	0.000006
C(2)	D0	-0.043495	0.012183	-0.043865	0.003805
C(2)	M1	4.023671	0.034832	4.028448	0.015258
C(2)	O0	0.248927	0.006863	0.248672	0.001369
C(2)	O2+	-0.151403	0.005071	-0.151880	0.001074
C(2)	O2-	-0.025729	0.004378	-0.025555	0.001829
C(2)	Q0	0.059561	0.008632	0.060834	0.003490
C(2)	Q2+	0.188424	0.005219	0.187991	0.002004
C(2)	Q2-	0.027364	0.004408	0.027586	0.001273
C(2)	U11	0.017207	0.000060	0.017206	0.000014
C(2)	U12	0.001246	0.000040	0.001248	0.000012
C(2)	U13	-0.002674	0.000041	-0.002678	0.000012
C(2)	U22	0.020172	0.000063	0.020170	0.000013
C(2)	U23	0.001733	0.000044	0.001732	0.000010
C(2)	U33	0.028523	0.000075	0.028523	0.000017
C(2)	X	0.248062	0.000017	0.248062	0.000005
C(2)	Y	0.467311	0.000018	0.467311	0.000005
C(2)	Z	0.424365	0.000016	0.424365	0.000004
C(3)	C111	-0.000684	0.000119	-0.000688	0.000042
C(3)	C112	0.000168	0.000049	0.000167	0.000024
C(3)	C113	0.000611	0.000054	0.000602	0.000018
C(3)	C122	0.000168	0.000049	0.000167	0.000024
C(3)	C123	-0.000653	0.000044	-0.000652	0.000011
C(3)	C133	0.000049	0.000032	0.000045	0.000011
C(3)	C222	-0.000684	0.000119	-0.000688	0.000042
C(3)	C223	0.000611	0.000054	0.000602	0.000018
C(3)	C233	0.000049	0.000032	0.000045	0.000011
C(3)	C333	0.000090	0.000083	0.000062	0.000037
C(3)	D1+	-0.002117	0.009992	0.001322	0.006314
C(3)	D1-	-0.007198	0.012788	-0.005606	0.005254
C(3)	M1	1.922709	0.065921	1.912289	0.021577
C(3)	O1+	-0.026404	0.006444	-0.025837	0.003736
C(3)	O1-	-0.074668	0.005949	-0.075118	0.003673
C(3)	O3+	0.112050	0.004683	0.110947	0.003003
C(3)	O3-	-0.014146	0.004090	-0.013652	0.002516
C(3)	Q0	-0.061694	0.008735	-0.061670	0.005862
C(3)	Q2+	-0.002515	0.004069	-0.002369	0.003325
C(3)	Q2-	0.028052	0.005302	0.027376	0.003416
C(3)	U11	0.034569	0.000088	0.034565	0.000047
C(3)	U12	-0.013888	0.000110	-0.013887	0.000049
C(3)	U13	-0.001310	0.000049	-0.001306	0.000019
C(3)	U22	0.034569	0.000088	0.034565	0.000047

C(3)	U23	-0.001310	0.000049	-0.001306	0.000019
C(3)	U33	0.021064	0.000099	0.021057	0.000059
C(3)	X	0.427453	0.000079	0.427447	0.000031
C(3)	Y	0.427453	0.000079	0.427447	0.000031
C(3)	Z	0.197494	0.000102	0.197463	0.000050
H(2)	D0	0.162007	0.015566	0.161849	0.005759
H(2)	M1	0.986409	0.028052	0.987035	0.010876
H(2)	U11	0.033244	0.002442	0.033227	0.000771
H(2)	U12	-0.001342	0.002028	-0.001105	0.000583
H(2)	U13	-0.003815	0.001876	-0.003767	0.000730
H(2)	U22	0.041706	0.002849	0.041529	0.001094
H(2)	U23	0.000676	0.001927	0.000587	0.000545
H(2)	U33	0.045151	0.002537	0.045397	0.000797
H(3)	D0	0.223610	0.034210	0.229729	0.012756
H(3)	M1	1.051921	0.049024	1.057560	0.017770
H(3)	U11	0.058312	0.006308	0.059262	0.003642
H(3)	U12	-0.023084	0.003526	-0.023558	0.002063
H(3)	U13	0.000585	0.003314	0.000701	0.000921
H(3)	U22	0.085952	0.003953	0.086075	0.001362
H(3)	U23	0.022624	0.003107	0.022293	0.000997
H(3)	U33	0.046117	0.003013	0.046179	0.001332

A6.5. Paracyclophane: XDRfree results for the bond critical points

Atom1	Atom2	property	refined	esd	mean	std
C1	C2	R1	0.6905	-	0.690715	0.001519
C3	C1	R1	0.7349	-	0.735360	0.004173
H2	C2	R1	0.3918	-	0.391590	0.004275
H3	C3	R1	0.4548	-	0.458495	0.008016
C1	C2	R2	0.7089	-	0.708665	0.001556
C3	C1	R2	0.7712	-	0.771005	0.004378
H2	C2	R2	0.6912	-	0.691415	0.004275
H3	C3	R2	0.6484	-	0.644760	0.007959
C1	C2	Rij	1.3994	-	1.399375	0.000055
C3	C1	Rij	1.5061	-	1.506360	0.000463
H2	C2	Rij	1.0830	-	1.083000	0
H3	C3	Rij	1.1032	-	1.103240	0.000712
C1	C2	X	2.393230	-	2.393162	0.001099
C3	C1	X	3.084955	-	3.084838	0.001981
H2	C2	X	1.499251	-	1.500352	0.003132
H3	C3	X	2.790924	-	2.793899	0.005652
C1	C2	Y	3.228336	-	3.228276	0.000826
C3	C1	Y	3.084955	-	3.084838	0.001981
H2	C2	Y	4.040268	-	4.039505	0.003300
H3	C3	Y	3.525766	-	3.523844	0.005701
C1	C2	Z	3.550557	-	3.551026	0.001013
C3	C1	Z	2.494673	-	2.494832	0.003668
H2	C2	Z	3.575232	-	3.572480	0.003404

H3	C3	Z	1.483600	-	1.484562	0.003266
C1	C2	ell	0.21	-	0.2105	0.002236
C3	C1	ell	0.02	-	0.0205	0.009987
H2	C2	ell	0.05	-	0.0500	0
H3	C3	ell	0.08	-	0.0845	0.008256
C1	C2	lap	-19.921	0.011	-19.93720	0.092576
C3	C1	lap	-12.353	0.012	-12.30430	0.186377
H2	C2	lap	-17.580	0.071	-17.59375	0.105535
H3	C3	lap	-13.457	0.116	-13.49595	0.309352
C1	C2	rho	2.119	0.005	2.12060	0.003485
C3	C1	rho	1.690	0.010	1.69065	0.004332
H2	C2	rho	1.787	0.023	1.78825	0.007525
H3	C3	rho	1.662	0.052	1.66460	0.012266

A6.6. Paracyclophane: Model quality indicators

Left: Normal probability plot (top left), weighting parameters: 0.017 and 0.002. The fractal dimension plot (top right) and the variation of grouped observed and calculated structure factors with the resolution (bottom).

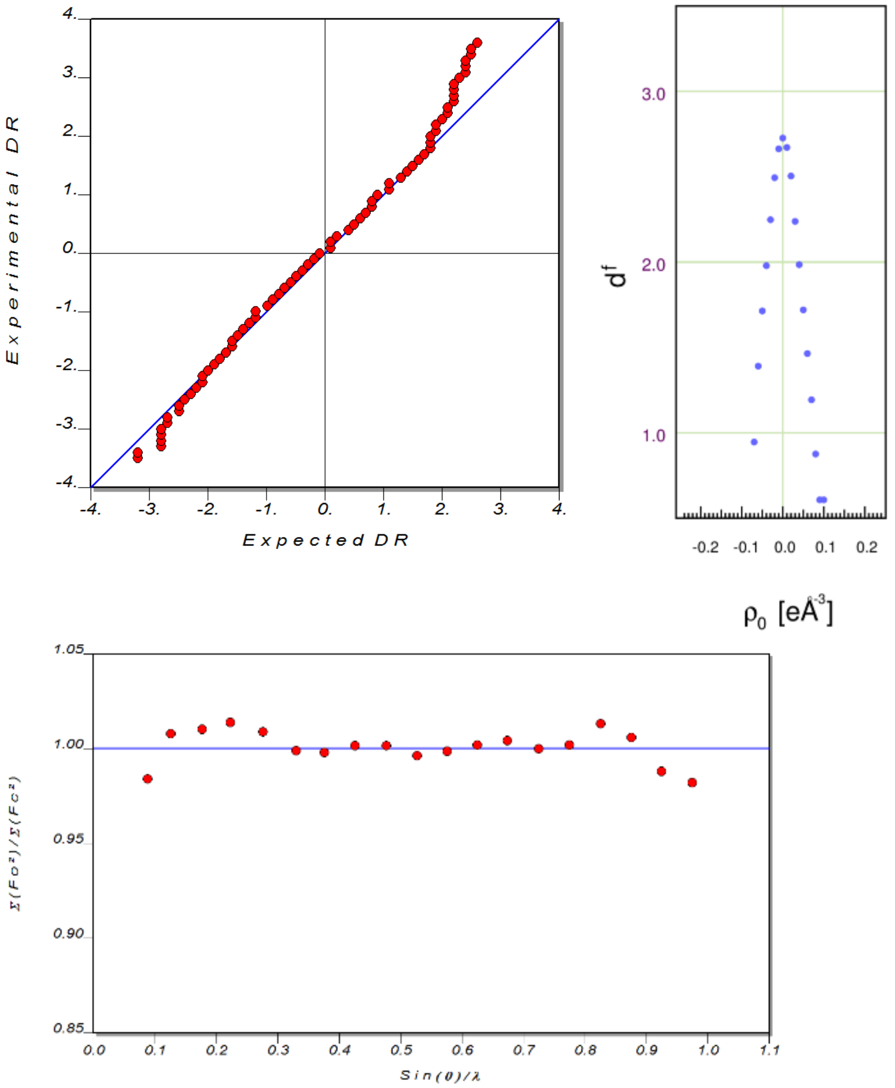

DMSDA of selected bonds.

Atom 1	Atom 2	isotropic H	rigid-body H	anisotropic H
C(1)	C(2)	-1	0	-1
C(1)	C(3)	4	4	1
C(2)	H(2)	-	58	204
C(3)	H(3)	-	72	266

A6.7. *i*Pr$_2$SPAnH: Absorption correction and data scaling

Equivalent reflections defined by the point group *mmm* were used for the scaling and the error model determination, applied odd/even spherical harmonics: 7/8, effective data to parameter ratio for parameter determination 22.06. Established error model 0: $K = 1$, $g = 0$, $g_{ini} = 0$. Estimated minimum and maximum transmission: 0.8845 – 0.9285, additional spherical absorption correction applied with $\mu \cdot r = 0.05$. Correction factor for the low energy contamination: 0.003.

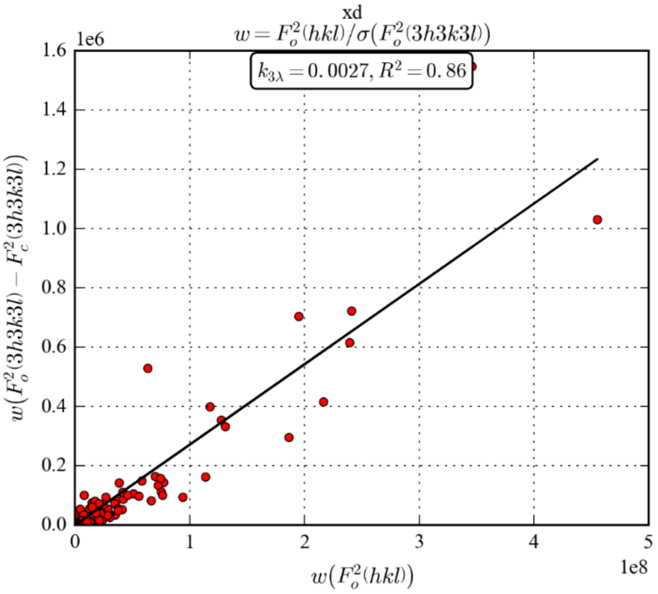

A6.8. *i*Pr$_2$SPAnH: *XPREP* data statistics

Resolution			#Data	#Theory	%Completeness	Multiplicity	$R_{\mathrm{r.i.m.}}$	$R_{\mathrm{p.i.m.}}$
Inf	-	2.40	176	178	98.88	24.88	0.0119	0.0024
2.40	-	2.00	114	115	99.13	29.57	0.0139	0.0026
2.00	-	1.60	248	250	99.2	31.42	0.0157	0.0027
1.60	-	1.20	675	675	100	29.77	0.0211	0.0038
1.20	-	1.10	339	339	100	21.40	0.0260	0.0055
1.10	-	1.00	485	485	100	18.58	0.0287	0.0065
1.00	-	0.90	723	723	100	21.44	0.0277	0.0059
0.90	-	0.85	487	487	100	22.38	0.0306	0.0064
0.85	-	0.80	620	620	100	21.71	0.0348	0.0074
0.80	-	0.75	799	799	100	20.47	0.0459	0.0101
0.75	-	0.70	1031	1031	100	14.40	0.0406	0.0104
0.70	-	0.65	1366	1367	99.93	11.64	0.0356	0.0103
0.65	-	0.60	1863	1863	100	10.77	0.0446	0.0134
0.60	-	0.58	911	911	100	7.84	0.0484	0.0170
0.58	-	0.56	1069	1069	100	7.16	0.0521	0.0194
0.56	-	0.54	1221	1221	100	6.94	0.0656	0.0247
0.54	-	0.52	1394	1394	100	6.64	0.0741	0.0285
0.52	-	0.50	1661	1661	100	6.33	0.0909	0.0357

0.50	-	0.49	925	925	100	6.06	0.1027	0.0414
0.49	-	0.48	990	990	100	5.88	0.1068	0.0435
0.48	-	0.47	1096	1096	100	5.70	0.1114	0.0461
0.47	-	0.46	1187	1187	100	5.44	0.1169	0.0495
0.46	-	0.45	1306	1313	99.47	5.06	0.1168	0.0509
0.45	-	0.45	13	37	35.14	0.51	0.3325	0.1968
0.55	-	0.45	9189	9220	99.66	5.95	0.0934	0.0376
Inf	-	0.45	20699	20736	99.82	11.23	0.0256	0.0060

A6.9. *i*Pr$_2$SPAnH: Refinement strategy

Multipole refinement strategy for (iPr)$_2$SPAnH. Abbreviations: *D*, dipoles; *Q*, quadrupoles; *O*, octapoles; *H*, hexadecapoles; *M*, monopoles; *xyz*, positional coordinates; xyz-H, hydrogen coordinates; U_{ij}, displacement parameters; GC3 and GC4, anharmonic Gram-Charlier parameters of 3rd and 4th order, respectively; κ, spherical expansion parameters; κ’, aspherical expansion parameters.

XDLSM results	
Number of data	19329
Rejected based on OBS	894
Rejected based on SIGOBS	894
Rejected based on SINTHL	0
Total number of rejections	894
Included in the refinement	18435
$R(F)$	0.0201
$R(F^2)$	0.0149
$wR(F)$	0.0081
$wR(F^2)$	0.0163
*w*GoF	1.2849
GoF	1.2849
Nref/Nv	55.90

A6.10. *i*Pr$_2$SPAnH: *XDRfree* parameter distribution

atom	parameter	pval	esd	mean	std
KS	KS01	0.988615	0.000951	0.988643	0.000664
KS	KS02	0.989029	0.001721	0.989123	0.000945
KS	KS03	1.000776	0.001930	1.000758	0.001249
KS	KS04	1.010473	0.001116	1.010499	0.000488
KS	KS05	1.002042	0.001086	1.002068	0.000803
KS	KS06	1.006146	0.001016	1.006174	0.000538
KS	KS07	1.007240	0.001798	1.007216	0.001117
KS	KS08	0.958742	0.002081	0.958858	0.000996
KS	KS09	0.959341	0.001652	0.959408	0.000643
S(1)	D0	0.003367	0.005881	0.003761	0.003264
S(1)	H0	0.029942	0.005660	0.029919	0.003283
S(1)	M1	6.460373	0.014080	6.460930	0.013880
S(1)	O0	0.063187	0.005504	0.063156	0.002919
S(1)	Q0	-0.165268	0.005332	-0.165025	0.004769
S(1)	U11	0.011358	0.000014	0.011358	0.000008

S(1)	U12	-0.003248	0.000012	-0.003247	0.000003
S(1)	U13	0.004332	0.000012	0.004331	0.000004
S(1)	U22	0.016155	0.000016	0.016154	0.000005
S(1)	U23	-0.003780	0.000012	-0.003780	0.000003
S(1)	U33	0.018223	0.000016	0.018222	0.000005
S(1)	X	0.604066	0.000008	0.604066	0.000002
S(1)	Y	0.330804	0.000005	0.330804	0.000003
S(1)	Z	0.535804	0.000004	0.535804	0.000002
P(1)	D1+	-0.022415	0.005895	-0.022340	0.005115
P(1)	D1-	0.108233	0.006601	0.107706	0.005188
P(1)	H0	0.021860	0.005917	0.021732	0.002113
P(1)	H2+	-0.057341	0.005823	-0.057212	0.003380
P(1)	H2-	0.091237	0.005812	0.091322	0.002711
P(1)	H4+	0.028494	0.005292	0.028313	0.002453
P(1)	H4-	0.003807	0.005333	0.003855	0.002438
P(1)	M1	4.757299	0.024372	4.756930	0.016523
P(1)	O1+	-0.158429	0.005742	-0.158117	0.002766
P(1)	O1-	-0.291365	0.006097	-0.291215	0.003519
P(1)	O3+	0.281299	0.005853	0.280956	0.002952
P(1)	O3-	-0.034365	0.004983	-0.034243	0.002845
P(1)	Q0	-0.044567	0.006291	-0.044398	0.004607
P(1)	Q2+	0.015114	0.005922	0.015262	0.003693
P(1)	Q2-	-0.066967	0.005440	-0.066561	0.003410
P(1)	U11	0.009523	0.000013	0.009523	0.000004
P(1)	U12	-0.000740	0.000011	-0.00074	0.000004
P(1)	U13	0.001023	0.000011	0.001023	0.000003
P(1)	U22	0.009293	0.000013	0.009292	0.000004
P(1)	U23	-0.000799	0.000010	-0.000799	0.000002
P(1)	U33	0.008739	0.000013	0.008738	0.000005
P(1)	X	0.436724	0.000003	0.436724	0.000001
P(1)	Y	0.298216	0.000002	0.298216	0.000001
P(1)	Z	0.563275	0.000002	0.563275	0.000001
C(1)	D0	-0.009743	0.005717	-0.009628	0.003054
C(1)	D1-	0.001693	0.003264	0.001631	0.002646
C(1)	H0	0.027899	0.007153	0.027787	0.003225
C(1)	H1-	-0.015357	0.005560	-0.015208	0.002104
C(1)	H2+	0.005099	0.006474	0.005136	0.002752
C(1)	H3-	-0.003285	0.005235	-0.003283	0.002173
C(1)	H4+	-0.017915	0.005692	-0.017926	0.003720
C(1)	M1	4.116975	0.019785	4.117306	0.011969
C(1)	O0	0.218968	0.005863	0.218545	0.004400
C(1)	O1-	-0.020146	0.004519	-0.019902	0.001914
C(1)	O2+	0.130328	0.005603	0.130099	0.002495
C(1)	O3-	-0.010027	0.004036	-0.009875	0.002246
C(1)	Q0	0.045953	0.005094	0.046216	0.002445
C(1)	Q1-	0.000412	0.003849	0.000467	0.002372
C(1)	Q2+	-0.132977	0.005143	-0.13286	0.002284
C(1)	U11	0.011841	0.000049	0.011842	0.000014
C(1)	U12	-0.000709	0.000046	-0.000709	0.000016

C(1)	U13	0.000375	0.000041	0.000375	0.000011
C(1)	U22	0.010514	0.000049	0.010514	0.000016
C(1)	U23	-0.000703	0.000038	-0.000703	0.000009
C(1)	U33	0.008699	0.000048	0.008696	0.000017
C(1)	X	0.402034	0.000014	0.402034	0.000006
C(1)	Y	0.314543	0.000010	0.314543	0.000004
C(1)	Z	0.648702	0.000007	0.648702	0.000002
C(2)	D0	0.003279	0.003744	0.003139	0.001446
C(2)	D1-	0.019279	0.003109	0.019160	0.001573
C(2)	H0	0.000310	0.003993	0.000414	0.002029
C(2)	H1-	-0.016776	0.003472	-0.016711	0.001270
C(2)	H2+	-0.012128	0.003351	-0.012028	0.001627
C(2)	H3-	-0.006862	0.003084	-0.006815	0.001363
C(2)	H4+	0.005180	0.002630	0.005091	0.001420
C(2)	M1	3.977951	0.010767	3.978205	0.006286
C(2)	O0	-0.215900	0.003547	-0.215817	0.001666
C(2)	O1-	0.001635	0.002920	0.001663	0.001115
C(2)	O2+	-0.160591	0.002917	-0.160682	0.001322
C(2)	O3-	-0.008166	0.002393	-0.008150	0.001071
C(2)	Q0	0.109417	0.003491	0.109360	0.001186
C(2)	Q1-	-0.004275	0.002883	-0.004248	0.001382
C(2)	Q2+	-0.149979	0.002520	-0.149926	0.001332
C(2)	U11	0.011418	0.000049	0.011417	0.000014
C(2)	U12	-0.000210	0.000041	-0.000209	0.000011
C(2)	U13	0.000887	0.000039	0.000886	0.000008
C(2)	U22	0.011369	0.000049	0.011369	0.000014
C(2)	U23	-0.000026	0.000038	-0.000026	0.000012
C(2)	U33	0.009275	0.000047	0.009274	0.000012
C(2)	X	0.303085	0.000013	0.303085	0.000006
C(2)	Y	0.264623	0.000010	0.264623	0.000003
C(2)	Z	0.676375	0.000007	0.676375	0.000002
C(3)	D0	0.001302	0.003638	0.001479	0.001562
C(3)	D1-	-0.009450	0.004154	-0.009497	0.002222
C(3)	H0	0.033298	0.003798	0.033076	0.002280
C(3)	H1-	-0.005084	0.003969	-0.004959	0.002477
C(3)	H2+	0.015550	0.003532	0.015431	0.001520
C(3)	H3-	-0.002007	0.003695	-0.001956	0.001600
C(3)	H4+	0.017050	0.003442	0.017070	0.001206
C(3)	M1	4.135488	0.011895	4.135395	0.009004
C(3)	O0	-0.245379	0.003469	-0.245166	0.001949
C(3)	O1-	-0.014885	0.003189	-0.014918	0.001348
C(3)	O2+	-0.152249	0.003382	-0.152128	0.001782
C(3)	O3-	-0.026275	0.003185	-0.026173	0.001776
C(3)	Q0	0.098229	0.002993	0.098276	0.001541
C(3)	Q1-	-0.016287	0.003456	-0.016393	0.001555
C(3)	Q2+	-0.168099	0.003558	-0.168052	0.001583
C(3)	U11	0.011218	0.000051	0.011219	0.000013
C(3)	U12	-0.001291	0.000044	-0.001291	0.000015
C(3)	U13	0.000820	0.000042	0.000820	0.000014

C(3)	U22	0.014894	0.000056	0.014893	0.000018
C(3)	U23	-0.000479	0.000041	-0.000478	0.000010
C(3)	U33	0.011180	0.000051	0.011179	0.000012
C(3)	X	0.206908	0.000014	0.206908	0.000006
C(3)	Y	0.221081	0.000010	0.221081	0.000004
C(3)	Z	0.640944	0.000007	0.640944	0.000003
C(4)	D0	0.020187	0.003171	0.020212	0.001504
C(4)	D1-	0.023201	0.003546	0.022977	0.001860
C(4)	H0	0.016945	0.003400	0.016993	0.001949
C(4)	H1-	0.003202	0.003377	0.003174	0.001719
C(4)	H2+	0.005578	0.003179	0.005697	0.001828
C(4)	H3-	-0.003464	0.003243	-0.003374	0.001446
C(4)	H4+	-0.002642	0.003047	-0.002637	0.001701
C(4)	M1	4.042535	0.009236	4.042328	0.006275
C(4)	O0	-0.236023	0.003006	-0.235912	0.001985
C(4)	O1-	-0.013910	0.002713	-0.013936	0.001628
C(4)	O2+	-0.155730	0.002986	-0.155586	0.002036
C(4)	O3-	0.020109	0.002740	0.020036	0.001157
C(4)	Q0	0.086965	0.003088	0.086928	0.001665
C(4)	Q1-	0.006874	0.003099	0.006817	0.001369
C(4)	Q2+	-0.175410	0.003069	-0.175249	0.001738
C(4)	U11	0.012383	0.000054	0.012381	0.000016
C(4)	U12	-0.002637	0.000049	-0.002637	0.000012
C(4)	U13	0.001615	0.000044	0.001615	0.000013
C(4)	U22	0.017414	0.000059	0.017413	0.000018
C(4)	U23	0.000192	0.000048	0.000191	0.000011
C(4)	U33	0.014894	0.000056	0.014897	0.000015
C(4)	X	0.119009	0.000014	0.119009	0.000005
C(4)	Y	0.168343	0.000011	0.168343	0.000007
C(4)	Z	0.669890	0.000008	0.669890	0.000003
C(5)	U11	0.014647	0.000059	0.014645	0.000020
C(5)	U12	-0.002744	0.000051	-0.002744	0.000015
C(5)	U13	0.003093	0.000048	0.003094	0.000015
C(5)	U22	0.019040	0.000065	0.019038	0.000023
C(5)	U23	0.002560	0.000048	0.002560	0.000009
C(5)	U33	0.015508	0.000059	0.015511	0.000021
C(5)	X	0.117008	0.000015	0.117008	0.000006
C(5)	Y	0.156671	0.000011	0.156671	0.000005
C(5)	Z	0.736839	0.000008	0.736839	0.000004
C(6)	U11	0.015446	0.000057	0.015445	0.000016
C(6)	U12	-0.000733	0.000051	-0.000734	0.000013
C(6)	U13	0.002720	0.000045	0.002720	0.000017
C(6)	U22	0.017366	0.000059	0.017366	0.000017
C(6)	U23	0.002645	0.000046	0.002644	0.000012
C(6)	U33	0.012056	0.000053	0.012055	0.000021
C(6)	X	0.200112	0.000015	0.200112	0.000005
C(6)	Y	0.203313	0.000011	0.203313	0.000005
C(6)	Z	0.773013	0.000007	0.773013	0.000003
C(7)	U11	0.013243	0.000054	0.013242	0.000015

C(7)	U12	0.000345	0.000043	0.000344	0.000014
C(7)	U13	0.001200	0.000042	0.001199	0.000010
C(7)	U22	0.013263	0.000052	0.013262	0.000011
C(7)	U23	0.000772	0.000040	0.000771	0.000010
C(7)	U33	0.009576	0.000048	0.009577	0.000015
C(7)	X	0.293182	0.000014	0.293182	0.000004
C(7)	Y	0.258723	0.000010	0.258723	0.000004
C(7)	Z	0.744461	0.000007	0.744461	0.000003
C(8)	D0	0.001513	0.005549	0.001568	0.002138
C(8)	D1-	0.010644	0.003252	0.010411	0.002515
C(8)	H0	0.064955	0.006951	0.064610	0.003842
C(8)	H1-	0.001264	0.005370	0.001261	0.004364
C(8)	H2+	0.015363	0.006437	0.015412	0.003627
C(8)	H3-	-0.000312	0.005457	-0.000412	0.003685
C(8)	H4+	-0.002280	0.006084	-0.002149	0.003895
C(8)	M1	4.049344	0.017548	4.049292	0.012332
C(8)	O0	-0.266425	0.005784	-0.266076	0.003452
C(8)	O1-	-0.007053	0.004195	-0.007200	0.001990
C(8)	O2+	-0.158191	0.005734	-0.157890	0.003138
C(8)	O3-	0.002310	0.004261	0.002361	0.002959
C(8)	Q0	0.069891	0.004881	0.070091	0.001682
C(8)	Q1-	0.002345	0.003562	0.002441	0.001907
C(8)	Q2+	-0.197074	0.005452	-0.197057	0.002958
C(8)	U11	0.016836	0.000061	0.016837	0.000015
C(8)	U12	-0.000447	0.000054	-0.000449	0.000022
C(8)	U13	0.000001	0.000045	0.000001	0.000013
C(8)	U22	0.015535	0.000059	0.015537	0.000018
C(8)	U23	0.000026	0.000043	0.000026	0.000012
C(8)	U33	0.009049	0.000052	0.009043	0.000015
C(8)	X	0.374464	0.000016	0.374464	0.000006
C(8)	Y	0.307698	0.000011	0.307697	0.000003
C(8)	Z	0.782642	0.000008	0.782642	0.000003
C(9)	U11	0.015950	0.000056	0.015948	0.000018
C(9)	U12	-0.000064	0.000045	-0.000063	0.000015
C(9)	U13	-0.001478	0.000042	-0.001478	0.000012
C(9)	U22	0.012114	0.000051	0.012114	0.000013
C(9)	U23	-0.000762	0.000040	-0.000762	0.000011
C(9)	U33	0.009276	0.000047	0.009276	0.000013
C(9)	X	0.462788	0.000014	0.462789	0.000004
C(9)	Y	0.365436	0.000010	0.365436	0.000003
C(9)	Z	0.756438	0.000007	0.756438	0.000002
C(10)	U11	0.020621	0.000066	0.020621	0.000020
C(10)	U12	-0.001473	0.000052	-0.001473	0.000015
C(10)	U13	-0.003772	0.000047	-0.003772	0.000017
C(10)	U22	0.015960	0.000060	0.015960	0.000016
C(10)	U23	-0.001608	0.000045	-0.001608	0.000010
C(10)	U33	0.010848	0.000053	0.010846	0.000017
C(10)	X	0.540521	0.000016	0.540521	0.000007
C(10)	Y	0.418289	0.000011	0.418289	0.000005

C(10)	Z	0.797180	0.000007	0.797180	0.000003
C(11)	U11	0.021112	0.000069	0.021112	0.000016
C(11)	U12	-0.003237	0.000053	-0.003237	0.000023
C(11)	U13	-0.004879	0.000051	-0.004879	0.000013
C(11)	U22	0.015877	0.000061	0.015877	0.000026
C(11)	U23	-0.002234	0.000047	-0.002234	0.000013
C(11)	U33	0.014395	0.000059	0.014395	0.000021
C(11)	X	0.625725	0.000016	0.625724	0.000007
C(11)	Y	0.477391	0.000011	0.477391	0.000005
C(11)	Z	0.772955	0.000008	0.772956	0.000003
C(12)	U11	0.021181	0.000067	0.021181	0.000019
C(12)	U12	-0.005870	0.000053	-0.005869	0.000017
C(12)	U13	-0.002607	0.000051	-0.002607	0.000014
C(12)	U22	0.014824	0.000059	0.014823	0.000016
C(12)	U23	-0.001470	0.000047	-0.001470	0.000017
C(12)	U33	0.014820	0.000060	0.014820	0.000016
C(12)	X	0.634578	0.000016	0.634578	0.000006
C(12)	Y	0.487661	0.000011	0.487662	0.000004
C(12)	Z	0.706139	0.000008	0.706139	0.000004
C(13)	U11	0.019287	0.000060	0.019286	0.000021
C(13)	U12	-0.004814	0.000051	-0.004814	0.000015
C(13)	U13	-0.001120	0.000048	-0.001120	0.000013
C(13)	U22	0.012592	0.000052	0.012592	0.000014
C(13)	U23	-0.000576	0.000042	-0.000576	0.000008
C(13)	U33	0.011739	0.000052	0.011736	0.000017
C(13)	X	0.563092	0.000015	0.563092	0.000006
C(13)	Y	0.437052	0.000010	0.437052	0.000004
C(13)	Z	0.665663	0.000007	0.665663	0.000003
C(14)	U11	0.013859	0.000052	0.013858	0.000015
C(14)	U12	-0.000744	0.000043	-0.000744	0.000013
C(14)	U13	-0.001084	0.000040	-0.001083	0.000011
C(14)	U22	0.010179	0.000048	0.010178	0.000014
C(14)	U23	-0.000630	0.000038	-0.000630	0.000010
C(14)	U33	0.009393	0.000047	0.009394	0.000016
C(14)	X	0.476508	0.000014	0.476508	0.000005
C(14)	Y	0.370881	0.000010	0.370881	0.000003
C(14)	Z	0.688537	0.000007	0.688537	0.000002
C(15)	D1+	0.026390	0.003936	0.026239	0.002943
C(15)	D1-	0.066006	0.004470	0.065795	0.001939
C(15)	H0	0.040978	0.004619	0.040711	0.002122
C(15)	H2+	-0.031898	0.004408	-0.032038	0.002379
C(15)	H2-	0.060283	0.005325	0.060656	0.004092
C(15)	H4+	0.055562	0.004351	0.055517	0.004256
C(15)	H4-	0.069566	0.004215	0.069488	0.003570
C(15)	M1	4.182873	0.024880	4.183092	0.015127
C(15)	O1+	-0.155061	0.004172	-0.155031	0.003066
C(15)	O1-	-0.234737	0.004631	-0.234688	0.002684
C(15)	O3+	0.209926	0.003872	0.209730	0.002562
C(15)	O3-	-0.063451	0.003595	-0.063352	0.003829

C(15)	Q0	-0.008123	0.003940	-0.007986	0.002530
C(15)	Q2+	-0.015372	0.003639	-0.015463	0.002477
C(15)	Q2-	-0.013154	0.003350	-0.013149	0.002836
C(15)	U11	0.013326	0.000055	0.013326	0.000020
C(15)	U12	-0.000690	0.000043	-0.000691	0.000016
C(15)	U13	0.001345	0.000039	0.001345	0.000013
C(15)	U22	0.010449	0.000051	0.010450	0.000016
C(15)	U23	-0.001970	0.000039	-0.001970	0.000013
C(15)	U33	0.012071	0.000050	0.012069	0.000015
C(15)	X	0.416884	0.000014	0.416884	0.000005
C(15)	Y	0.173948	0.000010	0.173948	0.000004
C(15)	Z	0.546449	0.000006	0.546448	0.000003
C(16)	D0	-0.065853	0.003891	-0.066055	0.003673
C(16)	H0	0.065155	0.003905	0.064467	0.004763
C(16)	H3-	0.082802	0.003994	0.082643	0.002318
C(16)	M1	4.297219	0.020665	4.296571	0.009734
C(16)	O0	0.347014	0.004349	0.346379	0.003049
C(16)	O3-	-0.177144	0.003706	-0.176617	0.002576
C(16)	Q0	-0.003329	0.003570	-0.003045	0.002276
C(16)	U11	0.018498	0.000061	0.018499	0.000025
C(16)	U12	-0.001011	0.000049	-0.001011	0.000020
C(16)	U13	0.002010	0.000047	0.002011	0.000011
C(16)	U22	0.016569	0.000060	0.016568	0.000014
C(16)	U23	-0.005136	0.000044	-0.005135	0.000012
C(16)	U33	0.013272	0.000054	0.013269	0.000018
C(16)	X	0.437589	0.000015	0.437589	0.000007
C(16)	Y	0.153510	0.000010	0.153509	0.000005
C(16)	Z	0.476004	0.000007	0.476005	0.000004
C(17)	U11	0.026249	0.000077	0.026249	0.000031
C(17)	U12	0.004379	0.000054	0.004381	0.000021
C(17)	U13	-0.003333	0.000057	-0.003333	0.000021
C(17)	U22	0.013283	0.000059	0.013283	0.000024
C(17)	U23	0.000039	0.000049	0.000039	0.000020
C(17)	U33	0.018796	0.000063	0.018795	0.000021
C(17)	X	0.504152	0.000017	0.504151	0.000009
C(17)	Y	0.118317	0.000011	0.118317	0.000005
C(17)	Z	0.588103	0.000008	0.588103	0.000003
C(18)	U11	0.012607	0.000054	0.012607	0.000018
C(18)	U12	-0.000509	0.000045	-0.000510	0.000013
C(18)	U13	0.000194	0.000042	0.000195	0.000014
C(18)	U22	0.013161	0.000054	0.013161	0.000021
C(18)	U23	0.002070	0.000042	0.002070	0.000016
C(18)	U33	0.011134	0.000049	0.011131	0.000016
C(18)	X	0.316864	0.000014	0.316864	0.000007
C(18)	Y	0.362568	0.000011	0.362568	0.000003
C(18)	Z	0.519437	0.000007	0.519437	0.000002
C(19)	U11	0.022758	0.000072	0.022758	0.000029
C(19)	U12	0.000121	0.000056	0.000122	0.000016
C(19)	U13	0.001475	0.000050	0.001476	0.000017

C(19)	U22	0.022899	0.000073	0.022900	0.000026
C(19)	U23	0.005360	0.000050	0.005361	0.000020
C(19)	U33	0.012064	0.000055	0.012060	0.000023
C(19)	X	0.358716	0.000016	0.358716	0.000008
C(19)	Y	0.389092	0.000012	0.389093	0.000005
C(19)	Z	0.452695	0.000008	0.452695	0.000004
C(20)	U11	0.023748	0.000073	0.023748	0.000022
C(20)	U12	0.007958	0.000054	0.007957	0.000013
C(20)	U13	0.000802	0.000054	0.000803	0.000016
C(20)	U22	0.016938	0.000064	0.016936	0.000030
C(20)	U23	0.000571	0.000052	0.000570	0.000014
C(20)	U33	0.018379	0.000064	0.018379	0.000023
C(20)	X	0.277753	0.000016	0.277753	0.000008
C(20)	Y	0.448336	0.000012	0.448335	0.000004
C(20)	Z	0.556245	0.000008	0.556245	0.000005
H(3)	D0	0.121690	0.001606	0.121756	0.000890
H(3)	M1	0.903546	0.002890	0.903551	0.001893
H(3)	U11	0.014917	0.000026	0.014916	0.000008
H(4)	U11	0.017877	0.000028	0.017877	0.000008
H(5)	U11	0.019676	0.000030	0.019678	0.000009
H(6)	U11	0.017946	0.000028	0.017947	0.000008
H(8)	U11	0.016568	0.000028	0.016567	0.000007
H(10)	U11	0.018973	0.000030	0.018971	0.000011
H(11)	U11	0.020555	0.000031	0.020554	0.000012
H(12)	U11	0.020331	0.000031	0.020330	0.000009
H(13)	U11	0.017446	0.000027	0.017446	0.000008
H(15)	D0	0.123394	0.003363	0.123401	0.002254
H(15)	M1	0.840225	0.006819	0.840276	0.003014
H(15)	U11	0.014339	0.000025	0.014338	0.000009
H(16A)	D0	0.118566	0.001671	0.118554	0.001424
H(16A)	M1	0.885385	0.004629	0.885555	0.001972
H(16A)	U11	0.024172	0.000037	0.024168	0.000010
H(16B)	U11	0.024172	0.000037	0.024168	0.000010
H(16C)	U11	0.024172	0.000037	0.024168	0.000010
H(17A)	U11	0.029162	0.000043	0.029164	0.000017
H(17B)	U11	0.029162	0.000043	0.029164	0.000017
H(17C)	U11	0.029162	0.000043	0.029164	0.000017
H(18)	U11	0.014763	0.000026	0.014759	0.000007
H(19A)	U11	0.028861	0.000043	0.028859	0.000015
H(19B)	U11	0.028861	0.000043	0.028859	0.000015
H(19C)	U11	0.028861	0.000043	0.028859	0.000015
H(20A)	U11	0.029531	0.000043	0.029531	0.000014
H(20B)	U11	0.029531	0.000043	0.029531	0.000014
H(20C)	U11	0.029531	0.000043	0.029531	0.000014

A7. SPAnPS – the radiant polymorph

A7.1. Powder diffraction

SPAnPS@toluene, top (black): experiment, bottom (green): simulation.

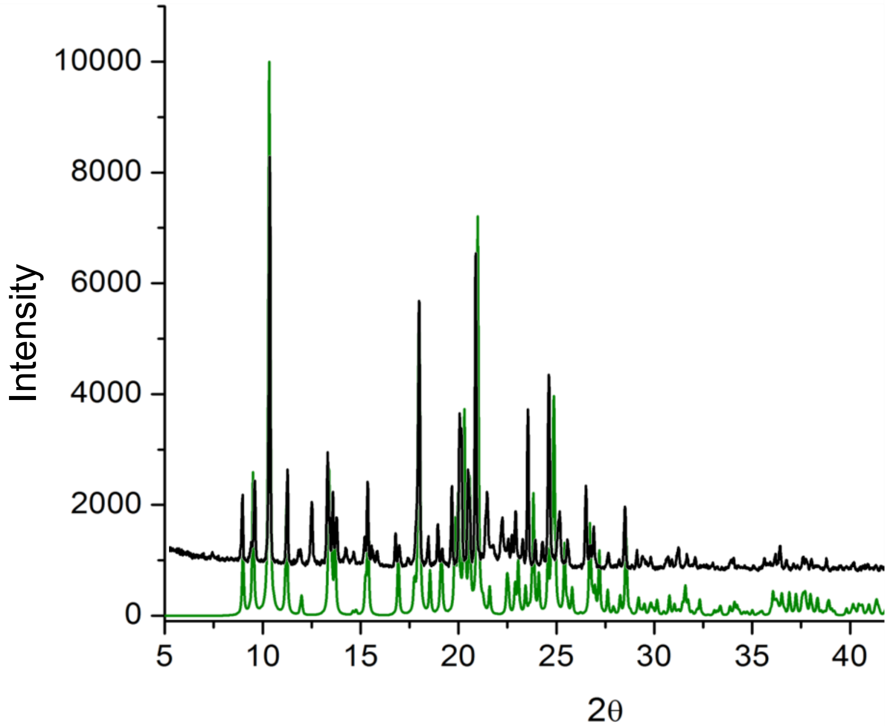

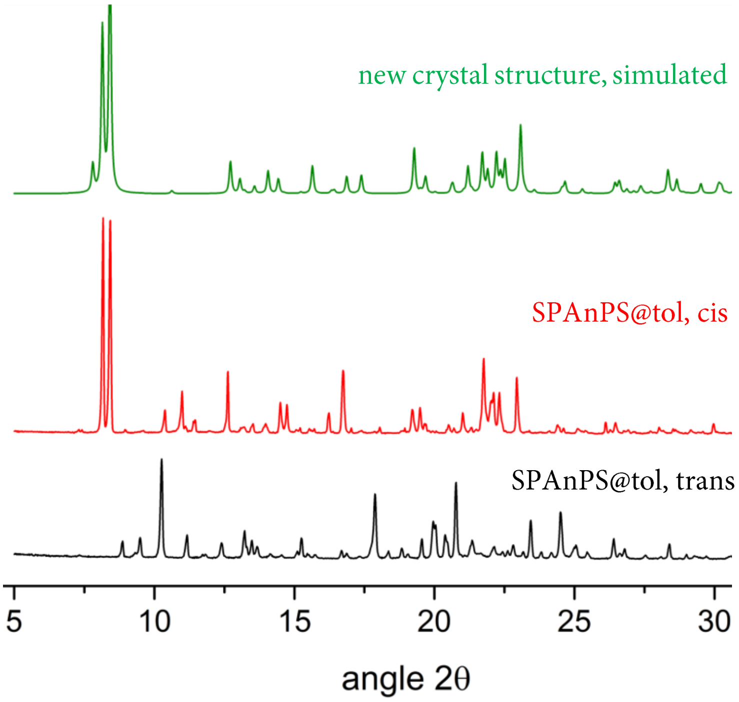

A7.2. From *trans* to *cis*

trans-SPAnPS@Toluene	*trans*-SPAnPS@Toluene	*cis*-SPAnPS@Toluene
$P2_1/n$	$P\bar{1}$	$C2/m$
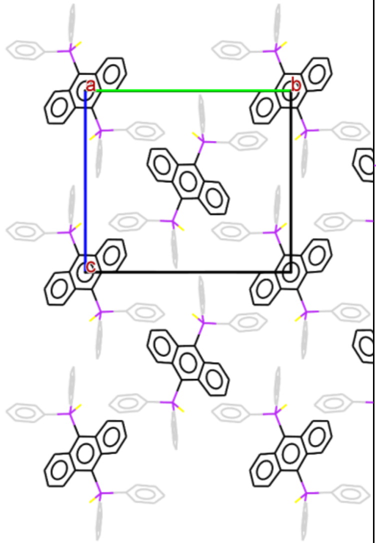	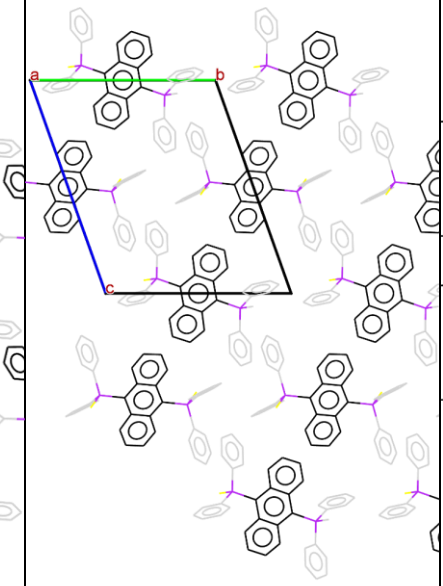	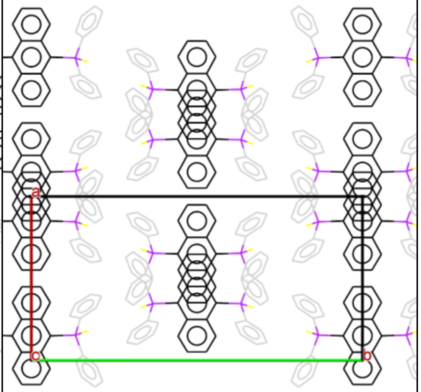
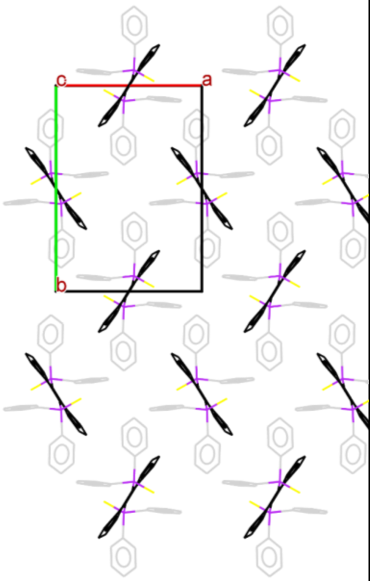	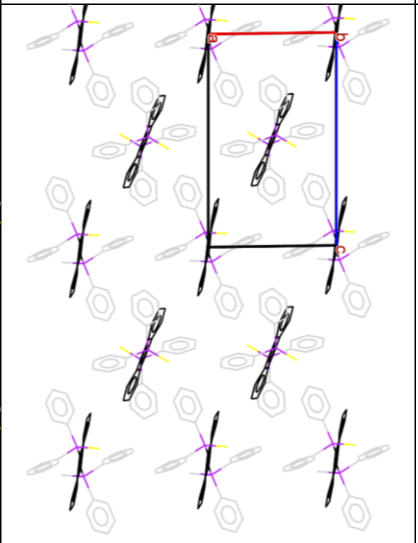	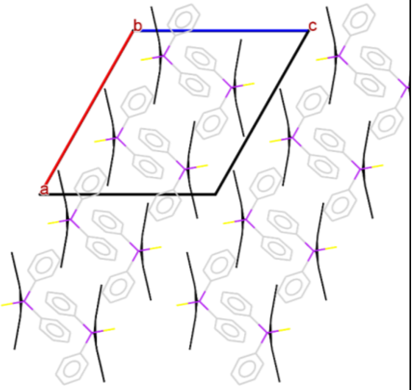

A7.3. Variation in emission intensity with crystal size. Emission spectra of *trans*-SPAnPS@benzene

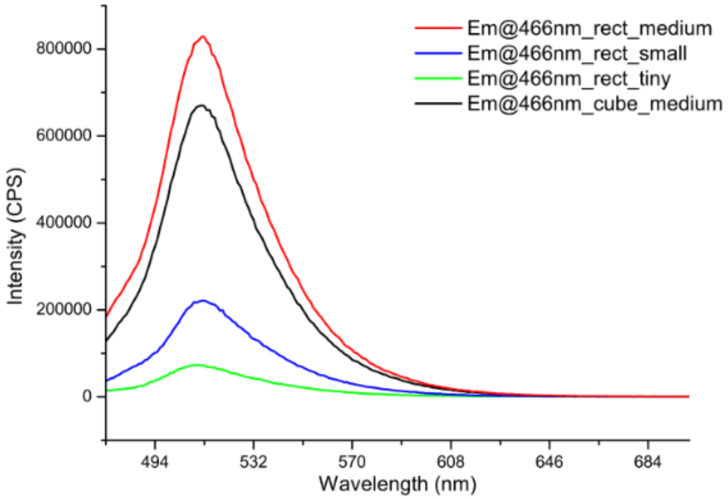

A7.4. Orientation dependence of the emission intensity of *trans*-SPAnPS@benzene

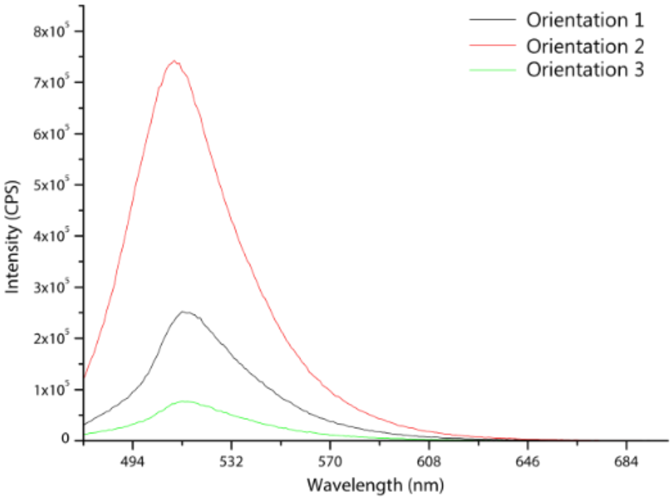

A7.5. Anisotropic fluorescence

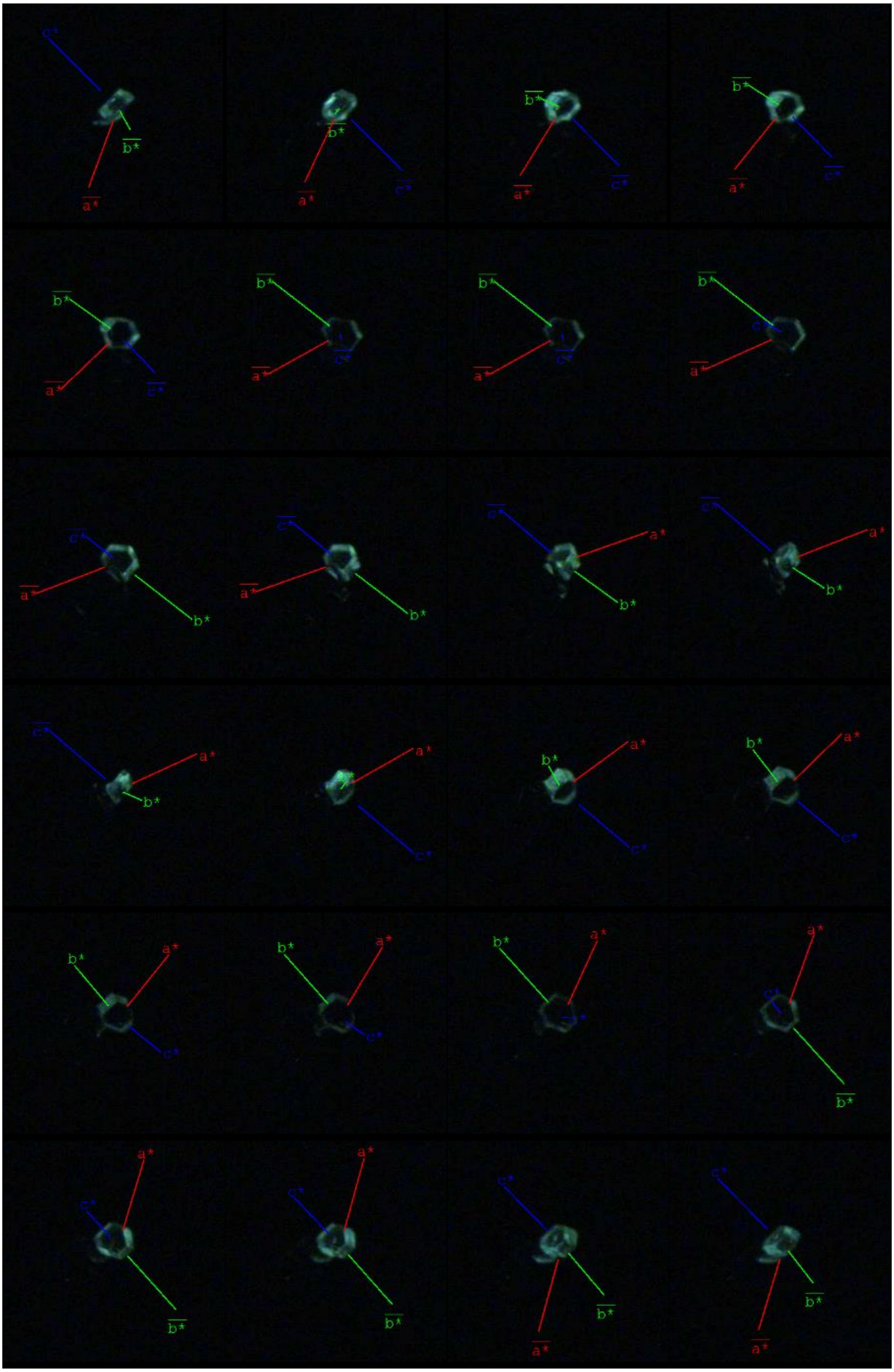

A7.6. *XD2006* refinement strategy and results

XDLSM refinement output

Number of data	25048
Rejected based on OBS	2040
Rejected based on SIGOBS	2040
Rejected based on SINTHL	0
Total number of rejections	2040
Included in the refinement	23008
$R(F)$	0.0276
$R(F^2)$	0.0197
$wR(F)$	0.0209
$wR(F^2)$	0.0396
*w*GoF	0.9901
GoF	1.3362
Nref/Nv	37.4723

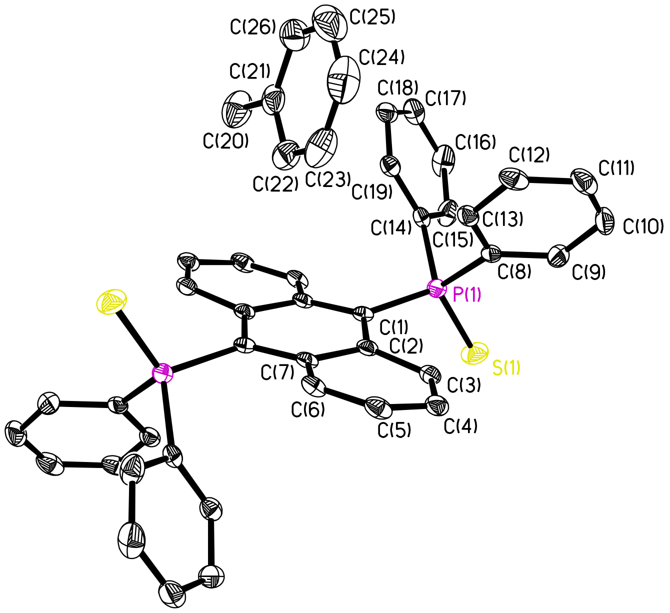

Abbreviations: *D*, dipoles; *Q*, quadrupoles; *O*, octapoles; *H*, hexadecapoles; *M*, monopoles; *xyz*, positional coordinates; *xyz*(H), hydrogen coordinates; *U*2, displacement parameters; *U*3 and *U*4, 3rd- or 4th-order Gram-Charlier parameters; κ, spherical expansion parameters, *κ*', aspherical expansion parameter; *d*: data, *p*: parameter, d_l: data truncated to $\sin(\theta)/\lambda < 0.5$, p_{mp}: mono- and multipole parameter.

step	**refined parameters**							***d***	***p***	***d/p***	d_l	p_{mp}	**κ**	d_l/p_{mp}
01	scalefactor							23008	10	2300.80	2139	0	0	-
02	-	-	-	-	-	*D Q O H*	-	23008	123	187.06	2133	113	0	18.88
03	-	-	-	-	*M*	*D Q O H*	-	23008	139	165.53	2133	130	0	16.41
04	*xyz*	*U*2	-	-	*M*	*D Q O H*	-	23008	391	58.84	2133	130	0	16.41
05	*xyz*(H)	-	-	-	-	-	-	2133	76	30.47	2133	0	0	-
06	*xyz*	*U*2	-	-	*M*	*D Q O H*	-	23008	391	58.84	2133	130	0	16.41
07	-	-	-	-	-	-	*κ*	23008	24	-	2133	0	14	-
08	*xyz*	*U*2	-	-	*M*	*D Q O H*	*κ*	23008	429	53.63	2133	154	14	12.70
09	*xyz*	*U*2	$U3^{\#}$	-	*M*	*D Q O H*	*κ*	23008	599	38.41	2133	154	14	12.70
10	*xyz*	*U*2	$U3^{\#}$	*U*4(S)	*M*	*D Q O H*	*κ*	23008	614	37.47	2133	154	14	12.70
11	-	-	-		-	-	*κ*'	23008	38	-	2133	0	14	-
12	*xyz*	*U*2	$U3^{\#}$	*U*4(S)	*M*	*D Q O H*	*κ*	23008	614	37.47	2133	154	14	12.70

$^{\#}$*U*3@C20, C21, C22, C23, C24, C25, C26, S1, P1, C9, C10, C11, C12, C16, C17, C18, C19

A7.7. Resolution dependent errors

Variation of $\sum F_o^2 / \sum F_c^2$ with respect to the resolution. Top, using one scale factor, left shows the results using 10 resolution dependent scale factors and right shows the distribution after the application of an empirical correction for resolution dependent errors according to (Niepötter et al., 2015).

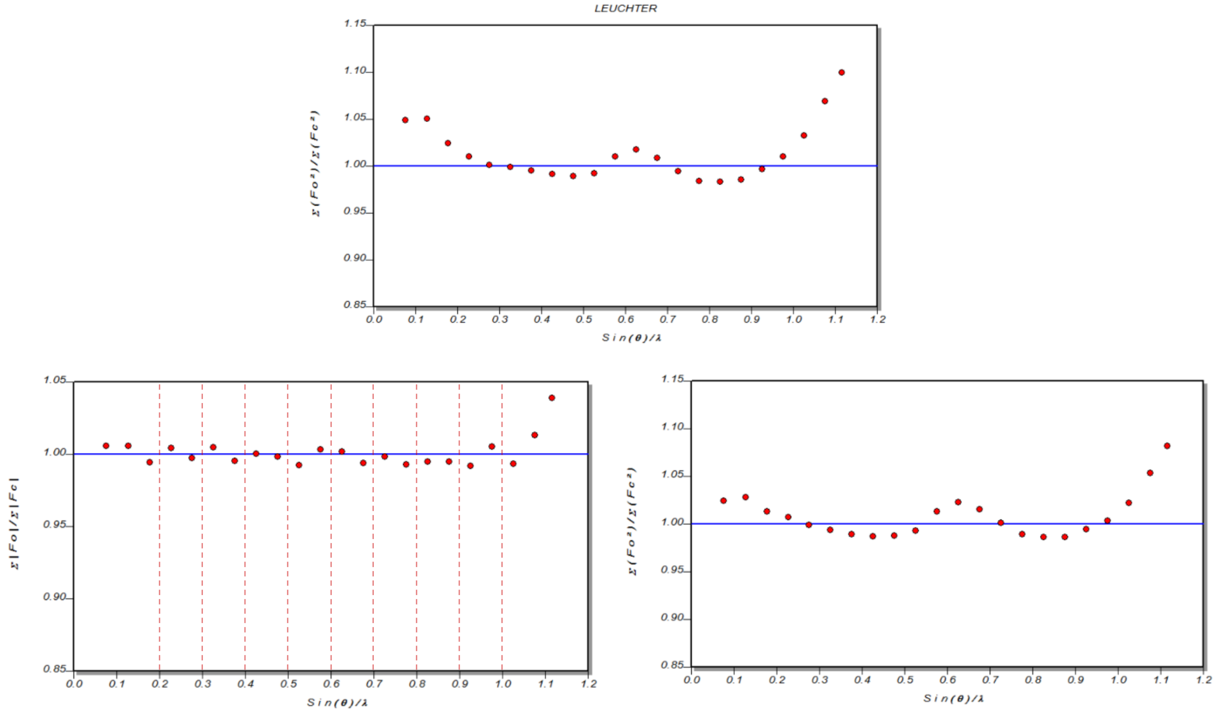

A7.8. Anharmonic motion

The table shows the minimum required resolution for a meaningful refinement of anharmonic motion (Gram-Charlier coefficients), for each anisotropic atom (mean displacement amplitude, M.D.A. in Å). See: Kuhs, W. F. (1992) Acta Cryst A48, 80-98.

Atom	Principal M.D.A's (Å)			Min. resolution (sin(θ)/λ)		Atom	Principal M.D.A's (Å)			Min. resolution (sin(θ)/λ)	
				n = 3	n = 4					n = 3	n = 4
C(20)	0.265	0.194	0.146	0.66	0.76	C(9)	0.182	0.153	0.109	0.89	1.03
C(21)	0.195	0.187	0.122	0.79	0.91	C(10)	0.205	0.170	0.118	0.81	0.94
C(22)	0.213	0.200	0.139	0.72	0.83	C(11)	0.195	0.150	0.129	0.83	0.96
C(23)	0.271	0.196	0.155	0.64	0.74	C(12)	0.172	0.135	0.133	0.89	1.03
C(24)	0.294	0.198	0.164	0.61	0.70	C(13)	0.14	0.130	0.122	0.99	1.15
C(25)	0.277	0.205	0.174	0.60	0.70	C(14)	0.146	0.125	0.101	1.06	1.22
C(26)	0.234	0.182	0.168	0.67	0.78	C(15)	0.226	0.145	0.102	0.87	1.00
H(20A)	0.432	0.238	0.223	0.46	0.53	C(16)	0.271	0.156	0.105	0.79	0.91
H(20B)	0.439	0.252	0.175	0.48	0.56	C(17)	0.226	0.154	0.111	0.82	0.95
H(20C)	0.5	0.279	0.214	0.42	0.48	C(18)	0.167	0.155	0.116	0.90	1.04
H(22)	0.287	0.266	0.185	0.54	0.62	C(19)	0.155	0.126	0.116	0.99	1.14
H(23)	0.379	0.251	0.211	0.48	0.55	H(3)	0.232	0.166	0.144	0.73	0.84
H(24)	0.385	0.261	0.196	0.48	0.55	H(4)	0.24	0.188	0.138	0.70	0.81
H(25)	0.362	0.298	0.197	0.47	0.54	H(5)	0.235	0.197	0.134	0.70	0.81
H(26)	0.315	0.255	0.205	0.51	0.59	H(6)	0.231	0.184	0.137	0.72	0.83
S(1)	0.212	0.173	0.105	0.83	0.95	H(9)	0.252	0.238	0.132	0.65	0.75

P(1)	0.14	0.117	0.101	1.09	1.26
C(1)	0.124	0.119	0.104	1.12	1.29
C(2)	0.127	0.118	0.104	1.12	1.29
C(3)	0.149	0.125	0.111	1.02	1.18
C(4)	0.161	0.136	0.111	0.96	1.11
C(5)	0.164	0.139	0.109	0.95	1.10
C(6)	0.15	0.130	0.108	1.01	1.17
C(7)	0.126	0.119	0.103	1.12	1.29
C(8)	0.14	0.118	0.109	1.06	1.23
H(10)	0.279	0.263	0.136	0.60	0.69
H(11)	0.255	0.240	0.158	0.61	0.70
H(12)	0.243	0.218	0.156	0.64	0.74
H(13)	0.224	0.190	0.136	0.72	0.83
H(15)	0.33	0.197	0.136	0.63	0.72
H(16)	0.398	0.219	0.125	0.58	0.67
H(17)	0.317	0.223	0.135	0.61	0.71
H(18)	0.259	0.211	0.147	0.65	0.75
H(19)	0.272	0.169	0.138	0.70	0.81

A7.9. *XDPDF* output

The following table shows a summary of the *XDPDF* output.
INP: Total integrated negative probability [%]
IPP: Total integrated positive probability [%]
MAX: maximum PDF value
MIN: minimum PDF value
VNP: Integrated volume for negative probability [Å^3]
VPP: Integrated volume for positive probability [Å^3]

	INP	IPP	MAX	MIN	VNP	VPP
C(9)	-0.005	100.004	42078.92	-8.55	0.659	3.563
C(10)	-0.011	100.002	31247.01	-14.94	0.767	3.455
C(11)	-0.034	100.034	33735.86	-36.94	0.893	3.329
C(12)	-0.004	100.004	41352.89	-6.41	0.787	3.435
C(16)	0	99.903	28764.56	-0.22	1.035	3.187
C(17)	-0.003	99.969	32923.25	-2.90	1.188	3.034
C(18)	-0.003	100.003	42638.96	-2.57	1.119	3.103
C(19)	-0.001	100.001	56491.54	-1.53	0.635	3.587
C(20)	-0.132	100.05	17482.48	-59.99	0.972	3.250
C(21)	-0.011	100.008	28684.83	-11.10	0.599	3.623
C(22)	-0.007	100.001	21627.33	-4.43	0.781	3.441
C(23)	-0.012	99.962	15498.29	-7.51	0.535	3.687
C(24)	-0.022	99.660	13434.59	-18.2	0.234	3.988
C(25)	-0.081	99.787	13190.80	-41.22	0.585	3.637
C(26)	-0.031	100.016	17940.24	-16.47	0.900	3.322
P(1)	-0.011	100.011	83177.63	-23.96	0.388	3.834
S(1)	-0.001	100	34462.82	-1.45	0.070	4.152

12 Bibliography

Books and book sections:

Araki, K. & Mutai, T. (2016). *Highlights in Photochemistry - Packing-directed tuning and switching of organic solid-state luminescence* in: *Photochemistry*, edited by A. Albini & E. Fasani, pp. 191-221. Croydon: The Royal Society of Chemistry.

Bader, R. F. W. (1990). *Atoms in Molecules - A Quantum Theory*. Oxford: Oxford University Press.

Bennett, D. W. (2010). *Understanding Single-Crystal X-Ray Crystallography*. Weinheim: Wiley-VCH.

Coppens, P. (1997). *X-ray Charge Densities and Chemical Bonding*. New York: Oxford University Press.

Flierler, U. & Stalke, D. (2012). *More than Just Distances from Electron Density Studies* in: *Electron Density and Chemical Bonding I: Experimental Charge Density Studies*, edited by D. Stalke, pp. 1-20. Berlin, Heidelberg: Springer Berlin Heidelberg.

Fourier, J. B. J. (1822). *Théorie Analytique de la Chaleur*. Cambridge: Cambridge University Press.

Gatti, C. & Macchi, P. (2012). *Modern Charge-Density Analysis*. Dordrecht, Heidelberg, London, New York: Springer.

Johnson, C. K. & Levy, H. A. (1974). *International Tables for X-Ray Crystallography*. Birmingham: Kynoch Press.

Kitai, A. H. (1993). *Solid State Luminescence*. Dordrecht: Springer Science+Business Media.

Lakowicz, J. R. (2006). *Principles of Fluorescence Spectroscopy*, 3rd ed. New York: Springer.

Massa, W. (2009). *Kristallstrukturbestimmung*, 6 ed. Wiesbaden: Springer Fachmedien Wiesbaden GmbH, Vieweg+Teubner Verlag.

Miller, W. H. (1839). *A Treatise on Crystallography*. Cambridge: J. & J.J. Deighton, London : J.W. Parker.

Montel, M. (1957). *X-ray Microscopy and Microradiography*. New York: Academic Press.

Nakatsuji, H. (1997). *SAC-CI Method: Theoretical Aspects and Some Recent Topics* in: *Computational Chemistry: Reviews of Current Trends*, pp. 62-124. Singapore: World Scientific Publishing Co. Pte. Ltd.

Pieper, J. & Freiberg, A. (2014). *The Biophysics of Photosynthesis*. New York: Springer New York.

Popelier, P. L. A. (2016). *Quantum Chemical Topology* in: *The Chemical Bond II*, pp. 71-117. Berlin: Springer International Publishing.

Quina, F. H. (1982). *Photophysical Concepts in Condensed Media* in: *Chemical and Biological Generation of Excited States*, edited by W. Adam & G. Cilento, pp. 1-32. New York: Academic Press.

Stalke, D. (2016). *Charge Density and Chemical Bonding* in: *The Chemical Bond I: 100 Years Old and Getting Stronger*, edited by D. M. P. Mingos, pp. 57-88. Cham: Springer International Publishing.

Storm, A. B., Michaelsen, C., Oehr, A. & Hoffmann, C. (2004). *Multilayer optics for Mo-radiation-based crystallography* in: *X-Ray Sources and Optics*, edited by C. A. MacDonald, A. T. Macrander, T. Ishikawa, C. Morawe & J. L. Wood, pp. 177-181. Bellingham, WA.

Thakkar, A. J. & Lupinetti, C. (2006). *Atomic Polarizabilities and Hyperpolarizabilities: A Critical Compilation* in: *Atoms, Molecules and Clusters in Electric Fields*, edited by G. Maroulis, pp. 505-529. London: Imperial College Press

Journal articles, articles, theses and programs:

Abramov, Y. A. (1997). *Acta Cryst.* **A53**, 264-272.

Agilent (2014). *CrysAlis PRO.*

Allen, F. H. & Bruno, I. J. (2010). *Acta Cryst.* **B66**, 380-386.

An, B.-K., Kwon, S.-K., Jung, S.-D. & Park, S. Y. (2002). *J. Am. Chem. Soc.* **124**, 14410-14415.

Angel, R. J. (2015). *Private communication.*

Arndt, U. (1990). *J. Appl. Cryst.* **23**, 161-168.

Arnold, O., Bilheux, J. C., Borreguero, J. M., Buts, A., Campbell, S. I., Chapon, L., Doucet, M., Draper, N., Ferraz Leal, R., Gigg, M. A., Lynch, V. E., Markvardsen, A., Mikkelson, D. J., Mikkelson, R. L., Miller, R., Palmen, K., Parker, P., Passos, G., Perring, T. G., Peterson, P. F., Ren, S., Reuter, M. A., Savici, A. T., Taylor, J. W., Taylor, R. J., Tolchenov, R., Zhou, W. & Zikovsky, J. (2014). *Nucl. Instrum. Meth. A* **764**, 156-166.

Azhakar, R., Ghadwal, R. S., Roesky, H. W., Hey, J., Krause, L. & Stalke, D. (2013). *Dalton Trans.* **42**, 10277-10281.

Bader, R. F. W. (1975). *Acc. Chem. Res.* **8**, 34-40.

Bader, R. F. W. (1991). *Chem. Rev.* **91**, 893-928.

Bader, R. F. W. (2009). *J. Phys. Chem. A* **113**, 10391-10396.

Bader, R. F. W. & Beddall, P. M. (1973). *J. Am. Chem. Soc.* **95**, 305-315.

Bader, R. F. W., Beddall, P. M. & Cade, P. E. (1971). *J. Am. Chem. Soc.* **93**, 3095-3107.

Becke, A. D. (1988). *Phys. Rev. A* **38**, 3098-3100.

Becke, A. D. (1993). *J. Chem. Phys.* **98**, 1372-1377.

Becker, P. J. & Coppens, P. (1974a). *Acta Cryst.* **A30**, 129-147.

Becker, P. J. & Coppens, P. (1974b). *Acta Cryst.* **A30**, 148-153.

Blessing, R. H. (1995a). *Acta Cryst.* **A51**, 33-38.

Blessing, R. H. (1995b). *Acta Cryst.* **B51**, 816-823.

Blessing, R. H. (1997). *J. Appl. Cryst.* **30**, 421-426.

Borek, D., Minor, W. & Otwinowski, Z. (2003). *Acta Cryst.* **D59**, 2031-2038.

Bruker (2009a). *SAINT.* Version 7.68A. Bruker AXS Inc., Madison, Wisconsin (USA).

Bruker (2009b). *APEX2.* Version 2012.2-0. Bruker AXS Inc., Madison, Wisconsin (USA).

Bruker (2013). *SAINT.* Version 8.30C. Bruker AXS Inc., Madison, Wisconsin (USA).

Bruker (2014a). *APEX2.* Version 2014.2-0. Bruker AXS Inc., Madison, Wisconsin (USA).

Bruker (2014b). *SADABS.* Version 2014/4. Bruker AXS Inc., Madison, Wisconsin (USA).

Bruker (2015). *XPREP.* Version 2015/2. Bruker AXS Inc., Madison, Wisconsin (USA).

Brünger, A. T. (1992). *Nature* **355**, 472-475.

Brünger, A. T. (1997). *Methods Enzymol.* **277**, 366-396.

Busing, W. R. & Levy, H. A. (1957). *Acta Cryst.* **10**, 180-182.

Chiba, M., Fedorov, D. G. & Kitaura, K. (2007). *J. Chem. Phys.* **127**, 104108.

Clark, S. J., Segall, M. D., Pickard, C. J., Hasnip, P. J., Probert, M. J., Refson, K. & Payne, M. C. (2005). *Z. Kristallogr.* **220**, 567-570.

Cochran, W. G. & Wishart, J. (1934). *Math. Proc. Cambridge* **30**, 178.

Coles, S. J. & Gale, P. A. (2012). *Chem. Sci.* **3**, 683-689.

Coles, S. J. & Hursthouse, M. B. (2004). *J. Appl. Cryst.* **37**, 988-992.

Collard, K. & Hall, G. G. (1977). *Int. J. Quantum Chem*, 623-637.

Cook, A. F. & Moffatt, J. G. (1968). *J. Am. Chem. Soc.* **90**, 740-746.

Coppens, P. (2005). *Angew. Chem. Int. Ed.* **44**, 6810-6811; *Angew. Chem.* **117**, 6970-6972.

Dectris Ltd. (2015). *PILATUS3: User Manual V3.*

Dectris Ltd. (2016). *PILATUS3 X CdTe - The detectors the hard X-ray community has been waiting for!*

Destro, R., Loconte, L., Presti, L. L., Roversib, P. & Soave, R. (2004). *Acta Cryst.* **A60**, 365-370.

Dexter, D. L. (1953). *J. Chem. Phys.* **21**, 836-850.

Diederichs, K. (2010). *Acta Cryst.* **A66**, 733-740.

Dittrich, B., Hübschle, C. B., Pröpper, K., Dietrich, F., Stolper, T. & Holstein, J. J. (2013). *Acta Cryst.* **B69**, 91-104.

Dittrich, B., Koritsánszky, T. & Luger, P. (2004). *Angew. Chem. Int. Ed.* **43**, 2718-2721; *Angew. Chem.* **116**, 2773-2776.

Dominiak, P. M. & Coppens, P. (2006). *Acta Cryst.* **A62**, 224-227.

Dominiak, P. M., Volkov, A., Li, X., Messerschmidt, M. & Coppens, P. (2006). *J. Chem. Theory Comput.* **3**, 232-247.

Dong, B., Wang, M., Xu, C., Feng, Q. & Wang, Y. (2012). *Cryst. Growth Des.* **12**, 5986-5993.

Dubler, E., Vedani, A. & Oswald, H. R. (1983). *Acta Cryst.* **C39**, 1143-1146.

Dudka, A. (2010). *J. Appl. Cryst.* **43**, 27-32.

Dunitz, J. D. & Gavezzotti, A. (2009). *Chem. Soc. Rev.* **38**, 2622-2633.

Eickerling, G., Hauf, C., Scheidt, E.-W., Reichardt, L., Schneider, C., Muñoz, A., Lopez-Moreno, S., Humberto Romero, A., Porcher, F., André, G., Pöttgen, R. & Scherer, W. (2013). *Z. Anorg. Allg. Chem.* **639**, 1985-1995.

Emsley, P. & Cowtan, K. (2004). *Acta Cryst.* **D60**, 2126-2132.

Emsley, P., Lohkamp, B., Scott, W. G. & Cowtan, K. (2010). *Acta Cryst.* **B66**, 486-501.

Evans, P. R. & Murshudov, G. (2013). *Acta Cryst.* **D69**, 1204-1214.

Farrugia, L. J. (2007). *Acta Cryst.* **E63**, i142.

XD2006: Program Version XD2016.01, User Manual Version 2016 (2016).

Farrugia, L. J., Evans, C. & Tegel, M. (2006). *J. Phys. Chem. A* **110**, 7952-7961.

Fei, Z., Kocher, N., Mohrschladt, C. J., Ihmels, H. & Stalke, D. (2003). *Angew. Chem. Int. Ed.* **42**, 783-787; *Angew. Chem.* **115**, 807-811.

Feng, X., Tong, B., Shen, J., Shi, J., Han, T., Chen, L., Zhi, J., Lu, P., Ma, Y. & Dong, Y. (2010). *J. Phys. Chem. B* **114**, 16731-16736.

Finkelmeier, N. (2013). *PhD Thesis,* Georg-August University, Göttingen.

Förster, T. (1949). *Z. Naturforsch.* **4**, 321-327.

Frisch, M. J., Trucks, G. W., Schlegel, H. B., Scuseria, G. E., Robb, M. A., Cheeseman, J. R., Scalmani, G., Barone, V., Mennucci, B., Petersson, G. A., Nakatsuji, H., Caricato, M., Li, X., Hratchian, H. P., Izmaylov, A. F., Bloino, J., Zheng, G., Sonnenberg, J. L., Hada, M., Ehara, M., Toyota, K., Fukuda, R., Hasegawa, J., Ishida, M., Nakajima, T., Honda, Y., Kitao, O., Nakai, H., Vreven, T., J. A. Montgomery, J., Peralta, J. E., Ogliaro, F., Bearpark, M., Heyd, J. J., Brothers, E., Kudin, K. N., Staroverov, V. N., Keith, T., Kobayashi, R., Normand, J., Raghavachari, K., Rendell, A., Burant, J. C., Iyengar, S. S., Tomasi, J., Cossi, M., Rega, N., Millam, J. M., Klene, M., Knox, J. E., Cross, J. B., Bakken, V., Adamo, C., Jaramillo, J., Gomperts, R., Stratmann, R. E., Yazyev, O., Austin, A. J., Cammi, R., Pomelli, C., Ochterski, J. W., Martin, R. L., Morokuma, K., Zakrzewski, V. G., Voth, G. A., Salvador, P., Dannenberg, J. J., Dapprich, S., Daniels, A. D., Farkas, O., Foresman, J. B., Ortiz, J. V., Cioslowski, J. & Fox, D. J. (2010). *Gaussian 09, Revision C.01.*

Gavezzotti, A. (2002). *J. Phys. Chem. B* **106**, 4145-4154.

Gavezzotti, A. (2003). *J. Phys. Chem. B* **107**, 2344-2353.

Gavezzotti, A. (2008). *Molecular Physics* **106**, 1473-1485.

Gonzalez, L., Escudero, D. & Serrano-Andres, L. (2012). *ChemPhysChem* **13**, 28-51.

Görbitz, C. H. (1999). *Acta Cryst.* **B55**, 1090-1098.

Grimme, S. (2006). *J. Comput. Chem.* **27**, 1787-1799.

Gruner, S. M. (2002). *Rev. Sci. Instrum.* **73**, 2815-2842.

Gruszecki, W. a. I. (1991). *J. Biol. Phys.* **18**, 99-109.

Guillot, B., Viry, L., Guillot, R., Lecomte, C. & Jelsch, C. (2001). *J. Appl. Cryst.* **34**, 214-223.

Guzei, I. A., Bikzhanova, G. A., Spencer, L. C., Timofeeva, T. V., Kinnibrugh, T. L. & Campana, C. F. (2008). *Cryst. Growth Des.* **8**, 2411-2418.

Haaland, A., Shorokhov, D. J. & Tverdova, N. V. (2004). *Chem. - Eur. J.* **10**, 4416-4421.

Hamilton, W. (1965). *Acta Cryst.* **18**, 502-510.

Hansen, N. K. & Coppens, P. (1978). *Acta Cryst.* **A34**, 909-921.

Hariharan, P. C. & Pople, J. A. (1973). *Theor. Chim. Acta* **28**, 213-222.

Harmening, T., van Wüllen, L., Eckert, H., Rodewald, U. C. & Pöttgen, R. (2010). *Z. Anorg. Allg. Chem.* **636**, 972-976.

State-of-the-art Multilayer Optics for X-ray Diffractometry (2010).

He, J., Xu, B., Chen, F., Xia, H., Li, K., Ye, L. & Tian, W. (2009). *J. Phys. Chem. C* **113**, 9892-9899.

Henn, J. & Meindl, K. (2010). *Acta Cryst.* **A66**, 676-684.

Herbst-Irmer, R., Henn, J., Holstein, J. J., Hübschle, C. B., Dittrich, B., Stern, D., Kratzert, D. & Stalke, D. (2013). *J. Phys. Chem. A* **117**, 633-641.

Herbst-Irmer, R. & Sheldrick, G. M. (1998). *Acta Cryst.* **B54**, 443-449.

Hertlein, F., Kroth, S., Michaelsen, C., Oehr, A. & Wiesmann, J. (2008). *Adv. Eng. Mat.* **10**, 686-691.

Hey, J. (2013). *PhD Thesis,* Georg-August University, Göttingen.

Hirshfeld, F. L. (1976). *Acta Cryst.* **A32**, 239-244.

Hirshfeld, F. L. (1977). *Theor. Chim. Acta* **44**, 129-138.

Hohenberg, P. & Kohn, W. (1964). *Phys. Rev.* **136**, B864-B871.

Hong, Y., Lam, J. W. & Tang, B. Z. (2009). *Chem. Commun.*, 4332-4353.

Hong, Y., Lam, J. W. & Tang, B. Z. (2011). *Chem. Soc. Rev.* **40**, 5361-5388.

Hopf, H. (1926). *Math. Ann.* **95**, 340-367.

Horiba (2008). *FluorEssence.* Version 3.0.

Hu, R., Leung, N. L. & Tang, B. Z. (2014). *Chem. Soc. Rev.* **43**, 4494-4562.

Huber, R. & Kopfmann, G. (1969). *Acta Cryst.* **A25**, 143-152.

Hübschle, C. B. & Dittrich, B. (2011). *J. Appl. Cryst.* **44**, 238-240

Hübschle, C. B., Sheldrick, G. M. & Dittrich, B. (2011). *J. Appl. Cryst.* **44**, 1281-1284.

Jacquemin, D., Preat, J., Perpète, E. A. & Adamo, C. (2010). *Int. J. Quantum Chem* **110**, 2121-2129.

Jayanty, S. & Radhakrishnan, T. P. (2004). *Chem. - Eur. J.* **10**, 791-797.

Jayatilaka, D. & Grimwood, D. J. (2003). *Tonto: A Fortran Based Object-Oriented System for Quantum Chemistry and Crystallography.*

Jha, K. K., Dutta, S., Kumar, V. & Munshi, P. (2016). *CrystEngComm* **18**, 8497-8505.

Johnson, E. R., Keinan, S., Mori-Sanchez, P., Contreras-Garcia, J., Cohen, A. J. & Yang, W. (2010). *J. Am. Chem. Soc.* **132**, 6498-6506.

Jørgensen, M. R. V., Hathwar, V. R., Sist, M., Wang, X., Hoffmann, C. M., Briseno, A. L., Overgaard, J. & Iversen, B. B. (2014). *Acta Cryst.* **A70**, 679-681.

Jørgensen, M. R. V., Svendsen, H., Schmøkel, M. S., Overgaard, J. & Iversen, B. B. (2012). *Acta Cryst.* **A68**, 301-303.

Kabsch, W. (2010). *Acta Cryst.* **D66**, 133-144.

Kamino, S., Muranaka, A., Murakami, M., Tatsumi, A., Nagaoka, N., Shirasaki, Y., Watanabe, K., Yoshida, K., Horigome, J., Komeda, S., Uchiyama, M. & Enomoto, S. (2013). *PCCP* **15**, 2131-2140.

Kaminski, R., Domagala, S., Jarzembska, K. N., Hoser, A. A., Sanjuan-Szklarz, W. F., Gutmann, M. J., Makal, A., Malinska, M., Bak, J. M. & Wozniak, K. (2014). *Acta Crystallogr. A* **70**, 72-91.

Karle, J. & Hauptman, H. (1950). *Acta Cryst.* **3**, 181-187.

Katayama, C. (1986). *Acta Cryst.* **A42**, 19-23.

Kirschbaum, K., Martin, A. & Pinkerton, A. A. (1997). *J. Appl. Cryst.* **30**, 514-516.

Kocher, N., Leusser, D., Murso, A. & Stalke, D. (2004). *Chem. - Eur. J.* **10**, 3622-3631.

Kopfmann, G. & Huber, R. (1968). *Acta Cryst.* **A24**, 348-351.

Koritsanszky, T. S. & Coppens, P. (2001). *Chem. Rev.* **101**, 1583-1628.

Kottke, T. & Stalke, D. (1993). *J. Appl. Cryst.* **26**, 615-619.

Kratzert, D. (2013). *PhD Thesis,* Georg-August University, Göttingen.

Krause, L., Herbst-Irmer, R., Sheldrick, G. M. & Stalke, D. (2015). *J. Appl. Cryst.* **28**, 3-10.

Kuhs, W. F. (1992). *Acta Cryst.* **A48**, 80-98.

Langhals, H., Potrawa, T., Nöth, H. & Linti, G. (1989). *Angew. Chem. Int. Ed.* **28**, 478-480; *Angew. Chem.* **101**, 497-499.

Lee, C., Yang, W. & Parr, R. G. (1988). *Phys. Rev. B* **37**, 785-789.

Lennard-Jones, J. E. (1931). *P. Phys. Soc.* **43**, 461-482.

Levitus, M., Schmieder, K., Ricks, H., Shimizu, K. D., Bunz, U. H. F. & Garcia-Garibay, M. A. (2001). *J. Am. Chem. Soc.* **123**, 4259-4265.

Lewis, G. N. (1916). *J. Am. Chem. Soc.* **38**, 762-785.

Li, C., Hanif, M., Li, X., Zhang, S., Xie, Z., Liu, L., Yang, B., Su, S. & Ma, Y. (2016). *J. Mater. Chem. C* **4**, 7478-7484.

Liu, J., Lam, J. W. & Tang, B. Z. (2009). *Chem. Rev.* **109**, 5799-5867.

London, F. (1928). *Z. Phys.* **46**, 455-477.

Lübben, J. & Grüne, T. (2015). *P. Natl. Acad. Sci. USA* **112**, 8999-9003.

Lübben, J., Volkmann, C., Grabowsky, S., Edwards, A., Morgenroth, W., Fabbiani, F. P., Sheldrick, G. M. & Dittrich, B. (2014). *Acta Cryst.* **A70**, 309-316.

Luo, J., Xie, Z., Lam, J. W. Y., Cheng, L., Tang, B. Z., Chen, H., Qiu, C., Kwok, H. S., Zhan, X., Liu, Y. & Zhu, D. (2001). *Chem. Commun.*, 1740-1741.

Macchi, P., Bürgi, H.-B., Chimpri, A. S., Hauser, J. & Gál, Z. (2011). *J. Appl. Cryst.* **44**, 763-771.

Macchi, P. & Coppens, P. (2001). *Acta Cryst.* **A57**, 656-662.

Macchi, P., Proserpio, D. M., Sironi, A., Soave, R. & Destro, R. (1998). *J. Appl. Cryst.* **31**, 583-588.

Madsen, A. Ø. (2006). *J. Appl. Cryst.* **39**, 757-758.

Makarov, N. S., Drobizhev, M., Wicks, G., Makarova, E. A., Lukyanets, E. A. & Rebane, A. (2013). *J. Chem. Phys.* **138**, 214314.

Martinez, C. R. & Iverson, B. L. (2012). *Chem. Sci.* **3**, 2191-2201.

Mei, J., Hong, Y., Lam, J. W., Qin, A., Tang, Y. & Tang, B. Z. (2014). *Adv. Mater.* **26**, 5429-5479.

Meindl, K. & Henn, J. (2008). *Acta Cryst.* **A64**, 404-418.

Michaelsen, C., Wiesmann, J., Hoffmann, C., Oehr, A., Storm, A. B. & Seijbel, L. J. (2004). *Proc. SPIE* **5193**, 211-219.

Mutai, T., Satou, H. & Araki, K. (2005). *Nat. Mater.* **4**, 685-687.

Mutai, T., Shono, H., Shigemitsu, Y. & Araki, K. (2014). *CrystEngComm* **16**, 3890-3895.

Mutai, T., Tomoda, H., Ohkawa, T., Yabe, Y. & Araki, K. (2008). *Angew. Chem. Int. Ed.* **47**, 9522-9524; *Angew. Chem.* **120**, 9664-9666.

Niepötter, B., Herbst-Irmer, R., Kratzert, D., Samuel, P. P., Mondal, K. C., Roesky, H. W., Jerabek, P., Frenking, G. & Stalke, D. (2014). *Angew. Chem. Int. Ed.* **53**, 2766-2770; *Angew. Chem.* **126**, 2806-2811.

Niepötter, B., Herbst-Irmer, R. & Stalke, D. (2015). *J. Appl. Cryst.* **48**, 1485-1497.

North, A. C. T., Phillips, D. C. & Mathews, F. S. (1968). *Acta Cryst.* **A24**, 351-359.

Obata, M., Machida, S. & Horie, K. (1999). *J. Polym. Sci. B* **37**, 2173-2181.

Ooyama, Y., Nakamura, T. & Yoshida, K. (2005). *New J. Chem.* **29**, 447-456.

Ozdemir, T., Atilgan, S., Kutuk, I., Yildirim, L. T., Tulek, A., Bayindir, M. & Akkaya, E. U. (2009). *Org. Lett.* **11**, 2105-2107.

Palatinus, L. (2013). *Acta Cryst.* **B69**, 1-16.

Park, S.-Y., Ebihara, M., Kubota, Y., Funabiki, K. & Matsui, M. (2009). *Dyes Pigments* **82**, 258-267.

Patterson, A. L. (1949). *Acta Cryst.* **A2**, 339-340.

Paul, A., Kubicki, M., Jelsch, C., Durand, P. & Lecomte, C. (2011). *Acta Cryst.* **B67**, 365-378.

Pendas, A. M., Francisco, E., Blanco, M. A. & Gatti, C. (2007). *Chem. - Eur. J.* **13**, 9362-9371.

Pickard, C. J. & Mauri, F. (2001). *Phys. Rev. B*, 245101.

Pietro, W. J., Francl, M. M., Hehre, W. J., DeFrees, D. J., Pople, J. A. & Binkley, J. S. (1982). *J. Am. Chem. Soc.* **104**, 5039-5048.

Pulay, P. (2011). *Int. J. Quantum Chem* **111**, 3273-3279.

Renge, I. (1992). *Journal of the Optical Society of America B* **9**, 719-723.

Rohrmoser, B., Eickerling, G., Presnitz, M., Scherer, W., Eyert, V., Hoffmann, R.-D., Rodewald, U. C., Vogt, C. & Pöttgen, R. (2007). *J. Am. Chem. Soc.* **129**, 9356-9365.

Saleh, G., Gatti, C. & Lo Presti, L. (2012a). *Comp. Theor. Chem.* **998**, 148-163.

Saleh, G., Gatti, C., Lo Presti, L. & Contreras-Garcia, J. (2012b). *Chem. - Eur. J.* **18**, 15523-15536.

Saleh, G., Presti, L. L., Gatti, C. & Ceresoli, D. (2013). *J. Appl. Cryst.* **46**, 1513-1517.

Saouane, S., Norman, S. E., Hardacre, C. & Fabbiani, F. P. A. (2013). *Chem. Sci.* **4**, 1270-1280.

Scherer, W., Hauf, C., Presnitz, M., Scheidt, E.-W., Eickerling, G., Eyert, V., Hoffmann, R.-D., Rodewald, U. C., Hammerschmidt, A., Vogt, C. & Pöttgen, R. (2010). *Angew. Chem. Int. Ed.* **49**, 1578-1582; *Angew. Chem.* **122**, 1623-1627.

Schomaker, V. & Trueblood, K. N. (1968). *Acta Cryst.* **B24**, 63-76.

Schomaker, V. & Trueblood, K. N. (1998). *Acta Cryst.* **B54**, 507-514.

Schultz, A. J., Jørgensen, M. R. V., Wang, X., Mikkelson, R. L., Mikkelson, D. J., Lynch, V. E., Peterson, P. F., Green, M. L. & Hoffmann, C. M. (2014). *J. Appl. Cryst.* **47**, 915-921.

Schultz, A. J., Srinivasan, K., Teller, R. G., Williams, J. M. & Lukehart, C. M. (1984). *J. Am. Chem. Soc.* **106**, 999-1003.

Schulz, T., Meindl, K., Leusser, D., Stern, D., Graf, J., Michaelsen, C., Ruf, M., Sheldrick, G. M. & Stalke, D. (2009). *J. Appl. Cryst.* **42**, 885-891.

Schuster, M. & Göbel, H. (1995). *J. Phys. D: Appl. Phys.* **28**, A270-A275.

Schwab, G. (2004). *Diploma Thesis,* Julius-Maximilians-Universität, Würzburg.

Schwab, G. (2008). *PhD Thesis,* Georg-August University, Göttingen.

Scott, J. L., Yamada, T. & Tanaka, K. (2004). *New J. Chem.* **28**, 447-450.

Shapiro, S. S. & Wilk, M. B. (1965). *Biometrika* **52**, 591-611.

Sheldrick, G. (2008). *Acta Cryst.* **A64**, 112-122.

Sheldrick, G. M. (2015a). *Acta Cryst.* **A71**, 3-8.

Sheldrick, G. M. (2015b). *Acta Cryst.* **C71**, 3-8.

Shigemitsu, Y., Mutai, T., Houjou, H. & Araki, K. (2014). *PCCP* **16**, 14388-14395.

Shimizu, M. & Hiyama, T. (2010). *Chem. - Asian J.* **5**, 1516-1531.

Shimizu, M., Takeda, Y., Higashi, M. & Hiyama, T. (2009). *Angew. Chem. Int. Ed.* **48**, 3653-3656; *Angew. Chem.* **121**, 3707-3710.

So long sulphur (2009). *Nat. Chem.* **1**, 333.

Spackman, M. A. (1986). *J. Chem. Phys.* **85**, 6579-6586.

Spackman, M. A. (2015). *Cryst. Growth Des.* **15**, 5624-5628.

Spackman, M. A. & Jayatilaka, D. (2009). *CrystEngComm* **11**, 19-32.

Spackman, M. A., Wolff, S. K., Grimwood, D. J., McKinnon, J. J., Turner, M. J. & Jayatilaka, D. (2012). *CrystalExplorer (Version 3.1).*

Stalke, D. (1998). *Chem. Soc. Rev.* **27**, 171-178.

Stalke, D. (2011). *Chem. - Eur. J.* **17**, 9264-9278.

Stalke, D. (2014). *Acta Cryst.* **B70**, 781-782.

Stanton, J. F. & Bartlett, R. J. (1993). *J. Chem. Phys.* **98**, 7029-7039.

Stewart, R. F. (1972). *J. Chem. Phys.* **57**, 1664-1668.

Stewart, R. F. (1973). *J. Chem. Phys.* **58**, 1668-1676.

Su, Z. & Coppens, P. (1998). *Acta Cryst.* **A54**, 646-652.

Tang, W., Xiang, Y. & Tong, A. (2009). *J. Org. Chem.* **74**, 2163-2166.

Tickle, I. J., Laskowski, R. A. & Moss, D. S. (2000). *Acta Cryst.* **D56**, 442-450.

Toby, B. H. (2001). *J. Appl. Cryst.* **34**, 210-213.

Turner, M. J., Grabowsky, S., Jayatilaka, D. & Spackman, M. A. (2014). *J. Phys. Chem. Lett.* **5**, 4249-4255.

Turner, M. J., McKinnon, J. J., Jayatilaka, D. & Spackman, M. A. (2011). *CrystEngComm* **13**, 1804-1813.

Turner, M. J., Thomas, S. P., Shi, M. W., Jayatilaka, D. & Spackman, M. A. (2015). *Chem. Commun.* **51**, 3735-3738.

Visscher, A. (2016). *PhD Thesis,* Georg-August University, Göttingen.

Volkov, A., Abramov, Y. A. & Coppens, P. (2001). *Acta Cryst.* **A57**, 272-282.

Volkov, A. & Coppens, P. (2001). *Acta Cryst.* **A57**, 395-405.

Volkov, A., Koritsanszky, T. & Coppens, P. (2004). *Chemical Physics Letters* **391**.

Volkov, A., Macchi, P., Farrugia, L. J., Gatti, C., Mallinson, P., Richter, T. & Koritsanszky, T. (2006). *XD2006.* Version 6.03/2016.01.

Weiss, M. (2001). *J. Appl. Cryst.* **34**, 130-135.

Wenger, E., Dahaoui, S., Alle, P., Parois, P., Palin, C., Lecomte, C. & Schaniela, D. (2014). *Acta Cryst.* **B70**, 783-791.

Williams, D. E. & Cox, S. R. (1984). *Acta Cryst.* **B40**, 404-417.

Wolf, H. (2014). *PhD Thesis,* Georg-August University, Göttingen.

Wolf, H., Jørgensen, M. R. V., Chen, Y.-S., Herbst-Irmer, R. & Stalke, D. (2014a). *Acta Cryst.* **B71**, 10-19.

Wolf, H., Leusser, D., Mads, R. V. J., Herbst-Irmer, R., Chen, Y. S., Scheidt, E. W., Scherer, W., Iversen, B. B. & Stalke, D. (2014b). *Chem. - Eur. J.* **20**, 7048-7053.

Wolf, H., Lock, N., Parker, S. F. & Stalke, D. (2015). *Chem. - Eur. J.* **21**, 4556-4560.

Wolstenholme, D. J. & Cameron, T. S. (2006). *J. Phys. Chem. A* **110**, 8970-8978.

Wolstenholme, D. J., Matta, C. F. & Cameron, T. S. (2007). *J. Phys. Chem. A* **111**, 8803-8813.

Yates, J. R., Pickard, C. J. & Mauri, F. (2007). *Phys. Rev. B* **76**.

Yokota, K., Hagimori, M., Mizuyama, N., Nishimura, Y., Fujito, H., Shigemitsu, Y. & Tominaga, Y. (2012). *Beilstein J. Org. Chem.* **8**, 266-274.

Zachariasen, W. H. (1952). *Acta Cryst.* **A5**, 68-73.

Zarychta, B., Zaleski, J., Kyziol, J., Daszkiewicz, Z. & Jelsch, C. (2011). *Acta Cryst.* **B67**, 250-262.

Zavodnik, V., Stash, A., Tsirelson, V., de Vries, R. & Feil, D. (1999). *Acta Cryst.* **B55**, 45-54.

Zhurov, V. V., Zhurova, E. A. & Pinkerton, A. A. (2008). *J. Appl. Cryst.* **41**, 340-349.